

## Interplay between Magnetism and Superconductivity in Iron Based High Temperature Superconductors

Stephen Price







Forschungszentrum Jülich GmbH  
Jülich Centre for Neutron Science (JCNS-2)

# **Interplay between Magnetism and Superconductivity in Iron Based High Temperature Superconductors**

Stephen Price

Schriften des Forschungszentrums Jülich  
Reihe Schlüsseltechnologien / Key Technologies

Band / Volume 77

---

ISSN 1866-1807

ISBN 978-3-89336-921-8

Bibliographic information published by the Deutsche Nationalbibliothek.  
The Deutsche Nationalbibliothek lists this publication in the Deutsche  
Nationalbibliografie; detailed bibliographic data are available in the  
Internet at <http://dnb.d-nb.de>.

Publisher and  
Distributor: Forschungszentrum Jülich GmbH  
Zentralbibliothek  
52425 Jülich  
Tel: +49 2461 61-5368  
Fax: +49 2461 61-6103  
Email: [zb-publikation@fz-juelich.de](mailto:zb-publikation@fz-juelich.de)  
[www.fz-juelich.de/zb](http://www.fz-juelich.de/zb)

Cover Design: Grafische Medien, Forschungszentrum Jülich GmbH

Printer: Grafische Medien, Forschungszentrum Jülich GmbH

Copyright: Forschungszentrum Jülich 2013

Schriften des Forschungszentrums Jülich  
Reihe Schlüsseltechnologien / Key Technologies, Band / Volume 77

D 82 (Diss., RWTH Aachen, University, 2013)

ISSN 1866-1807  
ISBN 978-3-89336-921-8

The complete volume is freely available on the Internet on the Jülicher Open Access Server (JUWEL)  
at [www.fz-juelich.de/zb/juwel](http://www.fz-juelich.de/zb/juwel)

Neither this book nor any part of it may be reproduced or transmitted in any form or by any  
means, electronic or mechanical, including photocopying, microfilming, and recording, or by any  
information storage and retrieval system, without permission in writing from the publisher.

# Kurzfassung

Die vorliegende Arbeit behandelt Untersuchungen magnetischer Eigenschaften Eisen-basierter Hochtemperatur-Supraleiter mittels Neutronenstreutechniken.

In unter dotiertem  $\text{Ba}(\text{Fe}_{0.95}\text{Co}_{0.05})_2\text{As}_2$  wurde das Spektrum kollektiver magnetischer Anregungen der Fe-Momente mit Propagationsvektor  $\mathbf{Q}=(0.5, 0.5, 0)$  untersucht. Die kollektiven Anregungen wurden quantitativ ausgewertet mit Hilfe eines Spin Wellen Models und eines Models basierend auf dem Mechanismus der Spin Diffusion. Es wurden magnetische Anregungen in drei Phasen des Phasendiagramms untersucht, die paramagnetische Phase oberhalb der magnetischen Ordnungstemperatur, die magnetisch geordnete Phase oberhalb des supraleitenden Phasenübergangs und die Phase der Koexistenz von Supraleitung und magnetischer Ordnung.

Das Spektrum kollektiver magnetischer Anregungen mit Propagationsvektor  $\mathbf{Q}=(0.5, 0.5, 0)$  in optimal dotiertem  $\text{CaFe}_{0.88}\text{Co}_{0.12}\text{AsF}$  zeigt in der supraleitenden Phase eine Anregungslücke für niedrige Energien und ein Resonanzsignal oberhalb der Lücke. Beide Effekte sind charakteristisch für magnetische Anregungen in Hochtemperatur-Supraleitern. Die Beobachtung des Resonanzsignals wird als ein Indiz für die  $s_{\pm}$  Symmetrie des supraleitenden Ordnungsparameters interpretiert. Die magnetisch geordnete Phase von undotiertem  $\text{CaFeAsF}$  zeigt Spin Wellen ähnliche Anregungen für Energien bis 20 meV und Temperaturen unterhalb des magnetischen Phasenübergangs. Oberhalb der Ordnungstemperatur sind die Anregungen stark gedämpft und von eher zweidimensionalem Charakter, bleiben jedoch sichtbar für Temperaturen bis zu 270 K.

In supraleitendem  $\text{FeSe}_{0.5}\text{Te}_{0.5}$  zeigt eine Untersuchung mittels polarisierter Neutronenstreuung, dass das Spektrum kollektiver Anregungen mit Propagationsvektor  $\mathbf{Q}=(0.5, 0.5, 0)$  und Energien bis zu 30 meV aus einer isotropen Verteilung von Anregungen mit fluktuierendem magnetischem Moment in ab- sowie in c-Richtung besteht. Gleiches gilt für das Resonanzsignal, welches in das Spektrum bei  $\mathbf{Q}=(0.5, 0.5, 0)$  integriert ist und ebenfalls zu gleichen Teilen aus Anregungen mit fluktuierendem Moment in ab- wie in c-Richtung besteht.

In  $\text{Eu}(\text{Fe}_{1-x}\text{Co}_x)_2\text{As}_2$  und  $\text{EuFe}_2(\text{As}_{1-x}\text{P}_x)_2$  wurde der Effekt von P- sowie Co-Dotierung auf die statische Ordnung der Eu-Momente untersucht. Die Dotierung mit Kobalt sorgt für einen Übergang der antiferromagnetischen Ordnung der Eu-Momente der undotierten Materialien in eine Helix-Ordnung, wobei die Eu-Momente weiterhin parallel zur ab-Ebene verbleiben. Im Gegensatz dazu sorgt eine Dotierung mit Phosphor für eine Verkipfung der Momente in c-Richtung. Die ferromagnetische Ordnung, resultierend aus den gekippten Momenten parallel zur c-Achse, koexistiert mit Supraleitung für Temperaturen unterhalb der Ordnungstemperatur der Eu-Momente.





# Abstract

In this thesis, magnetic properties of a series of different Fe-based superconducting materials have been studied by means of neutron scattering techniques.

Magnetic correlations in underdoped  $\text{Ba}(\text{Fe}_{0.95}\text{Co}_{0.05})_2\text{As}_2$  have been investigated for three phases of the phase diagram. It was possible to detect the spin gap and spin resonance signal, two features of the particle hole excitation spectrum at  $\mathbf{Q}=(0.5, 0.5, 0)$ , characteristic for the superconducting phase. The spin wave excitations present in the ordered phase have been analyzed quantitatively in terms of a linear spin wave model, whereas a spin diffusion model was applied to the collective excitations of the paramagnetic phase. However, it was found that both models can be applied to excitations in all three phases.

In optimally doped  $\text{CaFe}_{0.88}\text{Co}_{0.12}\text{AsF}$ , a spin resonance signal was detected as part of the spin excitation spectrum at  $\mathbf{Q}=(0.5, 0.5, 0)$ . The observation of the spin resonance signal supports the  $s_{\pm}$  symmetry of the superconducting gap function. In the undoped  $\text{CaFeAsF}$  compound three dimensional spin wave like excitations of the static Fe-SDW order have been observed at  $\mathbf{Q}_{AFM}=(0.5, 0.5, 0.5)$ , for temperatures below  $T_N$ . Above  $T_N$  and for energies below 20 meV, the spin wave like excitations are replaced by short range two dimensional paramagnetic excitations, which persist up to 270 K.

In superconducting  $\text{FeSe}_{0.5}\text{Te}_{0.5}$  polarized neutron scattering investigations revealed the magnetic nature of the spin resonance signal and the excitation spectrum at  $\mathbf{Q}=(0.5, 0.5, 0)$  up to 30 meV. The whole excitation spectrum including the spin resonance signal consists of an isotropic distribution of spin excitations with magnetic moments fluctuating in the ab-plane and perpendicular to the ab-plane,  $\chi''_{ab}(\mathbf{Q}, \omega) \approx \chi''_c(\mathbf{Q}, \omega)$ .

In  $\text{Eu}(\text{Fe}_{1-x}\text{Co}_x)_2\text{As}_2$  and  $\text{EuFe}_2(\text{As}_{1-x}\text{P}_x)_2$  the effect of impurity doping on the static order of the magnetic lattice of the  $\text{Eu}^{2+}$ -moments has been studied by means of polarized and non-polarized neutron diffraction experiments. The introduction of cobalt leads to a helical type structure of the Eu-sublattice with  $\text{Eu}^{2+}$ -moments oriented parallel to the ab-plane. Whereas, partial replacement of arsenic by phosphorous leads to a ferromagnetic type structure and eventually results in a coexistence of long range ferromagnetic order and superconductivity.



# Contents

<b>1</b>	<b>Introduction</b>	<b>1</b>
<b>2</b>	<b>Introduction to Superconducting Materials</b>	<b>5</b>
2.1	Conventional Superconductivity : BCS-Materials . . . . .	5
2.2	High $T_c$ Superconductivity in Cuprate Materials . . . . .	6
2.2.1	Discovery of High $T_c$ Superconductivity . . . . .	6
2.2.2	Magnetism and Superconductivity . . . . .	7
2.3	High $T_c$ Superconductivity in Fe-based Materials . . . . .	9
2.3.1	Structural Properties . . . . .	10
2.3.2	The Phase Diagrams . . . . .	11
2.3.3	Magnetic Properties . . . . .	13
2.3.4	Band Structure and Fermiology . . . . .	18
2.3.5	Superconducting Gap Symmetry . . . . .	21
2.3.6	The Spin Resonance Mode . . . . .	26
<b>3</b>	<b>Experimental and Theoretical Basics</b>	<b>33</b>
3.1	Scattering Basics . . . . .	33
3.1.1	Basic Neutron Scattering Formulas . . . . .	34
3.1.2	The Fluctuation-Dissipation Theorem . . . . .	40
3.1.3	Longitudinal Polarization Analysis . . . . .	41
3.2	Neutron Scattering Instruments . . . . .	43
3.2.1	The Three Axis Spectrometer . . . . .	43
3.2.2	The Time of Flight Neutron Spectrometer . . . . .	45
<b>4</b>	<b>Effect of P- and Co-Doping on the <math>\text{Eu}^{2+}</math> Magnetic Sublattice in <math>\text{EuFe}_2\text{As}_2</math></b>	<b>51</b>
4.1	Introduction . . . . .	51
4.1.1	Motivation . . . . .	51
4.1.2	Nuclear and Magnetic Structure of Undoped $\text{EuFe}_2\text{As}_2$ . . . . .	51
4.1.3	Pressure Induced Superconductivity in $\text{EuFe}_2\text{As}_2$ . . . . .	54
4.1.4	Doping Induced Superconductivity in $\text{EuFe}_2\text{As}_2$ . . . . .	54
4.2	Experimental Details . . . . .	55
4.3	Results and Discussion . . . . .	57
4.3.1	Magnetic Structure of $\text{EuFe}_2(\text{As}_{1-x}\text{P}_x)_2$ $x=0.05$ , $x=0.15$ . . . . .	57
4.3.2	Magnetic Structure of $\text{Eu}(\text{Fe}_{1-x}\text{Co}_x)_2\text{As}_2$ $x=0.014$ , $x=0.025$ . . . . .	65



4.4	Conclusion . . . . .	69
<b>5</b>	<b>ToF Neutron Scattering on Magnetic Excitations in <math>\text{Ba}(\text{Fe}_{0.95}\text{Co}_{0.05})_2\text{As}_2</math></b>	<b>71</b>
5.1	Introduction . . . . .	71
5.1.1	Motivation . . . . .	71
5.1.2	Coexistence of Superconductivity and Static Magnetic Order . . .	71
5.1.3	A Dispersive Spin Resonance Signal . . . . .	72
5.2	Experimental Details . . . . .	76
5.3	Results and Discussion . . . . .	77
5.3.1	Spin Gap and Spin Resonance in the Superconducting State . . .	77
5.3.2	Linear Spin Wave Model Analysis of Magnetic Excitations . . . .	82
5.3.3	Spin Diffusion Model Analysis of Magnetic Excitations in the Paramagnetic State . . . . .	98
5.3.4	Spin Diffusion Model Analysis of Magnetic Excitations in the Mag- netically Ordered State . . . . .	107
5.4	Conclusion . . . . .	112
<b>6</b>	<b>ToF Neutron Scattering on Magnetic Excitations in <math>\text{CaFe}_{1-x}\text{Co}_x\text{AsF}</math> with <math>x=0</math> ; <math>x=0.12</math></b>	<b>115</b>
6.1	Introduction . . . . .	115
6.1.1	Motivation . . . . .	115
6.1.2	Basic Properties of $\text{CaFe}_{1-x}\text{Co}_x\text{AsF}$ Materials . . . . .	116
6.2	Experimental Details . . . . .	118
6.3	Results and Discussion . . . . .	119
6.3.1	Magnetic Excitations in Superconducting $\text{CaFe}_{0.88}\text{Co}_{0.12}\text{AsF}$ . . .	119
6.3.2	Spin Wave Excitations in Parent $\text{CaFeAsF}$ . . . . .	126
6.4	Conclusion . . . . .	132
<b>7</b>	<b>Inelastic Neutron Scattering on Magnetic Excitations in Superconducting <math>\text{FeTe}_{0.5}\text{Se}_{0.5}</math></b>	<b>133</b>
7.1	Introduction . . . . .	133
7.1.1	Motivation . . . . .	133
7.1.2	Magnetic Excitations in Doped $\text{Fe}_{1-y}\text{Te}_{1-x}\text{Se}_x$ Materials . . . .	134
7.2	Experimental Details . . . . .	135
7.2.1	Longitudinal Polarization Analysis . . . . .	136
7.3	Results and Discussion . . . . .	137
7.4	Conclusion . . . . .	146
<b>8</b>	<b>Summary and Outlook</b>	<b>149</b>
<b>A</b>	<b>Appendix</b>	<b>153</b>
A.1	Spin Fluctuations in Metallic Materials . . . . .	153

A.1.1	The Magnetic Susceptibility in the Itinerant Approach . . . . .	153
A.1.2	The Response Function of the One Dimensional Electron Gas . . .	157
A.1.3	Instabilities in a One Dimensional Electron Gas . . . . .	160
A.1.4	The Spin Density Wave Groundstate . . . . .	162
A.2	Details of Time-of-Flight Neutron Data Treatment . . . . .	166
A.2.1	The Resolution of a ToF Instrument . . . . .	166
A.2.2	Resolution Correction for the Spin Wave Analysis . . . . .	167
A.2.3	Resolution Correction for the Spin Diffusion Model Analysis . . .	174
A.3	Additional Data . . . . .	178
A.3.1	FeTe <sub>0.5</sub> Se <sub>0.5</sub> Transverse Constant Energy Scans . . . . .	178

## Bibliography

179



# 1 Introduction

More than 25 years after its first discovery by Bednorz and Müller [1], the phenomenon of high-temperature superconductivity has not lost any of its original fascination. However, despite the tremendous effort made by scientists over the years the phenomenon of high  $T_c$  has not lost any of its mystery either. As conventional superconductivity and its corresponding effects are very well understood and described by the BCS theory [2], high  $T_c$  superconductivity still lacks a conclusive theoretical description which can be confirmed by experimental results. In BCS theory the formation of pairs of electrons with opposite momentum and spin  $[\mathbf{k}, \uparrow]$ ,  $[-\mathbf{k}, \downarrow]$  resulting in pairs with zero total net momentum  $\mathbf{k} = 0$  and zero total net spin  $S=0$ , so-called Cooper pairs, and the resulting creation of a condensate state of these Cooper pairs, is capable of explaining the characteristic effects, such as the zero electric resistivity and the Meissner effect. As the operating coupling mechanism responsible for these Cooper pairs, the BCS theory considers electron phonon coupling effects as the main driving mechanism, with an exchange of virtual phonons providing the pairing of the particles. In high  $T_c$  materials, however, the electron phonon coupling alone does not supply coupling strengths sufficient to explain the high critical temperatures observed in these materials. So in order to maintain the concept of Cooper pairs for unconventional superconductivity, the main task is to find a coupling mechanism capable of handling the high critical temperatures. The proximity of magnetically ordered states and superconductivity in the phase diagram of high  $T_c$  materials, is the main motivation for the consideration of possible relations between the pairing mechanism of Cooper pairs and magnetic degrees of freedom, where an exchange of spin fluctuations is discussed as possible contribution to the coupling of electrons to Cooper pairs. Magnetic degrees of freedom, in this case magnons or paramagnons, however, are much more difficult to investigate than phonons, as in the case of BCS materials. As a consequence, the role of magnetism in high  $T_c$  superconductivity remains unclear and the pairing mechanism of high  $T_c$  materials is still a mystery to this day.

Since the discovery of unconventional superconductivity in Fe-based materials in 2008 great effort has been made in investigating properties of these materials, theoretically as well as experimentally by applying a variety of different techniques. With its direct access to magnetic properties in general and especially dynamical magnetic excitations, neutron scattering plays a major role in the investigations of magnetism in these materials.

This thesis contains results obtained via experimental work. The scope of this work



was to investigate magnetic properties of Fe-based superconducting materials by means of neutron scattering techniques. By taking advantage of the versatility of neutron scattering it was possible to address very diverse aspects of magnetism in the Fe-based superconducting materials on a list of different compositions representative for the three main classes of Fe-based materials.

This thesis is organized in eight chapters which will be introduced briefly in the following:

- Chapter 2 gives a brief introduction to the main characteristics of Fe-based superconducting materials. The intention of this chapter is not to provide a detailed overview of this particular field but to introduce some of the main characteristics of these materials and it is clearly limited to properties which in one way or the other are related to effects investigated in the experimental work of this study. The chapter might be most useful for the reader not familiar with the field of superconductivity in Fe-based materials.
- Chapter 3 provides a brief introduction to the theoretical background of the experimental techniques, including the basic formulae of neutron scattering. The following experimental chapters refer to this background information at several occasions.
- Chapter 4 discusses the effect of impurity doping on the long range static magnetic order of the sublattice of  $\text{Eu}^{2+}$  magnetic moments in  $\text{Eu}(\text{Fe}_{1-x}\text{Co}_x)_2\text{As}_2$  and  $\text{EuFe}_2(\text{As}_{1-x}\text{P}_x)_2$  compositions, investigated via polarized and non polarized neutron diffraction experiments. Previous to the presented studies it has been shown via characterization techniques that doping with either phosphorous or cobalt leads to the onset of superconductivity. It was further shown that a coexistence of superconductivity and static magnetic order of the Eu-sublattice is present in these materials. The motivation of the presented work on these materials is to investigate this possible coexistence and to determine the exact effect of doping on the magnetic structure of the Eu-sublattice.
- Chapter 5 focuses on the excitation spectrum of spin fluctuations and spin wave excitations with propagation vector  $\mathbf{Q}_{AFM}=(0.5, 0.5, 1)$  in underdoped  $\text{Ba}(\text{Fe}_{0.95}\text{Co}_{0.05})_2\text{As}_2$ . The unique feature of this composition is a coexistence of static SDW-(Spin Density Wave)-order of the  $\text{Fe}^{2+}$  magnetic moments and bulk superconductivity. This coexistence enables to directly study a possible interplay of magnetic properties and superconductivity. In addition, the nature of magnetism in undoped Fe-based materials is still an ongoing topic, and investigations of the spin wave excitation spectrum of the static SDW-order can provide valuable insight to whether the magnetism in these materials should be regarded as localized or itinerant. The spin excitations have been studied for three different temperatures corresponding to three phases of the phase diagram, the phase of coexistence of static magnetic order and superconductivity, the phase of static magnetic order for temperatures above  $T_c$  and the paramagnetic phase above  $T_N$ .

- 
- Chapter 6 is dedicated to the studies of magnetic excitations at  $\mathbf{Q}_{AFM}=(0.5, 0.5, 0)$  in undoped CaFeAsF and superconducting CaFe<sub>0.88</sub>Co<sub>0.12</sub>AsF. Previous to this study the excitation spectrum of the spin fluctuations in these compositions was mostly unknown, and so the current investigations provide valuable information on the spin excitations in this class of oxygen free 1111-materials.
  - Chapter 7 addresses the excitation spectrum of spin fluctuations with propagation vector  $\mathbf{Q}_{AFM}=(0.5, 0.5, 0)$  in superconducting FeTe<sub>0.5</sub>Se<sub>0.5</sub>. The spin resonance, a characteristic feature of the particle hole excitation spectrum in the superconducting phase, present in a large number of high-temperature superconducting materials is still strongly debated considering its microscopic nature and impact on the superconducting phase. Several characteristics of the spin resonance mode have been investigated by performing a Linear Polarization Analysis of the data obtained via polarized neutron spectroscopy experiments.
  - Chapter 8 provides a brief summary of the obtained results discussed in detail in the previous chapters.



# 2 Introduction to Superconducting Materials

## 2.1 Conventional Superconductivity : BCS-Materials

Superconducting materials are characterized by the presence of mainly two characteristic effects, the effect of zero electric resistivity and the Meissner-Ochsenfeld effect, a complete exclusion of any interior magnetic field from the sample, for temperatures below a critical temperature  $T_c$  [3, 4]. The effect of superconductivity was first observed by Kamerlingh Onnes in 1911 while investigating the electric resistivity of mercury at low temperatures [3]. He found that when cooling below  $T_c=4.2$  K the resistivity abruptly dropped to a value close to zero and the material became superconducting. The discovery of the phenomenon of zero electric resistivity in mercury was soon followed by the observation of the effect in other materials, such as tin, lead and metallic alloys. A microscopic understanding of the phenomenon, however, was not given until about 46 years after the first discovery when Bardeen, Cooper and Schrieffer provided a theoretical approach suitable to describe the observed effects [2] by developing the so-called BCS theory. The main point of the BCS theory is the formation of so-called Cooper pairs. Below the critical temperature pairs of always two electrons with opposite momenta and spins  $[\mathbf{k}, \uparrow]$ ,  $[-\mathbf{k}, \downarrow]$  form a paired state with zero total net momentum  $\mathbf{k}=0$ , zero total net spin  $S=0$  and a consequential S-wave symmetry of the Cooper pair wave function. The bosonic character of these Cooper pairs leads to the formation of a large Bose Einstein condensate, which is capable to explain many of the observed phenomena. In BCS theory the formation of the Cooper pairs is caused by an attractive potential between the two electrons due to the interaction via exchange bosons, in this case virtual phonons. In a descriptive picture: an electron that travels the positively charged lattice of atomic nuclei interacts with the positive charges and leaves behind a small deformation of the lattice. A second electron with opposite spin and momentum feels the attractive potential of the enhancement of positive charges caused by the lattice deformation and thus indirectly interacts with the first electron, and both electrons form the Cooper pair<sup>1</sup>. For low temperatures, when many of these electron pairs are formed, the quantum mechanic wave functions of the Cooper pairs align and form a collective state, the Bose-Einstein condensate of the superconducting state. Once the condensate

---

<sup>1</sup>Note that this over simplified picture in fact is misleading as the actual formation of the Cooper pairs does not take place in real space but is clearly restricted to the momentum space.



is formed the Cooper pairs don't feel potentials not sufficient to break up the Cooper pair state which prevents them from scattering processes with either the lattice or other particles. This results in the onset of superconductivity with zero electric resistivity and in a lowering of the superconducting groundstate energy and consequently in a gap in the single particle excitation spectrum as excitations are only possible for energies that break up the Cooper pairs. This energy gap has its greatest value for low temperature and gradually decreases to zero when approaching the critical temperature  $T_c$ ,

$$E = 3.52k_B T_c \sqrt{1 - \frac{T}{T_c}} \quad (2.1)$$

$T_c$  itself is proportional to the coupling strength of the Cooper pairs which is related to the interaction potential  $V$ ,

$$k_B T_c = 1.14 E_D e^{-1/N(E_F)V} \quad (2.2)$$

where  $k_B$  is Boltzmann's constant,  $E_D$  the Debye cut off energy,  $N(E_F)$  the density of states at the Fermi level and  $V$  the interaction potential responsible for pair formation of the Cooper pairs, which in BCS theory is provided by the electron phonon interactions. The weakness of electron phonon coupling in combination with the low Debye energy for BCS superconducting materials leads to typical critical temperatures not higher than 30 K. Many very good and classical books and articles have been written on this subject [2, 5–12] which should provide the interested reader with a deep and thorough introduction to the topic of BCS superconductivity including a derivation of all formulas introduced in this section.

## 2.2 High $T_c$ Superconductivity in Cuprate Materials

### 2.2.1 Discovery of High $T_c$ Superconductivity

The field of high  $T_c$  superconductivity began with the first discovery by Bednorz and Müller in 1986 [1] when they found superconductivity in  $\text{La}_{2-x}\text{Ba}_x\text{CuO}_4$  with a critical temperature of  $T_c=30$  K. This was a rather shocking discovery for the majority of the solid state physics community as it immediately became obvious that this new superconducting material was not compatible with BCS theory. This impression was even reinforced by the soon followed discoveries of further materials with even higher critical temperatures easily surpassing the temperature of liquid nitrogen, as reports of superconductivity in  $\text{YBa}_2\text{Cu}_3\text{O}_{7-\delta}$  with  $T_c=93$  K [13],  $\text{BiSrCa}_2\text{CuO}_x$  with  $T_c=105$  K [14],  $\text{Tl}_2\text{Ba}_2\text{Ca}_2\text{Cu}_3\text{O}_{10}$  with  $T_c=120$  K [15] or even  $\text{HgBa}_2\text{Ca}_2\text{Cu}_3\text{O}_8$  with  $T_c=163$  K (under pressure) [16] were made. These findings really caused a lot of confusion in the condensed matter community as they clearly were against any predictions made by BCS theory which at that time was working very well in describing the then known

superconducting materials and was believed to be a theory capable of describing superconductivity in general. Another point that complicated things even more was the fact that these cuprate materials in their so-called parent phase were highly correlated Mott-type insulators with long range static antiferromagnetic order. This showed that these new superconducting cuprate materials most likely were a different type of superconductors with a different type of coupling mechanism as BCS theory was not capable of explaining neither the high coupling strengths of the Cooper pairs needed for those high transition temperatures nor the presence of magnetism in the system.

### 2.2.2 Magnetism and Superconductivity

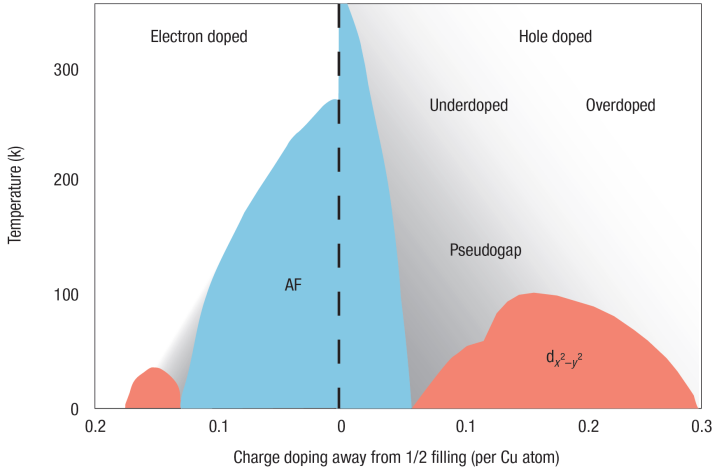
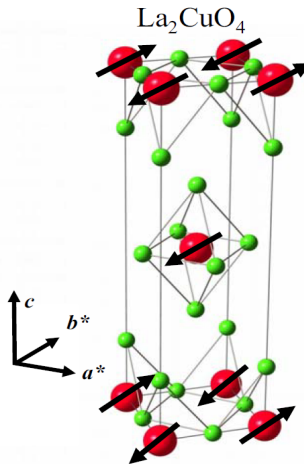


**Figure 2.1:** Typical phase diagram of electron or hole doped cuprate high  $T_c$  superconductors. Light blue regions illustrate the presence of static long range antiferromagnetic order of  $\text{Cu}^{2+}$ -moments. Red regions symbolize the superconducting phase with  $d_{x^2-y^2}$  wave symmetry of the superconducting gap function. Grey shaded region symbolizes the presence of the pseudo gap feature. Figure taken from reference [17].

In contrast to the BCS materials, where magnetism is harmful to the formation of superconducting states as it acts as pair breaking to the Cooper pairs, all superconducting cuprate materials universally descend from undoped parent materials which are Mott insulators and exhibit static long range magnetic order. Even though band structure calculations show that the  $d_{x^2-y^2}$ -orbitals of the  $\text{Cu}^{2+}$  ions are located close to the Fermi surface which would suggest a metallic character for the materials, the strong on-site Coulomb repulsion results in a splitting of the  $d_{x^2-y^2}$ -band into two Hubbard bands with only the lower Hubbard band filled and with an energy gap of several eV separating both

**Figure 2.2:** Crystal and magnetic structure of  $\text{La}_2\text{CuO}_4$ . Only Cu (red) and O (green) ions are shown. Black arrows illustrate the collinear static structure of magnetic  $\text{Cu}^{2+}$ -moments. Figure taken from reference [18].



bands. This causes the strong localization of the unpaired electrons and consequently leads to the insulating character. The highly correlated unpaired electrons lead to a localized magnetic moments of spin  $S=1/2$ . Below  $T_N$  these localized  $\text{Cu}^{2+}$  moments form a long range antiferromagnetic structure with moments confined in the basal-planes of the crystal. For these insulating materials, magnetism can be very well described using a local moment approach with spin correlations mediated via nearest and next nearest neighbor exchange interactions of localized magnetic moments. Doping the system with either holes or electrons<sup>2</sup> continuously suppresses the static magnetic order and eventually induces superconductivity. With increasing doping concentration  $T_c$  increases until a maximal  $T_c$  is reached, from where further increased doping concentration leads to a suppression of superconductivity. With the static magnetic order suppressed, strong magnetic fluctuations remain for the entire superconducting phase. This proximity of two phenomena which are incompatible in BCS-materials due to the pair breaking effect of the magnetism, and the presence of strong spin fluctuations throughout the entire superconducting phase were the main motivation for the proposal of magnetic degrees of freedom playing a leading role in the pairing mechanism of Cooper pairs in these materials. Despite over twenty-five years of intensive research and a tremendous gain of understanding of the materials, however, the role of magnetism in the mechanism behind high  $T_c$  superconductivity is still a mystery.

---

<sup>2</sup>In this case, hole or electron doping considers character of the additional charge carries introduced to the system due to the introduction of the foreign atoms.

## 2.3 High $T_c$ Superconductivity in Fe-based Materials

For years the effect of high  $T_c$  superconductivity has been studied mainly in cuprate materials which almost lead to the conclusion that substantial copper content might be an obligatory condition for materials to exhibit high-temperature superconductivity. In 2008 this misconception was clearly disproved as Kamihara et al. discovered high-temperature superconductivity in a copper free material,  $\text{LaFeAsO}_{1-x}\text{F}_x$  with  $T_c=26$  K [19]. This finding, which immediately was followed by the discovery of superconductivity for a great number of other Fe-based superconducting materials, caused a lot of excitement in the community and propelled the field of high  $T_c$  superconductivity, which at that time had slowed down a bit compared to the beginnings in 1986, back to be one of the most exciting fields in condensed matter physics again. With the discovery by Kamihara et al. a real rush for new compositions with even higher critical temperatures was started and within a short span of time numerous discoveries were made. It was found that by replacing lanthanum in  $\text{LaFeAsO}_{1-x}\text{F}_x$  by magnetic rare earths such as Ce, Sm, Nd or Pr the critical temperature could easily be increased up to 56 K [20–23]. Materials with this type of composition crystallize in the tetragonal  $\text{ZrCuSiAs}$ -type structure and are labeled the 1111-class of Fe-based materials. Simultaneously another class of Fe-based materials was discovered as Rotter et al. observed superconductivity with  $T_c=38$  K in  $\text{Ba}_{0.6}\text{K}_{0.4}\text{Fe}_2\text{As}_2$  [24]. Later further materials with this type of composition were found, which all crystalize in the body-centered tetragonal  $\text{ThCr}_2\text{Si}_2$ -type structure and are labeled the 122-class of Fe-based superconducting materials. In addition to the 1111- and 122-type materials two further classes were found, the 111-type represented by  $\text{LiFeAs}$  with  $T_c=18$  K [25–27] and the binary 11-type  $\alpha\text{FeSe}$  materials first observed by Hsu et al. with  $T_c=8$  K [28].

By now the field of Fe-based superconductors has been fully established and has become a very active field in solid state research with an uncountable number of scientific publications, a long list of international research groups working on a variety of different topics. Many different materials have been discovered with a range of different properties investigated with almost every experimental technique imaginable. The following sections will try to give a brief introduction to some of the basic properties of these Fe-based superconducting materials. However, the following sections should not be mistaken as a complete review of the field or anything close to this as this would clearly be beyond the scope of this thesis.

### 2.3.1 Structural Properties

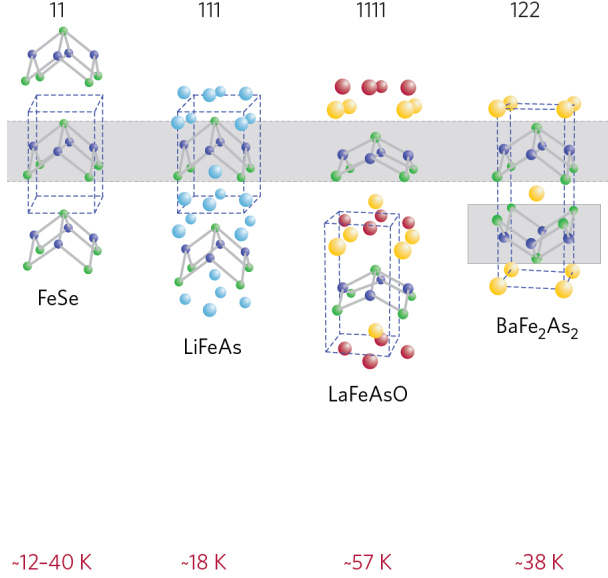


**Figure 2.3:** Crystal structure of the four main classes of Fe-based materials. Also listed are the maximal observed critical temperatures for that particular class of Fe-based superconductors. The blue shaded area highlights the Fe<sub>2</sub>As<sub>2</sub>-layers consisting of Fe-atoms (blue spheres) surrounded by As-tetrahedra (green spheres), present in all Fe-based materials. Blue dashed boxes illustrate unit cells of the various structures. The red numbers at the bottom are the respective  $T_c$  of the particular composition. Figure taken from reference [29].

Similar to the previously discussed cuprate materials, Fe-based superconductors crystallize in layered crystal structures. As illustrated in figure 2.3 for the four main classes of Fe-based materials, these layered crystal structures are organized in an alternate stacking of Fe<sub>2</sub>As<sub>2</sub>-layers and layers containing the other elements of the composition. The only exception are the 11-materials<sup>3</sup> as here the Fe<sub>2</sub>As<sub>2</sub>-layers are substituted by Fe<sub>2</sub>(Se/Te)<sub>2</sub>-layers, with the absence of additional buffer layers. From band structure calculations it is known that the density of states at the Fermi energy  $N(E_F)$  is dominated by the Fe 3d states and thus it is believed that the Fe<sub>2</sub>As<sub>2</sub>-layers (Fe<sub>2</sub>(Se/Te)<sub>2</sub>-layers) are responsible for the superconductivity in the system. These Fe<sub>2</sub>As<sub>2</sub>-layers are organized in a way where each Fe-atom is surrounded by a tetrahedron of four As-atoms. The shape

<sup>3</sup>The number-labeling shown in the figure is not restricted to one particular composition but labels a class of compounds which possess the same composition but which can vary in the included elements.

of these tetrahedra surrounding the Fe-atoms in fact might impact the formation of the superconducting phase as it has been suggested that less distorted tetrahedra lead to higher critical temperatures [30, 31]. As a result it was even proposed that the structural effects caused by doping might even be more important for the creation of superconductivity than the additional charge carries provided by the introduction of foreign atoms to the system [32].

At room temperature all structures exhibit a tetragonal symmetry which with decreasing temperature will transition into a phase with lower orthorhombic symmetry. With the introduction of foreign atoms to the structure this tetragonal-orthorhombic phase transition is gradually suppressed in temperature which is accompanied by a reduction of the orthorhombic distortion. This suppression of orthorhombic distortion might in fact be beneficial to the formation of superconductivity in the system [33].

### 2.3.2 The Phase Diagrams

The phase diagrams of the main classes of Fe-based superconducting materials show a great amount of similarities not just between the different classes of Fe-based materials but also to the phase diagrams of cuprate materials. Similar to the cuprates, all undoped Fe-based materials exhibit long range antiferromagnetic order, as in this case the  $\text{Fe}^{2+}$  moments form a magnetic sublattice. The magnetic order sets in after the crystal structure has transitioned from tetragonal to orthorhombic symmetry. In the 11-materials both phase transitions, magnetic and structural, occur simultaneously at the same temperature whereas for the 122-class the two transitions start to separate for higher doping concentrations. For 1111-class even the undoped materials exhibit a temperature difference of up to 20 K between the structural and magnetic transition. Orbital ordering and nematic ordering have been proposed [35] to explain this large temperature difference, but a conclusive explanation of this effect is not found to this date.

Doping the system with foreign atoms is one method to suppress the magnetic order and eventually induce superconductivity to the system. The doping can be conducted in several different ways, as basically all elements of the material can be replaced by foreign atoms. Depending if the introduction of these foreign atoms absorbs or emits electrons from or to the system the doping is referred to as either hole- or electron-doping. Increased doping concentration leads to a continuous suppression of the magnetic and nuclear transition temperatures which is accompanied by a continuous reduction of the ordered magnetic moment and orthorhombic distortion of the crystal structure. As soon as the long range order is suppressed the system becomes superconducting, and aside for a small phase present in 122-materials the superconducting phase is related to a tetragonal crystal structure. For some 122-materials [36–42] and 1111-materials [43, 44, 44, 45] superconductivity even sets in before the magnetic order is completely suppressed, which leads to a coexistence of static magnetic order and superconductivity, and which clearly illustrates the compatibility of magnetism and superconductivity in

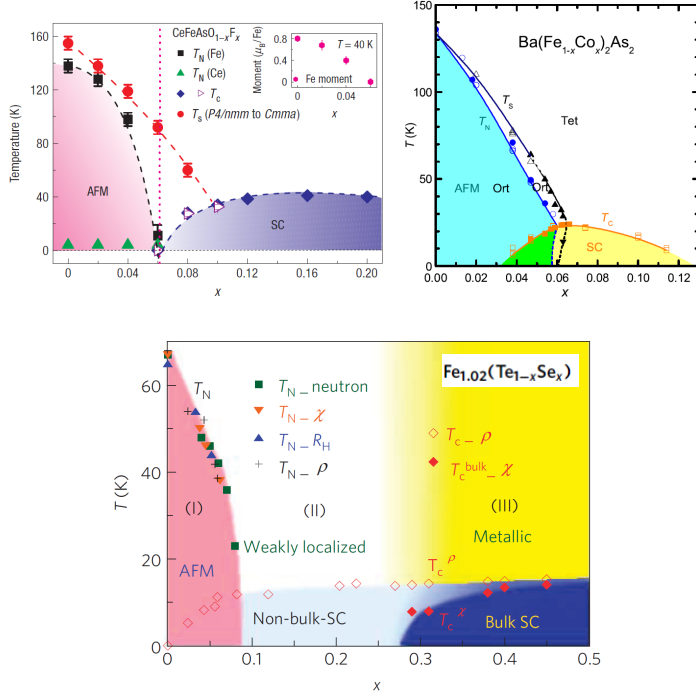


**Figure 2.4:** Temperature doping concentration phase diagrams of electron doped  $\text{CeFeAsO}_{1-x}\text{F}_x$  representative for 1111-type materials, of electron-doped  $\text{Ba}(\text{Fe}_{1-x}\text{Co}_x)_2\text{As}_2$  representative for 122-type materials and of isovalent doped  $\text{Fe}_{1.02}\text{Te}_{1-x}\text{Se}_x$  representing the binary 11-type materials. Illustrated phases in all phase diagrams are, tetragonal-paramagnetic for  $T > T_S$ ; orthorhombic-paramagnetic for  $T_S > T > T_N$  (only present for 1111- and 122-type materials); orthorhombic-antiferromagnetic for  $T < T_N$ ; tetragonal-superconducting for  $T < T_c$ . Green colored region in 122-phase diagram represents phase of coexistence of superconductivity and magnetic order. Light blue region in 11-phase diagram represents spin glass phase with filamentary superconductivity for  $x=0.1-0.3$  and  $T < T_c$ . Figures taken from references [31, 33, 34].

these materials. The superconducting phase forms a dome-like shape in the phase diagram where the highest  $T_c$  is reached for a certain doping level (optimal doped), whereas both lower doping (under doped) and higher doping concentrations (over doped) lead to lower  $T_c$  and an eventual complete suppression of superconductivity. In contrast to the 1111- and 122-materials, in the 11-materials the suppression of the long range magnetic order does not imply an immediate onset of superconductivity, and instead both phases are separated by a phase with short range spin glass like magnetic order and filamentary

superconductivity. Bulk superconductivity does not occur in these materials unless the short range spin glass order is completely suppressed [34, 46].

### 2.3.3 Magnetic Properties

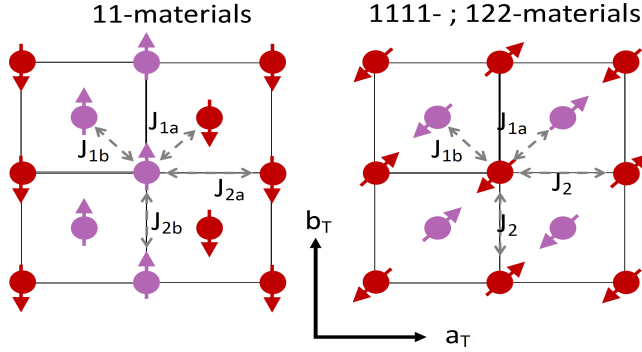


**Figure 2.5:** In-plane magnetic structure of the static long range order of Fe moments, expressed in tetragonal crystal symmetry and representative for 111-, 122- and 1111-type Fe-based materials (right panel) and 11-type materials (left panel).  $J_{1a}$ ,  $J_{1b}$  and  $J_2$  represent nearest and next nearest neighbor exchange coupling parameters, as used to describe the structure in a local moment approach.  $J_{ij}$  are expressed in orthorhombic notation. Only Fe-atoms are shown (red and purple dots). Red and purple arrows picture the magnetic moments, where different colored arrows belong to different antiferromagnetic sublattices for the 1111- and 122-figure and illustrate the double-stripes in the 11-figure. The magnetic correlations in crystallographic c-direction (not shown here) are invariably antiferromagnetic. Black boxes illustrate the in plane dimensions of the tetragonal unit cells. The orthorhombic unit cell is rotated by  $45^\circ$  with  $a_O$ - and  $b_O$ -axes pointing along the in-plane diagonal directions of the tetragonal unit cells.

Figure 2.5 illustrates the two magnetic structures of the static long range order of Fe moments in the four main classes of Fe-based materials. The static long range order of the 1111- and 122-materials can be expressed in terms of two antiferromagnetically ordered sublattices with a collinear Néel configuration and moments aligned along the orthorhombic a-direction (diagonal direction to the illustrated tetragonal cartesian). The out-of-plane correlations along the crystallographic c-direction are invariably antiferromagnetic. A combination of both sublattices results in a spin-stripe structure with antiferromagnetic correlations along the orthorhombic a-direction, ferromagnetic correlations along the orthorhombic b-direction, antiferromagnetic next nearest neighbor interactions along the orthorhombic diagonal direction plus an antiferromagnetic inter-layer coupling. This results for the 122-materials in a propagation vector  $\mathbf{Q}_{AFM} = (0.5, 0.5, 1)$  in tetragonal notation, where the odd L-value is a result of the antiferromagnetic



stacking in c-direction and the two  $\text{Fe}_2\text{As}_2$ -layers per unit cell. For the 1111-compositions with only one  $\text{Fe}_2\text{As}_2$ -layer per unit cell the tetragonal propagation vector is  $\mathbf{Q}_{AFM}=(0.5, 0.5, 0.5)$ . For some 1111-materials, however, this propagation vector can vary slightly to  $\mathbf{Q}_{AFM}=(0.5, 0.5, 0)$  due to a change of inter-layer correlations from antiferromagnetic to ferromagnetic [31, 47]. A similar composition related change of the static order is not observed for 122-materials. The static magnetic order is often referred to as Spin-Density-Wave (SDW) order, which is a remnant from the beginning of the field of Fe-based superconductors when the magnetism was believed to be of itinerant nature. The expression is still used even if the nature of the magnetism is still not completely understood but most likely is not entirely itinerant.

The two approaches discussed in this respect are, (1) a local moment picture where magnetic moments are localized at the crystallographic sites of the magnetic ions and nearest and next nearest neighbor exchange interactions provide the formation of the static order, or (2) an itinerant approach where magnetic properties are related to the itinerant electrons of the system and where nesting effects of the Fermi surface lead to the formation of a Spin density Wave order<sup>4</sup>.

Some properties of the Fe-based materials support the itinerant approach, such as the weak metallic nature, the matching of the antiferromagnetic propagation vector  $\mathbf{Q}_{AFM}$  and the nesting vector  $\mathbf{Q}_{nesting}=(0.5, 0.5, 0)$  or the small and strongly composition depending ordered moments in the range of  $\mu = 0.35 - 0.95 \mu_B$  for 1111-materials and  $\mu = 0.8 - 1.00 \mu_B$  for 122-materials [48]. However some effects can also be explained by a local moment picture, as for example the small and varying ordered moments might also result from strong frustration effects of a local moment magnetic structure [49, 50].

The situation in the 11-materials is slightly different as obvious from figure 2.5. In contrast to the two antiferromagnetic sublattices with moments aligned along the orthorhombic a-direction as in the 1111- and 122-materials, the 11-compounds exhibit a double-stripe structure with moments aligned along the tetragonal b-direction. The propagation vector  $\mathbf{Q}_{AFM}=(0.5, 0, 0.5)$  [51] of this double-stripe structure does not match the nesting vector, in contrast to the SDW-order of the 1111- and 122-compounds, but has an in-plane angle of  $45^\circ$  to  $\mathbf{Q}_{nesting}=(0.5, 0.5, 0)$ <sup>5</sup>. Where for the 1111- and 122-materials the matching of  $\mathbf{Q}_{AFM}$  and the nesting vector leads to the conclusion of possible itinerant contributions to the formation of the static magnetic order, the mismatch between  $\mathbf{Q}_{AFM}=(0.5, 0, 0.5)$  and  $\mathbf{Q}_{nesting}=(0.5, 0.5, 0)$  in the 11-materials makes contributions by nesting effects rather unlikely. Thus, it is believed that magnetism in the 11-materials might be more on the localized side than on the itinerant, which indeed is supported by theory [52]. However, recent scattering results on  $\text{Fe}_{1.1}\text{Te}$  suggest that the magnetic mechanism in the 11-materials might in fact be neither purely localized nor purely itinerant but rather a complicated interaction of local moments and itinerant

---

<sup>4</sup>A closer description of this mechanism can be found in the appendix.

<sup>5</sup>Will be discussed below.

electrons [53].

A variation of the amount of incorporated interstitial iron, the  $x$  in  $\text{Fe}_{1+x}\text{Te}$ , away from the stoichiometric value, can lead to a modification of the magnetic structure, from the commensurate structure with wave vector  $\mathbf{Q}_{AFM}=(0.5, 0, 0.5)$  to an incommensurate structure with  $\mathbf{Q}_{AFM;inc}=(\pm\delta, 0, 0.5)$  [51].

### Spin Wave Excitations of the Fe-SDW Order

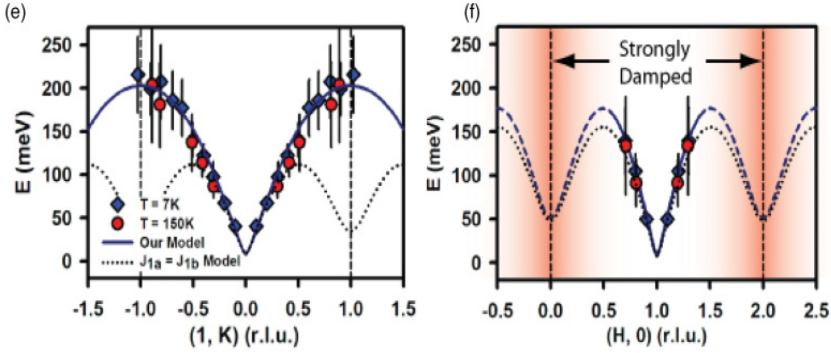


**Figure 2.6:**  $\mathbf{Q}$ -energy-dispersion of spin wave excitations with propagation vector  $\mathbf{Q}_{AFM}=(1, 0, 1)_{ortho}$  in  $\text{BaFe}_2\text{As}_2$ , obtained via single crystal inelastic time-of-flight neutron scattering. (e) Dispersion along transverse  $(1, K)$ -direction for temperatures 7 K and 150 K. Blue solid line represents a Heisenberg model calculation using anisotropic exchange couplings  $SJ_{1a} = 59.2 \pm 2.0$ ,  $SJ_{1b} = -9.2 \pm 1.2$ ,  $SJ_2 = 13.6 \pm 1.0$ ,  $SJ_c = 1.8 \pm 0.8$  meV. Dotted line represents the same Heisenberg model calculation using isotropic exchange couplings  $SJ_{1a} = SJ_{1b} = 18.3 \pm 1.4$ ,  $SJ_2 = 28.7 \pm 0.5$ ,  $SJ_c = 1.8$  meV. (f) Dispersion along longitudinal  $(H, 0)$ -direction. Figure and exchange parameters are taken from ref. [54].

Aside from the static order, a comprehension of spin dynamics present in the superconducting state but also in the ordered state of the undoped material is very important, in order to gain an overall understanding of magnetism, also with respect to a possible contribution to superconductivity. Consequently, in the last four years a large number of experimental investigations on the spin dynamics have been performed, and several characteristics of the spin excitations in parent and superconducting Fe-based materials have been established, which will be outlined in the following.

For temperatures below  $T_N$ , the spin excitations in the undoped Fe-based materials exhibit a narrow mostly three dimensional spin wave like character. The excitations are steeply dispersing with bandwidths of up to 200 meV [54–58]. Below 10 meV the excitation spectra are gapped suggesting strong single ion anisotropy effects

[59–64], with recent reports even proposing multiple gaps for in-plane and out-of-plane excitations, respectively [65]. For temperatures above  $T_N$ , and energies below 100 meV, the narrow and three dimensional spin wave excitations are replaced by quasi two dimensional short ranged paramagnetic excitations with correlations mostly restricted to the ab-planes [61, 63].

Several quantitative studies of spin wave excitations have been performed, with the majority of these studies using a local moment spin wave model to describe the magnetic excitations. Even if the nature of magnetism in the Fe-based materials is not believed to be solely localized it was shown that a spin wave model based on a local moment Hamiltonian is indeed capable of describing the larger part of the spin wave excitation spectrum in a reasonable way [54–58]. The most commonly used linear spin wave model is based on a local moment Heisenberg Hamiltonian, similar to [62],

$$\begin{aligned}
H = & J_{1a} \sum_{\langle jk \rangle_a} \mathbf{S}_j \cdot \mathbf{S}_k + J_{1b} \sum_{\langle jk \rangle_b} \mathbf{S}_j \cdot \mathbf{S}_k + J_2 \sum_{\langle jk \rangle_{ab}} \mathbf{S}_j \cdot \mathbf{S}_k \\
& + J_c \sum_{\langle jk \rangle_c} \mathbf{S}_j \cdot \mathbf{S}_k + \sum_j \left\{ K_c (S_z^2) + K_{ab} (S_y^2 - S_x^2)_j \right\}
\end{aligned} \tag{2.3}$$

where the  $J_{i,j}$  are the nearest and next nearest neighbor exchange parameters and  $K_{ab}$  and  $K_c$  the in-plane and out-of-plane single ion anisotropy constants.

These spin wave analyses on  $\text{CaFe}_2\text{As}_2$  [55],  $\text{BaFe}_2\text{As}_2$  [54] and  $\text{SrFe}_2\text{As}_2$  [56] revealed highly anisotropic in-plane exchange interactions between nearest neighbor (NN) and next nearest neighbor (NNN) spins, with strong antiferromagnetic (NN) coupling along the orthorhombic  $a$ -direction ( $J_{1a}$ ), much weaker ferromagnetic (NN) coupling along the  $b$ -direction ( $J_{1b}$ ) and antiferromagnetic (NNN) coupling along the  $(1, 1, 0)$ -direction ( $J_2$ ), similar to what is shown in the caption of figure 2.6 for  $\text{BaFe}_2\text{As}_2$ <sup>6</sup>.

Numerous mechanisms have been proposed in order to explain this in-plane anisotropy, such as electronic nematic ordering [66] or orbital ordering [35]. The anisotropy in the exchange interactions is not just present in the orthorhombic, magnetically ordered phase but also remains in the paramagnetic phase for temperatures above  $T_N$  [54, 56], which is puzzling especially considering the directional variation of the exchange interactions in combination with the underlying fourfold symmetry of the tetragonal crystal structure.

The paramagnetic excitations in  $\text{BaFe}_2\text{As}_2$  exhibit another puzzling feature as the short range quasi 2D paramagnetic excitations observed for energies below 100 meV [61, 63], are replaced by narrow spin wave like excitations for high energies [54]. These results combined with results from other experimental techniques [67–69] are interpreted as indications of a nematic spin liquid present in these materials and which could explain some of the above mentioned magnetic properties. A comprehensive model or complete understanding of these magnetic properties, however, is still absent.

---

<sup>6</sup>The definition of the various exchange parameters is illustrated in figure 2.5.

The most experimental results on the spin wave excitations have been obtained for 122-materials, mainly due to the relatively large crystals available for these materials. However, a recent report on a neutron scattering spin wave study on  $\text{Fe}_{1.05}\text{Te}$  showed that a linear spin wave model based on a local moment Heisenberg Hamiltonian similar to the ones used for the 122-materials, also provides a reasonable description of the spin waves in 11-materials, and also with a highly anisotropic in-plane exchange coupling [57].

### Spin Excitations in doped Fe-based Materials

Doping the system successfully suppresses the static magnetic order and induces superconductivity to the systems. The break down of the long range static magnetic order is also visible from the excitation spectrum of the spin wave excitations. In the underdoped 122-materials, where the static order is still present and coexists with superconductivity, the spin wave excitations still exhibit strong three dimensional character [40, 70], and in general are very similar to the undoped materials. Once the static magnetic order is completely suppressed, however, the narrow three dimensional spin wave excitations of the static magnetic order with propagation vector  $\mathbf{Q}_{AFM}=(0.5, 0.5, 1)$  are replaced by short range quasi 2 dimensional spin fluctuations, with strongly weakened interlayer correlations. These short range spin fluctuations have a propagation vector matching the nesting vector  $\mathbf{Q}_{nesting}=(0.5, 0.5, 0)$  and are present for all Fe-based superconducting materials, even for the 11-materials, where the static magnetic order has a different wave vector  $\mathbf{Q}_{AFM}=(0.5, 0, 0.5)$ . They are mostly 2 dimensional with almost zero correlations along the  $(0, 0, L)$ -direction [71–73], and are reduced in in-plane correlation lengths, comparable to the broadened low energy paramagnetic excitations present in the parent 122-compound [61, 74]. When overdoping the system  $T_c$  starts to drop again until superconductivity is completely suppressed, and also the spin excitations are affected. For 24% Co-doped  $\text{Ba}(\text{Fe}_{1-x}\text{Co}_x)_2\text{As}_2$  seemingly all spin fluctuations are completely suppressed [75]. A similar effect has been reported for  $\text{LaFeAsO}_{1-x}\text{F}_x$  where increasing doping concentration eventually leads to the suppression of the spin fluctuations [76].

### 2.3.4 Band Structure and Fermiology

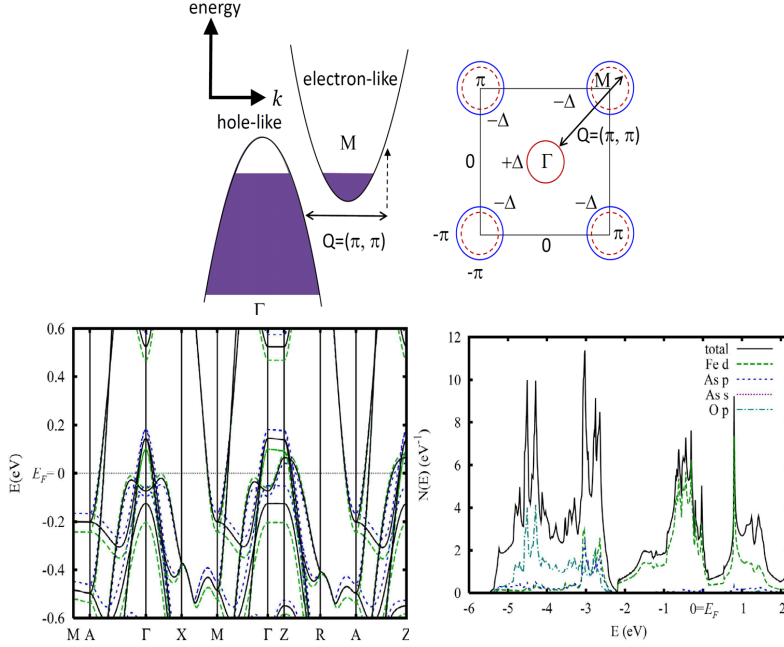


**Figure 2.7:** (upper row left panel) Sketch of energy- $k$  band structure of a semi metal. (upper row right panel) Sketch of the Fermi surface of Fe-based superconductors in the  $k_x$ - $k_y$  plane. The hole- (red solid circle) and electron pockets (red dashed circles) at the  $\Gamma$ -point and  $M$ -points are of similar size. It was neglected the fact that two electron pockets and two hole pockets are present at the  $\Gamma$ - and  $M$ -points, respectively. The nesting vector  $\mathbf{Q}_{nesting} = (\pi, \pi) = (0.5, 0.5)$  in tetragonal notation illustrates the nesting of the Fermi surfaces. With electron doping electron pockets are enlarged (solid blue circles) and perfect nesting condition is destroyed.  $\pm\Delta$  illustrate the opposite signs of the superconducting gap function  $\Delta$  with  $s_{\pm}$ -symmetry. (lower row left panel) Band structure of LaFeAsO. Dashed lines represent band structures of the various elements of the composition. Obvious are the hole-like and electron-like bands crossing the Fermi energy at the  $\Gamma$ - and  $M$ -point, respectively. Colors match the legend in the right figure. (lower row right panel) Density of states of LaFeAsO obtained via band structure calculations for the various element states. Two LaFeAsO figures are taken from ref. [77].

Aside from the magnetic properties, band structures, Fermi surface topologies and density of states at the Fermi energy  $N(E_F)$  provide important information on the properties of superconducting materials, given the fact that only states close to the Fermi surface contribute to the electronic properties, magnetic susceptibility or the formation of a

superconducting ground state. Thus, many band structure calculations and ARPES measurements have been performed, and several characteristics of the band structures of Fe-based materials have been established [48, 52, 77–83]. In contrast to the cuprate materials, which are Mott-like insulators the Fe-based materials are weakly metallic and in fact are considered semi metals. Semi metals are materials with band structures similar to the sketch in figure 2.7, where valence and conduction bands overlap in energy but are separated in  $\mathbf{k}$ -space. Due to this overlap electrons from the valence band are transferred to the conduction band until the highest occupied states in both bands are of identical energy,  $E_F$ . This leaves empty states in the valence band (hole band) and occupied states in the conduction band (electron band) and both bands contribute to the electronic properties of the system. Band structure calculations on a variety of Fe-based materials reveal exactly this type of band structure, with hole and electron bands crossing the Fermi surface at the  $\Gamma$ - and M-point of the Brillouin zone, as shown in figure 2.7. This leads to a Fermi surface consisting of electron and hole pockets of comparable size and distributed in the  $k_x$ - $k_y$  plane of the Brillouin zone as illustrated in figure 2.7. The similar sizes and shapes of the hole and electron pockets lead to nesting effects of the different parts of the Fermi surface separated by the nesting vector  $\mathbf{Q}_{nesting} = (\pi, \pi) = (0.5, 0.5)$  in tetragonal notation. A Fermi surface is nested when it possesses parallel parts which can be placed on top of each other with a reasonable matching of the two surfaces, when translated by the nesting vector, in this case the hole and electron pockets in 2.7. Nested Fermi surfaces drastically enhance the magnetic response of the system to perturbations with this particular wave vector  $\mathbf{Q}_{nesting}$ , and the system can become unstable to the formation of ordered ground states, such as Spin Density Waves, Charge Density Waves or superconductivity<sup>7</sup>.

As figure 2.7 shows, the density of states at the Fermi energy  $N(E_F)$  is dominated by the Fe 3d states, whereas the As 4p bands are approximately 3 eV below  $E_F$ . At this energy region, 3 eV below  $E_F$ , Fe and As bands show a strong hybridization, which illustrates the strong Fe-As bonding in the system. Surprisingly all five Fe 3d orbitals are at about the same energy even though one would expect an energy splitting of the five 3d orbitals into three  $t_{2g}$  and two  $e_g$  orbitals caused by the tetrahedron of four electronegative anions surrounding the iron. The fact that the density of states near the Fermi surface is dominated by these five Fe 3d orbitals with just very little contribution by the As 4p states [48, 77, 80–82, 84, 85] shows that direct Fe-Fe hopping is the predominant mechanism for the metallic conduction in the Fe-based materials. This is supported by the short Fe-Fe distance in the 122-materials which indeed is just about 10% larger than for pure metallic iron.

Whereas, in cuprate materials each Cu-pair is separated by an O atom and conduction is performed by Cu-O-Cu hopping processes. As a result, the O 2p orbitals have strong contributions to the density of states near the Fermi surface and the localized copper spins exhibit strong antiferromagnetic superexchange interactions.

---

<sup>7</sup>A slightly more detailed discussion on nesting effects can be found in the appendix.

## Unit Cells and Brillouin Zones

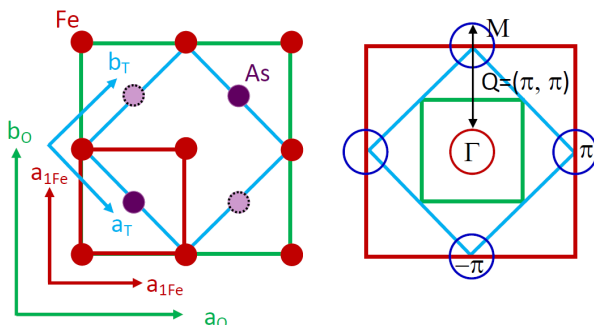


**Figure 2.8:** (left panel) On-top view of one Fe-As layer with three possible real space unit cells. Illustrated are Fe atoms (red dots) and As atoms (light and dark purple dots). Light purple As atoms are located above and dark purple As atoms are located below the Fe plane. Red box illustrates the 1-Fe unit cell, blue box the 2-Fe tetragonal unit cell and green box marks the orthorhombic unit cell. (right panel) Illustration of the first Brillouin zones corresponding to unit cells in the left panel, where matching colors indicate correlated zones and cells. Blue and red circles depict the hole and electron Fermi surfaces at the  $\Gamma$ -point and  $M$ -points, respectively. The labeling is done in tetragonal notation which leads to the nesting vector  $\mathbf{Q}_{nesting} = (\pi, \pi) = (0.5, 0.5)$  similar to figure 2.7.

When discussing the electronic properties of materials one should also mention the preferred Brillouin zones and the corresponding real space unit cells in order to avoid possible confusion due to unclear notations. In Fe-based materials basically three unit cells are used frequently in literature. The simplest of the three is the 1-Fe unit cell which is highlighted by the red square in the sketch in figure 2.8. As the name indicates, the 1-Fe unit cell is oriented in the  $ab$  plane in a way that it connects four Fe atoms and as a consequence it contains one Fe atom per unit cell per Fe layer. The corresponding Brillouin zone is referred to as the *unfolded* zone as it covers the largest possible area in reciprocal space. The main advantage of the 1-Fe Brillouin zone is its simplicity as for this *unfolded* zone the fewest number of electron bands needs to be considered. On the other side, however the drawback of the 1-Fe description is that the corresponding 1-Fe cell is not the correct real space unit cell, which becomes obvious from the figure. Due to a varying height of As atoms, illustrated in the sketch by the light and dark colored As atoms, the height or  $z$ -positions of the As create an alternating pattern in reference to the Fe  $z$ -positions. The consequence of this is that the correct real space unit cell needs to be rotated by  $45^\circ$  and enlarged by a factor of 2 in comparison to the 1-Fe cell. The new cell, twice as large as the 1-Fe cell, contains two Fe atoms per cell per Fe layer and thus is labeled the 2-Fe cell. This is the correct real space description for a tetragonal

crystal structure with identical in plane lattice constants  $a = b$ , illustrated in blue in figure 2.8. In order to consider the orthorhombic distortion present at low temperatures of weakly doped materials, the unit cell again needs to be rotated by  $45^\circ$  and enlarged by 2, highlighted by the green box. As the real space unit cells of the tetragonal and orthorhombic description are enlarged in reference to the 1-Fe cell the corresponding Brillouin zones are reduced in size and can be created by a *folding* of the *unfolded* 1-Fe Brillouin zone and thus are often referred to as *folded* zones. One consequence of the folding of the zone is an increase in the number of bands that need to be considered to discuss the physics of the first Brillouin zone. All three mentioned Brillouin zones and unit cells, 1-Fe, 2-Fe tetragonal and orthorhombic create a legitimate description of the physics of the materials and all have their own advantages and disadvantages. As the intention of this paragraph is solely to introduce the possible notations, for a more detailed discussion of the subject one might want to look elsewhere [48, 86]. Throughout this text only the tetragonal and orthorhombic description will be used, and the preferred notation will be labeled which should minimize the potential for confusion.

### 2.3.5 Superconducting Gap Symmetry

Similar to the cuprate materials, electronic pairing mechanisms have also been discussed for the Fe-based materials as possible driving forces for Cooper pair formation. One reason for these considerations of magnetic degrees of freedom is the proximity of magnetically ordered and superconducting states in the phase diagram. Another reason is the fact that electron phonon mechanisms are believed to be not capable of providing the needed pairing strengths required for the high transition temperatures [87]. The situation with possible phonon contributions, however, is not so clear in reality. Several experimental results indeed suggest a possible contribution of electron phonon coupling to the pairing mechanism [88–90]. On the other side, measurements of isotope effects, which is a smoking gun experiment for possible electron phonon coupling, provide mixed results, with reports of conventional isotope effects, supporting phonon contributions in some materials [91, 92] and contrary results in other materials [93, 94].

#### Spin Fluctuation Theory

The spin fluctuation theory as it has been proposed by Berk-Schrieffer [95] is one of the most popular candidates for electronic pairing mechanisms and has the ability to provide some qualitative results in case of the cuprate materials, as it is capable of explaining the present d-wave symmetry of the superconducting order parameter.

**Ferromagnetic Spin Fluctuations** Pairing of electrons to Cooper pairs via the exchange of ferromagnetic spin fluctuations was first proposed by Berk and Schrieffer [95]



for nearly ferromagnetic metals in 1966. In a descriptive picture, an electron that travels the medium of the nearly ferromagnetic metal and polarizes the surrounding spins ferromagnetically with its own spin. This lowers the energy of the system and results in a pulsating pattern of the polarized spin medium. Another electron with a parallel spin travels the system, feels the potential of the pulsating polarized spins and thus pairs with the initial electron spin. The bosons exchanged between the electron pairs are collective excitations, magnons and mostly paramagnons<sup>8</sup>. In the case of the exchange of ferromagnetic fluctuations the pairing potential is attractive for the formation of spin triplet pairs, Cooper pairs with total spin  $S=1$  and repulsive for singlet pairing with total spin  $S=0$ . If the repulsive potential of the spin fluctuations exceeds the attractive potential of electron-phonon interactions for example, the spin fluctuations act as pair-breaking. This is the case in Pd which is not BCS superconducting due to strong magnetic fluctuations.

Mathematically the spin fluctuation mediated pairing can be described in terms of effective pairing vertices<sup>9</sup> [86],

$$\Gamma_{\uparrow\uparrow} = \frac{-U^2\chi_0(\mathbf{k}' - \mathbf{k})}{1 - U^2\chi_0^2(\mathbf{k}' - \mathbf{k})} \quad (2.4)$$

$$\Gamma_{\uparrow\downarrow} = \frac{U}{1 - U^2\chi_0^2(\mathbf{k}' - \mathbf{k})} + \frac{U^2\chi_0(\mathbf{k}' + \mathbf{k})}{1 - U^2\chi_0^2(\mathbf{k}' + \mathbf{k})} \quad (2.5)$$

where  $U$  is the local Hubbard  $U$  and  $\chi_0$  is the noninteracting magnetic susceptibility of the Fermi gas, in other words the Lindhard function<sup>10</sup>. The total pairing vertex in the triplet and singlet channel reads as [86],

$$\Gamma_t = \frac{1}{2}\Gamma_{\uparrow\uparrow} \quad (2.6)$$

$$\Gamma_s = \frac{1}{2}(2\Gamma_{\uparrow\downarrow} - \Gamma_{\uparrow\uparrow}) \quad (2.7)$$

The negative sign in (2.4) (note that for nearly ferromagnetic metals it is given,  $\chi_0 > 0$  and  $U\chi_0 < 1$ ) illustrates that for ferromagnetic spin fluctuations triplet pairing is attractive, whereas singlet pairing is repulsive and therefore suppressed.

**Antiferromagnetic Spin Fluctuations** For the case of antiferromagnetic fluctuations the magnetic response is peaked at a given wave vector  $\mathbf{Q}$  and with some additional

---

<sup>8</sup>As magnons are the collective excitations of the static magnetic order paramagnons are magnetic collective excitations in the paramagnetic phase. In the paramagnetic phase the static magnetic order is suppressed but exchange interactions of the magnetic moments can still be present.

<sup>9</sup>The vertex, in a way, describes the point of highest probability for the interaction of two particles. Since in this case the particles are electrons the vertex is expressed in terms of  $\mathbf{k}$ -space. The particles, discussed here, interact via exchange of exchange bosons (paramagnons) and so the interaction can be either attractive or repulsive, depending on the type of exchange bosons.

<sup>10</sup>The appendix contains a slightly more detailed discussion of the magnetic response of metallic systems.

assumptions explained elsewhere [96–98] the singlet pairing vertex reads as [86]

$$\Gamma_s(\mathbf{k}', \mathbf{k}) = \frac{3}{2} U^2 \frac{\chi_0(\mathbf{k}' - \mathbf{k})}{1 - U\chi_0(\mathbf{k}' - \mathbf{k})} \quad (2.8)$$

This form of the vertex implies that  $\Gamma_s(\mathbf{k}', \mathbf{k})$  is also peaked at  $\mathbf{Q}$ , but due to the positive sign remains always repulsive. As a result, equation (2.9) the so-called BCS gap equation [12], which needs to be obeyed in order for a successful pairing, does not lead to a solution.

$$\Delta_{\mathbf{k}} = - \sum_{\mathbf{k}'} \Gamma_s(\mathbf{k}', \mathbf{k}) \frac{\Delta'_{\mathbf{k}'}}{2E'_{\mathbf{k}}} \tanh \frac{E'_{\mathbf{k}}}{2T}, \quad (2.9)$$

Obviously, from the BCS gap equation for the antiferromagnetic spin fluctuations, it becomes clear that for a conventional gap function<sup>11</sup> no pairing is achieved. But for a superconducting gap function with a sign change of the gap function for different positions on the Fermi surface

$$\Delta_{\mathbf{k}} = -\Delta_{\mathbf{k}+\mathbf{Q}} \quad (2.10)$$

a solution is possible and the repulsive pairing via antiferromagnetic spin fluctuations indeed provides a pairing mechanism<sup>12</sup>. For the Fe-based materials for which the magnetic susceptibility is strongly peaked for the nesting vector  $\mathbf{Q}_{\text{nesting}} = (\pi, \pi)$  the most probable symmetry of the superconducting gap function which provides pairing on the nearest neighbor bonds is

$$\Delta_{\mathbf{k}}^s = \Delta_0 (\cos(k_x a) \cos(k_y a)) \quad (2.11)$$

where  $\Delta_{\mathbf{k}}^s$  represents an isotropic s-wave symmetry, which has opposite signs for the hole and electron pockets of the Fermi surface, respectively, as illustrated in figure 2.9.

### Superconducting Gap Function for Fe-based Superconductors

To this date the most probable pairing symmetry in the Fe-based superconductors seems to be a singlet pairing with net spin  $S=0$  with an isotropic  $s_{\pm}$  symmetry of the gap function which is isotropic on each Fermi surface but changes its sign between electron and hole pockets of the Fermi surface respectively, as illustrated in figure 2.9. Several experimental results support this symmetry of the gap function, which was first proposed by Mazin et al. [78]. Experiments on the Knight shift on numerous different Fe-based materials [99–103] have shown that the pairing most likely is of singlet symmetry with total net spin  $S=0$ .

<sup>11</sup>A superconducting gap function is considered conventional if the gap value is identical for all  $\mathbf{k}$  and  $\mathbf{k}'$  of the Fermi surface  $\Delta_{\mathbf{k}} = \Delta_{\mathbf{k}'}$ , and consequently unconventional if  $\Delta_{\mathbf{k}} \neq \Delta_{\mathbf{k}'}$  for at least one point on the Fermi surface.

<sup>12</sup>As this obviously does not leave a really descriptive picture, one needs to keep in mind that the pairing exclusively takes place in momentum space and not in real space.

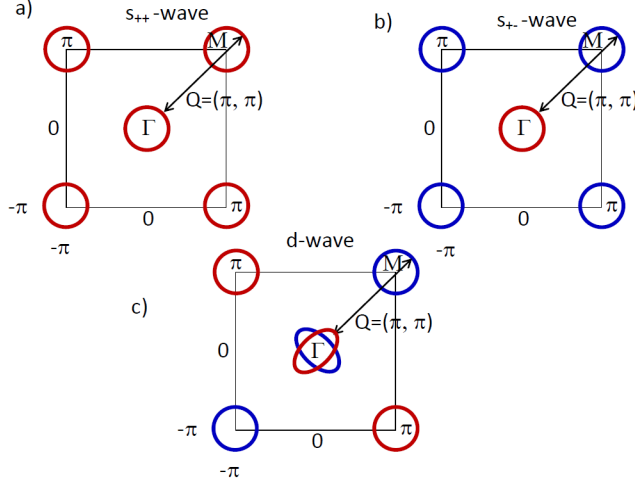


**Figure 2.9:** Gap function symmetries. a)  $s_{++}$  wave symmetry for a Fermi surface consisting of five pockets, similar to the Fe-based materials. The s-wave symmetry considers an isotropic gap value for  $\mathbf{k}$ -values on the Fermi surface. For  $s_{++}$  symmetry the gap function has identical sign on each Fermi surface. b)  $s_{\pm}$  symmetry. Isotropic gap value on each Fermi surface pocket, similar to the  $s_{++}$  symmetry, but with a sign change of the gap function between the center hole pocket and the four electron pockets. c) Unconventional d-wave symmetry. The gap function has the typical shape of the d-orbitals. The two ellipses on the centered hole Fermi surface illustrate the four lobes of the d-wave symmetry. The d-wave symmetry with alternating sign of the gap function on each lobe leads to an anisotropic gap value on the hole pocket, where the gap value becomes zero for wave vectors between the lobes. The gap function further changes sign between the electron pockets with opposite signs for neighboring pockets. Red color represents  $+\Delta$  positive sign of the gap function, whereas blue color represents  $-\Delta$  negative sign of the gap function.

Regarding the isotropic s-wave symmetry of the gap function the situation is not as clear. Several ARPES experiments [104–109] have shown nodeless superconducting gaps with uniform gap values over the hole and electron pockets, respectively, which is exactly what would be expected for s-wave symmetry. Contrary to this isotropic superconducting gap, however, other experimental techniques revealed anisotropic gap values with nodes in the superconducting gap for some materials [110–112]. How this is compatible with the proposed  $s_{\pm}$  gap function, which has a uniform value on each Fermi surface pocket, is still being debated [113–115].

The sign change of the gap function for the hole and electron pockets of the Fermi surface  $\Delta_{\mathbf{k}} = -\Delta_{\mathbf{k}+\mathbf{Q}}$  which is a main property of the  $s_{\pm}$  gap symmetry has a prominent effect on the magnetic response of the system. As Mazin et al. [78] predicted, when proposing a  $s_{\pm}$  gap symmetry for the Fe-based materials, the  $s_{\pm}$  gap function

results in a resonance feature in the dynamical spin susceptibility  $\chi''(\mathbf{Q}, \omega)$ , which is accessible through inelastic neutron scattering experiments. This resonance signal in the neutron scattering spectrum of spin flip particle hole excitations with wave vector  $Q_{nesting} = (0.5, 0.5, 0)$ , the so-called spin resonance mode has been observed for numerous Fe-based materials and will be discussed in the next section. From the current understanding the resonance signal does occur as a result of the sign change of the order parameter present for the  $s_{\pm}$  symmetry and is not compatible with for example the  $s_{++}$  symmetry, with  $\Delta_{\mathbf{k}} = \Delta_{\mathbf{k}+\mathbf{Q}}$  [116–118]. Thus, combined with the results from the Knight shift experiments which showed that the Cooper pairs are singlets and the ARPES results which showed the mostly nodeless superconducting gaps which excluded d-wave symmetry as possible gap symmetry, the occurrence of the resonance mode in the neutron scattering spin excitation spectra, is taken as a confirmation of the  $s_{\pm}$ -symmetry as the correct gap symmetry for the Fe-based materials.

## 2.3.6 The Spin Resonance Mode

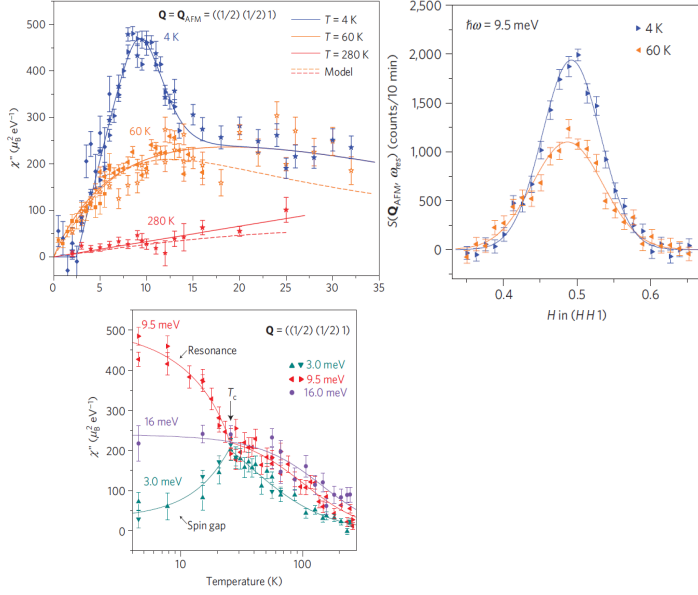


**Figure 2.10:** Inelastic neutron scattering investigations on the spin resonance signal in optimal doped  $\text{Ba}(\text{Fe}_{0.925}\text{Co}_{0.075})_2\text{As}_2$ . (Upper Left Panel) Energy dependence of the imaginary part of the magnetic susceptibility for temperatures 4 K (blue symbols), 60 K (yellow symbols) and 200 K (red symbols). (Right Panel) Wave vector dependence of the scattering function for temperatures 4 K (blue symbols), 60 K (yellow symbols), obtained in longitudinal direction through  $\mathbf{Q}_{AFM}=(0.5, 0.5, 1)$  at energy transfers 9.5 meV. (Lower Left Panel) Temperature dependence of the imaginary part of the magnetic susceptibility for wave vector  $\mathbf{Q}_{AFM}=(0.5, 0.5, 1)$  and excitation energies 3 meV (cyan symbols), 9.5 meV (red symbols) and 16 meV (purple symbols). Figures are taken from ref. [72].

The spin resonance signal is one of the most prominent features of the spin excitation spectrum in high  $T_c$ -superconductors and also one of the more studied and debated features as well. It was first observed in neutron scattering experiments on the magnetic excitation spectrum of the superconducting phase of bi-layer cuprates [119–123] and later in many other cuprate materials or heavy fermion systems [124, 125].

For the Fe-based superconductors, the signal was first predicted theoretically by Mazin et al. [78] almost immediately after the discovery of superconductivity in these materials, and was first observed experimentally in the neutron scattering spectrum of  $\text{Ba}_{0.6}\text{K}_{0.4}\text{Fe}_2\text{As}_2$  [126], and since then in a number of different iron based superconduct-

ing compositions, such as  $\text{Ba}(\text{Fe}_{1-x}\text{Co}_x)_2\text{As}_2$  [40, 70–72],  $\text{Ba}(\text{Fe}_{1-x}\text{Ni}_x)_2\text{As}_2$  [73, 127],  $\text{BaFe}_2(\text{As}_{1-x}\text{P}_x)_2$  [128],  $\text{FeTe}_{1-x}\text{Se}_x$  [129–132] and  $\text{LaFeAs}_{1-x}\text{F}_x$  [76, 133].

As illustrated in figure 2.10, the spin resonance signal is a feature of the spectrum of spin excitations with wave vector  $\mathbf{Q}_{\text{nesting}}=(0.5, 0.5, 0)$  and shows as an enhancement of scattering intensity at a specific excitation energy, once the sample temperature drops below  $T_c$ . The occurrence of the resonance signal usually is accompanied by a gap in the spectrum for energies right below the resonance energy, where magnetic intensities are almost completely suppressed. As known from polarized neutron scattering [120, 122, 134–137], the resonance signal is of magnetic nature but most likely has a microscopic origin very different from the antiferromagnetic collective excitations with propagation vector  $\mathbf{Q}_{AFM}=(0.5, 0.5, 0)$ . In energy the mode forms a relatively broad peak with 5–10 meV full width half maximum (FWHM) and the approximately  $0.15 \text{ \AA}^{-1}$  width in  $\mathbf{Q}$ -space corresponds to a correlation length of just several lattice spacings and thus fits to the rest of the spin excitation spectrum.

With increasing temperature the enhancement of scattering intensity of the resonance signal decreases and vanishes completely at  $T_c$  [72, 73, 126, 132, 133], which clearly relates the signal to the superconducting state.

Despite the large number of different cuprate and Fe-based superconducting materials that feature a spin resonance signal in the spin excitation spectrum in the superconducting phase, the resonance signal seems to follow a very simple linear relation between the resonance energy  $E_R$  and the transition temperature  $T_c$ . For the cuprate materials a universal ratio of  $E_R \approx 5.8 k_B T_c$  is reported [138]. The authors, however, further propose that aside from the observed relation between  $E_R$  and  $T_c$  the resonance energy more likely scales to  $2\Delta$  the superconducting electronic gap energy, and thus report for the cuprate materials a ratio of  $E_R/2\Delta = 0.64$ . The rather large deviation of the resonance energy from the theoretical value  $E_R = 2\Delta$ <sup>13</sup> can partly be explained by experimental inaccuracies. Especially the determination of the gap energy is experimentally rather difficult. The fact that both quantities are determined via different experimental techniques provides another source for error, as the gap value is determined via ARPES (angle resolved photoelectron spectroscopy), NMR (nuclear magnetic resonance),  $\mu\text{SR}$  (muon spin rotation) and a variety of other methods, whereas  $E_R$  is determined via inelastic neutron scattering. However, in case of the interpretation of the resonance signal as the spin 1 exciton, which will be discussed in the next section, the binding energy of the particle hole pair also leads to reduction of the resonance energy in reference to  $2\Delta$ .

For the Fe-based superconductors a very similar relation between  $E_R$  and  $T_c$  of  $E_R \sim (4.6 \pm 0.4) k_B T_c$ , has been reported [36, 72, 133, 139, 140], which is an appropriate description for most Fe-based materials. In contrast to the cuprates, however, the Fe-based materials seemingly do not follow a universal ratio between  $E_R$  and  $2\Delta$  [140], where especially materials with lower  $T_c$  deviate stronger from any universal ratio. As the universality of the ratio  $E_R/2\Delta = 0.64$  present in the cuprates has been interpreted

---

<sup>13</sup>Will be discussed below.

as an indication for a possible spin fluctuation mediated pairing mechanism, the authors in [140] suggest that the breakdown of this universality for the Fe-based materials might indicate a smaller contribution of spin fluctuations to the pairing mechanism.

For the Fe-based materials the relation between  $E_R$  and  $2\Delta$  might not hold a universal relation but individually the correlation between the two values is still believed to exist. Neutron scattering experiments on optimal doped  $\text{Ba}(\text{Fe}_{1-x}\text{Co}_x)_2\text{As}_2$  clearly support the correlation between  $E_R$  and  $2\Delta$ , as the experiments reveal a resonance energy  $E_R$  which gradually decreases to zero for temperatures increasing towards  $T_c$  [72], and thus exhibits a temperature dependence similar to the superconducting gap value which also decreases for increasing temperatures and disappears at  $T_c$ . However, contrary results are reported for  $\text{FeTe}_{0.6}\text{Se}_{0.4}$  [141] as in this composition the resonance energy  $E_R$  seemingly remains constant up to  $T_c$ .

### Theoretical Models for the Spin Resonance

Theoretically, the occurrence of the resonance signal for Fe-based materials is ascribed to the specific  $s_{\pm}$  symmetry of the superconducting gap function. This becomes obvious when one takes a look the Lindhard function  $\chi_0(\mathbf{q}, \omega) = \frac{f(\epsilon_{\mathbf{k}+\mathbf{q}}) - f(\epsilon_{\mathbf{k}})}{\omega - (E_{\mathbf{k}+\mathbf{q}} - E_{\mathbf{k}}) + i\delta}$  which is accessible through inelastic neutron scattering and which gives information on the momentum, energy, and temperature dependence of spin flip particle-hole excitations. When discussing particle hole excitations in the superconducting state it has to be considered that these excitations arise from a ground state consisting of a condensate of pairs of electrons with a macroscopic phase coherence of the Cooper pair wave functions plus an energy gap which separates the ground state from any possible excited states. These natural excitations in the superconducting state can be expressed in terms of Bogoliubov quasiparticles  $\gamma_{\mathbf{k}\uparrow}^{\dagger}$  which are superpositions of electron  $c_{\mathbf{k}\uparrow}^{\dagger}$  and hole excitations  $c_{-\mathbf{k}\downarrow}$ ,  $\gamma_{\mathbf{k}\uparrow}^{\dagger} = u_{\mathbf{k}}c_{\mathbf{k}\uparrow}^{\dagger} - v_{\mathbf{k}}c_{-\mathbf{k}\downarrow}$ . The coherence factors [2, 5]  $u_{\mathbf{k}}^2 = \frac{1}{2}\left(1 + \frac{\epsilon_{\mathbf{k}}}{\sqrt{\epsilon_{\mathbf{k}}^2 + \Delta_{\mathbf{k}}^2}}\right)$  and  $v_{\mathbf{k}}^2 = \frac{1}{2}\left(1 - \frac{\epsilon_{\mathbf{k}}}{\sqrt{\epsilon_{\mathbf{k}}^2 + \Delta_{\mathbf{k}}^2}}\right)$  with  $u_{\mathbf{k}}^2 + v_{\mathbf{k}}^2 = 1$  determine the probability the quasiparticle is either hole-like or electron-like. This approach translates to the particle hole excitation spectrum by the introduction of the BCS coherence factors  $1 \pm \frac{\epsilon_{\mathbf{k}}\epsilon_{\mathbf{k}+\mathbf{q}} + \Delta_{\mathbf{k}}\Delta_{\mathbf{k}+\mathbf{q}}}{E_{\mathbf{k}}E_{\mathbf{k}+\mathbf{q}}}$ , which affect the particle hole excitations in the superconducting state. The BCS Lindhard

function [142–144] reads as,

$$\begin{aligned} \chi_0^{BCS}(\mathbf{q}, \omega) = \sum_{\mathbf{k}} \left\{ \frac{1}{2} \left( 1 + \frac{\epsilon_{\mathbf{k}} \epsilon_{\mathbf{k}+\mathbf{q}} + \Delta_{\mathbf{k}} \Delta_{\mathbf{k}+\mathbf{q}}}{E_{\mathbf{k}} E_{\mathbf{k}+\mathbf{q}}} \right) \times \frac{f(E_{\mathbf{k}+\mathbf{q}}) - f(E_{\mathbf{k}})}{\omega - (E_{\mathbf{k}+\mathbf{q}} - E_{\mathbf{k}}) + i\delta} \right. \\ + \frac{1}{4} \left( 1 - \frac{\epsilon_{\mathbf{k}} \epsilon_{\mathbf{k}+\mathbf{q}} + \Delta_{\mathbf{k}} \Delta_{\mathbf{k}+\mathbf{q}}}{E_{\mathbf{k}} E_{\mathbf{k}+\mathbf{q}}} \right) \times \frac{1 - f(E_{\mathbf{k}+\mathbf{q}}) - f(E_{\mathbf{k}})}{\omega + (E_{\mathbf{k}+\mathbf{q}} + E_{\mathbf{k}}) + i\delta} \\ \left. + \frac{1}{4} \left( 1 - \frac{\epsilon_{\mathbf{k}} \epsilon_{\mathbf{k}+\mathbf{q}} + \Delta_{\mathbf{k}} \Delta_{\mathbf{k}+\mathbf{q}}}{E_{\mathbf{k}} E_{\mathbf{k}+\mathbf{q}}} \right) \times \frac{f(E_{\mathbf{k}+\mathbf{q}}) + f(E_{\mathbf{k}}) - 1}{\omega - (E_{\mathbf{k}+\mathbf{q}} + E_{\mathbf{k}}) + i\delta} \right\} \quad (2.12) \end{aligned}$$

where  $\epsilon_{\mathbf{k}}$  is the quasiparticle dispersion,  $\Delta_{\mathbf{k}}$  the superconducting gap function,  $E_{\mathbf{k}} = \sqrt{\epsilon_{\mathbf{k}}^2 + \Delta_{\mathbf{k}}^2}$  the quasiparticle energy and  $f(E_{\mathbf{k}})$  the Fermi distribution function. The three terms in (2.12) describe the quasiparticle scattering, the quasiparticle pair annihilation and the quasiparticle pair creation, respectively. For low temperatures the third term, the creation of quasiparticle pairs is the dominant contribution to the magnetic response and thus to the spin excitation spectrum observed in neutron scattering experiments. The pair creation process, which in other words describes the breaking up of a Cooper pair and the resulting creation of a pair of two quasiparticles, requires energies higher than the threshold energy of  $E_c = |\Delta_{\mathbf{k}} + \Delta_{\mathbf{k}+\mathbf{Q}}|$ , which marks the energy needed to break up a Cooper pair. Thus, for energies smaller than  $2\Delta$  Cooper pairs are not broken and no quasiparticle pairs are created, which results in a gap in the neutron excitation spectrum. For energies equal  $2\Delta$  the Cooper pairs are broken resulting in a pair of quasiparticles with energy for each quasiparticle  $E_{\mathbf{k}} = \Delta$ , with  $\epsilon_{\mathbf{k}} = 0$ . For a gap function which changes sign between the Fermi surfaces connected by  $\mathbf{Q}$  with  $\Delta_{\mathbf{k}} = -\Delta_{\mathbf{k}+\mathbf{Q}}$ , as is the case for the  $s_{\pm}$  symmetry, the coherence factor  $1 - \frac{\epsilon_{\mathbf{k}} \epsilon_{\mathbf{k}+\mathbf{q}} + \Delta_{\mathbf{k}} \Delta_{\mathbf{k}+\mathbf{q}}}{E_{\mathbf{k}} E_{\mathbf{k}+\mathbf{q}}}$  becomes maximal, whereas for energies higher than  $2\Delta$  the coherence factor decreases again. This leads to a resonance like enhancement of particle hole excitations with energies equal  $2\Delta$ . As a result the excitation spectrum features a gap for energies below  $2\Delta$  and a resonance like signal at energies close to  $E_c = |\Delta_{\mathbf{k}} + \Delta_{\mathbf{k}+\mathbf{Q}}|$ . Note that for a different gap symmetry, which does not change sign for different parts of the Fermi surface connected by  $\mathbf{Q}$ ,  $\Delta_{\mathbf{k}} = \Delta_{\mathbf{k}+\mathbf{Q}}$ , the coherence factor vanishes and no resonance signal occurs. The coherence factor is also zero if  $\Delta_{\mathbf{k}}$  exhibits a sign change but the propagation vector of the excitations does not match  $\mathbf{Q}$  for which the sign change  $\Delta_{\mathbf{k}} = -\Delta_{\mathbf{k}+\mathbf{Q}}$  occurs.

Several models have been proposed for the cuprate materials to give a microscopic description of the resonance mode, like a van Hove singularity in the Stoner continuum [145, 146], a soft mode related to excitations of the nearby antiferromagnetically ordered state [147], the  $\pi$ -resonance an antibound state in the particle-particle channel [148–150] or the spin 1 exciton, a bound state of a particle-hole pair [151].

For the Fe-based superconductors the most discussed models are the spin 1 exciton



[116–118, 152] and the  $\pi$ -resonance [148–150], which also often are referred to as singlet-triplet excitations. In an over-simplified picture, the spin 1 exciton is a bound state of two excited Bogoliubov quasiparticles, a bound state of a quasi-electron and a quasi-hole, so to speak. The idea of excitons as bound states of quasiparticles as possible collective excitations in superconductors has first been predicted for BCS superconductors in the mid 1950s [153].

In Fe-based superconductors the exciton model is able to describe some of the properties of the spin resonance signal. The energy of the resonance signal in the neutron scattering spectra is located in the energy region slightly below  $2\Delta$  and directly above the spin gap region, where all magnetic intensity is suppressed. As in the superconducting phase single particle excitations with energies not sufficient to break up Cooper pairs are suppressed, the lowest energy for any created particle hole pair in fact is  $2\Delta$ . The fact that the resonance peak in the neutron experiments appears slightly below  $2\Delta$  can be ascribed to the binding energy of the exciton, where the formation of the electron hole pair lowers the energy of the two excited quasiparticles, which leaves the exciton state slightly below  $2\Delta$  and so within the gap region. In this case, the difference between the resonance energy  $E_R$  and  $2\Delta$  is correlated to the binding energy of the electron hole pair. In the normal state with  $T > T_c$  the mode is believed to be strongly damped by the electron-hole excitations, which where suppressed below  $T_c$ . This damping causes a strong broadening of the resonance peak in energy and makes it unobservable in the neutron scattering experiments. This shows that the exciton mode really is enhanced by the opening of the superconducting gap and the energy of the mode is related to  $2\Delta$  and disappears from the excitation spectrum above  $T_c$ .

The other model, the  $\pi$ -resonance or  $\pi$ -mode is quite similar to the spin 1 exciton, in that regard, that it is a pair of quasiparticles with net total momentum  $\mathbf{Q} = (\pi, \pi, 0)$  and net total spin  $S=1$ . However, in contrast to the spin 1 exciton, which is a particle-hole bound state, the  $\pi$ -resonance is an antibound state of two particles with parallel spin. The resonance signal observed in the neutron scattering experiments thus is related to the pair creation of these antibound particle-particle states, where in a simplified picture the neutron scatters off one electron of the Cooper pair, flips the spin of that electron and transfers a momentum of  $\mathbf{Q} = (\pi, \pi, 0)$  to it. After the scattering process the electron-electron pair has a total net momentum  $\mathbf{Q} = (\pi, \pi, 0)$  and total net spin  $S=1$  and if the energy that has been transferred from the neutron to the pair matches the energy of the antibound state, the resonance is created. Usually, interactions in the particle-particle channel are not observable experimentally and the authors [148–150, 154] argue that the mixing of the particle-particle and particle-hole interaction channels in the superconducting state is responsible for the resonance signal in the neutron scattering experiments. Above  $T_c$  as the mixing of the interaction channels is abolished, the mode still exists but becomes undetectable again and thus disappears from the spin excitation spectrum in the scattering experiments. In contrast to the spin 1 exciton, for which the resonance energy  $E_R$  is related to

the superconducting gap energy and thus exhibits a temperature dependence, the  $\pi$ -resonance has a particular energy  $\sim -2\mu$ , where  $\mu$  is the chemical potential, and so  $E_R$  does not vary with temperature or is necessarily connected to  $2\Delta$ .

Both models are considered as possible descriptions for the resonance signal in Fe-based materials, however, a real consensus about the microscopic nature of the resonance signal is not present to this date. Further, so far no clear experimental evidence could be made that would unambiguously confirm or reject either of the two or any other model. Both models have been outlined at this point in an extremely short and over simplified way, solely in order to introduce two of the more transparent theoretical pictures that are discussed as possible microscopic origins of the resonance peak observed in neutron scattering experiments.

For a more detailed review on the spin resonance please turn to ref. [48, 155].



# 3 Experimental and Theoretical Basics

## 3.1 Scattering Basics

The history of neutron scattering has to begin with the first discovery of the neutron by J. Chadwick in 1932. Almost immediately after this historically very important discovery it was already discussed that the neutron could in fact be used as a probe for investigations in condensed matter physics. First suggested theoretically by Bloch in 1936 that neutrons could be scattered by crystalline samples the first magnetic neutron scattering experiments were performed by Shull, Wollan and Strausser [156, 157] in 1952. Since then, neutron scattering has developed into one of the most versatile and powerful techniques in experimental condensed matter physics. And with today's advanced neutron sources, the steady improvement of neutron scattering instruments and techniques such as polarized neutron scattering, it is still an unmatched tool in hard matter physics, especially in the field of magnetism. The success of the neutron as a microscopic probe in solid state physics is closely related to the fundamental physical properties of the particle, which enables neutron scattering to provide insight to material properties, hardly accessible by other techniques. Thermal neutrons possess wavelengths of the order of typical atomic distances in solid state materials. They interact with matter only very weakly and thus represent only a small perturbation to the system. Neutrons interact with the nuclei of the system via short range nuclear forces as well as with the magnetic densities via dipole-dipole interactions with the neutrons' magnetic moments. Both interactions are of similar strength and short range in nature and as a result elastic neutron scattering is able to deliver insight on correlations of nuclear as well as magnetic lattices on a microscopic scale. In addition to information on the static properties of the nuclear and magnetic lattices provided by elastic neutron scattering, inelastic neutron scattering gives insight to dynamic correlations and is by far the most important experimental tool for this field of solid state research. Only neutrons allow sizeable momentum transfers at energies typical for collective excitations of both nuclear and magnetic lattices. With a mass of  $m_n = 1.674928 \times 10^{-24}$  g a thermal neutron with typical wavelength of  $\lambda=2.4$  Å has an energy  $E \approx 14$  meV, which is of the order of typical collective excitations. In contrast to this, the energy of a photon with similar wavelength is close to 8 orders of magnitude larger and consequently the detection of a change of the photon energy in the meV range is very difficult and provides serious experimental challenges.

### 3.1.1 Basic Neutron Scattering Formulas

The following section provides a short introduction to some of the basic expressions needed to describe elastic and inelastic scattering events in a mathematical way.

The typical quantity obtained in a neutron scattering experiment is the number of neutrons with energy  $E$  scattered into a given solid angle  $d\Omega$ . This quantity is expressed in terms of the double differential cross section  $\frac{d^2\sigma}{d\Omega dE'}$ . In this chapter the cross sections for the basic scattering processes will be introduced briefly. However, all formulas presented in this section along with detailed derivations and discussion of the various cross sections can be found in many classical textbooks and review articles on neutron scattering [157–161].

In order to get access to the theory of neutron scattering it seems natural to start with so-called Fermi's Golden Rule, which represents the master formula of scattering theory on a quantum mechanic level:

$$\left( \frac{d^2\sigma}{d\Omega dE'} \right)_{\mathbf{k}_i \rightarrow \mathbf{k}_f} = \frac{1}{N} \frac{k_f}{k_i} \left( \frac{m}{2\pi\hbar} \right)^2 \sum_{\lambda_i, \sigma_i} p_{\lambda_i} p_{\sigma_i} \sum_{\lambda_f, \sigma_f} |\langle k_f \sigma_f \lambda_f | V(\mathbf{r}) | k_i \sigma_i \lambda_i \rangle|^2 \delta(\hbar\omega + E_{\lambda_i} - E_{\lambda_f}) \quad (3.1)$$

This formula expresses the process of a neutron with wave vector  $\mathbf{k}_i$ , spin state  $\sigma_i$  and energy  $E_{\lambda_i}$  being scattered by a given interaction potential  $V(\mathbf{r})$  into a state with wave vector  $\mathbf{k}_f$ , spin state  $\sigma_f$  and energy  $E_{\lambda_f}$  where further the quantum numbers  $\lambda_i$  and  $\lambda_f$  represent the initial and final states of the scattering system. Further, a possible change in energy of the scattering system  $\hbar\omega$  and the probability  $p_j$  for the system or the neutron of being in the quantum state  $j$  are considered in (3.1).

Fermi's Golden Rule describes the scattering process of particles on a quantum mechanical level in its most general form possible. In order to apply this formula on neutron scattering processes some modifications and specific assumptions regarding the interaction potential  $V(\mathbf{r})$  need to be made. In the following sections this will be demonstrated for nuclear and magnetic scattering processes, respectively.

#### Nuclear Neutron Scattering

The neutron interacts with the nuclei of the sample via short range nuclear forces. As a result of this very short range of interaction, much smaller than the typical neutron wavelength, the interaction potential of a crystalline sample can be interpreted as an assembly of point-like potentials. For such an assembly of  $N$  atoms at positions  $\mathbf{R}_j$ , for simplicity only the case of one single element will be discussed here, the interaction potential can be expressed as follows:

$$V_N(\mathbf{r}) = \frac{2\pi\hbar^2}{m} \sum_j b \delta(\mathbf{r} - \mathbf{R}_j). \quad (3.2)$$

Here  $\mathbf{r} - \mathbf{R}_j$  gives the distance between the neutron and the  $j$ -th atom and the  $\delta$ -function considers the point-like character of the interaction potential. Parameter  $b$  the nuclear scattering length which describes the scattering power of the given atom is element and isotope specific and varies depending on the total spin of the nucleus-neutron system. In neutron scattering it is a common procedure to use the momentum transfer of the scattered neutron  $\mathbf{Q} = \mathbf{k}_f - \mathbf{k}_i$  as the spatial variable instead of the neutron wave vectors. With the introduction of  $\mathbf{Q}$ , also known as the scattering vector, the differential cross sections for coherent and incoherent nuclear scattering are

$$\left( \frac{d^2\sigma}{d\Omega dE'} \right)_{coh} = \frac{1}{N} \frac{\sigma_{coh}}{4\pi} \frac{1}{2\pi\hbar} \frac{k_f}{k_i} \sum_{j,j'} \int_{-\infty}^{\infty} \langle e^{-i\mathbf{Q}\mathbf{R}_j(0)} e^{i\mathbf{Q}\mathbf{R}_{j'}(t)} \rangle e^{i\omega t} dt \quad (3.3)$$

$$\left( \frac{d^2\sigma}{d\Omega dE'} \right)_{inc} = \frac{1}{N} \frac{\sigma_{inc}}{4\pi} \frac{1}{2\pi\hbar} \frac{k_f}{k_i} \sum_j \int_{-\infty}^{\infty} \langle e^{-i\mathbf{Q}\mathbf{R}_j(0)} e^{i\mathbf{Q}\mathbf{R}_j(t)} \rangle e^{-i\omega t} dt \quad (3.4)$$

where  $\sigma_{coh} = 4\pi\bar{b}^2$  and  $\sigma_{inc} = 4\pi\bar{b}^2 - \bar{b}^2$  and  $\bar{b}$  account for the expectation value of the coherent and incoherent scattering length. The difference between coherent  $\sigma_{coh}$  and incoherent  $\sigma_{inc}$  scattering is the presence ( $\sigma_{coh}$ ) or absence ( $\sigma_{inc}$ ) of correlations between scattering potentials  $b_{j,j'}$ . These correlations lead to interference effects and result in so-called Bragg scattering with a characteristic  $\mathbf{Q}$ -dependence of the scattered intensity. All information on the lattice characteristics can be found in the coherent part of the scattering intensity, which will be the focus of the following discussion.

A way to express these correlations mathematically is by introducing the *pair correlation function* or *scattering function*  $S(\mathbf{Q}, \omega)$ . It considers correlations in space and time between pairs of scattering potentials and it is a common procedure in neutron scattering to express neutron cross sections in terms of this pair correlation function. If the coherent scattering function  $S(\mathbf{Q}, \omega)$  is defined as

$$S(\mathbf{Q}, \omega) = \frac{1}{N} \frac{1}{2\pi\hbar} \sum_{j,j'} \int_{-\infty}^{\infty} \langle e^{-i\mathbf{Q}\mathbf{R}_j(0)} e^{i\mathbf{Q}\mathbf{R}_{j'}(t)} \rangle e^{i\omega t} dt \quad (3.5)$$

the coherent nuclear cross section turns into

$$\left( \frac{d^2\sigma}{d\Omega dE'} \right)_{coh} = \frac{\sigma_{coh}}{4\pi} \frac{k_f}{k_i} S(\mathbf{Q}, \omega) \quad (3.6)$$

The scattering function  $S(\mathbf{Q}, \omega)$  considers all existing correlations in space and time between pairs of scattering potentials. Consequently,  $S(\mathbf{Q}, \omega)$  contains all desired information about the static and dynamic behavior of the system under investigation, expressed regarding the momentum and energy transfer.

**Elastic Nuclear Scattering from Crystalline Sample** Elastic scattering considers scattering processes where the neutron energy is conserved during the process and no energy transfer between the neutron and the sample takes place. For a crystalline sample with translation invariance  $\mathbf{j}$ , a unit cell containing  $d$  atoms, and considering the thermal motion of the atoms, which results in an oscillation of each atom around its equilibrium position  $\mathbf{d}$ , the position of atom  $d$  can be written as

$$\mathbf{R}_{j,d} = \mathbf{j} + \mathbf{d} + \mathbf{u}_d(j, t) \quad (3.7)$$

where  $\mathbf{u}_d(j, t)$  considers the displacement of atom  $d$  from its equilibrium position, caused by thermal oscillations. Because of the translation invariance of the crystal, that was taken as an assumption, equation (3.5) simplifies as the double sum over  $\mathbf{j}$  and  $\mathbf{j}'$  can be transformed into a single summation over the distances  $\mathbf{j} - \mathbf{j}'$ . As a result, the differential cross section for elastic scattering processes with zero energy transfer ( $\omega = 0$ ) transforms into

$$\left( \frac{d\sigma}{d\Omega} \right)_{coh}^{el} = \frac{(2\pi)^3}{v_0} \sum_{\boldsymbol{\tau}} |F_N(\mathbf{Q})|^2 \times \delta(\mathbf{Q} - \boldsymbol{\tau}) \quad (3.8)$$

where  $\boldsymbol{\tau}$  is a reciprocal lattice vector,  $v_0$  the unit cell volume and  $F_N(\mathbf{Q})$  the nuclear structure factor, which is defined by

$$F_N(\mathbf{Q}) = \sum_d \bar{b}_d e^{i\mathbf{Q}\mathbf{d}} e^{-W_d(\mathbf{Q})} \quad (3.9)$$

where  $\exp(-W_d(\mathbf{Q})) = \exp(\langle (\mathbf{Q}\mathbf{u}(j, d))^2 \rangle)$  represents the Debye-Waller factor, which accounts for the mean square displacement of each atom and further reduces the scattered intensity with increasing  $|\mathbf{Q}|$ . The structure factor is the desired quantity in a neutron diffraction experiment as it contains all structural information of the sample and is related to the scattered intensity.

**Inelastic Nuclear Scattering, One Phonon Approximation** Inelastic scattering processes describe the excitation or annihilation of collective or single particle excitations in the sample. During the process a non-zero energy transfer  $\hbar\omega = \frac{\hbar^2}{2m_N}(k_i^2 - k_f^2)$  between the neutron and the sample takes place, with  $k_i$  and  $k_f$  being the initial and final neutron wave vectors. For coherent nuclear scattering of a crystalline sample these excitations are collective excitations of the crystal lattice, so-called phonon excitations. With the restriction to the creation or annihilation of only one phonon per scattering processes the coherent cross section reads as:

$$\begin{aligned} \left( \frac{d^2\sigma}{d\Omega dE'} \right)_{coh}^{inel} &= \frac{k_f}{k_i} \frac{(2\pi)^3}{2v_0} \sum_{\boldsymbol{\tau}} \sum_{\nu, \mathbf{q}} \frac{1}{\omega_{\nu}(\mathbf{q})} \left| \sum_d \bar{b}_d e^{-W_d(\mathbf{Q})} e^{i\mathbf{Q}\mathbf{d}} \cdot \frac{\mathbf{Q}\mathbf{e}_d(\mathbf{q}, \nu)}{\sqrt{M_d}} \right|^2 \\ &\times \left( [n_{\nu}(\mathbf{q})\delta(E_i - E_f + \hbar\omega_{\nu}(\mathbf{q}))\delta(\mathbf{Q} + \mathbf{q} - \boldsymbol{\tau})] \right. \\ &+ \left. [(n_{\nu}(\mathbf{q}) + 1)\delta(E_i - E_f - \hbar\omega_{\nu}(\mathbf{q}))\delta(\mathbf{Q} - \mathbf{q} - \boldsymbol{\tau})] \right). \end{aligned} \quad (3.10)$$

Here  $M_d$  accounts for the mass of atom  $d$ ,  $n_\nu(\mathbf{q})$  stands for the thermal population factor for Bose particles,  $\mathbf{e}_\nu(\mathbf{q})$  is the polarization vector and  $\omega_\nu(\mathbf{q})$  is the frequency of the phonon  $\nu$  [17]. Obviously the coherent one phonon cross section consists of two parts: The second line in equation (3.10) describes the annihilation of a phonon with frequency  $\omega_\nu(\mathbf{q})$  which results in an energy transfer from the sample to the scattered neutron and thus an increase of the neutron energy in the scattering process. Whereas, the third line expresses the creation of a phonon via an energy transfer from the scattered neutron to the sample, which consequently lowers the energy of the scattered neutron. The  $\delta$ -functions in both lines provide the conservation of both energy and momentum throughout both processes. Following the principle of detailed balance, the contribution of these two processes to the cross section is asymmetric, such that the annihilation of a phonon with frequency  $\omega$  is counted with the single population function  $n_\nu(\mathbf{q})$ , whereas the phonon creation process contributes with  $n_\nu(\mathbf{q}) + 1$  to the summation.

### Magnetic Neutron Scattering

In *magnetic* scattering processes the incident neutron interacts with magnetization densities created by unpaired electrons in the sample via magnetic dipole interactions with the neutron spin. The interaction potential between a neutron in spin state  $\boldsymbol{\sigma}$  and a moving electron of momentum  $\mathbf{p}$  and spin  $\mathbf{s}$  is

$$\mathbf{V}_M(\mathbf{r}) = -\gamma\mu_N^2\mu_B\boldsymbol{\sigma} \cdot \left[ \text{curl} \left( \frac{\mathbf{s} \times \hat{\mathbf{R}}}{R^2} \right) + \frac{1}{\hbar} \frac{\mathbf{p} \times \hat{\mathbf{R}}}{R^2} \right] \quad (3.11)$$

where  $\gamma = 1.9132$  is the gyromagnetic ratio,  $\mu_n$  and  $\mu_B$  represent the nuclear and the Bohr magneton and  $\mathbf{R}$  illustrates the distance between the two particles. For an unpolarized incident neutron beam, with arbitrary spin orientations of the incident neutrons, and if further the interaction potential  $\mathbf{V}_M(\mathbf{r})$  in (3.11) is introduced into Fermi's Golden Rule the differential cross section for magnetic scattering reads as,

$$\left( \frac{d^2\sigma}{d\Omega dE'} \right)_{mag} = \frac{(\gamma r_0)^2 k_f}{\hbar k_i} \sum_{\alpha, \beta} \left( \delta_{\alpha, \beta} - \frac{Q_\alpha Q_\beta}{Q^2} \right) S^{\alpha, \beta}(\mathbf{Q}, \omega) \quad (3.12)$$

Here  $r_0$  embodies the classic electron radius and  $\alpha$  and  $\beta$  are spatial coordinates with  $\alpha, \beta \in [x, y, z]$ .  $S^{\alpha, \beta}(\mathbf{Q}, \omega)$  the magnetic scattering function will be defined by spin-spin correlations as follows,

$$S^{\alpha, \beta}(\mathbf{Q}, \omega) = \frac{1}{2\pi} \int_{-\infty}^{\infty} \sum_{j, d} \frac{1}{2} g_d f_d(\mathbf{Q}) e^{-W_d(\mathbf{Q})} e^{i\mathbf{Q} \cdot (\mathbf{j} + \mathbf{d})} \langle S_0^\alpha(0) S_{\mathbf{j} + \mathbf{d}}^\beta(t) \rangle e^{-i\omega t} dt \quad (3.13)$$

where  $f_d(\mathbf{Q})$  is the atomic form factor of atom  $d$  in unit cell  $j$ ,  $g$  is the Landé factor and  $\mathbf{S}$  describes the local magnetic moment. Missing from the above cross section are any contributions from magneto-vibrational scattering processes [158].



**Elastic Magnetic Scattering** In analogy to the case of nuclear scattering, in elastic magnetic scattering the structure factor, in this case magnetic structure factor  $\mathbf{F}_M(\mathbf{Q})$ , again is the desired quantity:

$$\mathbf{F}_M(\mathbf{Q}) = \gamma r_0 \sum_d \frac{1}{2} g_d f_d(\mathbf{Q}) \langle \mathbf{S}_d \rangle e^{i\mathbf{Q} \cdot \mathbf{d}} e^{-W_d(\mathbf{Q})}. \quad (3.14)$$

In magnetic neutron scattering neutrons only from the component of the local magnetization density perpendicular to the scattering vector  $\mathbf{Q}$ . In order to consider this fact, a new parameter is introduced,  $\mathbf{F}_{M\perp}(\mathbf{Q}) = \hat{\mathbf{Q}} \times \mathbf{F}_M \times \hat{\mathbf{Q}}$ , which defines the component of  $\mathbf{F}_M(\mathbf{Q})$  perpendicular to  $\mathbf{Q}$ , where  $\hat{\mathbf{Q}} = \mathbf{Q}/Q$  is a unit vector in direction of the scattering vector  $\mathbf{Q}$ . This leads to the cross section for elastic magnetic scattering,

$$\left( \frac{d\sigma}{d\Omega} \right)_{mag}^{el} = \frac{(2\pi)^3}{v_0} \sum_{\tau_M} |\mathbf{F}_{M\perp}(\tau_M)|^2 \times \delta(\mathbf{Q} - \tau_M). \quad (3.15)$$

Even though, the cross sections for elastic magnetic and elastic nuclear scattering look very similar. Both interaction potentials exhibit some characteristic differences which enable for a clear separation between nuclear and magnetic scattering processes.

One fundamental difference between the two processes considers the respective scattering power of magnetic and nuclear processes. In  $\mathbf{F}_M(\mathbf{Q})$  each spin that contributes to the scattering process is considered a certain scattering power  $p = 1/2\gamma r_0 g f_d(\mathbf{Q})$ .<sup>1</sup> Here the magnetic form factor  $f_d(\mathbf{Q})$  takes into account that the neutron interacts with the magnetization density that exhibits a not negligible spacial extent. Due to this spatial extent the magnetic scattering power  $p$  decreases rapidly with increasing  $|\mathbf{Q}|$ , with the result of a characteristic  $|\mathbf{Q}|$ -dependence of magnetic scattering intensity. In contrast to this, for nuclear scattering processes, where the nuclear scattering length  $b$  is almost point-like, the correlating scattered intensity was found to be  $|\mathbf{Q}|$  independent. This strong  $|\mathbf{Q}|$ -dependence of the magnetic intensity is accompanied by the fact that only the perpendicular component of the magnetic moment contributes to the scattered intensity. And as result, magnetic intensity always exposes a characteristic decrease with increasing  $|\mathbf{Q}|$ , with an additional sensitive dependence on the angle  $\alpha$  between the scattering vector  $\mathbf{Q}$  and the magnetic moment  $\mathbf{S}$ .

**Inelastic Magnetic Scattering, Spin Waves: One Magnon Cross Section** Coherent inelastic magnetic scattering corresponds to the excitation or annihilation of collective excitations of the static magnetic order. These collective excitations, so-called magnon or spin wave excitations, are transverse excitations of the static magnetic order. Due to the vector character of the magnetic moment spin waves exhibit a quantization axis and in a semi-classical picture can be thought of as a precession of the magnetic

---

<sup>1</sup> $p$  has the dimension of a length and for  $\mathbf{Q} = 0$  this so-called magnetic scattering length is comparable to the value of a typical nuclear scattering length  $b$ .

moments around this axis. So for a quantization axis along the z-axis, the z-component of the magnetization remains constant and only terms with  $\alpha = \beta$  contribute to the scattering function  $\mathbf{S}(\mathbf{Q}, \omega)$ . This leads to the following cross section:

$$\begin{aligned} \left( \frac{d^2\sigma}{d\Omega dE'} \right)_{mag} &\propto \left( 1 - \frac{Q_z^2}{Q^2} \right) \frac{1}{2\pi\hbar} \int_{-\infty}^{\infty} \sum_j e^{i\mathbf{Qj}} \langle S_0^z(0) S_j^z(t) \rangle e^{-i\omega t} dt \\ &+ \sum_{\alpha \in [x,y]} \left( 1 - \frac{Q_\alpha^2}{Q^2} \right) \frac{1}{2\pi\hbar} \int_{-\infty}^{\infty} \sum_j e^{i\mathbf{Qj}} \langle S_0^\alpha(0) S_j^\alpha(t) \rangle e^{-i\omega t} dt. \end{aligned} \quad (3.16)$$

The first part of the equation (3.16) considers the z-component of the magnetization and since it was assumed to be constant, reproduces the elastic magnetic scattering, discussed in the previous section. Consequently, the inelastic part of the scattered intensity is determined only by the transverse correlations  $\langle S_0^{x,y}(0) S_j^{x,y}(t) \rangle$ . The evaluation of these transverse spin correlation terms for a given complex magnetic structure, however, can be a challenging task, and so only the simplest possible case, the Heisenberg ferromagnet with nearest-neighbor exchange only, shall be discussed here. The related Hamiltonian of the Heisenberg ferromagnet on a square lattice reads as

$$\mathcal{H} = - \sum_{i,j} J_{i,j} S_i S_j = - \sum_{i,j} J_{i,j} \left( S_i^z S_j^z + \frac{1}{2} (S_i^+ S_j^- + S_i^- S_j^+) \right) \quad (3.17)$$

and can easily be diagonalized using the Holstein-Primakoff transformation, which leads to the prominent q-energy dispersion for a Heisenberg ferromagnet,

$$\hbar\omega(\mathbf{q}) = 4S(J_{\mathbf{q}=0} - J(\mathbf{q})) = 4JS \cdot (2 - \cos(q_x a) - \cos(q_y a)). \quad (3.18)$$

This finally leads to the transverse cross section for spin wave scattering from a ferromagnet,

$$\begin{aligned} \left( \frac{d^2\sigma}{d\Omega dE'} \right)_{mag}^{inel} &= (\gamma r_0)^2 \frac{1}{2} S \left( \frac{1}{2} g f(\mathbf{Q}) \right)^2 \frac{k_f}{k_i} \left( 1 + \frac{Q_z^2}{Q^2} \right) e^{-W(\mathbf{Q})} \\ &\times \sum_{\tau_M, \mathbf{q}} \left( n(\mathbf{q}) \delta(E_i - E_f + \hbar\omega_{\mathbf{q}}) \delta(\mathbf{Q} - \mathbf{q} - \tau_m) \right. \\ &\left. + (n(\mathbf{q}) + 1) \delta(E_i - E_f - \hbar\omega_{\mathbf{q}}) \delta(\mathbf{Q} + \mathbf{q} - \tau_m) \right). \end{aligned} \quad (3.19)$$

Analogous to the phonon case the spin wave cross section consists of two parts regarding the creation and annihilation of a magnon with energy  $\hbar\omega_{\mathbf{q}}$ . For large moments  $S_i$  the expectation values of the transverse correlations obey the equations

$$\langle S_0^x(0) S_j^x(t) \rangle \propto \cos(\mathbf{qj} - \omega t) \quad (3.20)$$

$$\langle S_0^y(0) S_j^y(t) \rangle \propto \sin(\mathbf{qj} - \omega t) \quad (3.21)$$

These equations describe the already mentioned semi classical picture of the spin wave, as a precession of the spins circulating around the z-axis.

### 3.1.2 The Fluctuation-Dissipation Theorem

$$S(\mathbf{Q}, \omega) = \frac{\chi''(\mathbf{Q}, \omega)}{1 - e^{-\hbar\omega/k_B T}} \quad (3.22)$$

Sometimes it is more convenient to express the information obtained via a neutron scattering experiment in terms of the imaginary part of the magnetic susceptibility  $\chi''(\mathbf{Q}, \omega)$  instead of the scattering function  $S(\mathbf{Q}, \omega)$ . Both quantities are related to each other via the fluctuation-dissipation theorem [159, 160], as defined in equation (3.22), which relates the spectrum of the spontaneous fluctuations of an order parameter  $\langle m \rangle$  of a sample to the linear response of the system to a small external perturbation from its equilibrium state via the Bose-factor or thermal-population-factor  $(1 - e^{-\hbar\omega/k_B T})^{-1}$ . The thermal-population-factor accounts for the temperature driven population of excitation states of the fluctuation spectrum. According to this fluctuation-dissipation theorem the spectrum of spontaneous fluctuations  $S(\mathbf{Q}, \omega)$  and the dissipative linear response  $\chi''(\mathbf{Q}, \omega)$  to an external small perturbation show similar wave-vector and energy evolution.

When a neutron travels through a crystal and scatters on either nuclear or magnetic potentials of the sample, it can cause the system to have a transition from one quantum state to another. However the scattering of the neutron introduces just a small perturbation to the equilibrium state of the system and therefore may cause a transition between two quantum states of the system but does not change the states themselves. The energy that is then transferred from the neutron to the sample through an inelastic scattering process, is irreversibly absorbed by the sample and its dissipative energy evolution is similar to the energy evolution of the spontaneous fluctuations of the systems unperturbed state. This dissipative response of the system to small wave-vector and energy depending external perturbations is expressed by  $\chi''(\mathbf{Q}, \omega)$ , according to linear response theory.

Consequently, the theorem relates the excitation spectrum of the systems spontaneous excitations to the spectrum of the induced excitations resulting from the interaction of the neutron beam with the sample. Thus, during an inelastic neutron scattering measurement one actually has access to the excitation spectrum of the spontaneous fluctuations of a systems ordering parameter and not just the spectrum of the perturbed state. When correcting the obtained intensities for the thermal population factor, one transforms the intensity  $S(\mathbf{Q}, \omega)$  into the dynamical susceptibility of the system  $\chi''(\mathbf{Q}, \omega)$ . Further by correcting the obtained intensity for this thermal-population-factor, one corrects the intensity of the obtained inelastic signal for the temperature dependent population of excitation states. This thermal population of the excitation states of course effects the intensity of the inelastic signal as highly populated states give rise to signal with high intensity.

### 3.1.3 Longitudinal Polarization Analysis

As it has been mentioned earlier, the neutron interacts with matter via two processes: (1) The interaction with atomic nuclei via the strong nuclear force, provides access to nuclear properties of the sample. (2) The interaction via electro-magnetic interactions between the neutron spin and magnetic moments in the sample, with the magnetization densities of the sample gives access to magnetic properties.

As this versatility of neutron scattering obviously has many advantages it also provides a challenge in itself, as obtained intensities can originate from either nuclear or magnetic processes. A solution to this problem is the neutron spin. Considered as an additional degree of freedom, as it is done in polarized neutron scattering, it enables to separate both nuclear and magnetic processes but also to gain a much more detailed insight on magnetic properties.

With the spin as an additional degree of freedom it is possible to distinguish between two scattering processes, which are indistinguishable for non-polarized neutron scattering. (1) The non-spin-flip (NSF) scattering process, for which the spin of the scattered neutron remains parallel to the spin of the incoming neutron. (2) The spin-flip (SF) process, for which the spin of the scattered neutron is flipped in course of the scattering process and is oriented anti-parallel to the spin of the incoming neutron. Which of the two processes occurs depends on whether the scattering process is nuclear or magnetic as well as on the orientation neutron spin in reference to the direction of the magnetization density in the sample. A rule of thumb says that nuclear scattering is always (NSF) whereas magnetic scattering is (SF) if the neutron spin is parallel to the moment direction, but is (SF) if the neutron spin is perpendicular to the sample moments. Here three different spin directions, or neutron polarizations  $\mathbf{P}$ , are distinguished. A neutron polarization  $\mathbf{P}$  parallel to the scattering vector  $\mathbf{Q} = \mathbf{k}_f - \mathbf{k}_i$ , here  $\mathbf{k}_i$  and  $\mathbf{k}_f$  are the incident and final neutron wave vectors, is referred to as x-polarization. A neutron polarization perpendicular to the scattering vector but still within the scattering plane is referred to as y-polarization. Whereas a neutron spin perpendicular to the scattering plane is referred to as z-polarization. This leads to a right-handed cartesian coordinate system, which is bound to the experimental set up.

The technique of Longitudinal Polarization Analysis includes the acquisition of six different neutron cross sections, which correspond to three different incoming neutron polarization directions x, y or z times the two processes (SF) and (NSF),  $\sigma_\alpha^{NSF}$  and  $\sigma_\alpha^{SF}$ , with  $\alpha=x, y, z$ . For a detailed derivation of the inelastic neutron scattering cross section as a function of neutron polarization please turn to refs [159, 162–164]. As an example, the spin flip cross section for a neutron polarization direction  $\mathbf{P}$  parallel to  $\mathbf{Q}$  reads as

$$\sigma_{xx}^{SF} = \left( \frac{d^2\sigma}{d\Omega dE} \right)_{\mathbf{P} \parallel \mathbf{x}}^{SF} = \frac{k_f (\gamma r_e)^2}{k_i} \frac{1}{g^2 \mu_B^2} \frac{1}{\pi} F^2(\mathbf{Q}) \times \frac{\chi''_{yy}(\mathbf{Q}, \hbar\omega) + \chi''_{zz}(\mathbf{Q}, \hbar\omega)}{1 - \exp(-\hbar\omega/k_B T)} \quad (3.23)$$

with the magnetic form factor  $F^2(\mathbf{Q})$  and the generalized susceptibility for magnetic fluctuations along the  $\alpha=x, y, z$  direction  $\chi''_{\alpha\alpha}(\mathbf{Q}, \hbar\omega)$ .

As previously mentioned, magnetic neutron scattering is only sensitive to the components of the magnetic moments perpendicular to the scattering vector. This makes it impossible to determine  $\chi''_{xx}(\mathbf{Q}, \hbar\omega)$  using the longitudinal polarization analysis technique. However it is possible to determine the in-plane  $\chi''_{yy}(\mathbf{Q}, \hbar\omega)$  and out-of-plane  $\chi''_{zz}(\mathbf{Q}, \hbar\omega)$  components, which usually is sufficient when considering symmetries of the underlying crystal structure. The Longitudinal Polarization Analysis provides the possibility to completely separate the two components, the in-plane  $\chi''_{yy}(\mathbf{Q}, \hbar\omega)$  and out-of-plane  $\chi''_{zz}(\mathbf{Q}, \hbar\omega)$  magnetic susceptibility. This is possible because of the following two properties of magnetic neutron scattering: (1) Neutrons only scatter from magnetic fluctuations perpendicular to the scattering vector  $\mathbf{Q}$ , (2) fluctuations perpendicular to the neutron polarization  $\mathbf{P}$  scatter in the spin-flip (SF) channel, whereas fluctuations parallel to the incident neutron polarization scatter in the non-spin-flip (NSF) channel. The six different spin dependent neutron cross sections [159], which are available read as,

$$\begin{aligned}
\sigma_{xx}^{NSF} &\propto N(\mathbf{Q}, \omega) + BG^{NSF} \\
\sigma_{yy}^{NSF} &\propto \chi''_{yy}(\mathbf{Q}, \omega) + N(\mathbf{Q}, \omega) + BG^{NSF} \\
\sigma_{zz}^{NSF} &\propto \chi''_{zz}(\mathbf{Q}, \omega) + N(\mathbf{Q}, \omega) + BG^{NSF} \\
\sigma_{xx}^{SF} &\propto \chi''_{yy}(\mathbf{Q}, \omega) + \chi''_{zz}(\mathbf{Q}, \omega) + BG^{SF} \\
\sigma_{yy}^{SF} &\propto \chi''_{zz}(\mathbf{Q}, \omega) + BG^{SF} \\
\sigma_{zz}^{SF} &\propto \chi''_{yy}(\mathbf{Q}, \omega) + BG^{SF}
\end{aligned} \tag{3.24}$$

where any contributions by nuclear spin incoherent scattering processes have been neglected.  $BG^{NSF}$  and  $BG^{SF}$  stand for the background contributions for the various configurations, whereas  $N(\mathbf{Q}, \omega)$  is the coherent nuclear cross section, which, in this case, considers phonon scattering. In the above listed cross sections only inelastic scattering processes are considered.

Obvious from (3.24) is the possibility to completely separate nuclear from magnetic intensities by using a neutron polarization parallel to the scattering vector, as magnetic scattering only occurs in the (SF) channel whereas nuclear scattering only occurs in the (NSF) channel.

In addition to the separation of magnetic and nuclear signals, the in-plane and out-of-plane components  $\chi''_{yy}(\mathbf{Q}, \hbar\omega)$  and  $\chi''_{zz}(\mathbf{Q}, \hbar\omega)$  can now be separately extracted by performing simple subtractions of the various cross sections listed above.

$$\begin{aligned}
\sigma_{xx}^{SF} - \sigma_{yy}^{SF} &= \sigma_{yy}^{NSF} - \sigma_{xx}^{NSF} \propto \chi''_{yy}(\mathbf{Q}, \omega) \\
\sigma_{xx}^{SF} - \sigma_{zz}^{SF} &= \sigma_{zz}^{NSF} - \sigma_{xx}^{NSF} \propto \chi''_{zz}(\mathbf{Q}, \omega)
\end{aligned} \tag{3.25}$$

Equations (3.25) show that both the subtraction of the (NSF) cross sections as well

as the (SF) cross sections lead to the same result. Whether (SF) or (NSF) intensities should be chosen depends on characteristics of the particular experiment.

## 3.2 Neutron Scattering Instruments

For an investigation of Q-energy dispersions of excitations in condensed matter samples via inelastic neutron scattering, it is mandatory to be able to determine the neutron energies, both of the incoming neutrons as well as the scattered ones. To determine the neutron energy in a neutron scattering experiment, two very different approaches can be made, which demand two conceptional very different designs of neutron scattering instruments. For the three axis spectrometer, the wave character of the neutron is used and changes in wavelength of incoming and scattered neutrons are used to determine the energy transfers between the neutrons and the sample. Whereas the time-of-flight spectrometer is a concept which is based on the particle character of the neutron, and velocities and times-of-flight are measured in order to determine the energy transfers.

### 3.2.1 The Three Axis Spectrometer

The three axis spectrometer is a very versatile instrument designed to investigate excitations in single crystalline samples. It considers the wave properties of the neutron and takes advantage of Bragg scattering to select the incident neutron energy as well as to determine the energy transfer which occurred during the scattering process. The basic principle of the instrument is based on Bragg's law [159, 160]

$$n\lambda = 2d \sin(\theta). \quad (3.26)$$

where, for orthorhombic crystals

$$d = \frac{1}{\sqrt{\left(\frac{h}{a}\right)^2 + \left(\frac{k}{b}\right)^2 + \left(\frac{l}{c}\right)^2}} \quad (3.27)$$

is the so-called  $d$ -spacing considering the spacing between adjacent Bragg planes, indexed by the Miller indices  $(h, k, l)$ .

Operated on continuous neutron sources, the instrument is confronted with a white incident neutron beam. The device used to select the neutrons with desired incident energy from the white beam, is a monochromator crystal, which is placed in the incident neutron beam with an angle so that a certain reflection of the crystal obeys the scattering condition (3.26) and neutrons are reflected towards the sample. According to (3.26) a variation of the scattering angle results in a variation of the wavelength  $\lambda$  of the neutrons that are scattered towards the sample, whereas neutrons with a different wavelength do not obey the scattering condition and are not Bragg scattered. The main principle of the analyzer is identical to the one of the monochromator. The incoming neutrons with

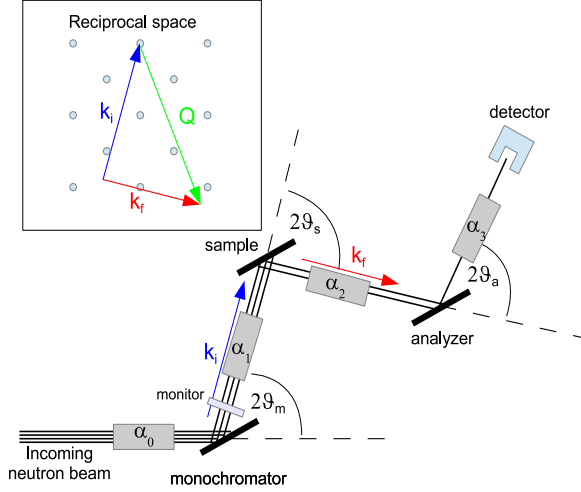


**Figure 3.1:** Classical W-configuration of a three-axis spectrometer with three rotation axes, the monochromator crystal, the sample and the analyzer crystal. Further illustrated is a sketch of the reciprocal space for an inelastic scattering process.

wavelength  $\lambda$  are scattered by the sample and by obeying Bragg's law for a certain reflection of interest are scattered with an angle of  $2\theta_{sample}$  towards the analyzer crystal. The neutrons arriving at the analyzer in principle can have any wavelength, depending on the energy transfer they performed with the sample. In order to determine this energy transfer one needs to select one of these wavelengths of the scattered neutrons. The energy transfer is then  $\hbar\omega = \frac{\hbar^2}{2m_N}(k_i^2 - k_f^2)$ , where  $k_i$  and  $k_f$  are the initial and final wave vectors of the neutron beam related with the wavelength via  $k = |\mathbf{k}| = 2\pi/\lambda$ . The selection of the wavelength of the scattered neutrons is again conducted by elastic Bragg scattering, where only neutrons with certain wavelengths are reflected towards the detector, whereas neutrons with different wavelengths do not hit the detector. In order to investigate different values of energy transfer, one value  $k_i$  or  $k_f$  is fixed whereas the other is varied in a way that  $\hbar\omega = \frac{\hbar^2}{2m_N}(k_i^2 - k_f^2)$  provides the desired energy transfer.

The investigation of an excitation dispersion is conducted by performing one dimensional scans through the dispersion in the 4 dimensional energy- $\mathbf{Q}$  space. Scans can be performed in two distinct ways, either a certain value of energy transfer is fixed and the scan is performed in  $\mathbf{Q}$ -space by varying the momentum transfer  $\mathbf{Q} = \mathbf{k}_f - \mathbf{k}_i$ , a so-called constant energy or Q-scan. Or the momentum transfer is held at a fixed value

and the energy transfer is varied, so-called energy scan. Given that the performed scan crosses the dispersion of the excitation spectrum, either scan will provide one point of the excitations energy-Q dispersion. This means that a typical three-axis experiment determines the dispersion of a given excitation point by point. Even with the use of area detectors, which provides a 2D map of the Q-space with each scan, each scan provides information only for one particular energy transfer.

### 3.2.2 The Time of Flight Neutron Spectrometer

The other approach to inelastic neutron scattering considers the particle properties of the neutron as a particle with a certain mass  $m_n$ , energy  $\mathbf{E}_n = 1/2m_n\mathbf{v}_n^2$  and thus velocity  $\mathbf{v}_nm_n = \hbar\mathbf{k}$  in order to determine the energy transferred  $\hbar\omega = \frac{\hbar^2}{2m_n}(k_i^2 - k_f^2)$  between the neutron and the sample during the scattering process.

Practically this can be conducted by determining the time a neutron with certain velocity needs to travel a certain distance until it is detected at the detector. If all quantities, the incident velocity and the distances of travel, are known, the velocity of the scattered neutron and thus the velocity change, which corresponds to the energy transfer can be identified. This different approach from the three axis spectrometer obviously demands a different approach in instrument design.

Figure 3.2 shows a sketch of a classical neutron time-of-flight instrument in top-view.

For a classical ToF instrument the main difference to the three axis instrument is the absence of monochromator as well as analyzer crystals. Where the three axis spectrometer takes advantage of the wave properties of the neutron and uses Bragg's law to select the desired incoming neutron wavelength, the Time-of-Flight approach considers solely the particle properties of the neutron. Instead of a monochromator crystal, incident neutron energies are selected by using a set of choppers, which are rotating devices placed in the neutron path between the source and the sample and open and close the flight path periodically. For each period the neutron path is opened for a certain opening time  $t_0$  for which the neutrons are able pass the distance between the choppers  $l_0$  and due to the finite time  $t_0$  and finite distance  $l_0$  neutrons need to travel to exit the chopper pair, only neutrons with certain velocity  $v_0 = l/t_0$  are able to pass the choppers and travel the instrument towards the sample. Right in front of the sample another chopper is placed. The opening of this chopper starts the counting of the time-of-flight a neutron needs to travel the distance from the sample chopper to the detector. The counting time will be reset for every new opening of the chopper and thus for every new emitted neutron pulse the time will be counted separately. After passing the sample chopper the neutrons reach and interact with the sample and finally reach the detector bank, with a sample-detector-distance  $L_3$ . The detector bank consists of multiple position sensitive detector tubes, which provide a wide solid angle in order to cover a wide range of possible momentum transfers and collect as much intensity as possible. Each detected neutron event is recorded with three quantities characterizing



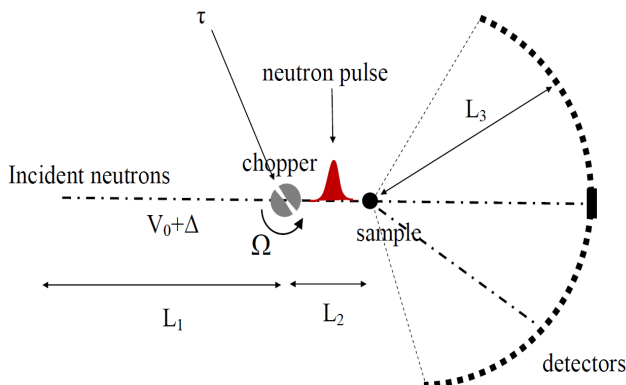


**Figure 3.2:** Sketch of the generic set up of a classical ToF instrument (top-view). Incident neutrons with velocity distribution  $v + \Delta v$  travel the neutron guide from the source/moderator pass the sample chopper, interact with the sample and get detected at the detector bank, in distance  $L_3$  to the sample. The chopper rotates with frequency  $\Omega$  and thus presents an opening for the incident neutrons for a time window  $t_0$ . The time between transmitted neutron pulses is defined by  $\tau = 1/N\Omega$ .

the event, the detector  $d$ , the neutron was detected at, the position  $h$  the neutron hit detector  $d$  and the time-of-flight  $t$  that passed between chopper opening and the arrival of the detected neutron. To enhance the collected intensity, neutrons detected in the same detector pixel with times-of-flight within a certain interval  $\Delta\tau$ , time bin, are collected and form the overall intensity for that particular detector pixel, time-of-flight channel  $K$  and width of the time bin  $\Delta\tau$ .

Figure 3.3 shows a time-flight-path diagram of normal scattering incidents occurring during a time of flight experiment. The diagram reads as follows.

A monochromatic neutron pulse with neutron velocity  $v_0$  travels the instrument towards the sample, illustrated as the dashed diagonal line. The neutrons that interact with the sample without energy transfer and thus don't change their velocity and reach the detector at a certain time  $t_2 + t_3 = (L_2 + L_3)/v_0$ , correspond to the dashed line. In the red spectrum, which illustrates a typical time-of-flight intensity spectrum, these neutrons result in the strong middle peak, which represents the elastic line, resulting from elastic scattering processes with zero energy transfer. Neutrons that are involved in inelastic interactions with the sample, where energy is transferred from either the neutron to the sample (energy loss) or the sample to the neutron (energy gain), change their velocity and thus reach the detector in a shorter time (energy gain) or longer

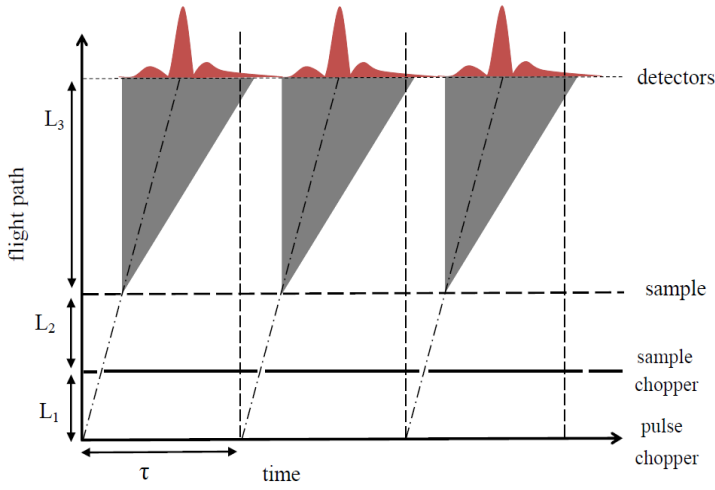


**Figure 3.3:** Time-flight-path diagram for a typical ToF experiment. Dashed line represents a neutron pulse with certain velocity traveling the instrument and interacting elastically with the sample. The gray shaded triangles, starting from the sample position, symbolize all possible inelastic scattering processes, both for neutron energy gain and neutron energy loss processes. The red spectrum on top of the figure illustrates a possible time-of-flight intensity spectrum with the strong peak in the center of the spectrum representing intensity from elastic scattering processes and the smaller humps left and right from the elastic peak representing intensities from energy gain and energy loss inelastic scattering processes, respectively.

time (energy loss) than the neutrons scattered elastically. This is illustrated by the gray shaded triangle. The energy gain side (left side of the triangle) of course has a clear defined cut off, which is represented by the vertical axis of the triangle, which corresponds to the theoretical limit of neutrons that would travel the sample-detector distance in zero time resulting from an infinite energy transfer from the sample and an infinite neutron velocity. For the energy loss side of the spectrum in principle no such clear defined cut off is present, as neutrons can transfer any amount of energy up to their complete kinetic energy to the sample, which in principle would result in a horizontal line for neutrons traveling the sample-detector distance with zero velocity, which would take an infinite time-of-flight. This intensity, resulting from very slow neutrons is illustrated in the red time-of-flight intensity spectrum as the fading tail towards high ToF values. These very slow neutrons reach the detector at the same time as faster neutrons from the following pulse and thus result in a background contribution occurring for every detected pulse. This frame overlap can cause severe background problems, especially if large parts of the spectrum are overlapping with parts of the spectrum of the following pulse, as it cannot be distinguished which pulse the detected

neutrons have to be allocated to.

After recording the times-of-flight of all detected neutrons and the formation of time bins, the energy transfer, which is aside from the momentum transfer the defining quantity of an inelastic scattering experiment, can be determined by determining the difference in time-of-flight of neutrons involved in inelastic scattering processes and neutrons scattered without energy transfer. In course of a time-of-flight experiment the detected neutrons, however, are recorded with the characterizing experimental parameters, detector pixel and time-of-flight, and several transformations are needed to be performed in order to express the obtained intensity in the common parameters, energy and momentum transfer:

$$\omega(t) = \frac{m_n}{2\hbar} L^2 \frac{t^2 - t_3^2}{t^2 t_3^2} \quad (3.28)$$

and

$$Q = \frac{m_n}{\hbar} L \sqrt{\frac{t^2 + t_3^2 - 2 \cos(2\theta) t_3 t}{t_3^2 t^2}}, \quad (3.29)$$

where  $2\theta$  is the scattering angle. Here every detector pixel has been associated with one specific scattering angle. These definitions for the momentum and energy transfer ((3.28) and (3.29)) lead to an expression for the obtained intensity expressed in terms of momentum and energy transfer,

$$I(2\theta, K) \propto \frac{k'}{k} 4\pi b^2 S(\mathbf{Q}, \omega(K\Delta\tau)) \frac{d\omega}{dt} \Delta\tau. \quad (3.30)$$

Here  $K$  represents a time-of-flight channel, regarding all events with this particular time-of-flight, whereas  $\Delta\tau$  stands for the time bin width.  $\omega(K\Delta\tau)$  thus considers the dependence of the energy transfer  $\omega$  on the time-of-flight of the detected neutron, where short times-of-flight correspond to small energy transfers whereas long ToF are caused by large energy transfers from the neutron to the sample - this is valid for the energy loss side of the spectrum and must be reversed for the energy gain side.

A time-of-flight experiment provides information regarding a three or even four dimensional area of the energy-Q space, with the size of this area depending on the energy- and Q-range that is accessible for that particular instrument and instrumental set up. The obtained data then is treated by performing 2 dimensional slices or 1 dimensional cuts through the three or four dimensional energy-Q space. These slices and cuts are comparable to the data obtained via a three axis experiment.

### Repetition Rate Multiplication

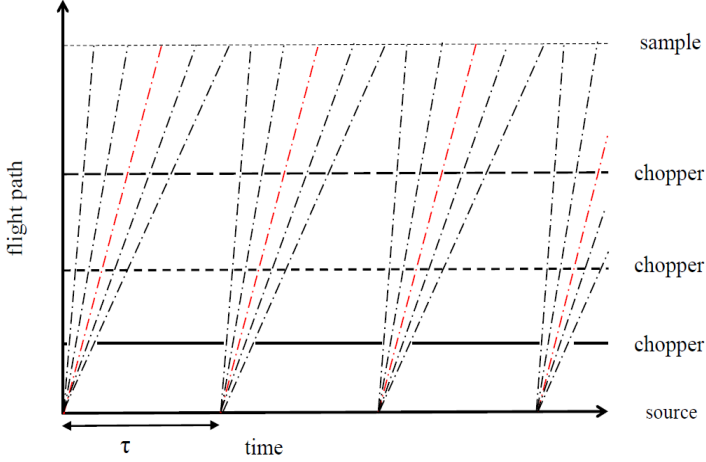


**Figure 3.4:** Time-flight-path diagram illustrating the Repetition Rate Multiplication principle. Note that only the source-sample distance is shown. Horizontal dashed lines represent the choppers used to create the monochromatic pulses. Colored dashed-dotted lines symbolize the monochromatic pulses where the steepness of the slopes is correlated to the neutron velocities. The red line represents the pulse with velocity identical to the pulses in figure 3.3. The spread of the arrows at the sample position illustrate that pulses of different energy reach the sample at different times.

As explained in the previous section, a conventional ToF instrument uses a set of choppers to create out of every pulse emitted by the source one monochromatic neutron pulse with neutrons of only one incident energy. As the source emits pulses in a certain frequency, pulses reach the sample with a certain time  $\tau = 1/N\Omega$  between two consecutive pulses. As illustrated in figure 3.3 this leads to a period between two pulses for which almost no neutrons are detected by the detector, except the few very slow ones that transferred a great portion of their incident energy to the sample. The repetition rate multiplication technique is a way to make use of this time between two pulses, for which in principle the instrument does not operate but waits for next neutrons to be emitted by the source. Figure 3.4 is a time-flight-path-diagram which illustrates the principle of the Repetition Rate Multiplication technique. The main difference to a conventional ToF instrument is the fact that each source pulse is not monochromatized into one pulse with one incident energy, but it is chopped into several monochromatic pulses, each with different incident energies. This is done by a set of special choppers that are placed in the neutron path and are synchronized in a specific way. As the newly created monochromatic pulses with different incident neutron energies travel the instrument they become

separated from each other, due to their different velocities, and thus reach the sample at different times. The incident energies of the new pulses need to be chosen in a way that a substantial frame overlap is prevented, which means that slow and fast neutrons of consecutive pulses do not reach the detector simultaneously. If this is done properly the advantage of the Repetition Rate Multiplication technique is obvious, as not only the waiting time between two pulses can be used for the experiment but for every run, data for several different incident energies can be obtained, in contrast to the single energy in case of a conventional instrument. These advantages obviously come to the cost of neutron flux per pulse, which is substantially reduced due to the chopping of the source pulse into several sub-pulses. As this section is only meant as basic introduction of the technique, please turn to reference [165] for a more detailed explanation of the principles of Repetition rate Multiplication.

# 4 Effect of P- and Co-Doping on the $\text{Eu}^{2+}$ Magnetic Sublattice in $\text{EuFe}_2\text{As}_2$

## 4.1 Introduction

### 4.1.1 Motivation

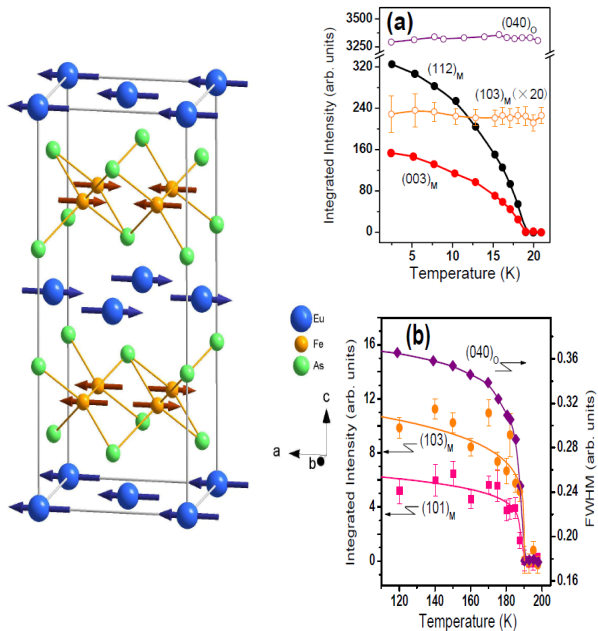
The motivation of this study is to investigate the effect Co- and P-doping on the static magnetic structure of the Eu-sublattice and a possible interplay between magnetism and superconductivity. Several effects of doping on the Eu-sublattice have been proposed, solely based on results obtained from characterization measurements. In order to unambiguously determine the magnetic structure, however, scattering experiments are indispensable. This leads to the motivation to investigate the doping effect on the Eu-sublattice using the techniques of single crystal neutron diffraction and polarized single crystal neutron diffraction. The results from this study will be discussed in the current chapter.

### 4.1.2 Nuclear and Magnetic Structure of Undoped $\text{EuFe}_2\text{As}_2$

The members of the  $\text{EuFe}_2\text{As}_2$  series hold a unique position in the family of 122-materials as the only member of this class of materials with magnetic rare earth ions incorporated into the crystal structure. Europium, which is integrated into the crystal structure in its  $\text{Eu}^{2+}$  state is an S-state rare-earth ion with  $4f^7$  electronic configuration, an overall spin  $S=7/2$  and a large resulting theoretical effective magnetic moment of  $g\sqrt{S(S+1)} = 7.94 \mu_B$  with  $g = 2$ , which eventually forms an antiferromagnetic sublattice below 18 K [167].

The parent compound  $\text{EuFe}_2\text{As}_2$  was first synthesized by Marchand et al. [168] in 1978 and was rediscovered in 2008 as a possible parent compound for another series of high  $T_c$  iron arsenide materials [169, 170]. Similar to other 122-pnictides,  $\text{EuFe}_2\text{As}_2$  crystallizes in the  $\text{ThCr}_2\text{Si}_2$ -type structure, which can be described as  $\text{Fe}_2\text{As}_2$ -layers stacked in c-direction and separated by  $\text{Eu}^{2+}$ -layers. For high temperatures the  $\text{ThCr}_2\text{Si}_2$ -type structure has a tetragonal symmetry with lattice parameters of  $a=b=3.911 \text{ \AA}$ ,  $c=12.110$

**Figure 4.1:** Nuclear and magnetic structure of undoped  $\text{EuFe}_2\text{As}_2$  obtained via single crystal neutron diffraction. Illustrated is one unit-cell in orthorhombic notation. (a) Temperature dependence of the  $\text{Eu}^{2+}$ -sublattice (black and red solid symbols), Fe-SDW (open yellow symbols) and crystal structure (open purple symbols). Obvious is the missing interplay between the long range Eu-order or either crystal structure or Fe-SDW order. (b) Temperature evolution of the Fe-SDW (yellow and pink symbols) and the crystal structure (purple symbols) between 120 and 200 K. All shown results are taken from [166].



Å. Around  $T=190$  K the structure transitions into a phase with lowered orthorhombic symmetry with lattice parameters  $a=5.537$  Å,  $b=5.505$  Å,  $c=12.057$  Å and space group  $Fmmm$  [166]. As typical for the 122-materials, the structural phase transition is accompanied by a magnetic phase transition, where the  $\text{Fe}^{2+}$ -moments form the SDW order with propagation vector  $\mathbf{Q}_{AFM}=(1, 0, 1)_{ortho}$ . The magnetic transition takes place almost simultaneously to the structural transition. In addition to the Fe-SDW magnetic sublattice, around 18 K the system experiences the formation of a second magnetic sublattice as the Eu-moments become organized in the long range antiferromagnetic A-type structure, first reported by Raffius et al. [167] in 1993 and later confirmed via characterization measurements [169, 170], as well as scattering techniques [166, 171]. Xiao et al.[166] confirmed via single crystal neutron diffraction the A-type structure of the Eu-sublattice, which forms as an antiferromagnetic stacking of ferromagnetic layers with moments oriented along the orthorhombic a-direction, as illustrated in figure 4.1. Their results further show a very weak, almost absent, interference of the Eu magnetic order with either structural effects or the present Fe-SDW order, figure 4.1 (a), which leads to a mostly autonomous sublattice of long range ordered  $\text{Eu}^{2+}$ -moments.

The formation of this Eu-sublattice most likely can be ascribed to the Ruderman-Kittel-Kasuya-Yosida (RKKY) mechanism [172–174], for which Eu-Eu interactions of the localized Eu-moments are of indirect nature, and are mediated via itinerant elec-

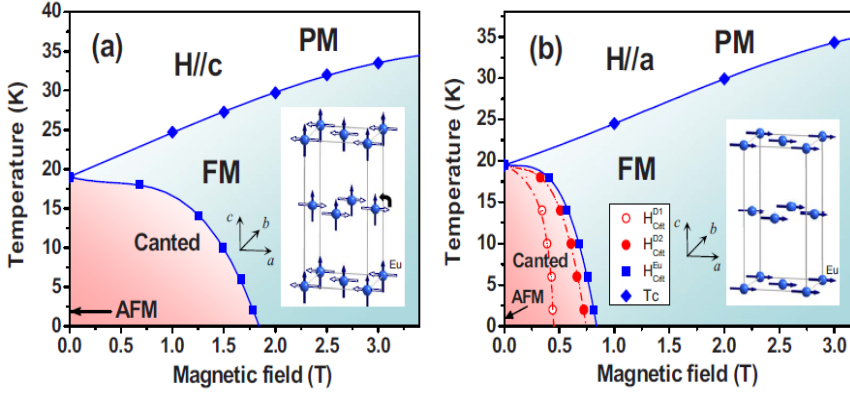


**Figure 4.2:** (a) Magnetic phase diagram for  $\text{EuFe}_2\text{As}_2$  with applied magnetic field parallel to crystallographic  $c$ -direction. Inset illustrates the symmetry of the Eu-sublattice, where open arrows correspond to the A-type structure without field, whereas filled arrows illustrate the field induced structure. (b) Magnetic phase diagram for  $\text{EuFe}_2\text{As}_2$  with applied magnetic field parallel to crystallographic  $a$ -direction. Figure taken from ref. [176]

trons. The unpaired electrons of the  $\text{Eu}^{2+}$ -ions occupy the Eu-4f orbitals, which possess very little spatial extension and are tightly bound to the atomic nucleus and this leads to a strong localization of the valence electrons and the resulting magnetic moments. Because of the small overlap of the Eu-4f orbitals of neighboring Eu-ions, caused by the little spatial expansion of the orbitals in combination with the average Eu-Eu distances in these materials, contributions by direct Eu-Eu interactions to the coupling mechanism can be neglected and the (RKKY) mechanism is most probable the predominant interaction.

The antiferromagnetic A-type structure of the Eu-sublattice is fragile and easily affected by perturbations such as externally applied pressure or magnetic field and doping. The results of these perturbations are a change of the sublattice symmetry from antiferromagnetic to ferromagnetic. Figure 4.2 illustrates how the A-type ferromagnetic structure can be transformed into a ferromagnetic structure by applying relatively moderate magnetic fields of just 1.75 T or 0.75 T, depending on the field direction [175, 176]. These results clearly show that the inter-layer coupling of neighboring Eu-layers is by far the weakest coupling and the first to be modified whereas the in-plane correlations remain unaffected, and so the transformation of antiferromagnetic structure into ferromagnetic symmetry takes place via a rotation of moment directions of complete ferromagnetic Eu-layers.



### 4.1.3 Pressure Induced Superconductivity in $\text{EuFe}_2\text{As}_2$

Aside from doping, which is one way to induce superconductivity to the system, applied external pressure provides another perturbation which can lead to a superconducting ground state. Increasing pressure gradually suppresses both the nuclear and magnetic phase transitions to the point where the Fe-SDW order is completely suppressed and superconductivity sets in. For a small window of external pressures between 2-2.7 GPa the system becomes superconducting with a maximal transition temperature of  $T_c=25$  K. For this pressure range the magnetic order of the Eu-sublattice remains unaffected and the antiferromagnetic A-type structure coexists with superconductivity for temperatures below 18 K [177–180]. For pressures as high as 6-7 GPa, for which the superconducting state is already suppressed, the structure of the Eu-sublattice transitions from antiferromagnetic A-type to a ferromagnetic structure. Surprisingly the induced ferromagnetic order shows a much higher transition temperature as it persists up to 50 K for external pressures around 8 GPa. Accidentally or not this is almost the exact pressure where a valence change of Eu-moments from  $\text{Eu}^{2+}$  to  $\text{Eu}^{3+}$  sets in [180]. For pressures around 20 GPa all magnetic order is completely suppressed.

### 4.1.4 Doping Induced Superconductivity in $\text{EuFe}_2\text{As}_2$

Impurity doping is another method to suppress the static magnetic Fe-SDW order and to induce superconductivity in  $\text{EuFe}_2\text{As}_2$ -materials. Partial replacement of each of the three elements in the  $\text{EuFe}_2\text{As}_2$  structure will eventually lead to superconductivity and further will affect the structure of the Eu-sublattice in a specific way.

**$\text{Eu}_{1-x}(\text{Na/K})_x\text{Fe}_2\text{As}_2$**  Doping the system with either sodium or potassium suppresses both the Fe-SDW and nuclear phase-transition and induces superconductivity, which is achieved for 30% Na or 10% K, with optimal  $T_c$ 's of 35 K [181] and 33 K [182], respectively. Increasing K-content gradually suppresses the Eu-sublattice magnetization until Eu-order is completely absent for  $x>0.65$ . A change of the magnetic structure of the Eu-sublattice is not reported [182–184], but instead the substitution of Eu with either Na or K weakens the Eu-Eu interaction and leads to a more short ranged magnetic order and eventually destroys it completely [183].

**$\text{Eu}(\text{Fe}_{1-x}(\text{Co/Ni})_x)_2\text{As}_2$**  Substituting Fe by either Ni or Co is another way to suppress both the Fe-SDW and nuclear phase-transition and in case of Co-doping induce superconductivity. Ni-doping does not induce superconductivity. Further, both doping methods have large effects on the Eu-sublattice, which, in contrast to Na/K doping remains long range ordered, but is gradually changed from the antiferromagnetic A-type structure to ferromagnetic symmetry [185].

In the Co-doped system, which becomes superconducting around  $0.05<x<0.15$ , a co-existence of long range magnetic order of the Eu-sublattice and superconductivity is

observed. Below  $T_c=21$  K the system becomes superconducting but experiences a reentrant type conductivity around 18 K due to the onset of long range Eu-order [186, 187], which seems to be harmful to superconductivity. For increasing Co-concentration the structure of the sublattice gradually changes from A-type to a ferromagnetic structure, where Eu-moments remain parallel to the ab-plane and complete ferromagnetic Eu-layers are rotated around the c-axis [186].

**$\text{EuFe}_2(\text{As}_{1-x}\text{P}_x)_2$**  Replacing arsenic by the isovalent phosphorous is probably the most interesting method to induce a superconducting phase in  $\text{EuFe}_2\text{As}_2$ . In contrast to the previously mentioned doped compositions, doping with phosphorous does not introduce additional charge carriers, due to the identical valence of arsenic and phosphorous. But because of the smaller ionic radius of phosphorous it induces strain to the crystal structure, which is why P-doping is also referred to as applying *chemical pressure*. Aside from the obvious effect of P-doping, the suppression of the Fe-SDW and the orthorhombic distortion and the subsequent onset of superconductivity, it further strongly affects the Eu-sublattice. In contrast to the effect of Ni/Co-doping, with increasing P-content all Eu-moments start tilting out of the ab-plane and eventually form a ferromagnetic structure with moments aligned along the c-axis [188–193]. The feature that makes the P-doped Eu-compounds unique among the pnictide and chalcogenide materials, is the coexistence of superconductivity and a ferromagnetic type structure, as for  $x=0.2$  the system is optimally doped with transition temperature  $T_c=28$  K [189] and the Eu-sublattice is transformed from the antiferromagnetic A-type structure into a structure with moments tilted in c-direction and a sizeable ferromagnetic component.

## 4.2 Experimental Details

To investigate the effect of P- and Co-doping on the static magnetic long range order of the  $\text{Eu}^{2+}$ -sublattice in  $\text{EuFe}_2\text{As}_2$  single crystal neutron diffraction as well as polarized single crystal neutron diffraction experiments have been performed. For this purpose, single crystals of  $\text{Eu}(\text{Fe}_{0.986}\text{Co}_{0.014})_2\text{As}_2$ ,  $\text{Eu}(\text{Fe}_{0.975}\text{Co}_{0.025})_2\text{As}_2$ <sup>1</sup> were synthesized by the tin flux method and were characterized by means of resistivity and magnetization by collaborating scientist Dr. A. Thamizhavel of the Department of Condensed Matter Physics and Material Sciences, Tata Institute of Fundamental Research, Homi Bhabha Road, Colaba, Mumbai 400 005, India. Further,  $\text{EuFe}_2(\text{As}_{0.95}\text{P}_{0.05})_2$  and  $\text{EuFe}_2(\text{As}_{0.85}\text{P}_{0.15})_2$ <sup>2</sup> were synthesized by Bridgeman methods and were characterized by resistivity and magnetization measurements by collaborating scientist Dr. H. S. Jeevan from the 1. Physikalisches Institut, Georg-August-Universität Göttingen [189]. The four crystals, used for the neutron experiments, had masses in the range of 5-20 mg and were of irregular plate-like

<sup>1</sup>The doping levels were determined by the sample grower by means of characterization techniques

<sup>2</sup>The doping levels were determined by the sample grower by means of characterization techniques

shape with dimensions in the range of  $2.5 \times 2.5 \times 0.3 \text{ mm}^3$  to  $5 \times 5 \times 0.5 \text{ mm}^3$ , respectively. The majority of the used crystals was of reasonable quality, however, the neutron scattering experiments as well as the conductivity measurements revealed a possible impurity phase in the  $\text{EuFe}_2(\text{As}_{0.85}\text{P}_{0.15})_2$  sample, most likely consisting of undoped  $\text{EuFe}_2\text{As}_2$ . However, this did not affect the scattering results. The physical properties of the samples were determined via characterization methods, where resistivity measurements revealed superconducting phases for the 2.5% Co-doped as well as the 15% P-doped samples.  $\text{EuFe}_2(\text{As}_{0.85}\text{P}_{0.15})_2$ , which is supposed to be close to optimal doped, showed a superconducting transition temperature around 30 K and even  $\text{Eu}(\text{Fe}_{0.975}\text{Co}_{0.025})_2\text{As}_2$ , which must be regarded as heavily underdoped, still exhibited weak superconducting behavior below 5 K.

The neutron diffraction experiments on  $\text{EuFe}_2(\text{As}_{0.85}\text{P}_{0.15})_2$  were performed on the single crystal diffractometer D23 located at the ILL [194], using a neutron wavelength of  $1.28 \text{ \AA}$ . This short wavelength was chosen in order to reduce the neutron absorption of the Eu containing material. The short wavelength of  $1.28 \text{ \AA}$  was a compromise between the shortest wavelength available and the optimal neutron flux at D23, which usually shows its best performance for incident neutrons in the thermal range.

The polarized neutron diffraction experiments, on all four samples, were carried out on the cold neutron diffractometer DNS located at the FRM2 [195]. Here the experiments were carried out using a wavelength of the incident neutrons of  $4.74 \text{ \AA}$ . One problem with this long wavelength is obviously the increased neutron absorption effects. However, due to the small sample mass of just about 10-20 mg and the thin plate-like shapes of the samples the observed intensities were still reasonable. The experiment further benefited from the orientation of the thin crystals of approximately  $3 \times 3 \times 0.25 \text{ mm}^3$  which were oriented with the c-axes parallel to the scattering plane, which resulted in a limited path of transmitted neutrons through the crystal and consequently in a reduction of absorption effects. The large magnetic moment of  $\approx 7\mu_B$  also helped to obtain reasonable results on the magnetic order of the Eu-sublattice.

Throughout the entire chapter, the orthorhombic notation will be used to describe the crystal structure, with space group Fmmm and lattice constants for the 15% P-doped compound of  $a=b=5.5 \text{ \AA}$ ,  $c=11.95 \text{ \AA}$  and  $a=b=5.5 \text{ \AA}$ ,  $c=12.1 \text{ \AA}$  for the 5% P-doped and both Co-doped samples. For consistency the orthorhombic notation is used for all samples, even though no signs for an orthorhombic splitting in any of the investigated crystals has been observed. Nonetheless, except for maybe the 15% P-doped sample, the crystal structure of the other three compounds is most likely orthorhombic, since both Co-doped samples as well as the 5% P-doped sample have to be located deep in the underdoped region of the corresponding phase diagrams. For both experiments, at D23 and DNS, the crystals were oriented with the orthorhombic (H, 0, 0)- and (0, 0, L)-axes within the scattering plane. In principle this would provide access to reflections arising from the Fe-SDW ordering with propagation vector  $\mathbf{Q}_{AFM}=(1, 0, 1)$  as well as the A-type  $\text{Eu}^{2+}$ - ordering with propagation vector  $\mathbf{Q}_{Eu}=(0, 0, 1)$ . The sample orientation should further provide access to any

type of ferromagnetic components to the Eu-sublattice, predicted for P-doped materials.

## 4.3 Results and Discussion

### 4.3.1 Magnetic Structure of $\text{EuFe}_2(\text{As}_{1-x}\text{P}_x)_2$ $x=0.05$ , $x=0.15$

As mentioned in the introduction, the feature that makes the P-doped  $\text{EuFe}_2(\text{As}_{1-x}\text{P}_x)_2$  series unique within the pnictide superconductors, is a proposed coexistence of superconductivity and long range ferromagnetic order of the Eu-sublattice. The first step in the investigation of this coexistence of superconductivity and ferromagnetic order was to determine a superconducting phase present in the samples, which were supposed to be used for the scattering experiments. For this, resistivity measurements were performed for all samples later used in the diffraction experiments. Figure 4.3 shows

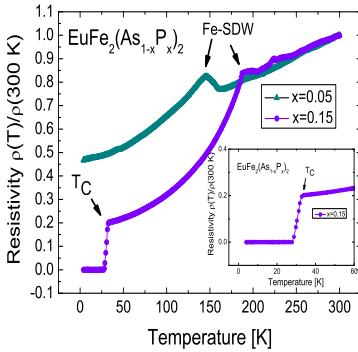


**Figure 4.3:** Temperature dependence of the in-plane resistivity normalized to room-temperature resistivity of  $\text{EuFe}_2(\text{As}_{0.95}\text{P}_{0.05})_2$  (cyan symbols) and  $\text{EuFe}_2(\text{As}_{0.85}\text{P}_{0.15})_2$  (violet symbols). The measurements were performed on two single crystal samples using a standard four-terminal method. The measurements were performed by collaborating scientist Dr. Y. Xiao of JCNS-2 on a Quantum Design Physical Property Measuring Device (PPMS).

the temperature dependence of normalized in-plane resistivity of the two samples that were used for the neutron scattering experiments. The prominent kink in the slope at 150 K of the 5%-doped sample (cyan symbols) marks the onset of the Fe-SDW order. The ordering temperature of  $T_N=150$  K is about 30 K reduced compared to the parent undoped compound. For low temperatures, no signs of a superconducting phase can be observed. Whereas, the 15% sample (violet symbols) shows a prominent resistivity drop to zero at  $T_c=32$  K, which clearly locates the sample in the optimal doped range of the phase diagram. However, the in-plane resistivity of this sample shows another prominent feature around 180 K, which most likely must be ascribed to the onset of Fe-SDW order. According to published phase diagrams for  $\text{EuFe}_2(\text{As}_{1-x}\text{P}_x)_2$  the long range SDW-order transition for a P-concentration of 15% occurs well below 100 K. The

reason why no sign for this transition has been observed is not clear, but the signal around 180 K, which is very close to the transition temperature in undoped  $\text{EuFe}_2\text{As}_2$ , is most likely caused by the already mentioned impurity phase, probably of undoped  $\text{EuFe}_2\text{As}_2$ . This impurity phase, however, did not affect the investigations on the magnetic structure of the Eu-sublattice, as both magnetic structures do not interfere but can easily be distinguished.

In order to get a first overview of the possibly modified magnetic structure of the Eu-sublattice, 2D maps of the reciprocal space were obtained using the polarized neutron diffraction technique. Figure 4.4 is a collection of 2D reciprocal space maps for the 5% (a), (b) and 15% (c)-(f) P-doped samples. The data were taken at 5 K using incident neutron polarizations parallel to the scattering vector  $\mathbf{Q}$  (x-polarization) and perpendicular to the scattering plane (z-polarization), respectively.

As discussed in chapter 3, when considering the neutron spin as an additional degree of freedom two scattering processes can be distinguished, which are undistinguishable with non-polarized neutrons scattering. The non-spin-flip (NSF) scattering process as a process which conserves the spin direction of the neutron, resulting in parallel spin directions the incident and scattered neutrons. And in contrast, the spin-flip (SF) process as a scattering process that flips the neutron spin and leaves the spin directions of incident and scattered neutrons to be anti-parallel. Whether a process flips or does not flip the neutron spin depends on the nature of the process, nuclear or magnetic, and for magnetic processes it further depends on the orientation of the neutron spin relative to the magnetization direction in the sample. For nuclear scattering all processes are (NSF) and maintain the neutron spin direction. Magnetic scattering processes can either be (SF) or (NSF). For processes with the neutron spin parallel to the magnetic moments of the sample, the neutron spin remains unchanged and the scattering process is (NSF). But for processes with neutron spin direction perpendicular to the direction of magnetic moments of the sample, the neutron spin is flipped and thus the process is (SF). The fact that magnetic neutron scattering is only sensitive to the component of the magnetic moment perpendicular to the scattering vector, leads to the situation that for a neutron polarization parallel to the scattering vector  $\mathbf{Q}$  (x-polarization), all magnetic scattering processes are exclusively (SF). Whereas, all nuclear processes are always (NSF). Consequently, x-polarization leads to a complete separation of magnetic and nuclear scattering intensities, as (SF) intensities are purely magnetic and (NSF) intensities are purely nuclear. Note that in case of the DNS experiments, which are discussed here, a neutron polarization parallel to the scattering vector  $\mathbf{Q}$  is not possible. With the multi-detector of the instrument which covers a wide range of scattering angles  $0 < 2\delta < 150$ , for every measurement several reflections can obey Bragg's law simultaneously. For x-polarization a polarization was chosen parallel to a  $\mathbf{Q}$  vector with moderate scattering angle, between minimum and maximum angles covered by the detector rack.

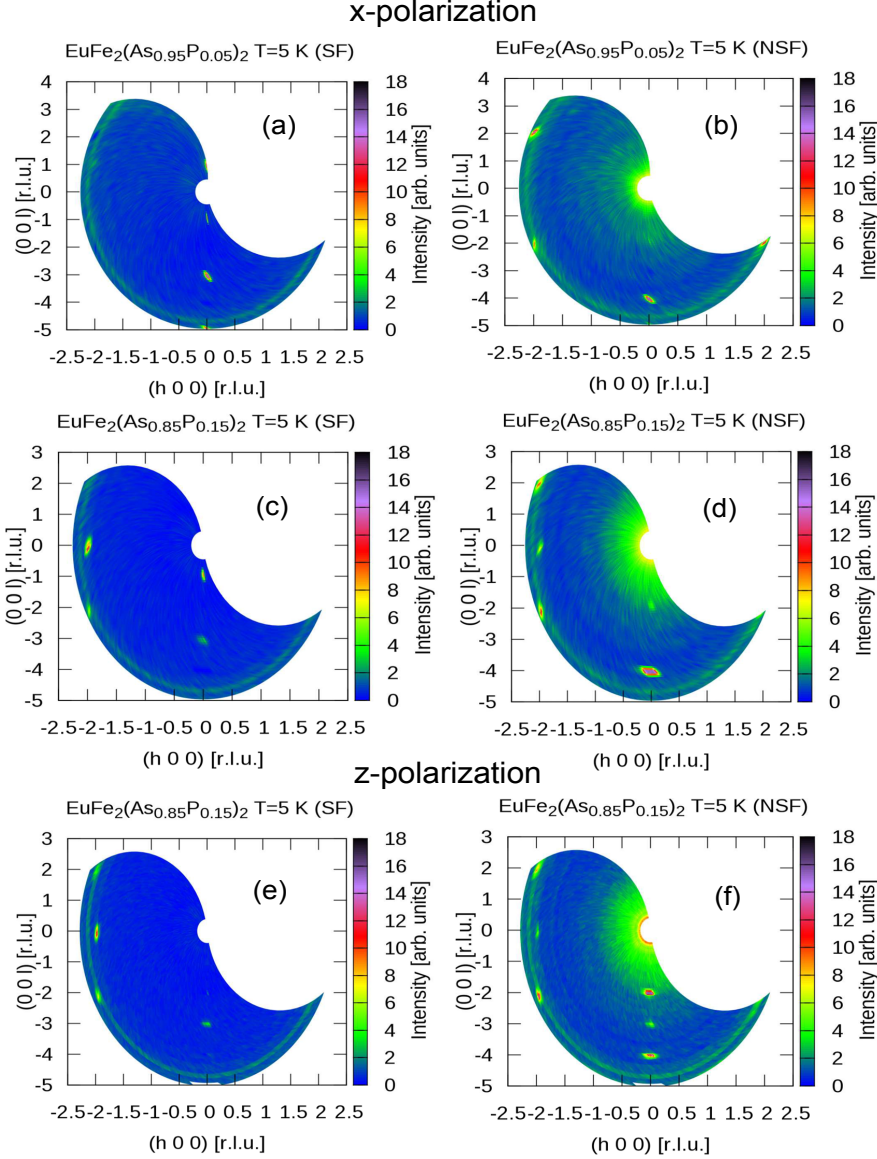


**Figure 4.4:** 2D maps of the  $(H, 0, L)$ -reciprocal plane for (a), (b)  $\text{EuFe}_2(\text{As}_{0.95}\text{P}_{0.05})_2$  and (c)-(f)  $\text{EuFe}_2(\text{As}_{0.85}\text{P}_{0.15})_2$ , obtained via polarized neutron diffraction with neutron polarizations parallel to the horizontal scattering plane (x-polarization) (a)-(d) and perpendicular to the scattering plane (z-polarization) (e), (f) and at 5 K temperature. Intensities in the (SF) channel (a), (c) exclusively correspond to magnetic scattering processes, intensities in the (NSF) channel (b), (d) solely originate from nuclear scattering.

From figures 4.4 (a) and (b) it is obvious that the magnetic structure of the 5% sample does not show any modification to the A-type structure of Eu sublattice in the undoped  $\text{EuFe}_2\text{As}_2$  compound. The intensity distribution of the 5% sample shows the identical pattern as the parent compound, as is shown in figure 2 of ref. [171]. The four spots in figure 4.4 (a) correspond to the  $(0, 0, 1)$ ,  $(0, 0, -1)$ ,  $(0, 0, -3)$  and  $(0, 0, -5)$  reflections, only appear in the (SF)-channel and thus can be related to the A-type structure of the Eu sublattice. Aside from these A-type reflections, no other magnetic reflections incompatible to the A-type propagation vector  $\mathbf{Q}_{\text{Eu}}=(0, 0, 1)$  were observed. Thus the magnetic structure of the  $\text{Eu}^{2+}$ -moments obviously remains of A-type symmetry, identical to the parent compound.

During the experiments, no magnetic intensity which could have been related to the Fe-SDW with propagation vector  $\mathbf{Q}_{\text{AFM}}=(1, 0, 1)$  has been observed. Admittedly, the Fe-SDW was not the focus of the experiments. Mainly because the experimental set up with the long wavelength, the small Eu-containing samples (10-20 mg) and the small ordered Fe-moment,  $\approx 0.8 \mu_B$  compared to the  $\approx 7 \mu_B$  of the Eu-moments, would not suit any reasonable investigation on the SDW, anyway.

Summarizing, the introduction of 5% phosphorous seems not sufficient to affect the magnetic structure of the Eu-moments in any way, as the symmetry of the Eu-sublattice clearly remains A-type with moments parallel to the ab-plane. According to Zapf et al. [192] a tilt of  $13^\circ$  of the Eu-moments in c-direction should be present even for the undoped compound. For the 5% doped sample, for which the tilt angle should be even larger than for the parent compound, this tilting of the  $\text{Eu}^{2+}$ -moments in out of the plane direction cannot be confirmed from the present results. With an effective ordered moment in the range of  $6\text{-}8 \mu_B$  even a tilting of just a few degrees would induce a sizeable ferromagnetic component, which should result in a reasonable (SF) intensity at the  $(2, 0, 0)$  reflection. Since figure 4.4 (a) obviously does not show any intensities at nuclear reflections the proposed tilting of the moments in c-direction, seems rather unlikely, at least for doping levels below 5%.

In contrast to the 5% P-doping, which seemingly is not sufficient to affect the Eu-order, 15% of introduced phosphorous induces quite a drastic change in the magnetic order of the Eu sublattice, as it is illustrated in figure 4.4 (c). One very obvious effect is the suppression of the magnetic intensity at  $(0, 0, -1)$  and  $(0, 0, -3)$ , which previously has been identified as corresponding to the A-type structure. This suppression of the A-type reflections is accompanied by strong magnetic intensity at  $(-2, 0, 0)$  and observable magnetic intensity at  $(-2, 0, -2)$ . Both reflections correspond to the orthorhombic nuclear structure with space group Fmmm but are forbidden reflections for the A-type magnetic structure with propagation vector  $\mathbf{Q}_{\text{Eu}}=(0, 0, 1)$ . Thus, the magnetic intensity at these nuclear  $(-2, 0, 0)$  and  $(-2, 0, -2)$  reflections is a strong indication for a modified magnetic

structure of the Eu-sublattice with a sizeable ferromagnetic component<sup>3</sup>. The fact that the strongest magnetic intensity of this ferromagnetic type structure is observed for the  $(-2, 0, 0)$  reflection, whereas no magnetic intensity is observed at the  $(0, 0, -2)$  and  $(0, 0, -4)$  reflections indicates that the moment direction of the ferromagnetic component must be along the crystallographic  $c$ -axis. This can be explained by the fact that any observed magnetic intensity requires a magnetic moment direction perpendicular to the direction of the scattering vector. Consequently, magnetic intensities at the nuclear reflections  $(0, 0, -2)$  and  $(0, 0, -4)$  require a ferromagnetic structure with moments perpendicular to the  $c$ -axis, whereas, magnetic intensities at the nuclear reflection  $(-2, 0, 0)$  require moments oriented along the  $c$ -axis. As a result, the most likely magnetic structure which produces a scattering pattern similar to the observed intensity distribution is a ferromagnetic type structure with the moment direction of the ferromagnetic component parallel the  $c$ -axis. Figure 4.5 illustrates three possible magnetic structures for the Eu-sublattice, with a ferromagnetic component with moments along the  $c$ -axis. The structures are results from a tilting of the Eu-moments of the A-type structure in  $c$ -direction.

The weak magnetic intensities present at  $(0, 0, -1)$  and  $(0, 0, -3)$  indicate the presence of an A-type structure with moments parallel to the  $ab$ -plane. This could be the in-plane component produced by the incomplete tilting of the moments in  $c$ -direction of a structure similar to the structure in figure 4.5 (a). The antiferromagnetic A-type symmetry of the in-plane component of this structure would in fact result in magnetic intensities at  $(0, 0, -1)$  and  $(0, 0, -3)$ . The intensities of these reflections are correlated to the tilting angle and the resulting magnetic moment size of the in-plane component, where a stronger tilting along the  $c$ -axis results in a smaller in plane component and consequently in weaker magnetic intensities of the A-type reflections. However, from the resistivity measurements it is known that the sample has a second phase, most likely of undoped  $\text{EuFe}_2\text{As}_2$ . The A-type structure of this impurity phase of course also leads to the observed antiferromagnetic intensity distribution.

The third structure in figure 4.5 (c), the canted ferromagnetic structure, which is observed in  $\text{EuFe}_2\text{P}_2$  [193], seems rather unlikely. The resulting ferromagnetic in-plane component leads to sizeable (SF) intensities at both  $(0, 0, -2)$  and  $(0, 0, -4)$ , or to (NSF) intensities at the  $(-2, 0, 0)$  for  $z$ -polarization. Since those intensities are not observed in the experiment, a canted ferromagnetic structure seems questionable.

As an additional investigation of this obviously modified magnetic structure of the Eu-sublattice in the 15%-doped superconducting compound, additional non-polarized neutron diffraction experiments have been performed using the thermal neutron diffractometer D23 at the ILL. Figure 4.6 shows a collection of rocking scans<sup>4</sup> that were

<sup>3</sup>An interference of magnetic and nuclear intensities is only possible when the magnetic and nuclear structures have identical unit cells, which is only possible for a ferromagnetic type structure.

<sup>4</sup>A rocking scan is performed by rotating the sample, while the detector position remains fixed at twice the scattering angle for that particular reflection. Intensity is only detected, when the sample rotation also obeys the scattering condition,  $n\lambda = 2d \cdot \sin(\theta)$ . The scan does not change the length of the scattering vector but rotates the vector around the origin in reciprocal space.



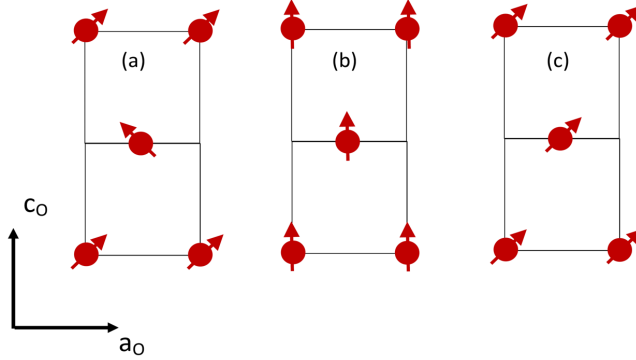


**Figure 4.5:** Sketch of three possible magnetic structures of the Eu-sublattice, with a ferromagnetic component with moment directions along the  $c$ -axis. (a) Incomplete tilting of the A-type ordered moments with an angle between the moments and the  $c$ -axis, and a resulting antiferromagnetic in-plane component. (b) Complete tilting with moments parallel to  $c$ -axis, resulting in a ferromagnetic structure. (c) Incomplete tilting, similar to (a) but with ferromagnetic in-plane component. Red symbols represent Eu-moments. View of each unit cell is along orthorhombic  $b$ -direction.

conducted on several different nuclear reflections, for temperatures above (22 K) and below (4 K) the Eu-ordering temperature  $T_N=18$  K. The striking feature in these plots is the additional intensity which occurs for a collection of reflections once the temperature drops below the Eu-ordering temperature. This additional intensity shows an order parameter like temperature dependence and disappears at approximately 18 K, very close to the ordering temperature of the Eu-magnetic sublattice of the undoped Eu-compound. Combined with the previous results from the polarization analysis, which proved that the signal is of magnetic nature, the intensity is identified to be related to the magnetic order of the  $\text{Eu}^{2+}$  sublattice. The results from the non-polarized experiments in figure 4.6 clearly confirm the results from the polarized experiments in figure 4.4, that the structure of the Eu-sublattice has a dominant ferromagnetic contribution with moments parallel to the  $c$ -axis. The degree of the tilting and thus the ratio of out-of-plane and in-plane components of the magnetic moment, however, is difficult to determine from the current data. Figure 4.7 shows rocking scans obtained for the (0, 0, 1) and (0, 0, 3) reflections, which also were observed in the polarized experiments in figures 4.4 (c) and (e), and which are correlated to the A-type structure of the Eu-sublattice. The main result in figure 4.7 is the strong reduction of intensity, which are just around 1-2 % of the magnetic intensity at (2, 0, 0), and the strong broadening of the two peaks. The ferromagnetic reflections in figure 4.6 are narrow with peak widths comparable to the widths of nuclear peaks. This clearly shows the long range nature of the ferromagnetic order of the Eu-moments. In contrast to this, the (0, 0, 1) and (0,

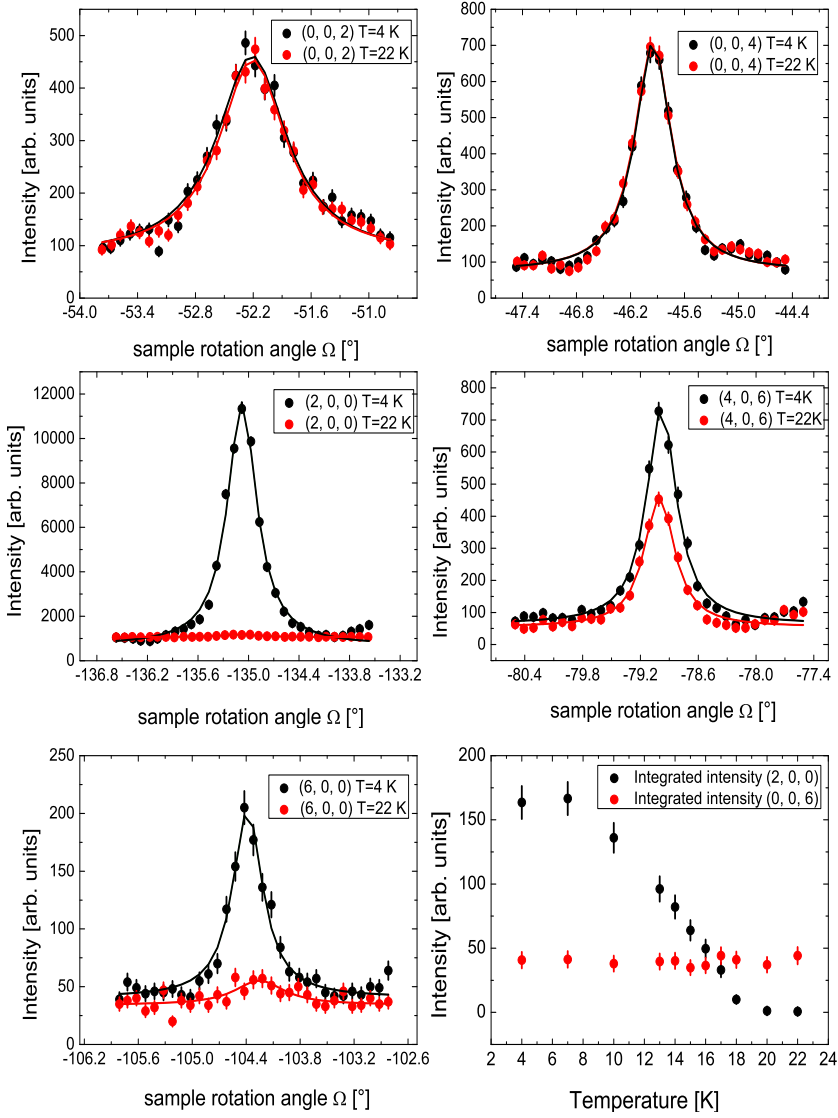


**Figure 4.6:** Collection of rocking scans performed on a series of reflections within the  $(H, 0, L)$ -reciprocal plane for superconducting  $\text{EuFe}_2(\text{As}_{0.85}\text{P}_{0.15})_2$  at temperatures of 4 K (black symbols) and 22 K (red symbols). (bottom right panel) Temperature dependence of integrated intensities, obtained via rocking scans, of reflections  $(2, 0, 0)$  (black symbols) and  $(0, 0, 6)$  (red symbols). Black and red solid lines are least square fits of Lorentzian peak functions and serve as guides to the eye.

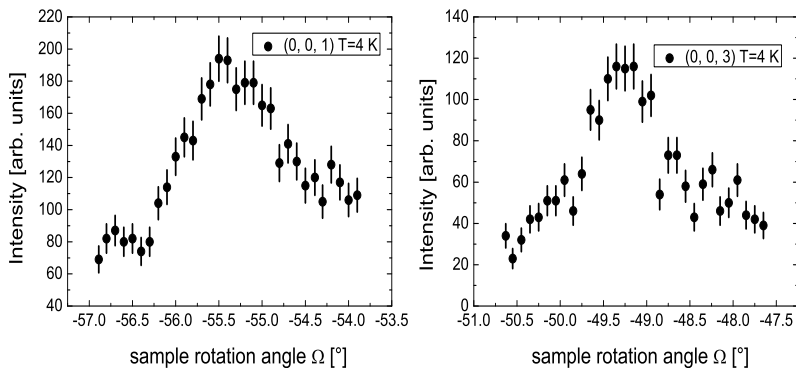


**Figure 4.7:** Rocking scans performed on antiferromagnetic reflections (0, 0, 1) and (0, 0, 3) for superconducting  $\text{EuFe}_2(\text{As}_{0.85}\text{P}_{0.15})_2$  at temperatures of 4 K. The reflections are correlated to the A-type ferromagnetic structure of undoped  $\text{EuFe}_2\text{As}_2$ .

(0, 0, 3) reflections are very broad which suggests that the corresponding antiferromagnetic structure is rather short ranged. This short range of the antiferromagnetic correlations is a good indication that this intensity indeed corresponds to the A-type structure of the assumed impurity phase of undoped  $\text{EuFe}_2\text{As}_2$  rather than to the in-plane component of the ferromagnetic type structure of the main phase. The antiferromagnetic in-plane component of structure (a) in figure 4.5 would show the same long range character as the ferromagnetic component along the c-direction. As consequence the intensity at (0, 0, 1) and (0, 0, 3) is identified as caused by the A-type structure of the Eu-sublattice of an impurity phase, most likely of undoped  $\text{EuFe}_2\text{As}_2$ . Since no other magnetic intensity has been observed that indicates a long range in-plane component, the results imply a magnetic structure of the Eu-sublattice with moments parallel to the c-axis. Consequently, for the Eu-sublattice of the 15 % P doped composition the magnetic structure of the Eu-sublattice is identified as a long range ferromagnetic order with moments along the c-axis and a large ordered moment, most likely as large as the  $\sim 6.8 \mu_B$  of the undoped composition. From the current data it is not possible to unambiguously determine a clear value for the ordered moment, but from literature it is not known that doping substantially modifies the size of the Eu-moment. Combined with the resistivity measurements the present results further prove the proposed coexistence between static ferromagnetic order with large ordered moments and bulk superconductivity.

### 4.3.2 Magnetic Structure of $\text{Eu}(\text{Fe}_{1-x}\text{Co}_x)_2\text{As}_2$ $x=0.014$ , $x=0.025$

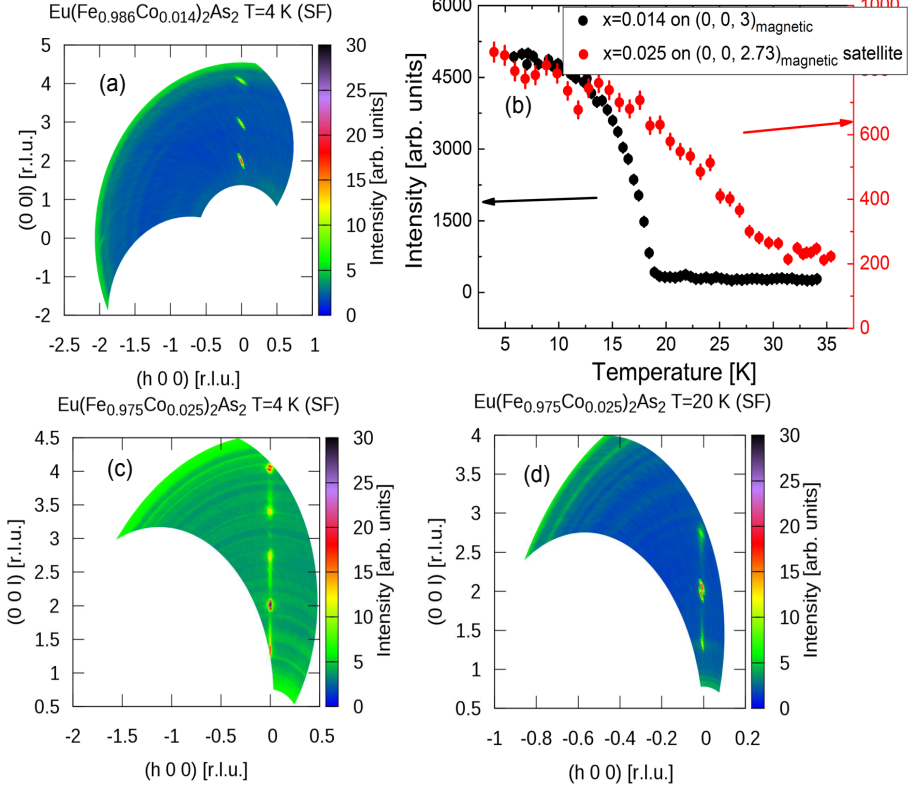
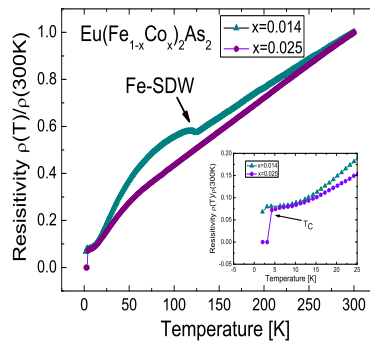


**Figure 4.8:** 2D maps of the  $(H, 0, L)$ -reciprocal plane for (a)  $\text{Eu}(\text{Fe}_{0.986}\text{Co}_{0.014})_2\text{As}_2$  and (c), (d)  $\text{Eu}(\text{Fe}_{0.975}\text{Co}_{0.025})_2\text{As}_2$ , obtained via polarized neutron diffraction for temperatures 4 K (a), (c) and 20 K (d). Data has been obtained for neutron polarization perpendicular to the scattering plane ( $z$ -polarization). Only intensities detected in the (SF) channel are illustrated. (b) Temperature dependence of scattering intensities of the  $(0, 0, 3)$  magnetic reflection from the  $x=0.014$  sample (black dots) and of the satellite reflection  $(0, 0, 2.73)$  obtained from the 2.5% doped sample. The temperature dependence was performed by collecting only the intensity from one detector, which covered the desired reflection, and sweeping the temperature with a ramp of 1 K per minute.

As mentioned in the introduction, substituting iron with cobalt is another method to induce superconductivity in  $\text{Eu}(\text{Fe}_{1-x}\text{Co}_x)_2\text{As}_2$  materials. To investigate the effect of Co-doping on the Eu-sublattice polarized neutron diffraction experiments have been

**Figure 4.9:** Temperature dependence of the in-plane resistivity normalized to room-temperature of  $\text{Eu}(\text{Fe}_{0.986}\text{Co}_{0.014})_2\text{As}_2$  (cyan symbols) and  $\text{Eu}(\text{Fe}_{0.975}\text{Co}_{0.025})_2\text{As}_2$  (violet symbols). The measurements were performed by collaborating scientist Dr. Y. Xiao of JCMS-2 on two single crystal samples using a standard four-terminal method on a Quantum Design Physical Property Measuring Device (PPMS).



conducted using two single crystals with Co-concentrations of 1.4% and 2.5%, respectively.

Figure 4.8 shows a collection of 2D intensity maps of the  $(H\ 0\ L)$ -reciprocal plane of spin-flip (SF) intensities obtained via polarized neutron scattering with  $z$ -polarization of the incident neutron beam (neutron spin perpendicular to the scattering plane). In contrast to the perviously discussed  $x$ -polarization,  $z$ -polarization does not provide an immediate separation of magnetic and nuclear intensities but has the advantage that the polarization direction can be controlled much easier as it can be held fixed during the measurement and does not have to follow the direction of the scattering vector as is the case for  $x$ -polarization.

Figure 4.8 (a) illustrates the (SF)-intensity obtained from single crystal scattering experiments on the 1.4% Co-doped sample at 4 K. The three spots apparent in figure 4.8 (a) correspond to the nuclear crystal structure, represented by  $(0, 0, 2)$  and  $(0, 0, 4)$ , and the A-type magnetic structure with propagation vector  $\mathbf{Q}_{Eu}=(0, 0, 1)$ , represented by  $(0, 0, 3)$ . Throughout the investigations of the 1.4 % Co-doped sample, no magnetic intensity was observed, which could not be explained by the A-type structure or which would suggest a different propagation vector. In addition to this, the observed magnetic intensity follows the same temperature dependence as the A-type structure of the Eu-sublattice in the parent compound with an almost identical transition temperature  $T_N=18$  K, figure 4.8 (b). This shows that the 1.4% of introduced Co is not sufficient to affect the magnetic structure of the  $\text{Eu}^{2+}$ -moments, similar to what has been observed for the 5% P-doped sample. Regarding the impact of the Co-doping on the Fe-SDW, the conductivity measurements (figure 4.9) clearly show a reduction of the Fe-SDW transition temperature to 130 K, which is about 50 K below the ordering temperature for the undoped material. Similar to the P-doped samples, which were of comparable mass, the diffraction experiments on the Co-doped samples were not suited

to detect any intensity from the Fe-SDW order. From the extensive knowledge about the doping dependence of the Fe-SDW in other 122-pnictides, however, there is no reason to expect any change in the structure of the Fe-magnetic moments in this compound.

The previous results show, that 1.4 % incorporated cobalt is not sufficient to affect the Eu-sublattice, as it maintains the A-type structure of the undoped compound. Figures 4.8 (c) and (d), however, reveal that just about one percent more of introduced cobalt and the magnetic structure obviously experiences a drastic change. The striking differences to the 1.4 % doped sample is that both magnetic peaks at  $(0, 0, 1)$  and  $(0, 0, 3)$  disappear and are replaced by incommensurate peaks located at  $(0, 0, 0.73 \pm 0.05)$  and  $(0, 0, 1.27 \pm 0.05)$  and  $(0, 0, 2.73 \pm 0.05)$  and  $(0, 0, 3.27 \pm 0.05)$ , respectively. This incommensurate splitting leads to a new propagation vector of the Eu-order of  $\mathbf{Q}_{heli} = (0, 0, 0.73 \pm 0.05)$ . Here it was assumed that the ferromagnetic order within the Eu-layers remains unaffected. However, this is indeed a reasonable assumption as first no additional reflections suggesting a change of the in-plane correlations were observed and second Xiao et al. [176] showed that the intra-layer ferromagnetic coupling is solid and by far the strongest of the Eu-Eu interactions. This leads to the new helical type structure of the Eu-sublattice, where Eu-moments remain parallel to the ab-planes but ferromagnetic Eu-layers are rotated around the c-axis resulting in an angle of  $\phi = (131 \pm 1)^\circ$  between two neighboring layers, as illustrated in figure 4.10.

Aside from the splitting of the magnetic peaks the obtained (H 0 L) intensity distribution exhibits a further prominent feature as the split magnetic peaks are smeared out in L-direction. This diffuse scattering intensity, which only occurs in direction towards the nuclear peaks indicates fluctuations corresponding to helices with angles between adjacent layers smaller than  $131^\circ$ . Whereas, the absence of diffuse intensity in direction towards the commensurate magnetic reflections tells that helices with a larger angle than  $131^\circ$  do not exist. As the diffuse intensities almost reaches the positions of nuclear peaks angles between  $131^\circ$  and almost  $0^\circ$  can occur, where  $0^\circ$  corresponds to ferromagnetic symmetry. However, since the satellite peaks are much stronger in intensity than the diffuse tails helices with  $131^\circ$  between adjacent Eu-layers are the dominating structure. In contrast to the smeared out intensity along the  $(0, 0, L)$  direction the peaks are narrow along  $(H, 0, 0)$ , which shows that the ferromagnetic correlations within the Eu-layers remain unaffected by the doping and are still solid and of long range, comparable to the undoped compound. Despite the reduced range of inter-layer magnetic order, which could be an indication for a loss of coupling strength, this new helical type structure is less fragile than the A-type or ferromagnetic structure and exhibits a much more robust temperature dependence as it persists up to 30 K. This is in contrast to all other doped samples that have been investigated in this study, whether these were doped by phosphorous or cobalt. One common feature all these samples stated was an ordering temperature of the Eu-moments in the range between 16-18 K, close to the 19 K observed for the parent compound.

Surprisingly, it was not possible to observe any signs of the Fe-SDW order, not even

from the in-plane resistivity measurements. This does not fit very well to results from resistivity measurements of Co-doped  $\text{Eu}(\text{Fe}_{1-x}\text{Co}_x)_2\text{As}_2$  [196], where the Fe-SDW order reportedly persists for Co-concentrations as high as 10%. This indicates a possible underestimation of the actual doping concentration, where the sample in fact is more likely overdoped than underdoped. The exact determination of the doping concentration was not possible, due a strong contamination of the crystal surface by tin, which was used as flux material during the growth process. The given value of 2.5% Co-concentration was determined by the sample growers by means of characterization methods.

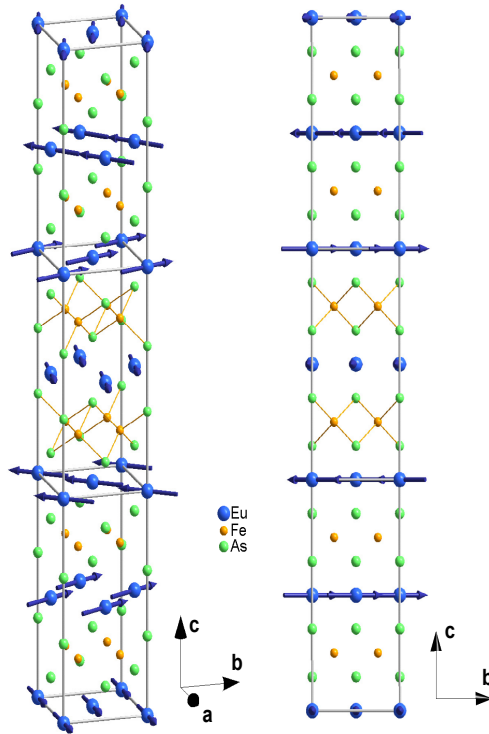


**Figure 4.10:** (Color online) Nuclear and magnetic structure of the Eu-sublattice of  $\text{Eu}(\text{Fe}_{0.975}\text{Co}_{0.025})_2\text{As}_2$ . Both figures show the same structure, viewed from different directions, both with crystallographic  $c$ -axis vertical and  $a$ - and  $b$ -axes horizontal. Three orthorhombic unit cells are shown. Blue arrows symbolize the  $\text{Eu}^{2+}$ -moments organized in the helical-type structure of the sublattice.

## 4.4 Conclusion

The effect of impurity doping on the long range order of the Eu-magnetic-sublattice in  $\text{Eu}(\text{Fe}_{1-x}\text{Co}_x)_2\text{As}_2$  and  $\text{EuFe}_2(\text{As}_{1-x}\text{P}_x)_2$  single crystal samples was studied by means of neutron diffraction and polarized neutron diffraction.

The obtained neutron scattering results on superconducting 15% P-doped  $\text{EuFe}_2(\text{As}_{1-x}\text{P}_x)_2$  clearly identify a ferromagnetic structure for the Eu-sublattice with moments aligned along the c-axis. From the current results it is most likely that the Eu-moments are completely parallel to the c-axis, as no indications of a remaining in-plane component was observed. The resulting structure of a ferromagnet with moments along the c-axis fits very well in the evolution of the Eu-sublattice, from the A-type structure of undoped  $\text{EuFe}_2\text{As}_2$  to the ferromagnetic structure with moments oriented along the c-direction present in  $\text{EuFe}_2\text{P}_2$ .

The tilting of the moments in c-direction results in a long-range ferromagnetic component with large ordered moments of approximately  $S_c = 6.8 \mu_B$ . The ordered moment is only estimated as the performed experiments did not allow a clear determination of the moment size. Since from literature no effect of doping on the size of the ordered moment is known, the  $6.8 \mu_B$  of the undoped material is assumed. The astonishing about this result is the fact that this sizeable ferromagnetically ordered moment coexists with bulk superconductivity. Combined with the results of local probes, such as Mössbauer spectroscopy [191] and characterization techniques, such as magnetization, specific heat and resistivity measurements [188–190, 192] which all suggest bulk superconductivity with the coexistence of long range ferromagnetism, the present neutron scattering study clearly proves the bulk coexistence of long range ferromagnetic order and superconductivity, in contrast to a possible phase separation of both phases. However, an explanation on how superconductivity can coexist with this large moment ferromagnetic structure cannot be given by the presented results and is still not understood to this date.

In contrast to the 15% P-doped compound, 5% of introduced phosphorous is not sufficient to affect the Eu-sublattice in any way, as it maintains its A-type structure of the undoped compound. Further, the results for this compound show no signs of an out-of-plane tilt of the Eu-moments, which is contradictory to an A-type structure with Eu-moments slightly tilted in c-direction proposed for undoped  $\text{EuFe}_2\text{As}_2$  [192]. Thus, according to the present scattering results, tilted moments in the A-type structure of the undoped compound are unlikely.

For the small amount of just 2.5% Co-concentration the Eu-order changes from A-type to a helical-type magnetic order, where Eu-moments remain oriented in the ab-plane and ferromagnetic Eu-layers are rotated around the c-axis resulting in an angle of  $\sim 130^\circ$  between neighboring layers. Aside from the in-plane rotation of the moments and the loss of antiferromagnetic inter-layer Eu-Eu correlations the ferromagnetic in-plane Eu-Eu correlations, in contrast, are obviously unaffected by the doping and



remain of long range. Surprisingly, this new magnetic order with its reduced inter-layer correlations appears to be more robust to temperature, as the Eu-ordering temperature for the helical structure increases up to 30 K.

Similar to the 5% P-doped sample, the 1.4% Co-content of the underdoped compound does not affect the Eu-sublattice, which maintains its A-type structure of the undoped compound.

The inter-layer correlations of the Eu-sublattice are seemingly weak and can easily be modified by perturbations, such as doping, applying external pressure [180] or magnetic fields [176]. Further, antiferromagnetic and ferromagnetic symmetry of the Eu-sublattice are energetically very close [189], and just small perturbations can cause the sublattice to order in one way or the other. This also shows in this study, as the common effect of doping on the Eu-sublattice obviously is a change of inter-layer correlations. This leads to the loss of the antiferromagnetic structure along the c-direction and results in either a rotation of the Eu-layers around the c-axis or a tilt of the layers along the c-axis. As already mentioned, the antiferromagnetic coupling of the Eu-sublattice is believed to be driven by a carrier mediated RKKY-type mechanism. The RKKY exchange coupling is  $J_{RKKY} \propto -\frac{\alpha \cos \alpha - \sin \alpha}{\alpha^4}$ , where  $\alpha = 2\mathbf{k}_F R$  with  $\mathbf{k}_F$  being the Fermi vector and  $R$  the distance between two magnetic moments. Obviously  $J_{RKKY}$  oscillates between antiferromagnetic (positive sign) and ferromagnetic (negative), depending on the value of  $\alpha$ . A reduction of  $R$ , present for P-doped materials in form of the shrunk  $c$  lattice parameter, which shortens about 2% for 30% P-doping [188] and about 1 Å for EuFe<sub>2</sub>P<sub>2</sub> [193], or a change of  $\mathbf{k}_F$ , in case of Co-doping a reduction of  $\mathbf{k}_F$  due to the introduction of additional charge carriers, can easily modify  $J_{RKKY}$  and eventually result in a crossover of the magnetic structure from antiferromagnetic to ferromagnetic symmetry [185, 197]. In this context, the helical-type structure observed for the Co-doped materials can be understood as an intermediate state between the AFM and FM structures. However, this modification of  $J_{RKKY}$  does not necessarily explain the tilting of the Eu-moments in c-direction observed in the P-doped materials. One interpretation of this effect is that it is caused by a reduction of As concentration in the structure. The As 4p states are spatially more extended than the P 3p states and thus have a greater influence on the interlayer Eu-Eu interactions than the P 3p states. A reduced concentration of As-ions in favor of P-ions then leads to less influence on the Eu-Eu interactions and as a result the tilting and the formation of a FM structure sets in, as it is observed in EuFe<sub>2</sub>P<sub>2</sub>.

# 5 ToF Neutron Scattering on Magnetic Excitations in $\text{Ba}(\text{Fe}_{0.95}\text{Co}_{0.05})_2\text{As}_2$

## 5.1 Introduction

### 5.1.1 Motivation

With its coexistence of superconductivity and static magnetic SDW order underdoped  $\text{Ba}(\text{Fe}_{0.95}\text{Co}_{0.05})_2\text{As}_2$  provides a unique possibility to directly investigate the mutual effect of both phenomena have on each other. One effect that has been observed by Pratt et al. [70] in a similar composition is a dispersion of the spin resonance. This effect most likely is attributed to the coexistence of long range static magnetic order and superconductivity. Thus, one focus of this study is to examine if a similar effect would also be observable in the 5% Co-doped composition. The main focus, however, is to investigate the spectrum of spin wave excitations of the long range SDW order. For this a linear spin wave model based on a local moment Heisenberg Hamiltonian was applied to the excitation spectrum, obtained for three different temperatures,  $T < T_c$ ,  $T_c < T < T_N$  and  $T > T_N$ . This provides the possibility to investigate a possible effect of superconductivity on the spin wave excitations, a possible doping effect on the exchange interactions in general as well as to investigate the excitations in the paramagnetic phase. These paramagnetic excitations were further analyzed by applying an additional model, based on spin diffusion theory. The results from this study will be discussed in the current chapter.

### 5.1.2 Coexistence of Superconductivity and Static Magnetic Order

One characteristic feature of the underdoped region of the phase diagram of several Fe-based materials is a phase of seeming coexistence of static magnetic order and superconductivity. This effect has been observed experimentally for a variety of Fe-based materials, such as  $\text{SmFeAsO}_{1-x}\text{F}_x$  [43],  $\text{LaFeAsO}_{1-x}\text{F}_x$  [44],  $\text{CaFe}_{1-x}\text{Co}_x\text{AsF}$  [44, 45],  $\text{Ba}_{1-x}\text{K}_x\text{Fe}_2\text{As}_2$  [41, 42],  $\text{Ba}(\text{Fe}_{1-x}\text{Ni}_x)_2\text{As}_2$  [36] and  $\text{Ba}(\text{Fe}_{1-x}\text{Co}_x)_2\text{As}_2$  [37–40]. One way to explain this apparent coexistence of both effects is via a phase separation of

the two phases, where magnetically ordered regions and superconducting regions occur simultaneously but are spatially separated within the crystal. Another possible situation of course is a real microscopic coexistence of both phenomena. A real conclusive explanation for this effect, however, is not available for most compositions, as contradictory experimental results are reported, with some suggesting a phase separation as in  $\text{Ba}_{1-x}\text{K}_x\text{Fe}_2\text{As}_2$  [42],  $\text{CaFe}_{1-x}\text{Co}_x\text{AsF}$  [44], whereas others suggest a phase coexistence as in  $\text{SmFeAsO}_{1-x}\text{F}_x$  [43],  $\text{Ba}_{1-x}\text{K}_x\text{Fe}_2\text{As}_2$  [41],  $\text{CaFe}_{1-x}\text{Co}_x\text{AsF}$  [45],  $\text{Ba}(\text{Fe}_{1-x}\text{Ni}_x)_2\text{As}_2$  [36] and  $\text{Ba}(\text{Fe}_{1-x}\text{Co}_x)_2\text{As}_2$  [39, 40].

Coexistence of long range antiferromagnetic order and superconductivity is not a new phenomena but has been observed for other high  $T_c$  materials before, such as the borocarbides ( $\text{RNi}_2\text{B}_2\text{C}$ , with  $\text{R}$ = rare earth) [198] or the ruthenates ( $\text{RuSr}_2\text{GdCu}_2\text{O}_8$ ) [199]. For these materials, however, it is believed that magnetic order and superconductivity occur independently from each other and do not originate from the same electrons, whereas, for materials, such as the heavy fermion systems  $\text{UPt}_3$  [200, 201] and  $\text{UNi}_2\text{Al}_3$  [202] superconductivity and long range antiferromagnetic order, not just coexist but most likely arise from the same electron bands. The overall consensus on this point is that this likely is the case also for the underdoped region in the 122-compounds  $\text{Ba}(\text{Fe}_{1-x}\text{Ni}_x)_2\text{As}_2$  [36] and  $\text{Ba}(\text{Fe}_{1-x}\text{Co}_x)_2\text{As}_2$  [29, 37–40, 203].

One effect that might support this idea that magnetic order and superconductivity could arise from the same electrons has been observed in neutron scattering experiments, and has been reported for underdoped  $\text{Ba}(\text{Fe}_{1-x}\text{Co}_x)_2\text{As}_2$  [39, 40] and  $\text{Ba}(\text{Fe}_{1-x}\text{Ni}_x)_2\text{As}_2$  [36]. The effect observed in these experiments, is an anomalous temperature dependence of the elastic magnetic Bragg intensity of reflections correlated to the static Fe-SDW order. As is illustrated in figure 5.1 (b), the magnetic intensity suddenly decreases once the temperature drops below  $T_c$ , which results in a kink in the temperature dependence of the order parameter. This reduction of magnetic intensity for  $T < T_c$  is absent for the non superconducting materials and has so far only been observed in the underdoped  $\text{Ba}(\text{Fe}_{1-x}\text{Co}_x)_2\text{As}_2$  and  $\text{Ba}(\text{Fe}_{1-x}\text{Ni}_x)_2\text{As}_2$  materials, for which superconductivity and magnetic order are detected simultaneously. The effect is interpreted as an indication for a possible coexistence of the two phases on a microscopic scale, where the reduction of the magnetic intensity results from a reduction of the ordered magnetic moment, caused by a competition of the two phases over the same electrons. This scenario is supported by theory [204, 205], as here the authors propose that a microscopic coexistence of the two states in fact supports the  $s_{\pm}$  symmetry for the superconducting gap function (figure 5.1 (c)). However a complete explanation of this effect is not available to this date.

### 5.1.3 A Dispersive Spin Resonance Signal

Two features that might also be characteristic for the underdoped 122-pnictides but so far have only been observed for the underdoped Ba-122 compounds, are a three dimensionality and a dispersion of the spin resonance signal. Both features most likely are consequences of the just discussed coexistence of long range magnetic order and

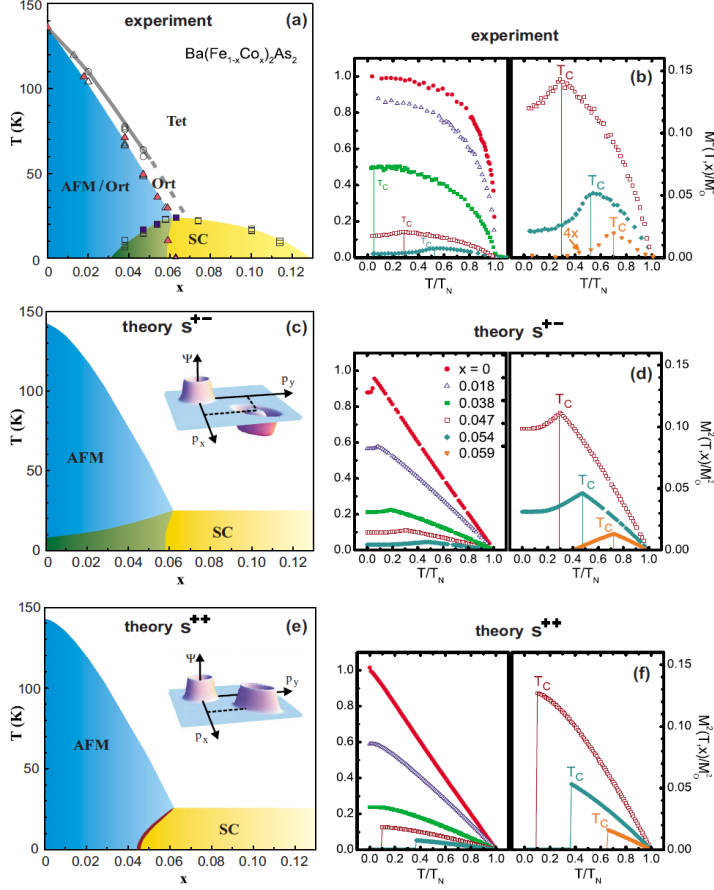
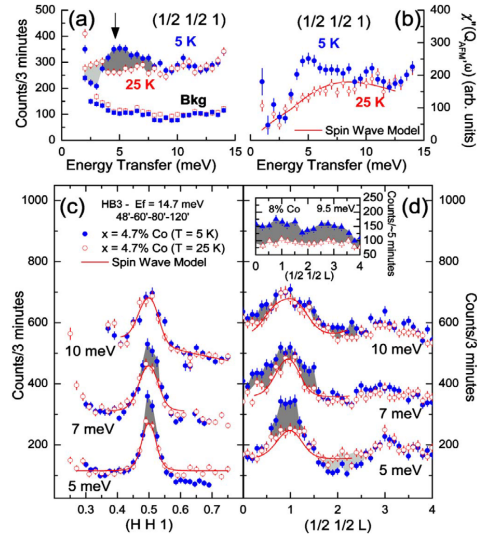


**Figure 5.1:** (a) Temperature-doping-concentration phase diagram of the  $\text{Ba}(\text{Fe}_{1-x}\text{Co}_x)_2\text{As}_2$  series determined via neutron diffraction experiments (filled symbols) and bulk characterization measurements (open symbols, [37]). *Tet* represents the paramagnetic tetragonal phase, *Ort* the paramagnetic orthorhombic phase, *AFM/Ort* the antiferromagnetic orthorhombic phase and *SC* the superconducting phase. (b) Squared normalized ordered magnetic moment against temperature as determined via neutron diffraction experiments. Data for five different Co-doping concentrations are shown. (c) and (e) Simulated phase diagrams for two different symmetries of the superconducting gap function  $s_{\pm}$  and  $s_{++}$ . Insets in (c) and (e) show the evolution of the superconducting gap function on the electron and whole pockets in the Brillouin zone with the momentum directions  $p_x$  and  $p_y$  being parallel to the tetragonal  $a$  and  $b$  axes. (d) and (f) Simulation of squared ordered moments for gap symmetries  $s_{\pm}$  and  $s_{++}$ , respectively. Figure taken from [204].

superconductivity. For most optimal doped pnictide materials, the spin resonance has a clear defined energy  $E_R$ , and is peaked at a  $\mathbf{Q}$ -position close to the nesting vector  $\mathbf{Q}_{AFM}=(0.5, 0.5, 0)$ . This integrates the mode into the spectrum of the short range spin excitations with propagation vector  $\mathbf{Q}_{AFM}=(0.5, 0.5, 0)$ , even though the microscopic nature of the mode most likely strongly differs from these collective excitations. Similar to the short range spin fluctuations peaked at  $\mathbf{Q}_{AFM}$ , which are regarded to be mostly two dimensional with correlations restricted to the (H, K, 0)-plane, the resonance signal also appears to be mostly two dimensional with almost no modulation along the (0, 0, L)-direction.

In contrast to the optimal doped materials, the spin excitations in the underdoped 122-compounds exhibit a prominent intensity modulation along the (0, 0, L)-direction with strong magnetic intensities at magnetic zone center reflections (0.5, 0.5, L=odd) and reduced intensities for zone boundary reflections (L=even) [70], as illustrated in fig. 5.2 (d). This intensity modulation indicates antiferromagnetic correlations along the (0, 0, L)-direction and can be ascribed to the three dimensionality of the spin wave excitations, which because of a similar propagation vector also contribute to the excitation spectrum at  $\mathbf{Q}_{AFM}=(0.5, 0.5, 0)$ . The spin resonance signal, present in the superconducting state, seemingly follows this three dimensionality as it exhibits a similar modulation along the (0, 0, L)-direction with stronger intensity of the signal for L=odd and weaker intensity at L=even.

**Figure 5.2:** (a) Energy scans performed at (0.5, 0.5, 1) at 5 K (blue filled symbols) and 25 K (red open symbols). The spin resonance is identified as the region of enhanced magnetic intensity in the 5 K data, highlighted as grey shaded area. (b) Energy dependence of the dynamical magnetic susceptibility  $\chi''(\mathbf{Q}, \omega)$  for both temperatures 5 K and 25 K. (c) Longitudinal constant energy cuts through  $\mathbf{Q}_{AFM}=(0.5, 0.5, 1)$  for different excitation energies. (d) Constant energy scans along (0.5, 0.5, L)-direction for different energies. The inset illustrates an identical scan for an optimal doped 8% compound at the resonance energy  $E_R=9.5$  meV. Figure taken from ref. [70].



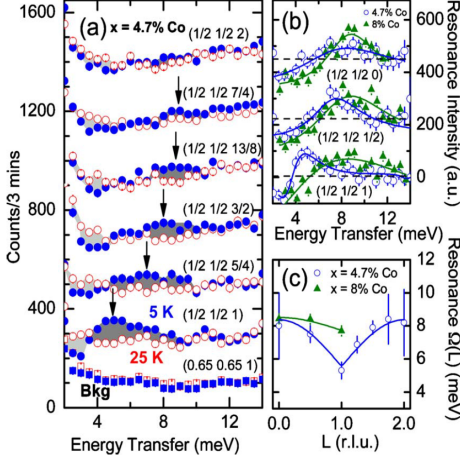


**Figure 5.3:** (a) Energy scans performed at  $(0.5, 0.5, L)$  for temperatures above (red open symbols) and below (blue filled symbols)  $T_c$ . The scans are performed for  $L$ -values from  $L=1$  (zone center) to  $L=2$  (zone boundary). The spin resonance is identified as the grey colored region. (b) Difference in scattering intensity for the 5 K and 25 K energy scans, for the 4% underdoped sample (open blue symbols) and the 8% optimal doped sample (green filled symbols). (c)  $(0, 0, L)$ -dispersion of the spin resonance in underdoped 4% (blue open symbols) and optimal doped 8% (green filled symbols). Figure taken from ref. [70].

This three dimensional character of the resonance signal in the underdoped compound is accompanied by a prominent dispersion, where the signal moves to higher energies when varying the propagation vector from the magnetic Brillouin zone center  $(0.5, 0.5, L=\text{odd})$  to the zone boundary  $(0.5, 0.5, L=\text{even})$  [70]. A similar effect is not observed in optimal doped compounds, where the signal remains at a constant energy, as illustrated in figure 5.3.

Both features can be related to the presence of the three dimensional SDW-order in the superconducting phase.

The RPA (Random Phase Approximation) form of the dynamical magnetic susceptibility in the superconducting state reads as [151],

$$\chi(\mathbf{Q}, \omega) = \frac{\chi_0(\mathbf{Q}, \omega)}{1 - V(\mathbf{Q})\chi_0(\mathbf{Q}, \omega)} \quad (5.1)$$

Here  $\chi_0(\mathbf{Q}, \omega)$  is the irreducible susceptibility from (A.3), and  $V(\mathbf{Q})$  is an effective spin-spin interaction between itinerant electrons. For a given wave vector  $\mathbf{Q}$  and the following conditions,

$$1 - V(\mathbf{Q})\text{Re}\chi_0(\mathbf{Q}, \omega) = 0 ; \text{Im}\chi_0(\mathbf{Q}, \omega) = 0 \quad (5.2)$$

the magnetic response becomes divergent, and the formation of collective excitations sets in. With the right energy  $E_R$ , and the right wave vector  $\mathbf{Q} = \mathbf{Q}_{AFM}$  one of the collective excitations will be the spin resonance mode. Along the  $(0, 0, L)$ -direction the resonance occurs as long as the condition  $V(\mathbf{Q}_{AFM} + L\hat{z})\chi_0(\mathbf{Q}_{AFM} + L\hat{z}, \omega) = 1$  is retained, and thus for the optimal doped compound, where both  $V(\mathbf{Q})$  and  $\chi_0(\mathbf{Q}, \omega)$  are almost two dimensional, the resonance mode shows no modulation along the  $(0, 0, L)$ -direction and

is of quasi 2D nature. For the underdoped compound the three dimensional SDW-order has to be taken into account, as it introduces an enhanced  $(0, 0, L)$ -dependence to  $V(\mathbf{Q})$ . This  $(0, 0, L)$ -modulation of  $V(\mathbf{Q})$  and maybe even  $\chi_0(\mathbf{Q}, \omega)$  obviously contributes to (5.2) and so eventually leads to the three dimensionality and the  $\mathbf{Q}$ -energy-dispersion of the spin resonance mode.

## 5.2 Experimental Details

Inelastic time-of-flight (ToF) neutron scattering experiments on a mosaic single crystal  $\text{Ba}(\text{Fe}_{0.95}\text{Co}_{0.05})_2\text{As}_2$  sample have been performed, in order to investigate the spin excitations of underdoped  $\text{Ba}(\text{Fe}_{1-x}\text{Co}_x)_2\text{As}_2$  materials. For the experiments a mosaic sample was prepared by co-aligning four high quality single crystals of  $\text{Ba}(\text{Fe}_{0.95}\text{Co}_{0.05})_2\text{As}_2$ , resulting in a combined mass of approximately 6.2 g. The alignment of the four single crystals produced a mosaic width of the assembly of less than  $1^\circ$ . The crystals of the mosaic sample were synthesized by the self flux method and their main properties,  $T_c = 16$  K,  $T_N = 58$  K,  $T_S = 65$  K, were precisely determined by characterization methods. The crystal growth and characterization measurements were performed by collaborating scientist Dr. T. Wolf of the Karlsruhe Institute of Technology, Institut für Festkörperphysik, Karlsruhe, Germany. The time-of-flight neutron scattering experiments were performed on the cold time-of-flight disc chopper spectrometer AMATERAS at the J-PARC spallation neutron source, JAPAN [206]. By taking advantage of the repetition rate multiplication technique, data sets were obtained for eight different incident neutron energies, covering a range from  $E_i = 5$  meV to  $E_i = 94$  meV. By sealing the sample in a cylindrical aluminum can filled with He exchange gas and mounting it to a top-loading closed-cycle cryostat, it was possible to collect data for three different temperatures  $T = 6$  K,  $T = 20$  K and  $T = 80$  K. These three temperatures correspond to three different phases, the phase of coexistence of superconductivity and magnetic order, the orthorhombic magnetically ordered phase above  $T_c$  and the tetragonal paramagnetic phase. The sample was oriented with the sample's crystallographic c-axis aligned parallel to  $\mathbf{k}_i$ , the incoming neutron beam. This way it was possible to investigate the in-plane dependence of the magnetic excitations at  $\mathbf{Q}_{AFM} = (1, 0, L)$ , for various energies and L-values. Because of the very small orthorhombic distortion of the crystal structure, which was too small to be resolved during the experiments, the lattice was described in tetragonal symmetry, with equal in-plane lattice constants  $a = b$ , for all temperatures. The indexing of the reflections, however, was done in orthorhombic notation with space group Fmmm and lattice parameters  $a = b = 5.5$  Å,  $c = 12.88$  Å. Consequently the propagation-vector for the long range Fe-SDW order reads  $\mathbf{Q}_{AFM} = (1, 0, 1)$ . Throughout this chapter, the orthorhombic notation will be used and wave-vectors will be expressed in reciprocal lattice units [r.l.u.].

In order to be able to compare intensities, which were obtained for different temperatures, the obtained intensities were corrected for the thermal population factor

$\left(1 - \exp\left(-\frac{\hbar\omega}{k_B T}\right)\right)$ . According to the fluctuation-dissipation theorem the thermal population factor relates the scattering function  $S(\mathbf{Q}, \omega)$  to the dissipative part of the magnetic susceptibility  $\chi''(\mathbf{Q}, \omega)$  via [159, 160],

$$\chi''(\mathbf{Q}, \omega) = S(\mathbf{Q}, \omega) \cdot \left(1 - \exp\left(-\frac{\hbar\omega}{k_B T}\right)\right). \quad (5.3)$$

For the remainder of this chapter all 1D cuts and 2D slices will show intensities corrected for this thermal population factor and thus will illustrate the imaginary part of the magnetic susceptibility. Exceptions, where  $S(\mathbf{Q}, \omega)$  is illustrated instead of  $\chi''(\mathbf{Q}, \omega)$  are specifically marked.

For the visualization of the 2D  $S(\mathbf{Q}, \omega)$  maps and the creation of the 1D constant energy cuts the MSLICE program [207] was used.

## 5.3 Results and Discussion

### 5.3.1 Spin Gap and Spin Resonance in the Superconducting State

At the time of this study no conclusive neutron scattering results were available to clearly determine the existence or absence of the spin gap in the underdoped compounds. To date the occurrence of the spin resonance in the Fe-based materials always is accompanied by the opening of a gap in the particle hole excitation spectrum for energies below the resonance energy. The opening of this gap in the superconducting phase is ascribed to the suppression of particle hole excitations with energies not sufficient to break up Cooper pairs. Consequently, a particle hole excitation spectrum without a spin gap would not fit the current understanding of spin excitations in the superconducting state.

Figure 5.4 shows two constant energy slices through the excitation spectrum for energies of 2 meV and temperatures of 6 K and 20 K. The elliptic red signal in figure (b) located at  $\mathbf{Q} = (1, 0, 3)$  in  $\mathbf{Q}$ -space corresponds to magnetic scattering arising from short range spin fluctuations, present in the normal state of the superconducting sample. The spin-wave excitations present in the magnetically ordered phase also possess the same propagation vector and in principle contribute to the magnetic intensity at this position as well. However, it is very likely that the spin wave spectrum is gapped for this low energy range, at least if the situation is similar to the spin wave spectrum of the parent compound, which has a gap below 10 meV [65]. In the low temperature color plot 5.4 (a) the magnetic intensity is absent, which proves the occurrence of the spin gap of the short range spin fluctuations, and also indicates a gap in the spin wave excitation spectrum, at least for energies below 4 meV.



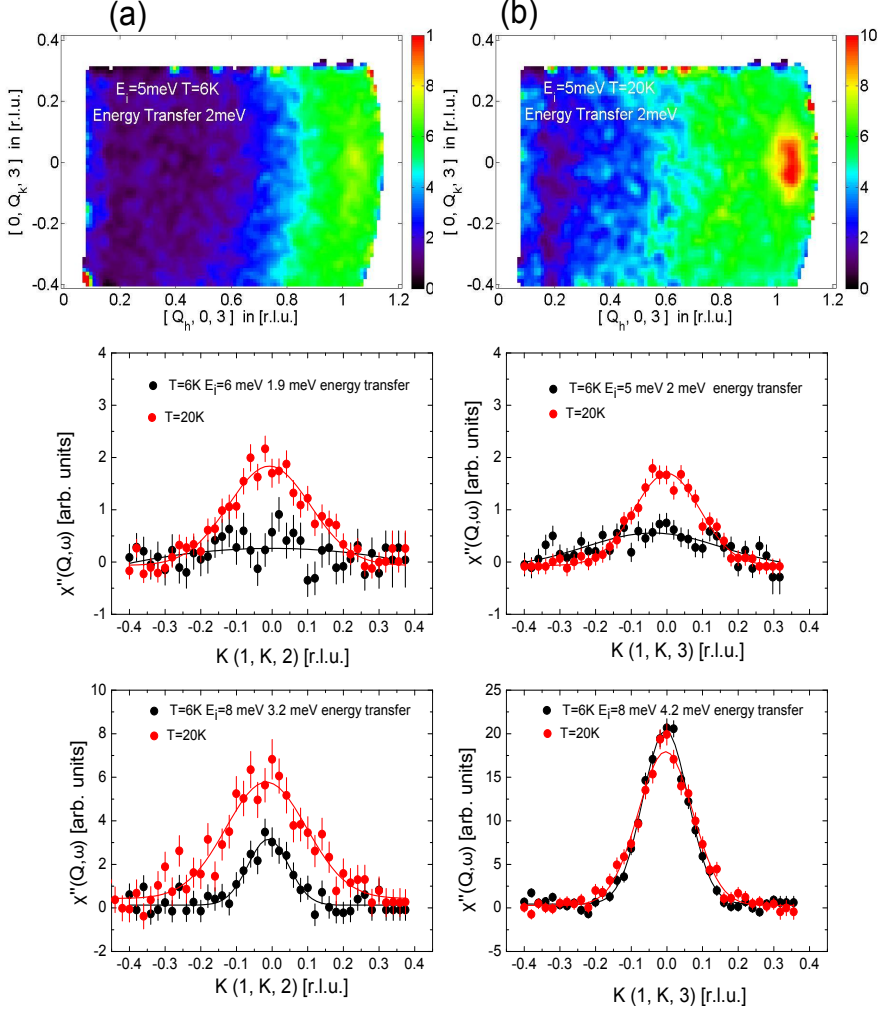


**Figure 5.4:** 2D  $\chi''(\mathbf{Q}, \omega)$  maps of  $\text{Ba}(\text{Fe}_{0.95}\text{Co}_{0.05})_2\text{As}_2$  at (a) 6 K and (b)  $T=20\text{ K}$ . The data were obtained via ToF neutron scattering experiments with an incident neutron energy of 5 meV. The two figures show 2D  $\mathbf{Q}_h - \mathbf{Q}_k$  slices at the position of the magnetic propagation vector  $\mathbf{Q}_{AFM} = (1, 0, L)$  at 2 meV energy transfer. Additional 1D constant energy cuts in  $\mathbf{Q}_k$ -direction are displayed. The cuts were performed at energy transfers corresponding to integer  $L$ -values of magnetic zone center ( $L=3$ ) and zone boundary ( $L=2$ ) reflections and temperatures 6 K (black dots) and 20 K (red dots) and were corrected for non-magnetic background contributions. They illustrate the continuous suppression of magnetic intensity in the superconducting phase, which corresponds to the opening of the spin gap. Black and red solid lines are fits with Gaussian peak functions and are used as guides to the eye.

Both features, the short ranged spin fluctuations, which are present in the superconducting phase of optimal doped materials, and the spin wave excitations of the long range static SDW-order, possess the same in-plane components of their propagation vectors,  $\mathbf{Q}_{AFM}=(1, 0, 1)$  for the SDW order and  $\mathbf{Q}_{nesting}=(1, 0, 0)$  for the 2D spin fluctuations. With identical in-plane components of the propagation vector, both signals interfere and occur at identical positions in the  $(H, K, 0)$ -reciprocal plane. Thus the inelastic magnetic signal observed at  $\mathbf{Q}_{AFM}$  in the underdoped material always contains contributions of both types of excitations, at least for temperatures below the Néel temperature  $T_N$ .

Figure 5.4 illustrates a collection of one dimensional constant energy cuts that were conducted in the  $(H, K)$ -reciprocal plane in a way that they cross the position of the magnetic propagation vector  $\mathbf{Q}_{AFM} = (1, 0, L)$  in transverse ( $K$ -cut) direction for temperatures 6 K (black) and 20 K (red). The illustrated cuts correspond to positions in reciprocal space related to magnetic zone center ( $L=\text{odd}$ ) and zone boundary ( $L=\text{even}$ ) reflections<sup>1</sup>. The illustrated data has been corrected for non magnetic background contributions as well as the thermal population factor.

Obviously, a clean spin gap opens at energies below approximately 4 meV for both zone center as well as zone boundary reflections. The mentioned spin gap shows in these transverse constant energy cuts as the suppression of  $\chi''(\mathbf{Q}, \omega)$  for the superconducting phase (6 K) in relation to the normal state (20 K).

One effect of the experimental set up with a fixed sample orientation with the incident neutron beam always parallel to the crystallographic  $c$ -axis, was a coupling of the  $(0, 0, L)$ -value of the excitation spectrum to the energy transfer. This means that  $(1, 0, L)$  reflections with different  $L$ -values would only be accessible at different energy transfers<sup>2</sup>. Consequently, the only way to investigate a given  $(1, 0, L)$ -reflection at various energy transfers was to vary the incident neutron energy. As a result, it was not possible to continuously vary the energy transfer for a given reflection or to vary the  $L$ -value of the reflection for a fixed energy transfer. However, the eight different incident neutron energies used in the experiment, provided a total of eight different energy transfers for a given  $(1, 0, L)$  reflection. This led to a collection of several  $(1, 0, L)$  reflections with integer  $L$  values in the relevant energy range below 10 meV.

<sup>1</sup>With a propagation vector of  $\mathbf{Q}_{AFM}=(1, 0, 1)$  for the magnetic long range order, reflections with odd  $L$ -values correspond to the center of that particular magnetic Brillouin zone. Whereas, reflections with an even value for  $L$  are located right on the boundary of two neighboring Brillouin zones, and consequently are referred to as zone boundary reflections.

<sup>2</sup>This effect becomes obvious from figures 5.6 and 5.7 which contain a series of  $\mathbf{Q}_h - \mathbf{Q}_k$  reciprocal maps at different energy transfers and corresponding  $(0, 0, L)$ -values. The figures illustrate the increasing reciprocal space which becomes accessible due to an increased incident neutron energy. They further show the correlation between  $E_i$ , energy transfer and  $(0, 0, L)$ , as different  $E_i$  or energy transfer lead to different  $(0, 0, L)$ -values.

Due to this effect, it was not possible to continuously follow the energy dependence of a given  $(1, 0, L)$  reflection and thus the gap energy can only be estimated for energies below 4 meV. For this energy range, however, a fully opened spin gap in the excitation spectrum can be reported, as for  $T < T_c$   $\chi''(Q, \omega)$  is heavily suppressed, and is almost featureless below 2 meV. This confirms that the emergence of the spin resonance, which will be discussed later, is indeed accompanied by the opening of a gap in the excitation spectrum, which fits nicely to the current understanding of magnetic excitations in the superconducting state.

The strong suppression of  $\chi''(Q, \omega)$  below 4 meV, of course is only possible when the spin wave excitation spectrum is gapped for this energy range as well. So, aside from the spin gap, which as a feature is related to the quasi 2D short range spin fluctuations, further a gap in the spin wave spectrum can be reported, at least for energies below 4 meV.

In order to investigate the spin resonance also in regard of a possible dispersion of the mode, as it is reported for a 4% underdoped  $\text{Ba}(\text{Fe}_{1-x}\text{Co}_x)_2\text{As}_2$  sample [70], multiple transverse cuts through  $(1, 0, L)$ -reflections, at different energies between 5 and 10 meV have been performed. The problem of the coupled  $(0, 0, L)$ -values and the energy transfer prevented a continuous analysis, and in this case resulted in even fewer reflections accessible with the right  $L$ -value at the right energy range. Figure 5.5 is a collection of transverse cuts through zone center  $(1, 0, L=3)$  and zone boundary  $(1, 0, L=2,4)$  reflections for temperatures of 6 K and 20 K. The resonance mode, which shows as an enhancement of  $\chi''(Q, \omega)$  in the 6 K cuts, emerges for zone center reflections between energies of 5-9 meV. Seemingly the resonance signal observed for the zone boundary  $(1, 0, 4)$  reflections is slightly reduced in intensity compared to the zone center  $(1, 0, 3)$  reflection, most obvious when comparing the integrated intensities  $I_0$  of the resonance signal for both reflections  $I_0(1, 0, 3) = 5.56 \pm 0.35$  [arb. units] and  $I_0(1, 0, 4) = 3.13 \pm 0.30$  [arb. units], obtained by subtracting the 30 K data from the 6 K data  $\chi''(6\text{ K}) - \chi''(30\text{ K})$ . This reduction indicates a possible three dimensionality of the resonance signal, similar to what has been reported by Pratt et al. [70]. However, this intensity reduction could also be a result of the different energy transfers at which both cuts were performed. In order to make a conclusive statement, spin resonance intensities for zone center and zone boundary reflections need to be obtained at identical excitation energies. As already explained, with the specific experimental set up this was not possible. Consequently the small number of accessible reflections and the coupling of the  $(0, 0, L)$ -value of the spectrum to the energy transfers do not allow a conclusive statement on a possible three dimensionality of the resonance signal in this compound. Regarding the proposed dispersion of the mode, again no unambiguous conclusions can be drawn. From the cuts at 9 meV for  $L=2$  and at 9.2 meV for  $L=3$  it is obvious that the zone center reflection shows no signs of the spin resonance anymore as peak intensities for both temperatures are identical, whereas the  $(1, 0, 2)$  reflection at 9 meV  $\chi''(Q, \omega)$

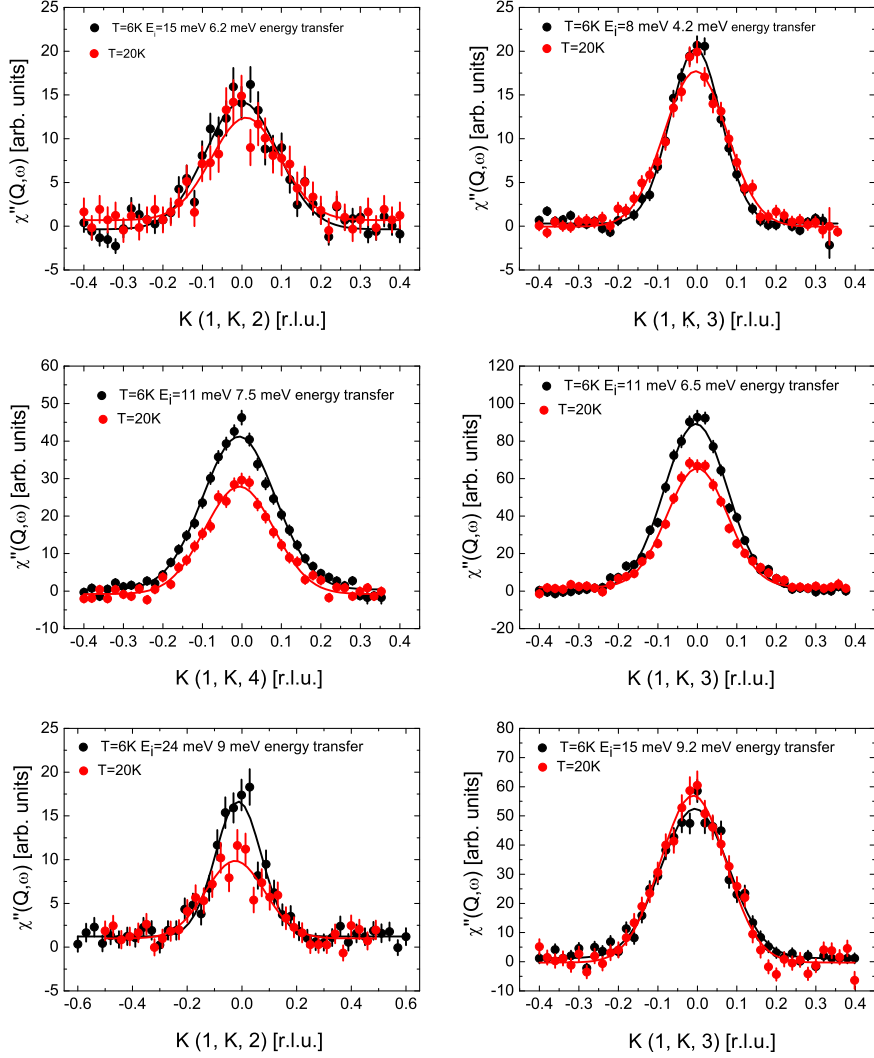


**Figure 5.5:**  $Q$ -dependence of  $\chi''(\mathbf{Q}, \omega)$  for temperatures 6 K (black dots) and 20 K (red dots) obtained by constant energy cuts at energies between 4 and 9 meV. The cuts were performed at energy transfers corresponding to integer  $L$ -values of magnetic zone center ( $L=3$ ) and zone boundary ( $L=2, 4$ ) reflections and were corrected for non-magnetic background contributions. The left column of figures illustrates the energy evolution of the spin resonance at magnetic zone boundary reflections ( $L=\text{even}$ ). Whereas the right column illustrates the evolution for zone center reflections ( $L=\text{odd}$ ). Black and red solid lines are fits with Gaussian peak functions and are used as guides to the eye.

still shows a sizeable enhancement. This result with consideration of the results by Pratt et al. [70] indicate that a similar dispersion of the mode is also present in this sample. However, the presented results alone do not allow an unambiguous conclusion, and in order to completely clarify this topic further experiments will be necessary, best using a three-axis spectrometer as this type of instrument is much better suited for this type of experiment.

### 5.3.2 Linear Spin Wave Model Analysis of Magnetic Excitations

As the previous section was solely focused on the very low energy part of the excitation spectrum, this following part of the data discussion will focus on the complete magnetic excitation spectrum, which was accessible during the experiments. Figure 5.6 shows a collection of constant energy slices through the excitation spectrum at  $\mathbf{Q}_{AFM}=(1, 0, L)$ . The magnetic excitations appear in these 2D slices as the elliptical spot located at the  $(1, 0, L)$  positions. The strong intensity present in some slices located around  $\mathbf{Q}_h=1.5$  [r.l.u.] is caused by non magnetic background, most likely from the sample holder, as the illustrated scans have not been corrected for background contributions<sup>3</sup>.

For low energies, the magnetic excitations exhibit an elliptic  $\mathbf{Q}_h - \mathbf{Q}_k$ -distribution with the extended direction along  $\mathbf{Q}_k$ . This in-plane anisotropy of the spin excitations has also been observed in parent compounds of various 122 materials. Reportedly,  $\text{CaFe}_2\text{As}_2$  [60, 208] and  $\text{SrFe}_2\text{As}_2$  [56] both exhibit a similar elliptical in-plane distribution of the magnetic excitations. For these compounds, however, the elliptical shaped signal develops into a elliptical ring like feature with increasing energy, exactly what one would expect for constant energy slices through a local moment spin wave excitation cone. In contrast to this elliptical ring like shape, the spin excitations in underdoped  $\text{Ba}(\text{Fe}_{1-x}\text{Co}_x)_2\text{As}_2$  develop into two distinct peaks split along the  $\mathbf{Q}_k$ -direction with increasing energies, obvious from fig. 5.7. This effect of a splitting into two peaks seems a special feature of the  $\text{Ba}(\text{Fe}_{1-x}\text{Co}_x)_2\text{As}_2$  materials, as it has also been reported for undoped [54], underdoped [209] as well as for optimal doped [74]  $\text{Ba}(\text{Fe}_{1-x}\text{Co}_x)_2\text{As}_2$  compositions, but not for any other 122-materials. One way to interpret this splitting into two distinct peaks is in terms of two counter propagating modes with distinct propagation vectors. This interpretation supports a mostly itinerant description of the magnetic excitations in the  $\text{Ba}(\text{Fe}_{1-x}\text{Co}_x)_2\text{As}_2$  materials. Another approach has been made by Harriger et al. [54] who proposed strong damping effects along the crystallographic  $a$ -axis, to be responsible for the suppression of intensities along

---

<sup>3</sup>Due to the sudden ending to the experiments, caused by the devastating earthquake striking Japan on the 11th March 2011, it was not possible to perform an empty-can-measurement and consequently the shown data are not corrected for background contributions. The background correction was done by correcting the 1D constant energy cuts shown in figures 5.9 to 5.12 separately, similar to how it was performed in the previous discussion of the spin gap and spin resonance.

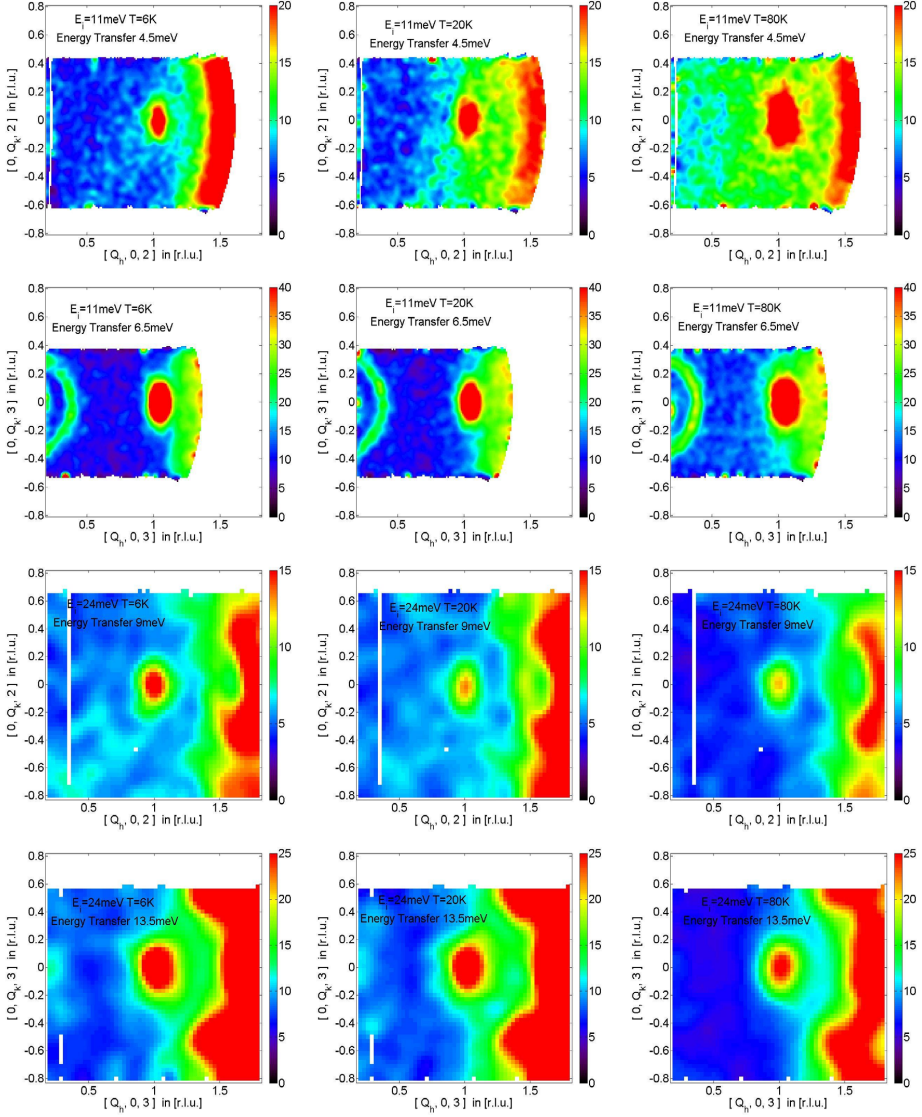


**Figure 5.6:** 2D  $\mathbf{Q}_h - \mathbf{Q}_k$  maps of  $\chi''(\mathbf{Q}, \omega)$ . The constant energy slices through the spectrum of spin excitations with propagation vector  $\mathbf{Q}_{AFM} = (1, 0, L)$  were performed at energy transfers corresponding to magnetic zone center ( $L = \text{odd}$ ) and zone boundary ( $L = \text{even}$ ) reflections. The left column of figures illustrates the energy evolution of the magnetic excitations for temperature  $T = 6 \text{ K}$ , the middle column for  $T = 20 \text{ K}$  and the right column corresponds to  $T = 80 \text{ K}$ . Descending figures correspond to neutron energy  $E_i$  : 11 meV, 11 meV, 24 meV, 24 meV and energy transfers : 4.5 meV, 6.5 meV, 9 meV, 13.6 meV.

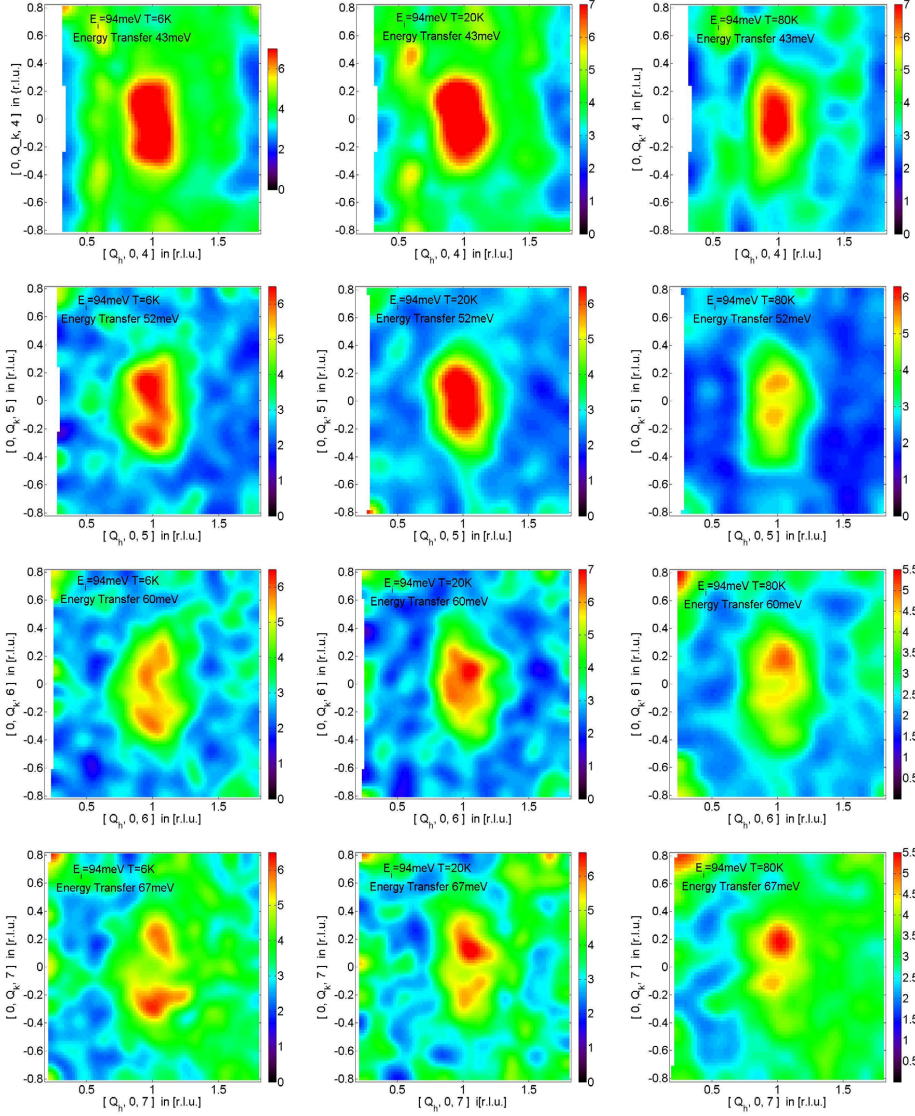


**Figure 5.7:** 2D  $\mathbf{Q}_h - \mathbf{Q}_k$  maps of  $\chi''(\mathbf{Q}, \omega)$ . The constant energy slices through the spectrum of spin excitations with propagation vector  $\mathbf{Q}_{AFM} = (1, 0, L)$  were performed at energy transfers corresponding to magnetic zone center ( $L=\text{odd}$ ) and zone boundary ( $L=\text{even}$ ) reflections. The left column of figures illustrates the energy evolution of the magnetic excitations for temperature  $T=6$  K, the middle column for  $T=20$  K and the right column corresponds to  $T=80$  K. Descending figures correspond to neutron energy  $E_i$  : 94 meV and energy transfers : 43 meV, 52 meV, 60 meV, 67 meV.

the  $H$ -direction and which transform the ring like feature into the two peaks. This approach obviously promotes a more localized nature of the spin wave excitations in the  $\text{Ba}(\text{Fe}_{1-x}\text{Co}_x)_2\text{As}_2$  materials.

In addition to this qualitative discussion of the spin excitation spectrum, the spin wave excitations of the Fe-SDW order have been analyzed in terms of a linear spin wave model. For this quantitative part of the analysis, data from five different incident energies have been used, 11 meV, 15 meV, 24 meV, 42 meV and 94 meV. This provided a coverage of excitation energies from 4 meV to 70 meV. Within this energy range, 1D constant energy cuts through the spectrum have been performed, along both in-plane directions, longitudinal and transverse, and for several different excitation energies. The energy integration for each cut was carefully chosen, so that each cut would represent a  $(1, 0, L)$  reflection with an integer  $L$ -value, for both zone center ( $L=\text{odd}$ ) and zone boundary ( $L=\text{even}$ ) reflections. This way, a total number of close to thirty cuts were collected and used for the fitting of the spin wave model simultaneously.

For the fitting process the tobyfit [210] program was used, a software tool developed at the ISIS neutron facility for simulations and least square fitting of single crystal data obtained via time-of-flight neutron scattering experiments. In tobyfit Monte Carlo methods are used to convolute user defined scattering functions with instrumental resolution effects and perform the least square fitting to the obtained data. Multiple one dimensional (1D) constant energy and constant  $Q$  cuts can be included into the fitting process and will be treated simultaneously.

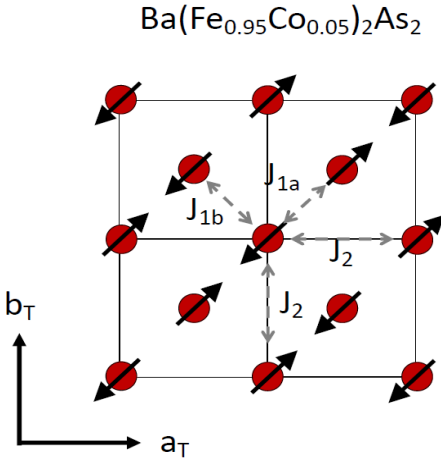


**Figure 5.8:** Spin configuration of the static long range magnetic order present in undoped 122-materials. Illustrated is the in-plane configuration depicted in tetragonal symmetry. Red dots embody the Fe-ions with spins oriented along the in-plane diagonal of the tetragonal unit cell. Further defined are the exchange coupling constants  $J_{ik}$ , the way they were used in the spin wave analysis using a local moment Heisenberg Hamiltonian.

Prior to this study it has been shown for several undoped 122 materials [40, 54–56, 62, 208] that a linear spin wave model based on a local moment Heisenberg Hamiltonian



indeed provides a reasonable description of the spin wave excitation spectrum, regardless of the fact that a strictly local moment approach most likely is not the correct description of magnetism in the Fe-based materials. This previous success was the reason why for the current study a similar linear spin wave model based on the following local moment Heisenberg Hamiltonian [62] was used.

$$H = J_{1a} \sum_{\langle jk \rangle_a} \mathbf{S}_j \cdot \mathbf{S}_k + J_{1b} \sum_{\langle jk \rangle_b} \mathbf{S}_j \cdot \mathbf{S}_k + J_2 \sum_{\langle jk \rangle_{ab}} \mathbf{S}_j \cdot \mathbf{S}_k \quad (5.4)$$

$$+ J_c \sum_{\langle jk \rangle_c} \mathbf{S}_j \cdot \mathbf{S}_k + \sum_j \left\{ K_c(S_z^2) + K_{ab}(S_y^2 - S_x^2)_j \right\} \quad (5.5)$$

Here, the first four summations consider contributions by nearest and next nearest neighbor pairs, where each pair is counted just once. The  $J_{ik}$  are the in plane and out of plane exchange parameters and define the local moment interactions as illustrated in figure 5.8. The fifth summation accounts for contributions by  $K_{ab}$  and  $K_c$ , the in plane and out of plane anisotropy constants, which consider possible gaps in the excitation spectrum due to single ion anisotropy effects. Diagonalization of equation (5.4) leads to two non-degenerate spin wave branches with the following dispersion:

$$\hbar\omega_{1,2}(\mathbf{Q}) = \sqrt{A_{\mathbf{Q}}^2 - (\mathbf{C} \pm D_{\mathbf{Q}})^2} \quad (5.6)$$

with

$$\begin{aligned} A_{\mathbf{Q}} &= 2S \left\{ J_{1b} \left[ \cos\left(\frac{\mathbf{Q} \cdot \mathbf{b}}{2}\right) - 1 \right] + J_{1a} + 2J_2 + J_c \right\} + S(3K_{ab} + K_c) \\ C &= S(K_{ab} - K_c) \\ D_{\mathbf{Q}} &= 2S \left\{ J_{1a} \cos\left(\frac{\mathbf{Q} \cdot \mathbf{a}}{2}\right) + 2J_2 \cos\left(\frac{\mathbf{Q} \cdot \mathbf{a}}{2}\right) \cos\left(\frac{\mathbf{Q} \cdot \mathbf{b}}{2}\right) + J_c \cos(\mathbf{Q} \cdot \mathbf{c}) \right\} \end{aligned} \quad (5.7)$$

With the neutron scattering cross section

$$\frac{d^2\sigma}{d\Omega dE_f} = \frac{k_f}{k_i} \left( \frac{\gamma r_0}{2} \right)^2 g^2 f^2(Q) \exp(-2W) \times \sum_{\alpha\beta} (\delta_{\alpha\beta} - \hat{Q}_\alpha \hat{Q}_\beta) S^{\alpha\beta}(\mathbf{Q}, \omega), \quad (5.8)$$

and

- $(\frac{\gamma r_0}{2})^2 = 72.8 \text{ mb}$  [62]
- $g$  is the g-factor for iron. Here  $g=2$  was assumed for a spin-only magnetic moment with a quenched orbital component. This usually is a reasonable assumption for transition metal elements.

- $f(\mathbf{Q})$  represents the form factor of iron [211].
- $\exp(-2W)$  is the Debye-Waller factor. The Debye Waller factor was assumed to be equal 1. This was done since the mean displacement of the atoms was not known and because the correction of the Debye Waller factor would not affect the outcome of the fitting process.
- $\hat{Q}_\alpha$  is the  $\alpha$  component of a unit vector parallel to the scattering vector  $\mathbf{Q}$
- $S^{\alpha\beta}(\mathbf{Q}, \omega)$  depicts the scattering function describing the  $\alpha\beta$  spin correlations,

the scattering function for magnon creation, or the neutron energy loss side of the spectrum, reads as,

$$\begin{aligned} S^{yy}(\mathbf{Q}, \omega) &= S_{eff} \frac{A_{\mathbf{Q}} - C - D_{\mathbf{Q}}}{\hbar\omega_1(\mathbf{Q})} \{n(\omega) + 1\} \delta[\omega - \omega_1(\mathbf{Q})] \\ S^{zz}(\mathbf{Q}, \omega) &= S_{eff} \frac{A_{\mathbf{Q}} + C - D_{\mathbf{Q}}}{\hbar\omega_2(\mathbf{Q})} \{n(\omega) + 1\} \delta[\omega - \omega_2(\mathbf{Q})] \end{aligned} \quad (5.9)$$

where  $S_{eff}$  is the effective spin and  $n(\omega)$  the boson occupation number. With a quantization axis of the spin wave along the x-axis and the fact that only the transverse spin correlations (in this case yy and zz) contribute to the linear spin wave cross section, only  $S^{yy}(\mathbf{Q}, \omega)$  and  $S^{zz}(\mathbf{Q}, \omega)$  are obtained. To account for the finite lifetime of the excitation, the delta function in equation (5.9) was replaced by a damped simple harmonic oscillator (DSHO)

$$\begin{aligned} S^{yy}(\mathbf{Q}, \omega) &= S_{eff} \frac{A_{\mathbf{Q}} - C - D_{\mathbf{Q}}}{\hbar\omega_1(\mathbf{Q})} \frac{\omega}{1 - e^{-\omega/k_B T}} \times \frac{4\Gamma\omega(\mathbf{Q})/\pi}{\left[\omega^2 - \omega_1^2(\mathbf{Q})\right]^2 + 4\left[\Gamma\omega\right]^2} \\ S^{zz}(\mathbf{Q}, \omega) &= S_{eff} \frac{A_{\mathbf{Q}} + C - D_{\mathbf{Q}}}{\hbar\omega_2(\mathbf{Q})} \frac{\omega}{1 - e^{-\omega/k_B T}} \times \frac{4\Gamma\omega(\mathbf{Q})/\pi}{\left[\omega^2 - \omega_2^2(\mathbf{Q})\right]^2 + 4\left[\Gamma\omega\right]^2} \end{aligned} \quad (5.10)$$

Figures 5.9 to 5.12 show a collection of 1D constant energy cuts, which were used for the fitting of the spin wave model, with the solid lines representing the best fits of the linear spin wave model.

During the fitting process the following parameters were free for variation: the in-plane exchange parameters  $J_{1a}$ ,  $J_{1b}$  and  $J_2$ , the out of plane parameter  $J_c$ , the scale factor  $S_{eff}$  and the damping factor  $\Gamma$ , which accounts for the finite lifetime of the excitations.

Due to the incomplete data set, which was limited to excitations below 70 meV, it was not possible to reach the region of the excitation spectrum where models with high in plane anisotropy and models with just very little in plane anisotropy, like the models used in earlier work [62, 208], become distinguishable. As illustrated in figure 2.6 in

the introduction part, the difference between models with high anisotropy and models with little anisotropy only starts to show for high energies around 100 meV [55], whereas for lower energies both models describe almost identical dispersions. As a consequence, during the fitting process it was not possible to free all exchange parameters simultaneously. Instead the in plane exchange parameters  $J_{1a}$ ,  $J_{1b}$  and  $J_2$  had to be linked to each other in certain ratios with just one parameter free for the fitting. The best fit to the data was achieved by linking the exchange parameters in a highly anisotropic way, very similar to the published values for  $\text{BaFe}_2\text{As}_2$  [54],  $J_2 = 0.4 \cdot J_{1a}$  and  $J_{1b} = -0.2 \cdot J_{1a}$ . This of course means that the data analysis does not allow an unambiguous statement on the degree of anisotropy of the in plane exchange coupling for the underdoped compound. The achieved results indeed suggest an anisotropy very similar to the parent compound, but in order to be able to address the anisotropy in the underdoped compound independently, a complete spectrum, including energies as high as 200 meV is required.

Since the obtained data is lacking any direct information of the spin wave dispersion along the  $(1, 0, L)$ -direction, a result of the fixed sample position with the  $c$ -axis parallel to the incident neutron beam, the out of plane exchange parameter  $J_c$  had to be determined by considering the difference in peak intensities between zone center and zone boundary reflections. For strong antiferromagnetic correlations in  $c$ -direction, and a consequently large  $J_c$ , one expects a prominent intensity modulation along  $(1, 0, L)$ -direction, with strong intensity located at zone center reflections  $(1, 0, L=\text{odd})$  and weaker intensity at zone boundary reflections with  $L=\text{even}$ . On the other side, for very little out of plane correlations the excitations are more or less two dimensional,  $J_c$  is small, and only very small intensity variation between zone center and zone boundary reflection occurs.

For data that has been normalized to a vanadium standard and hence is expressed in absolute units,  $S_{eff}$  represents the effective spin that contributes to the spin wave intensity. However, because of the sudden ending to the experiment<sup>4</sup> it was not possible to perform such a normalization of the obtained data sets,  $S_{eff}$  was used as a simple scale factor, which accounted for peak intensities but had no further physical meaning. The damping factor  $\Gamma$ , which accounts for the finite lifetime of the excitations, was handled in a way, where it was free for variation through out the fitting process, but it was considered energy independent and the same value was used to model excitations of different energies. This makes sense, as according to Diallo et al. [208]  $\Gamma$  remains more or less constant for energies up to 80 meV.

Caused by single ion anisotropy effects<sup>5</sup>, spin wave spectra of the parent 122-pnictides

---

<sup>4</sup>Due to the sudden ending to the experiments, caused by the devastating earthquake striking Japan on the 11th March 2011, it was not possible to complete the experiment as planned.

<sup>5</sup>For the long wavelength and low energy limit  $Q \rightarrow 0$  and  $\omega \rightarrow 0$ , the spin wave excitation corresponds to a complete rotation of the spin direction of the long range order. However, existing anisotropies, for example hard and easy axes of magnetization, prevent the system from this rotation and thus can cause a gap in the excitation spectrum. In the spin wave model the possible gap caused by this

all exhibit clear fully opened gaps with gap energies as high as 7-10 meV [54, 55, 60, 62–64, 208]. Just recently Qureshi et al. [65] even proposed that the spin wave excitation spectrum of undoped  $\text{BaFe}_2\text{As}_2$  in fact possesses two gaps, for in-plane and out-of-plane excitations and that the observed gap energies of 7-10 meV correspond only to the lower gap. In the current study, however, it was not possible to detect this anisotropy gap in the spin wave spectrum, aside from the gap opening below 4 meV, which has been discussed in the previous section. This absence of a gap in the spin wave spectrum is most likely due to the presence of the mentioned 2D short ranged spin fluctuations, which due to their similar propagation vector contribute to the low energy part of the spin wave excitation spectrum. This most likely leads to the situation where the low energy part of the spectrum is dominated by short range fluctuations which eventually fill up the region of the spin wave gap and make it undetectable. As a result, an unambiguous determination of the in-plane and out-of-plane anisotropy constants  $K_{ab}$  and  $K_c$  during the fitting process was not possible, but instead the parameters were kept fixed at zero, since they had no impact on the fitting results, in either way. Consequently, the situation of the anisotropy gap of the spin wave spectrum could not be solved, aside from the gap observed below 4 meV.

Table 5.1 illustrates the results obtained from the spin wave fitting. It further contains results reported for several parent 122-compounds, obtained via spin wave model analyses of ToF neutron scattering data. Comparing the values for the in-plane exchange parameters  $J_{1a}$ ,  $J_{1b}$  and  $J_2$  to the values reported for the parent compounds  $\text{CaFe}_2\text{As}_2$  [55],  $\text{SrFe}_2\text{As}_2$  [56] and  $\text{BaFe}_2\text{As}_2$  [54], it is obvious that the in-plane coupling in the underdoped compound is slightly weakened, reduced to about 75% of the interaction strength present in the parent compounds. This clearly indicates a weakened exchange coupling of the spin wave excitations in the underdoped compound. However, in a recent publication by Liu et al. [58] it was proposed that the spin wave excitations of the 122-pnictides in fact exhibit only very little doping dependence. The authors report that it is possible to describe spin excitations for  $\text{Ba}(\text{Fe}_{0.95}\text{Ni}_{0.05})_2\text{As}_2$  by a linear spin wave model using exchange parameters, previously obtained for spin waves in undoped  $\text{BaFe}_2\text{As}_2$ . According to these results, the only region, where the excitation spectra of doped and parent 122-compounds deviate, is for low energies below 100 meV. For higher excitation energies the spectra show almost no doping dependence as well as almost no temperature dependence. If this is indeed the case, so far no other group has reported comparable results, then the reduction of the in-plane exchange coupling, observed in the present study, very likely is caused by the data set, which is restricted to the low energy part of the excitation spectrum. A complete excitation spectrum, with excitation energies as high as 200 meV is required in order to address this issue.

The values for the exchange parameters obtained via the spin wave analysis, listed in

---

single ion anisotropy was taken into account by the two anisotropy parameters  $K_{ab}$  and  $K_c$  for gaps in the in-plane spectrum as well as the c-axis dispersion.

Ba(Fe <sub>0.95</sub> Co <sub>0.05</sub> ) <sub>2</sub> As <sub>2</sub>	$T = 6$ [K]	$T = 20$ [K]	$T = 80$ [K]
$S_{eff}$	$1.22 \pm 0.06$ meV	$1.24 \pm 0.06$ meV	$0.96 \pm 0.06$ meV
$\Gamma$	$66.50 \pm 1.68$ meV	$69.08 \pm 2.37$ meV	$79.60 \pm 3.28$ meV
$SJ_{1a}$	$46.61 \pm 4.58$ meV	$46.45 \pm 4.76$ meV	$46.45 \pm 0.00$ meV
$SJ_{1b}$	$-7.24 \pm 0.92$ meV	$-7.22 \pm 1.00$ meV	$-7.22 \pm 0.00$ meV
$SJ_2$	$10.71 \pm 1.83$ meV	$10.67 \pm 1.94$ meV	$10.67 \pm 0.00$ meV
$SJ_c$	$1.43 \pm 0.12$ meV	$2.62 \pm 0.11$ meV	$2.37 \pm 0.11$ meV
<hr/>			
BaFe <sub>2</sub> As <sub>2</sub> [54]	<i>LowTemperature</i>		
<hr/>			
$S_{eff}$			
$\Gamma$			
$SJ_{1a}$	$59.20 \pm 2.00$ meV		
$SJ_{1b}$	$-9.20 \pm 1.20$ meV		
$SJ_2$	$13.60 \pm 1.00$ meV		
$SJ_c$	$1.80 \pm 0.30$ meV		
<hr/>			
CaFe <sub>2</sub> As <sub>2</sub> [55]	$T = 10$ [K]		
<hr/>			
$S_{eff}$	$0.22 \pm 0.06$ meV		
$\Gamma$			
$SJ_{1a}$	$49.90 \pm 9.90$ meV		
$SJ_{1b}$	$-5.70 \pm 4.50$ meV		
$SJ_2$	$18.90 \pm 3.40$ meV		
$SJ_c$	$5.30 \pm 1.30$ meV		
<hr/>			
SrFe <sub>2</sub> As <sub>2</sub> [56]	$T = 6$ [K]		
<hr/>			
$S_{eff}$	$0.30 \pm 0.01$ meV		
$\Gamma$			
$SJ_{1a}$	$30.80 \pm 1.00$ meV		
$SJ_{1b}$	$-5.00 \pm 5.00$ meV		
$SJ_2$	$21.70 \pm 0.40$ meV		
$SJ_c$	$2.30 \pm 0.10$ meV		

**Table 5.1:** Exchange parameters obtained via spin wave fitting of ToF neutron data. Values for  $BaFe_2As_2$  are taken from [54], for  $CaFe_2As_2$  are taken from [55] and for  $SrFe_2As_2$  are taken from [56]

table 5.1, and the following equations (5.11)-(5.13) [48],

$$\hbar v_a = aS\sqrt{(2J_2 + J_{1a})(2J_2 + J_{1a} + J_c)} \quad (5.11)$$

$$\hbar v_b = bS\sqrt{(2J_2 - J_{1b})(2J_2 + J_{1a} + J_c)} \quad (5.12)$$

$$\hbar v_c = cS\sqrt{J_c(2J_2 + J_{1a} + J_c)} \quad (5.13)$$

$\text{Ba}(\text{Fe}_{0.95}\text{Co}_{0.05})_2\text{As}_2$	$T = 6 \text{ [K]}$	$T = 20 \text{ [K]}$	$T = 80 \text{ [K]}$
$\hbar v_a$	$378 \pm 33 \text{ meV\AA}$	$380 \pm 34 \text{ meV\AA}$	$379 \pm 34 \text{ meV\AA}$
$\hbar v_b$	$245 \pm 25 \text{ meV\AA}$	$247 \pm 25 \text{ meV\AA}$	$246 \pm 25 \text{ meV\AA}$
$\hbar v_c$	$128 \pm 8 \text{ meV\AA}$	$175 \pm 9 \text{ meV\AA}$	$166 \pm 8 \text{ meV\AA}$
$\text{BaFe}_2\text{As}_2$ [54]	Low Temperature		
$\hbar v_a$	$480 \pm 16 \text{ meV\AA}$		
$\hbar v_b$	$312 \pm 14 \text{ meV\AA}$		
$\hbar v_c$	$162 \pm 14 \text{ meV\AA}$		
$\text{CaFe}_2\text{As}_2$ [55]	$T = 10 \text{ [K]}$		
$\hbar v_a$	$496 \pm 55 \text{ meV\AA}$		
$\hbar v_b$	$312 \pm 48 \text{ meV\AA}$		
$\hbar v_c$	$258 \pm 41 \text{ meV\AA}$		
$\text{SrFe}_2\text{As}_2$ [56]	$T = 6 \text{ [K]}$		
$\hbar v_a$	$414 \pm 6 \text{ meV\AA}$		
$\hbar v_b$	$335 \pm 18 \text{ meV\AA}$		
$\hbar v_c$	$171 \pm 4 \text{ meV\AA}$		

**Table 5.2:** Spin wave velocities obtained via equations (5.11)-(5.13) and using the above listed exchange parameters.

result in spin wave velocities, listed in table 5.1. Not surprisingly, the resulting values for the underdoped compound are substantially reduced, compared to velocities present in the parent compounds.

The spin wave analysis was performed for data obtained at all three temperatures 6 K, 20 K and 80 K, corresponding to the three phases, superconducting, magnetically ordered and paramagnetic. Comparing the exchange parameters for the superconducting and the magnetic ordered phase (6 K and 20 K) one first result is that the in plane exchange parameters, as well as the damping factor, for the two phases are identical within the error bars. It is obvious that the coexistence of superconductivity and long range order has, if at all, only small effects on the spin interactions. At least as far as the present data allows, for the low energy range of the spectrum, no prominent differences between both phases, above and below  $T_c$ , can be observed. The difference in the excitation spectra for these two temperatures occurs in form of the spin gap and spin resonance in the superconducting phase. But these two features are attributed to the 2D short range spin fluctuations, which are not considered by the spin wave model. The spin wave excitations of the long range SDW order, however, seem to be

mostly unaffected by the onset of superconductivity, and neither the in-plane exchange interaction parameters  $J_{ij}$ ,  $S_{eff}$  nor the lifetime of the spin wave excitations, expressed by the damping factor  $\Gamma$ , show any effects. The only obviously effect seems to be a strong reduction of interlayer correlations, as  $J_c$  is reduced to about 55% of the higher temperature value. The reason for this drastic loss of inter-layer coupling is not entirely clear, but it most likely results from the interference of signals originating from the short ranged quasi 2D spin fluctuations and the three dimensional spin wave excitations. As previously mentioned, the only access to the out-of-plane exchange coupling was via peak intensity modulations of zone center and zone boundary reflections. In the superconducting phase the 2D spin fluctuations are strongly modified and enhanced compared to the normal state excitations, especially for the low energy region of the spectrum. Due to this enhanced contribution of the two dimensional fluctuations to spin wave excitation spectrum, the peak intensity modulation becomes less prominent, and in the fitting process this results in a reduction of  $J_c$ . This effect of the 2D fluctuations is even enhanced by the fact, that the excitation spectrum becomes independent of out of plane interactions for energies above  $16(2SJ_2 + SJ_{1a})SJ_c^{1/2} \simeq 51$  meV [48], which was determined using the exchange parameters for the 20 K ordered phase.

In the paramagnetic phase, the obtained results show strong similarities to previous works on the paramagnetic phase of parent 122-compounds [54, 61]. The signal broadens and decreases in intensity to about 75% compared to the ordered state. The decrease of intensity was considered by fitting  $S_{eff}$  and the in-plane broadening of the excitations by fitting the damping parameter  $\Gamma$ , whereas the in-plane exchange parameters were held fixed using the values obtained for the 20 K data. Only the out of plane parameter  $J_c$  was free for fitting. Harriger et al. [54] report that for high energies the spin waves in  $\text{BaFe}_2\text{As}_2$  almost show no temperature dependence and that the strong in plane anisotropy, observed in the ordered phase, also persists up to high temperatures, far into the paramagnetic phase. They further report, that the broadened paramagnetic excitations, observed in this study as well as for other compounds [61, 63]<sup>6</sup>, only occur for the low energy range of the spectrum and are replaced by narrow spin wave excitations for high energies and wave vectors close to magnetic Brillouin zone boundary. In order to consider this, the in-plane exchange parameters were held fixed with only  $J_c$ ,  $S_{eff}$  and  $\Gamma$  free for fitting. This lead to the above listed results. Aside from the already mentioned intensity reduction and in-plane broadening of the paramagnetic excitations, the c-axis exchange interactions are reduced about 10% compared to the ordered state. The results for  $J_c$ , in this case, are believed to be more reliable than the one obtained for the superconducting state, due to the reduced contribution by the short range 2D spin excitations. The result for  $J_c$  shows that the difference in interlayer exchange interactions between the ordered spin wave state and the paramagnetic state in this

---

<sup>6</sup>The drawback from these earlier works is that they only consider low energy excitations, covering a similar energy range as in this study.

compound is not very prominent and the inter-layer exchange coupling still seems to be rather strong, even for a temperature of 80 K, which corresponds to  $1.33 T_N$ . These out-of-plane correlations observed for the paramagnetic phase are very similar to what is reported for undoped  $\text{CaFe}_2\text{As}_2$  [61] but are contrary to reports for the paramagnetic phase of  $\text{BaFe}_2\text{As}_2$  [63] where no  $(0, 0, L)$ -modulation are observed.

The analysis with the spin wave model produced a  $J_c$ , which fits very well to published results by other groups that performed a similar data analysis [54–56]. Nonetheless, it should be mentioned here that different methods to determine  $J_c$  lead to much smaller values. Deriving  $J_c$  from accurately determined anisotropy gap values [64, 212], or by explicitly fitting the  $(0, 0, L)$ -dispersion obtained via three axis spectroscopy [40], leads to interlayer coupling, about 10 times smaller compared to the results obtained via the spin wave fitting to 3D ToF data<sup>7</sup>. This could mean that the method used here, where  $J_c$  was determined considering intensity variations between constant energy cuts, drastically overestimates the actual inter-layer exchange coupling. A solution for this problem is to perform a time of flight experiment with an additional sample rotation, as this rotation adds another spatial dimension to the obtained Q-energy dispersion data.

---

<sup>7</sup>3D in this case regards the dimensionality of the obtained data set. A ToF experiment without sample rotation leads to a 3D data set with information on two spatial dimensions and the energy transfer. A sample rotation, adds information for another third spatial dimension, which leads to a 4D data set, with information on the Q-energy dispersion along all three spatial directions.



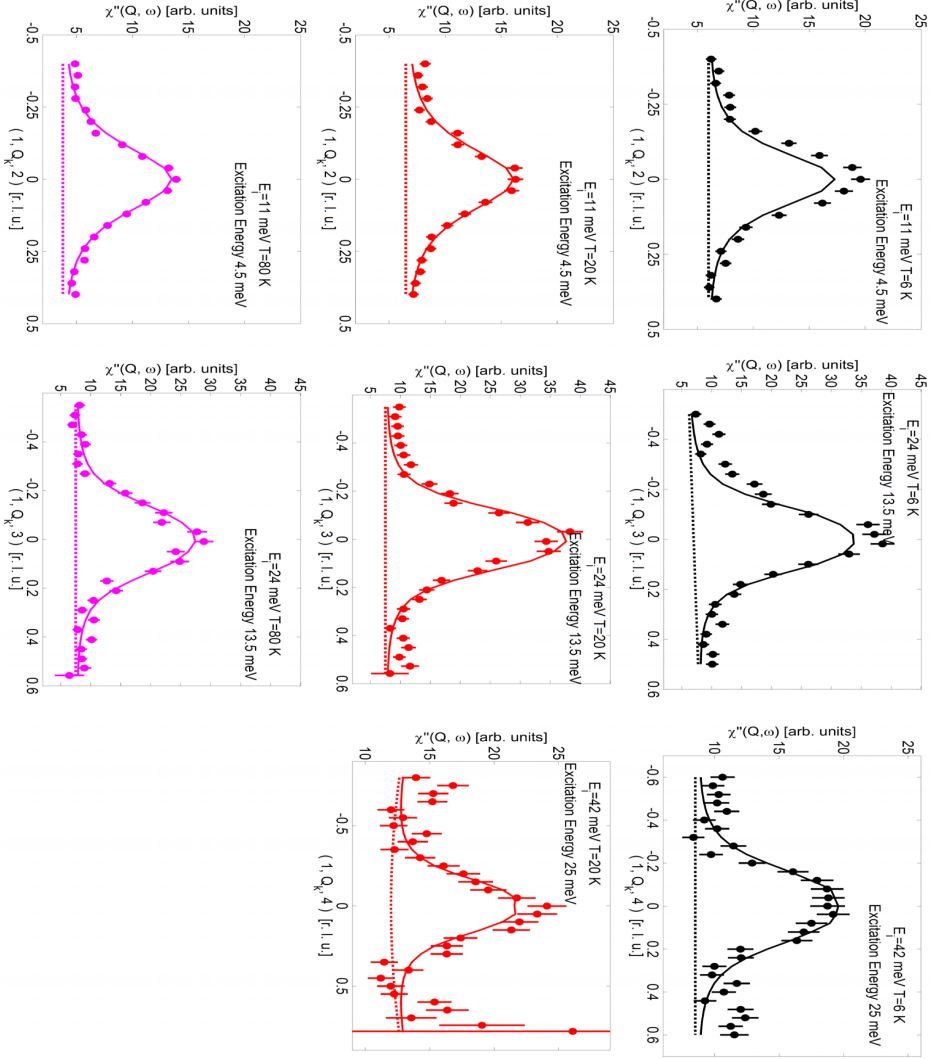


**Figure 5.9:** Collection of 1D constant energy cuts in  $\mathbf{Q}_k$ -direction through the spectrum of magnetic excitations with propagation vector  $\mathbf{Q}_{AFM}$ . The cuts were performed at energy transfers corresponding to magnetic zone center ( $L=\text{odd}$ ) and zone boundary ( $L=\text{even}$ ) reflections. The illustrated data were obtained at three different temperatures 6 K (black) and 20 K (red) and 80 K (magenta), representing three different phases in the phase diagram of  $\text{Ba}(\text{Fe}_{0.95}\text{Co}_{0.05})_2\text{As}_2$ . The solid lines illustrate the best fits of the local moment spin wave model to the data. Dashed lines illustrate non magnetic background contributions.

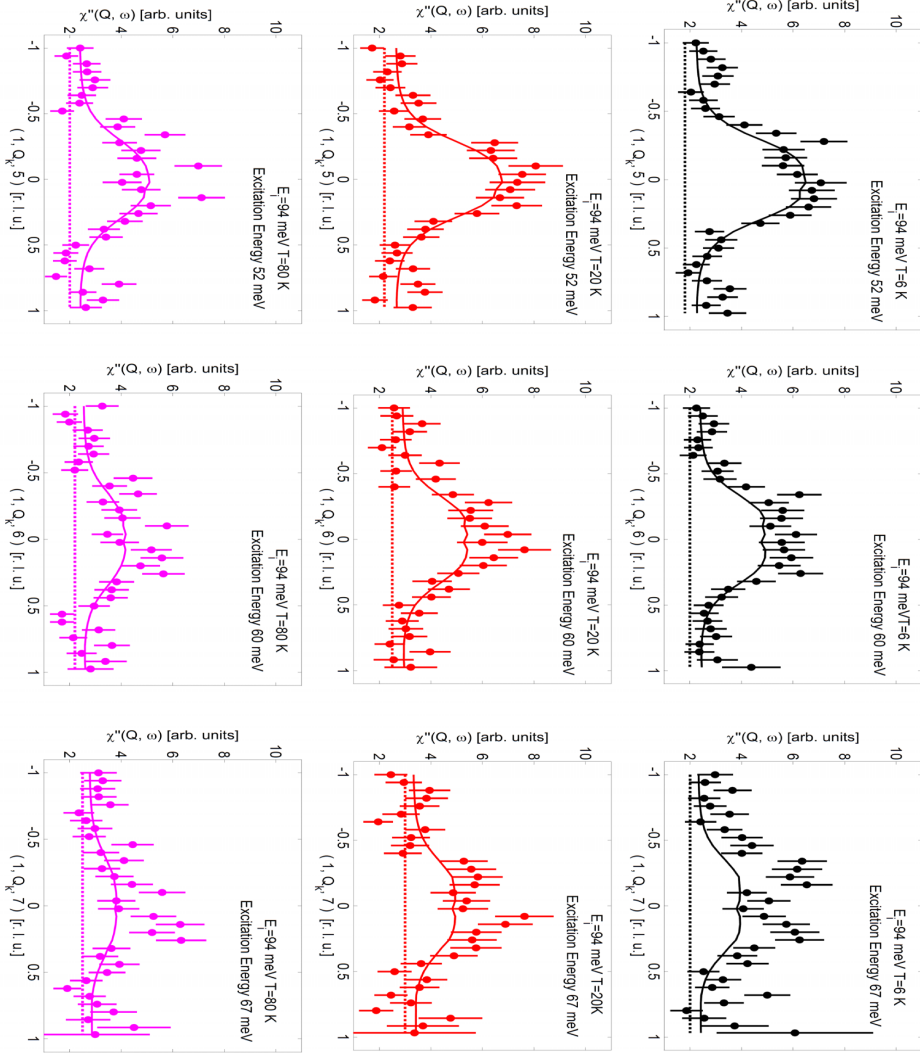


**Figure 5.10:** Collection of 1D constant energy cuts in  $\mathbf{Q}_k$ -direction through the spectrum of magnetic excitations with propagation vector  $\mathbf{Q}_{AFM}$ . The cuts were performed at energy transfers corresponding to magnetic zone center ( $L$ =odd) and zone boundary ( $L$ =even) reflections. The illustrated data were obtained at three different temperatures 6 K (black) and 20 K (red) and 80 K (magenta), representing three different phases in the phase diagram of  $\text{Ba}(\text{Fe}_{0.95}\text{Co}_{0.05})_2\text{As}_2$ . The solid lines illustrate the best fits of the local moment spin wave model to the data. Dashed lines illustrate non magnetic background contributions.

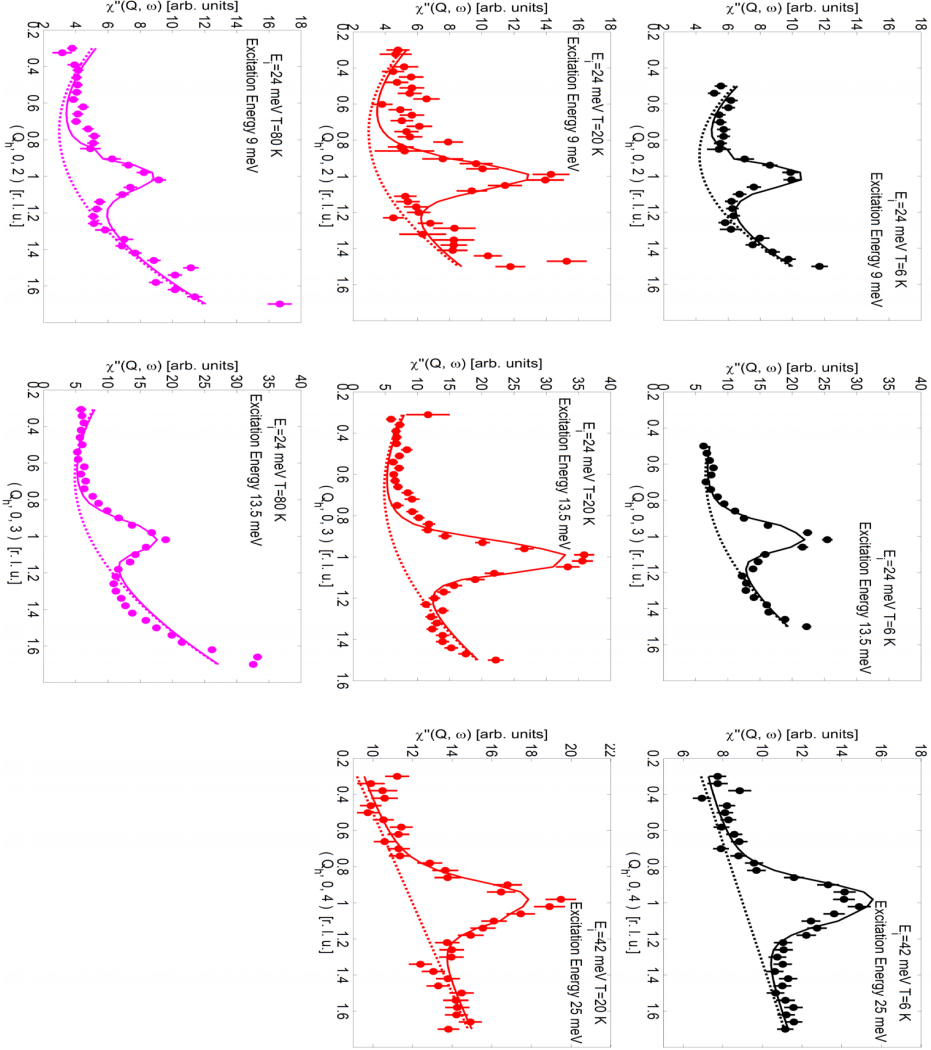


**Figure 5.11:** Collection of 1D constant energy cuts in  $\mathbf{Q}_h$ -direction through the spectrum of magnetic excitations with propagation vector  $\mathbf{Q}_{AFM}$ . The cuts were performed at energy transfers corresponding to magnetic zone center ( $L$ =odd) and zone boundary ( $L$ =even) reflections. The illustrated data were obtained at three different temperatures 6 K (black) and 20 K (red) and 80 K (magenta), representing three different phases in the phase diagram of  $\text{Ba}(\text{Fe}_{0.95}\text{Co}_{0.05})_2\text{As}_2$ . The solid lines illustrate the best fits of the local moment spin wave model to the data. Dashed lines illustrate non magnetic background contributions.

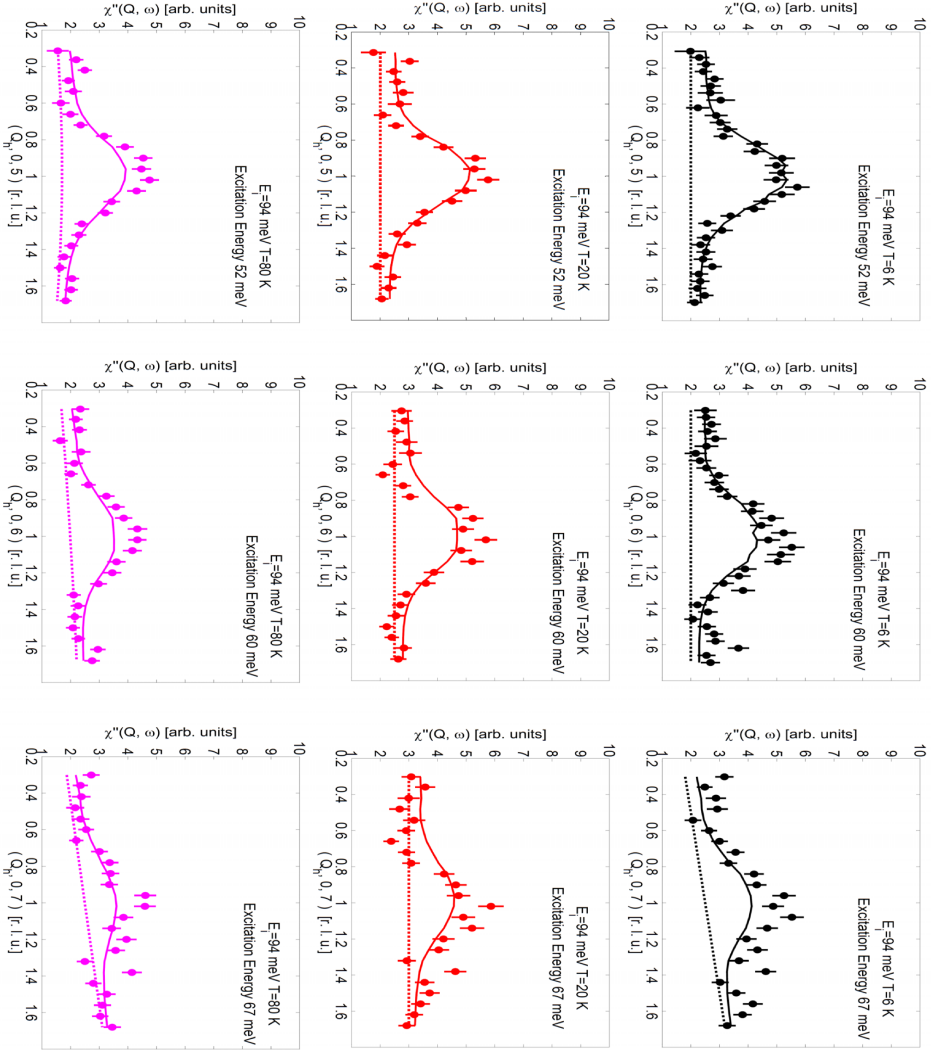


**Figure 5.12:** Collection of 1D constant energy cuts in  $\mathbf{Q}_h$ -direction through the spectrum of magnetic excitations with propagation vector  $\mathbf{Q}_{AFM}$ . The cuts were performed at energy transfers corresponding to magnetic zone center ( $L$ =odd) and zone boundary ( $L$ =even) reflections. The illustrated data were obtained at three different temperatures 6 K (black) and 20 K (red) and 80 K (magenta), representing three different phases in the phase diagram of  $\text{Ba}(\text{Fe}_{0.95}\text{Co}_{0.05})_2\text{As}_2$ . The solid lines illustrate the best fits of the local moment spin wave model to the data. Dashed lines illustrate non magnetic background contributions.

### 5.3.3 Spin Diffusion Model Analysis of Magnetic Excitations in the Paramagnetic State

In addition to the spin wave model, which is based on a local moment approach to magnetism, the paramagnetic spin excitations additionally have been analyzed in terms of a model based on spin diffusion effects. The idea of spin diffusion originates from the approach of the quasielastic response for nearly antiferromagnetic Fermi liquids [213, 214]. Here the term quasielastic means that the magnetic response of the system is diffuse and incoherent, where  $\chi''(\mathbf{Q}, \omega)/\omega$  is peaked for  $\omega = 0$  and thus no restoring force for spin waves exists and consequently no spin wave excitations occur. Based on the Fermi liquid theory the propagation of spin excitations in such materials works via spin diffusion. The mechanism of spin diffusion can be understood as the following, at high temperatures and with the absence of any long range magnetic order, the propagation of spin excitations is accomplished via an exchange process, where a given unit of spin is transferred from one atom to another. By a succession of these transfers from nearest neighbor atoms to nearest neighbor atoms the unit of spin, that started at the origin, arrives at distance  $\mathbf{r}$  at a probability, given by the theory of atomic diffusion. This spin diffusion model is valid for high temperatures, small propagation vectors and small energies, and in principle considers the propagation of spin excitations in the extreme opposite conditions to the spin wave model. As the spin wave model describes the propagation of spin excitations for the case of strong spin interactions, the diffusion model on the other hand regards a situation with almost no existing interactions, as it would be expected for a perfect paramagnet.

Most likely the model best suitable to explain the propagation of the paramagnetic spin excitations of the underdoped compound is located somewhere between these two extreme situations.

The quantitative number, the spin diffusion model, in the form it has been used in this study, can provide, is the in-plane coherence length  $\xi$  of the spin interactions. Prior to this study, the spin diffusion model has been applied on spin excitations in the paramagnetic phase of various Fe-based materials, such as undoped  $\text{CaFe}_2\text{As}_2$  [61] as well as optimal doped  $\text{Ba}(\text{Fe}_{1-x}\text{Co}_x)_2\text{As}_2$  [72, 74]. The success of those studies indicates that the model should also be applicable to the paramagnetic spin excitations in the underdoped compound. Equation (5.14) shows a version of the  $\mathbf{Q}$ -dependence of  $\chi''(\mathbf{Q}, \omega)$  expressed in terms of the spin diffusion model, as it was reported by Diallo et al. in their work on the paramagnetic phase of  $\text{CaFe}_2\text{As}_2$  [61],

$$\chi''(\mathbf{Q}, \omega) = \frac{\hbar\omega\gamma\chi_0}{(\hbar\omega)^2 + \gamma^2 \left\{ (q^2 + \eta q_x q_y) a^2 + \left( \frac{\xi_T}{a} \right)^{-2} + \eta_c [1 + \cos(\pi L)] \right\}^2} \quad (5.14)$$

where

- $a$  is the in plane lattice constant with  $a = b = 5.5 \text{ \AA}$

- $\xi_T$  defines the magnetic correlation length in Å for temperature T
- $\chi_0$  is the bulk magnetic susceptibility
- $\gamma$  labels the damping factor which originates from the decay of the spin fluctuations into single particle excitations
- $\eta$  is dimensionless and represents the in plane anisotropy of the spin correlations
- $\eta_c = J_c \chi_0$  represents the strength of the out of plane exchange coupling
- $\mathbf{q}$  is the propagation of the excitation mode, defined as  $\mathbf{Q} = \mathbf{Q}_{AFM} + \mathbf{q}$

With the introduction of two new temperature dependent parameters  $X_T = \chi_0(\frac{\xi_T}{a})^2$  and  $\Gamma_T = \gamma(\frac{a}{\xi_T})^2$  and the premise to neglect inter plane exchange coupling  $J_c = 0$ <sup>8</sup> equation (5.14) turns into

$$\chi''(\mathbf{Q}_{AFM}^{2D} + \mathbf{q}, \omega) = \frac{\hbar\omega\Gamma_T X_T}{(\hbar\omega)^2 + \Gamma_T^2 \left\{ 1 + q^2 \xi_{T\pm}^2 \right\}^2} \quad (5.15)$$

where  $\xi_{T+} = \xi_T(1 + \frac{\eta}{2})^{1/2}$  is the temperature dependent correlation length for the longitudinal direction (parallel to  $(H, 0, 0)$ ) and  $\xi_{T-} = \xi_T(1 - \frac{\eta}{2})^{1/2}$  in transverse direction (parallel to  $(0, K, 0)$ ). The temperature dependence of  $\xi$  is not so important for this study, since only data for one temperature will be considered.

Figures 5.15 and 5.16 show a collection of constant energy cuts, the same cuts previously used for the analysis using the spin wave model<sup>9</sup> (fig. 5.11), both in longitudinal and transverse direction. The solid red lines represent best fits of the diffusion model, as defined in equation (5.15).

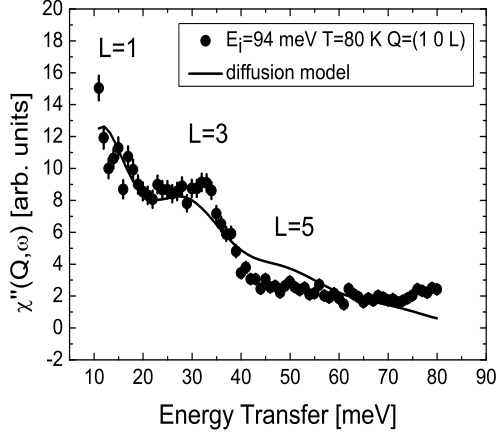
During the fitting process the damping factor  $\Gamma_T$  was held fixed to the value  $\Gamma_T = 11.3 \pm 1.5$  meV. This value was determined previously by fitting equation (5.14) to an energy cut, as illustrated in figure 5.13. For the fitting to the energy cut  $\Gamma_T$  provides the slope and  $\eta_c$  considers the antiferromagnetic out-of-plane correlations resulting in the peaks at 10 meV, 30 meV and 50 meV.

In order to fit  $\chi''(\mathbf{Q}_{AFM}^{2D} + \mathbf{q}, \omega)$  as expressed in (5.15) to the constant energy cuts, illustrated in figures 5.15 and 5.16, two parameters were free for variation,  $X_T$  and  $\xi_{T\pm}$ .  $X_T$  was used as a scale factor to handle peak intensities and since the data was not expressed in terms of absolute units the parameter had no further physical meaning.

<sup>8</sup>This may or may not be a reasonable assumption, depending on whether the values for  $J_c$  obtained via the spin wave model overestimate, as it is suggested by the results in ref. [40, 64, 212], or describe the interlayer exchange interactions in a reasonable way.

<sup>9</sup>The only difference is that for the present analysis the cuts were corrected for background contributions. For the spin wave analysis this was not necessary, because background contributions were considered during the fitting process.

**Figure 5.13:** Constant  $\mathbf{Q}$ -cut at the following  $\mathbf{Q}_h - \mathbf{Q}_k$  integration window  $\mathbf{Q}_h = 0.9 - 1.1$  [r.l.u.] ;  $\mathbf{Q}_k = -0.5 - 0.5$  [r.l.u.]. The displayed data was obtained for a temperature of 80 K and an incident neutron energy of 94 meV. The black solid line is the best fit of the diffusion model in the version of equation (5.14).



The second parameter  $\xi_{T\pm}$ , was used to modify the peak widths of  $\chi''(\mathbf{Q}_{AFM}^{2D} + \mathbf{q}, \omega)$  and thus represents the longitudinal and transverse correlation lengths of the spin interactions. All 20 longitudinal and transverse constant energy cuts, that were used for the data analysis, were treated separately and the resulting values for  $\xi_{T\pm}$  subsequently were used to determine an average value for the in-plane correlation lengths. During the process a correction for possible resolution effects was performed. A detailed description of this resolution correction can be found in the corresponding section in the appendix. The corrected and uncorrected results for both the in plane correlation length as well as the anisotropy parameter  $\eta = 2 \frac{\xi_{T+}^2 - \xi_{T-}^2}{\xi_{T+}^2 + \xi_{T-}^2}$  [61], which accounts for the anisotropy in correlation length between the two directions, longitudinal and transverse, are illustrated in table 5.3.

Even though, the mechanism of spin diffusion in principle should only be applicable for low excitation energies, the diffusion model provides a reasonable description of the paramagnetic excitations up to almost 70 meV. Especially for the longitudinal direction, where  $\chi''(\mathbf{Q}, \omega)$  is not split into two peaks but remains peaked at the antiferromagnetic wave-vector  $\mathbf{Q}_{AFM}$ , good fits are achieved over the whole energy range. In transverse direction the diffusion model works very well for energies below 40 meV. For energies higher than 40 meV the splitting into two peaks starts to become more evident, which creates some difficulties for the diffusion model. The spectral features described by the diffusion model are a single peak located at the antiferromagnetic wave vector  $\mathbf{Q}_{AFM}$ , with its half width half maximum (HWHM) depending on energy in the following way  $q_{HWHM}^2 = \xi^{-2}(\sqrt{2 + (\hbar\omega)^2\Gamma^{-2}} - 1)$  [74]. So, in order to consider the splitting into two peaks located in transverse direction, the model needed a slight

diffusion model	$\xi_{T+}$ [Å]	$\xi_{T-}$ [Å]	$\eta$
uncorrected	$11.5 \pm 0.4$	$6.2 \pm 0.3$	$1.10 \pm 0.06$
corrected	$12.5 \pm 0.4$	$6.6 \pm 0.3$	$1.13 \pm 0.07$
CaFe <sub>2</sub> As <sub>2</sub>	$8.0 \pm 1.0$	$6.0 \pm 1.5$	$0.55 \pm 0.36$
Ba(Fe <sub>0.926</sub> Co <sub>0.074</sub> ) <sub>2</sub> As <sub>2</sub>	$10.4 \pm 0.6$	$5.9 \pm 0.4$	$1.03 \pm 0.10$

double mode model	$\xi_{T+}$ [Å]	$\xi_{T-}$ [Å]	$\eta$	c [meVÅ]
uncorrected	$11.5 \pm 0.4$	$6.9 \pm 0.5$	$0.94 \pm 0.05$	
corrected	$12.5 \pm 0.4$	$7.6 \pm 0.5$	$0.92 \pm 0.06$	$260 \pm 10$
Ba(Fe <sub>0.926</sub> Co <sub>0.074</sub> ) <sub>2</sub> As <sub>2</sub>	$10.4 \pm 0.6$	$7.4 \pm 0.4$	$0.66 \pm 0.10$	$245 \pm 10$

**Table 5.3:** In-plane correlation lengths and anisotropy parameter obtained via fitting the diffusion and double mode model to 1D constant energy cuts, in longitudinal and transverse direction. All values are listed before and after correction for instrumental resolution effects. Data for CaFe<sub>2</sub>As<sub>2</sub> is taken from [61]. Correlation length values for Ba(Fe<sub>0.926</sub>Co<sub>0.074</sub>)<sub>2</sub>As<sub>2</sub> are taken from [74].

modification, which was done by incorporating an additional term that would provide the splitting of  $\chi''(\mathbf{Q}_{\text{AFM}}^{2D} + \mathbf{q}, \omega)$ . The new slightly modified double mode model reads as (5.16) [74].

$$\chi''(\mathbf{Q}_{\text{AFM}}^{2D} + \mathbf{q}, \omega) = \frac{\hbar\omega\Gamma_T X_T}{(\hbar\omega)^2 + \Gamma_T^2 \left\{ 1 + q^2 \xi_{T-}^2 - \frac{(\hbar\omega)^2 \xi_{T-}^2}{c^2} \right\}^2} \quad (5.16)$$

Since the difference between the diffusion model and the new double mode model is just the incorporation of an additional term, all parameters remain unchanged in their contribution including a constant damping factor  $\Gamma_T = 11.3$  meV and the two fitting parameters  $\xi_{T-}$  and  $X_T$ . However,  $\xi_{T-}$  now only considers the transverse correlation length, since the double mode model was only applied to the transverse cuts, where the splitting occurs. Consequently, the only new parameter in (5.16) is  $c$ , the excitation mode velocity, which represents the slope of the dispersion of the two modes in  $\mathbf{Q}$ -energy space and thus in (5.16) takes into account the increasing separation of the two peaks with increasing energy. In this model the splitting of the single peak into two peaks located in transverse direction is considered to be arising from two counter-propagating modes and not caused by a spin wave cone combined with anisotropic damping effects as discussed in the previous section. Prior to the fitting with (5.16), the value for  $c$  was determined by performing a linear fit to the  $\mathbf{Q}$ -energy-dispersion in the left panel of figure 5.14. This dispersion illustrates the evolution of the peak positions in  $\mathbf{Q}$ -space for increasing excitation energies (black data points). The corresponding peak positions were determined by fitting a set of two Voigt profile peaks to the transverse constant energy cuts. The resulting peak positions of the two Voigt profiles were then averaged



in order to eliminate anisotropic positions of the peaks in reference to  $\mathbf{Q}_{AFM}$ , and the averaged peak position then represented the final  $q$ -value shown in the figure.

Voigt profiles were used for the fitting in order to be able to consider any possible resolution related broadening effects, which could affect the exact determination of the real peak positions. A Voigt profile is created via a convolution of a Gaussian peak function and a Lorentzian peak function. By considering the Gaussian part as representing the  $\mathbf{Q}$ -dependence of the resolution function and the Lorentzian part to be representing the intrinsic signal from the sample, the Voigt profile can be thought of as an intrinsic signal convoluted by the instrumental resolution function. During the fitting process the width of the Gaussian was held fixed at a value, previously determined as the instrumental resolution for that particular energy transfer, and only the peak intensity and position, as well as the intensity, width and position of the Lorentzian part was free for variation.

The linear fit of  $\hbar\omega = cq$  to the dispersion of the two modes produced a mode velocity of  $c = 260 \pm 10 \text{ meV\AA}$ , which fits very well to the value for the transverse spin wave velocity  $\hbar v_b = 246.20 \pm 25.34 \text{ meV\AA}$  (listed in table 5.2), obtained in course of the spin wave model analysis. Knowing the correct value for  $c$  from the dispersion fit, had the advantage that it could be treated as a constant in the double mode model. This made it possible to treat each constant energy cut separately, because the energy dependent splitting of the peaks was already taken into account by  $c$ . Figure 5.15 shows a collection of transverse cuts including the best fits of the double mode model, which are visualized by the black solid lines. The fits show, that the double mode model indeed represents the data a little better than the diffusion model, due to the consideration of the peak splitting. However, admittedly the poor statistics of the 80 K data in principle allow both model descriptions, at least for the energy range that is covered by the present data. For higher energies the splitting is expected to become more prominent, which would clearly rule out the diffusion model.

The analysis with the double mode model produced a transverse correlation length of  $\xi_{T-} = 6.9 \pm 0.5 [\text{\AA}]$  and after resolution correction  $\xi_{T-} = 7.6 \pm 0.5 [\text{\AA}]$ . The resulting value for  $\xi_{T-}$  is slightly larger than the value obtained via the diffusion model, which is easy to understand when recalling that the correlation length is inversely proportional to the peak width and the double mode model uses two peaks to describe the data, in contrast to the single peak from the diffusion model.

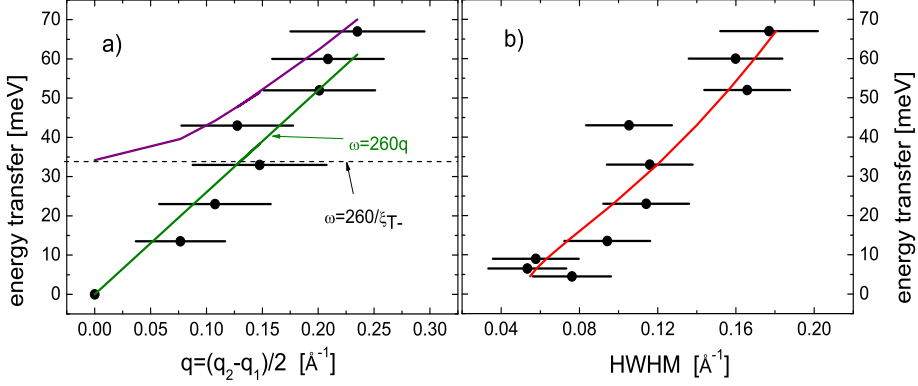


**Figure 5.14:** a) Energy dispersion of the peak positions in  $\mathbf{Q}_k$ -direction of the two propagating modes. Just one branch is shown, which was obtained through averaging and symmetrizing both branches. The peak positions were determined through Voigt profile fits to  $\mathbf{Q}_k$  constant energy cuts. The solid green line is a linear fit to the data, of  $\hbar\omega = c \cdot q$ . The solid purple line represents the peak positions determined via the double mode model  $q = \pm c^{-1} \sqrt{\omega^2 - c^2 \xi_{T-}^2}$ . b) Energy evolution of the longitudinal ( $\mathbf{Q}_h$ -direction) HWHM of the spin excitations located at  $(1, 0, L)$ . The HWHM were determined through Voigt profile fits and correspond to the Lorentzian HWHM of the Voigt profiles. The red solid line displays the HWHM predicted by the diffusion model  $q_{\text{HWHM}}^2 = \xi^{-2} (\sqrt{2 + (\hbar\omega)^2 \Gamma^{-2}} - 1)$ .

The left part of figure 5.14 illustrates the  $\omega$ -dependence of the peak positions, determined via the Voigt profile fits to the transverse cuts. The solid green line is the linear fit which was performed to receive the mode velocity  $c$ , whereas the solid purple line represents the peak positions, obtained via the double mode model  $q = \pm c^{-1} (\omega^2 - c^2 \xi_{T-}^2)^{1/2}$  [74]. Here  $\omega_d = c \xi_{T-}^{-1} = 33$  meV represents the lowest energy from which the splitting of the modes should become visible. In reality, however, a splitting is not visible below 50 meV. This effect must be ascribed to the poor experimental statistics of the data. The right part of figure 5.14 shows the energy evolution of the half width half maxima (HWHM) of the peaks in longitudinal direction, which were obtained via the diffusion model  $q_{\text{HWHM}}^2 = \xi^{-2} ((2 + (\hbar\omega)^2 \Gamma^{-2})^{1/2} - 1)$  (red solid line) and the HWHM of the Lorentzian parts of the Voigt profiles (black data points), which were fit to the longitudinal cuts in a way, where again the Gaussian part represented the resolution contribution and only the Lorentzian part was varied. Thus, the resulting Lorentzian HWHM are corrected for resolution effects and consequently can be compared to the resolution corrected HWHM from the diffusion model. Obvious from the figures, both models work really well in describing the excitation spectrum over the whole accessible energy range, regardless of the fact that in principle they

should only be applicable for low energies.

From table 5.3 it is obvious that the results obtained in this study fit very well to results reported in literature, from previous work on other 122 compounds. Especially the transverse correlation lengths  $\xi_{T-}$  are almost identical within the error bars for all three compositions. Whereas, the longitudinal correlation length  $\xi_{T+}$  is slightly larger than the reported values and fits much better to  $\xi_{T+}$  of optimal doped  $\text{Ba}(\text{Fe}_{0.926}\text{Co}_{0.074})_2\text{As}_2$  than of undoped  $\text{CaFe}_2\text{As}_2$ . This is not surprising as for  $\text{CaFe}_2\text{As}_2$  the spin excitations have a more elliptical shape in the  $(H, K, 0)$  reciprocal-plane, in contrast to the two split peaks that are present in the two  $\text{Ba}(\text{Fe}_{1-x}\text{Co}_x)_2\text{As}_2$  compounds. This elliptical shape results in a much shorter longitudinal correlation length in  $\text{CaFe}_2\text{As}_2$ , just about 2/3 of the value obtained in this analysis, and consequently a much smaller in plane anisotropy, just about half the value for this compound. As discussed in the previous section, it is not entirely clear if this splitting into two peaks observed for the Ba-compounds is due to two counter-propagating modes or due to anisotropic damping as proposed for the parent compound  $\text{BaFe}_2\text{As}_2$  [54, 74]. This anisotropic damping was not considered in the data treatment, but it would lead to a probably much shorter correlation length in  $H$ -direction, and most likely result in similar correlation lengths as observed in  $\text{CaFe}_2\text{As}_2$ . Nonetheless, aside from these small differences in longitudinal correlation length between the three compounds, the paramagnetic excitations in these three 122-materials, undoped, underdoped and optimal doped, still show tremendous similarities regarding the in-plane correlation lengths. Especially the transverse correlation length which is almost identical for all three materials, indicates that the paramagnetic excitations most likely are very similar for 122-materials regardless of their doping levels, just as proposed by Diallo et al. [61].

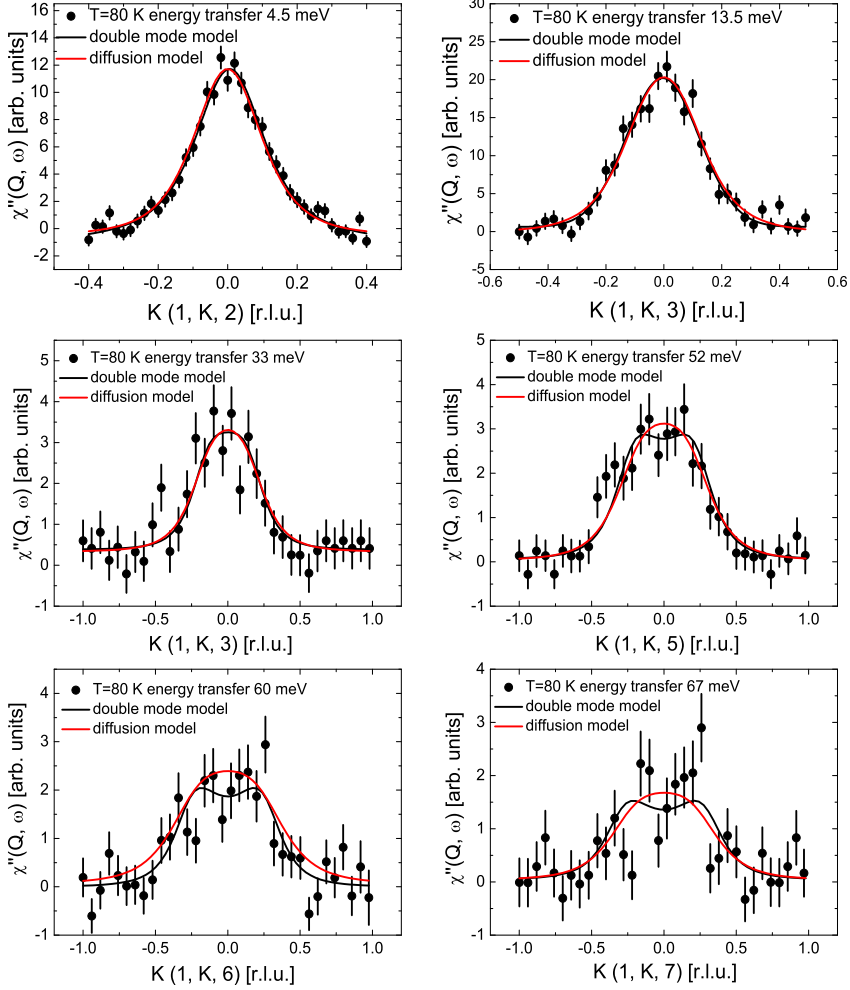


**Figure 5.15:** Collection of constant energy cuts in transverse  $\mathbf{Q}_k$ -direction. The cuts were performed at energy transfers corresponding to integer  $L$ -values of magnetic zone center ( $L$ =odd) and zone boundary ( $L$ =even) reflections and temperature 80 K. All data shown here are corrected for the thermal population factor and thus represent the wave-vector dependence of the dynamical magnetic susceptibility  $\chi''(\mathbf{Q}, \omega)$  of the system. The solid black line illustrates the best fit to the data of the double mode model, whereas the solid red line illustrates best fits of the diffusion model.

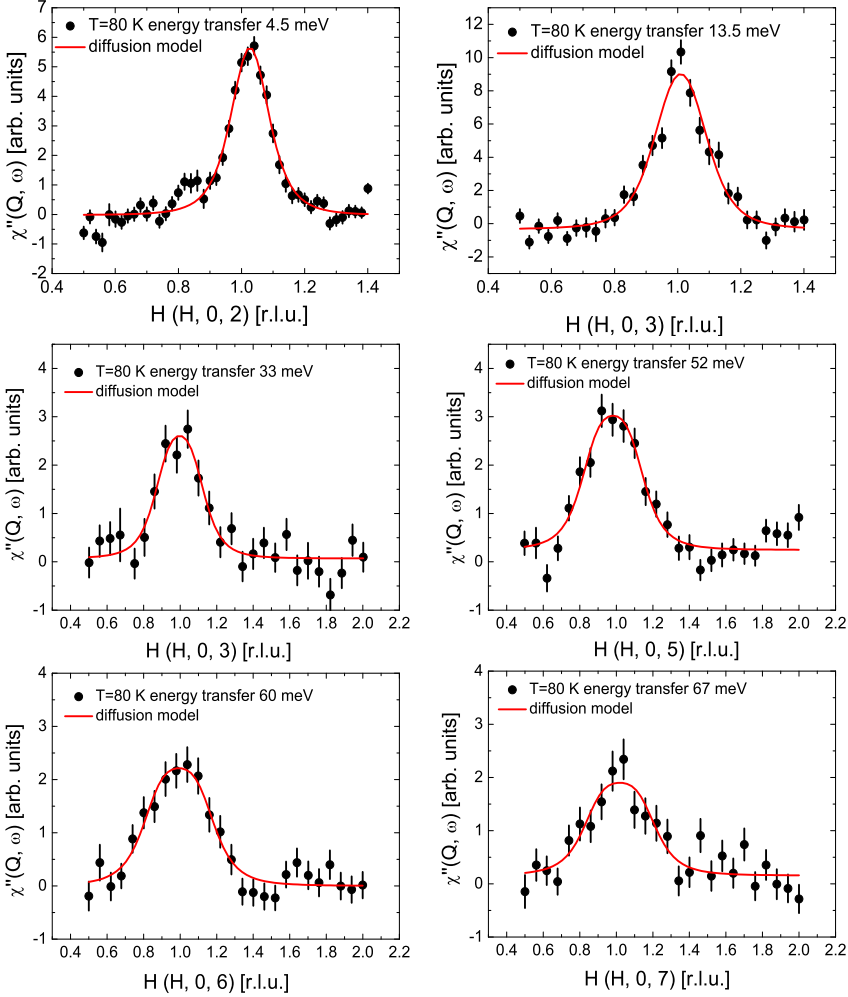


**Figure 5.16:** Collection of constant energy cuts in longitudinal  $\mathbf{Q}_h$ -direction. The cuts were performed at energy transfers corresponding to integer  $L$ -values of magnetic zone center ( $L$ =odd) and zone boundary ( $L$ =even) reflections and temperature 80 K. All data shown here were corrected for the thermal population factor and thus represent the wave-vector dependence of the dynamical magnetic susceptibility  $\chi''(\mathbf{Q}, \omega)$  of the system. The solid red line illustrates the best fit to the data of the diffusion model.

diffusion model	$\xi_{T+}$ [Å]	$\xi_{T-}$ [Å]
6 K	$14.4 \pm 0.5$	$7.8 \pm 0.3$
20 K	$14.6 \pm 0.4$	$7.6 \pm 0.4$
80 K	$12.5 \pm 0.4$	$6.6 \pm 0.5$
double mode model	$\xi_{T-}$ [Å]	
6 K	$8.9 \pm 0.5$	
20 K	$8.4 \pm 0.4$	
80 K	$7.6 \pm 0.4$	

**Table 5.4:** In-plane correlation lengths obtained via analysis of the spin diffusion and double mode model of 1D constant energy cuts, in longitudinal and transverse direction, as described in the previous section. All values are corrected for instrumental resolution effects.

### 5.3.4 Spin Diffusion Model Analysis of Magnetic Excitations in the Magnetically Ordered State

In addition to the paramagnetic phase the spin diffusion model was further applied to the magnetically ordered phase at 6 K and 20 K. As figures 5.17-5.20 clearly illustrate, both spin diffusion models give a reasonable description of the data even for the magnetically ordered phases. The correlation lengths obtained through the analysis with the diffusion and double mode model are just marginally different from the correlation lengths of the paramagnetic phase and also fit very well to the values reported in literature for other 122-materials, as listed in table 5.3. The slightly larger correlation lengths in the ordered phase is exactly what one would expect for an ordered phase, which in fact is characterized by the longer correlation length in comparison to the paramagnetic phase. Thus the interesting result is not the difference in correlation length between the ordered and paramagnetic phase, as this was expected, but rather the smallness of the difference of correlation lengths in the ordered and paramagnetic phase. However, this again fits very well to the results of the spin wave analysis, which already showed that the difference between excitations of the ordered and paramagnetic phase seemingly is rather small in this 5% underdoped material. This circumstance also fits very well to the fact that the spin diffusion model provides this good description of spin excitations in the ordered phase. As discussed in the previous section, the model of spin diffusion in principle is only suitable to describe magnetic excitations for high temperatures and consequently weak magnetic correlations and not for magnetically ordered phases with strong long range spin correlations. Thus, the fact that the model indeed is applicable to the excitations of the ordered state in this material indicates that the spin excitations in underdoped  $\text{Ba}(\text{Fe}_{0.95}\text{Co}_{0.05})_2\text{As}_2$  are not entirely spin wave like with strong spin interactions, as is the case for the undoped materials. Instead, the excitations show greater similarity to the short range spin fluctuations of the optimally doped materials, where spin excitations can be described by the spin diffusion model, even for low temperatures. However, since the spin wave model also provides a reasonable description of the data the spin excitations in

this underdoped composition need to be interpreted as to be of intermediate character, located between the spin wave like excitations of the undoped materials and the short range spin fluctuations of the optimally doped materials.

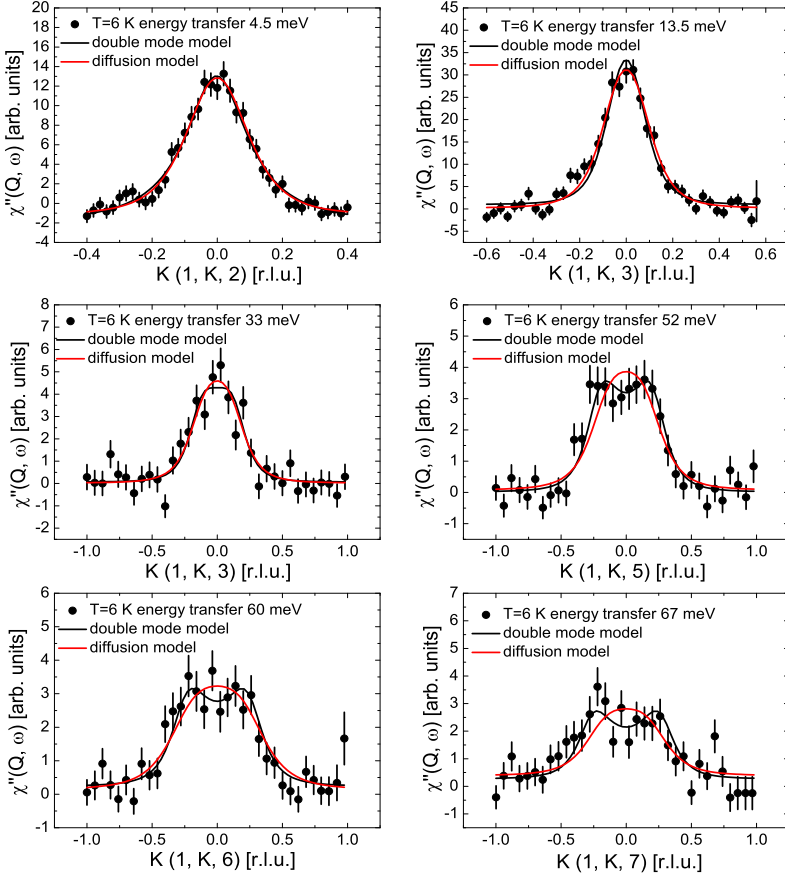


**Figure 5.17:** Collection of constant energy cuts in transverse  $\mathbf{Q}_k$ -direction. The cuts were performed at energy transfers corresponding to integer  $L$ -values of magnetic zone center ( $L$ =odd) and zone boundary ( $L$ =even) reflections and temperature 6 K. All data shown here are corrected for the thermal population factor and thus represent the wave-vector dependence of the dynamical magnetic susceptibility  $\chi''(\mathbf{Q}, \omega)$  of the system. The solid black line illustrates the best fit to the data of the double mode model, whereas the solid red line illustrates best fits of the diffusion model.

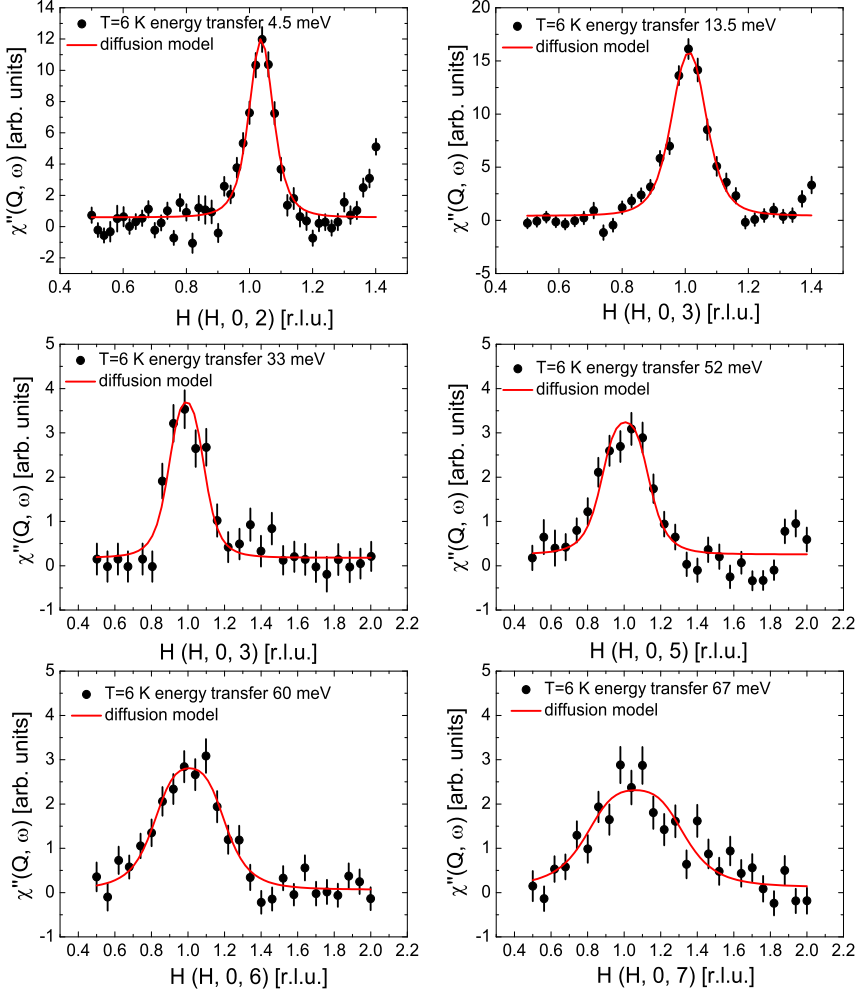


**Figure 5.18:** Collection of constant energy cuts in longitudinal  $\mathbf{Q}_h$ -direction. The cuts were performed at energy transfers corresponding to integer  $L$ -values of magnetic zone center ( $L=\text{odd}$ ) and zone boundary ( $L=\text{even}$ ) reflections and temperature 6 K. All data shown here were corrected for the thermal population factor and thus represent the wave-vector dependence of the dynamical magnetic susceptibility  $\chi''(\mathbf{Q}, \omega)$  of the system. The solid red line illustrates the best fit to the data of the diffusion model.



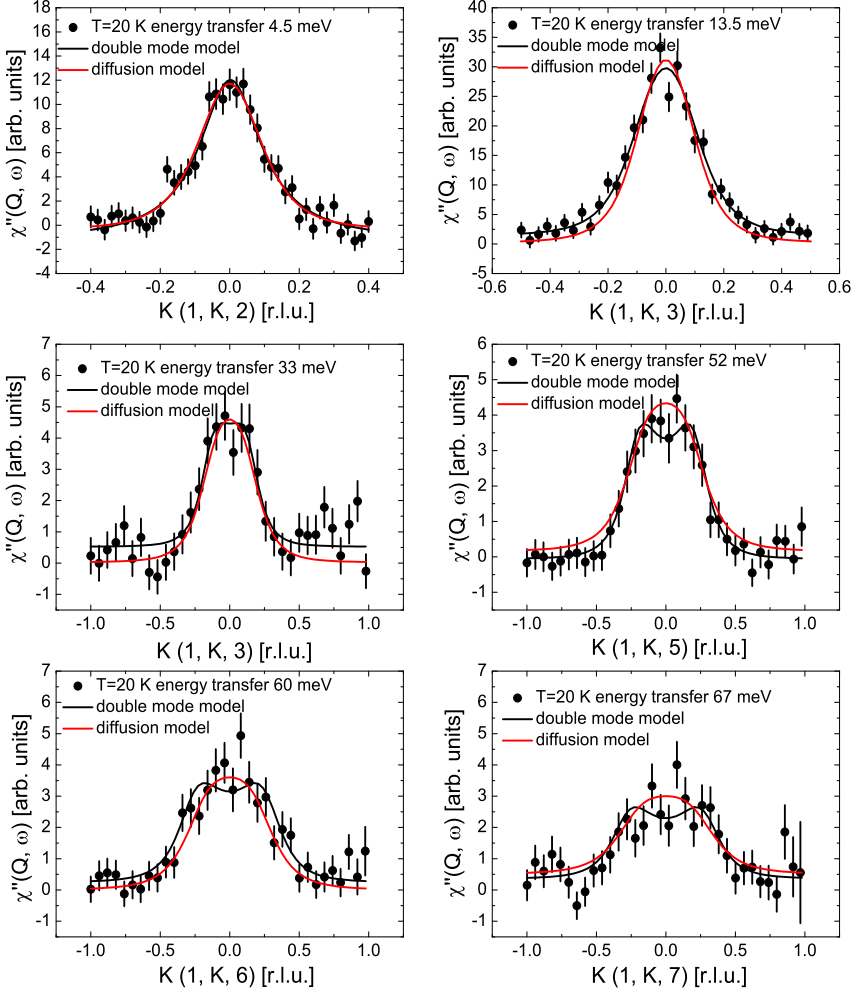


**Figure 5.19:** Collection of constant energy cuts in transverse  $\mathbf{Q}_k$ -direction. The cuts were performed at energy transfers corresponding to integer  $L$ -values of magnetic zone center ( $L$ =odd) and zone boundary ( $L$ =even) reflections and temperature 20 K. All data shown here are corrected for the thermal population factor and thus represent the wave-vector dependence of the dynamical magnetic susceptibility  $\chi''(\mathbf{Q}, \omega)$  of the system. The solid black line illustrates the best fit to the data of the double mode model, whereas the solid red line illustrates best fits of the diffusion model.

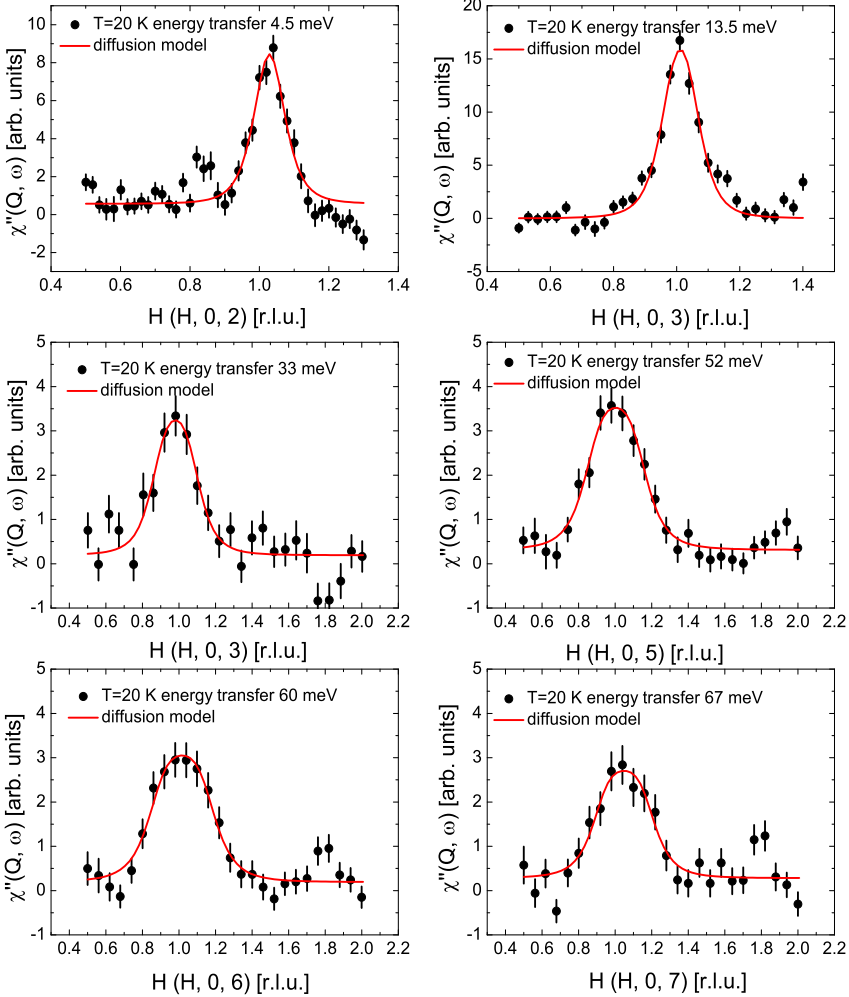


**Figure 5.20:** Collection of constant energy cuts in longitudinal  $\mathbf{Q}_h$ -direction. The cuts were performed at energy transfers corresponding to integer  $L$ -values of magnetic zone center ( $L=\text{odd}$ ) and zone boundary ( $L=\text{even}$ ) reflections and temperature 20 K. All data shown here were corrected for the thermal population factor and thus represent the wave-vector dependence of the dynamical magnetic susceptibility  $\chi''(\mathbf{Q}, \omega)$  of the system. The solid red line illustrates the best fit to the data of the diffusion model.

## 5.4 Conclusion

The spin excitation spectrum of under doped  $\text{Ba}(\text{Fe}_{0.95}\text{Co}_{0.05})_2\text{As}_2$  has been investigated by means of time-of-flight inelastic neutron scattering. Data has been obtained for the three phases of the phase diagram, the phase of coexistence of long range magnetic order and superconductivity, the phase of static magnetic order and the tetragonal paramagnetic phase.

It was possible to detect and thus confirm the existence of the spin gap in the excitation spectrum at  $\mathbf{Q}=(1, 0, L)$ , for energies below 4 meV. The observation of the spin gap can be ascribed to the suppression of particle hole excitations with energies less than  $2\Delta$  in the superconducting state, due to the opening of the superconducting gap. Thus, the occurrence of the spin gap in the underdoped compound fits very well the current understanding of spin excitations in the superconducting state.

In addition to the spin gap, a spin resonance signal has been observed. Unfortunately, the obtained results do not allow an unambiguous conclusion regarding the dimensionality of the spin resonance signal. The obtained results indicate a three dimensional spin resonance signal, as it is proposed for a 4% Co-doped Ba-122 composition [70]. In order to give a conclusive statement regarding this issue, however, further measurements are necessary. Similar needs to be said concerning a possible dispersion of the spin resonance signal. The results indicate a possible dispersion, similar to what has been reported for  $\text{Ba}(\text{Fe}_{0.96}\text{Co}_{0.04})_2\text{As}_2$  [70]. However, due to the set up of the experiment, which was not suited for this kind of investigation, a dispersing resonance cannot unambiguously be confirmed from the current results.

The linear spin wave model based on a local moment Heisenberg Hamiltonian, applied to the excitation spectrum, proved to provide a reasonable description of the spin excitations for energies up to 70 meV, and for all three temperatures. The best fit to the data was achieved for a strong anisotropy of the in-plane exchange parameters, similar to what has been reported for parent  $\text{BaFe}_2\text{As}_2$  [54]. The resulting in-plane coupling strengths are about 30% reduced to the ones reported for the undoped material. From the present data, however, it is not completely clear, if this reduced exchange coupling is a property of the underdoped compound or if it is resulting from the analysis of a data set, which was limited to low energy excitations. Recent neutron scattering results [58] suggest that a doping effect on the spin excitations in 122-compounds is restricted to excitation energies below 100 meV, whereas high energy excitations do not show a strong doping effect. If this is indeed the case, the present study most likely underestimates the strength of the in-plane exchange coupling of under doped  $\text{Ba}(\text{Fe}_{0.95}\text{Co}_{0.05})_2\text{As}_2$  materials. An extended investigation including the high energy part of the excitation spectrum of the underdoped compound would bring clarity to this point. Note that, due to devastating earthquake taking place in Japan on 11th March 2013 and which put a sudden end to our experiments it was not possible to complete the experiments as originally planned.

This plan included an investigation of the high energy part of the excitation spectrum with energies up to 200 meV. As a result, the obtained data miss the high energy part of the spectrum, and this resulted in a lot of uncertainties about the validity of the obtained results. As it became obvious through the course of this study and as it has been shown previously by other spin wave investigations on the Fe-based materials [54–56], in order to receive conclusive results on the spin wave excitation spectrum the high energy excitations need to be taken into account, as they provide valuable information which need to be included into the discussion.

The spin wave analysis performed for both magnetically ordered phases, above and below  $T_c$ , did not reveal any effect of superconductivity on the spin wave excitations of the SDW-order. Regardless of the effect superconductivity has on the static magnetic order, which shows in a reduction of elastic magnetic intensity for temperatures below  $T_c$ , the exchange coupling seemingly remains unaffected by the onset of superconductivity.

In addition to the magnetically ordered phase, the linear spin wave model further gave a reasonable description of magnetic excitations in the paramagnetic phase.

Additional to the spin wave model, two models, based on spin diffusion theory, were applied to the magnetic excitations in the paramagnetic phase. Both models are very well-suited to describe the paramagnetic excitations over the whole energy range that was accessible. By analyzing the data with the two spin diffusion models, it was possible to determine the in-plane correlation lengths of the paramagnetic spin excitations, in longitudinal and transverse direction. In reference to correlation lengths previously reported on parent and optimal doped 122-materials, the results for the transverse correlation length match the reported values very well. The results indicate that the in-plane properties of the low energy paramagnetic excitations of the 122-materials seem to be rather universal, and independent of the doping level. This of course does not include the in-plane splitting of the excitations observed in Ba-122 compounds, which still needs some clarification, whether it occurs due to anisotropic damping of the elliptical excitations or if it is caused by additional effects exclusively occurring in the Ba-122 compounds.

Interestingly the spin diffusion models were not only in good agreement with the magnetic excitations in the paramagnetic phase, but also lead to a reasonable description of the magnetic excitations in the magnetically ordered phase. This is very similar to the spin wave model, which was applicable to the ordered as well as the paramagnetic phase. The fact that both phases, ordered and paramagnetic phase, can be described by the same model shows that low energy excitations in both phases behave very similar, even if the long range static order is obviously broken down in the paramagnetic phase. The fact that both models, spin wave and spin diffusion, which in principle describe fundamentally different mechanisms, describe the magnetic excitations equally well, indicates that magnetic excitations in the 5% underdoped system are removed from the completely spin wave like character, of the undoped material. Instead, the magnetic excitations in  $\text{Ba}(\text{Fe}_{0.95}\text{Co}_{0.05})_2\text{As}_2$  are similar to the optimally doped materials, without magnetic order, where magnetic excitations can be described by the spin diffusion model, even at

low temperatures. However, the fact that the spin wave model still provides a reasonable description, shows that the spin wave character of the excitations is not completely suppressed yet. Instead, the spin excitations in underdoped  $\text{Ba}(\text{Fe}_{0.95}\text{Co}_{0.05})_2\text{As}_2$  need to be viewed as located between the spin wave like excitations of the Fe-SDW of the undoped materials and the short range fluctuations of the optimally doped materials, with contributions by both types of excitations.

# 6 ToF Neutron Scattering on Magnetic Excitations in $\text{CaFe}_{1-x}\text{Co}_x\text{AsF}$ with $x=0$ ; $x=0.12$

Parts of this chapter have been used to create a publication.

Price et al., *Journal of the Physical Society of Japan* **82**, 104716 (2013)

Note that all work considering this chapter, including execution of the experiment and data treatment as well as the writing and the creation of all figures was done by myself.

## 6.1 Introduction

### 6.1.1 Motivation

As it has been discussed in chapter 2, the occurrence of the spin resonance is believed to be intimately correlated to the symmetry of the superconducting gap function. Due to this circumstance an investigation of the resonance signal can provide some deeper insight to the pairing mechanism of the Cooper pairs. So aside from the microscopic nature of the spin resonance signal, which is still unknown and an interesting subject of study in itself but might not contribute much to a better understanding of superconductivity, a search for the resonance signal in new materials is important, because of its direct information on the present pairing symmetry. And this indeed is an important aspect regarding the pairing mechanism. To this date, the  $s_{\pm}$  gap symmetry with a sign change of the gap function between hole and electron Fermi surfaces is believed to be the gap symmetry present in the Fe-based materials. It is further discussed that this gap symmetry might be a universal feature and therefore might occur in all Fe-based superconductors. As a consequence, a spin resonance signal should also be observable in all Fe-based materials. Superconducting  $\text{CaFe}_{1-x}\text{Co}_x\text{AsF}$  was one material for which a spin resonance signal had not been observed yet, and so one focus of this study is to search for a possible resonance signal in this material.

Aside from the superconducting materials, gaining a complete understanding of the magnetic properties of the undoped Fe-based materials is another very important task in order to eventually understand a possible interplay between magnetism and super-

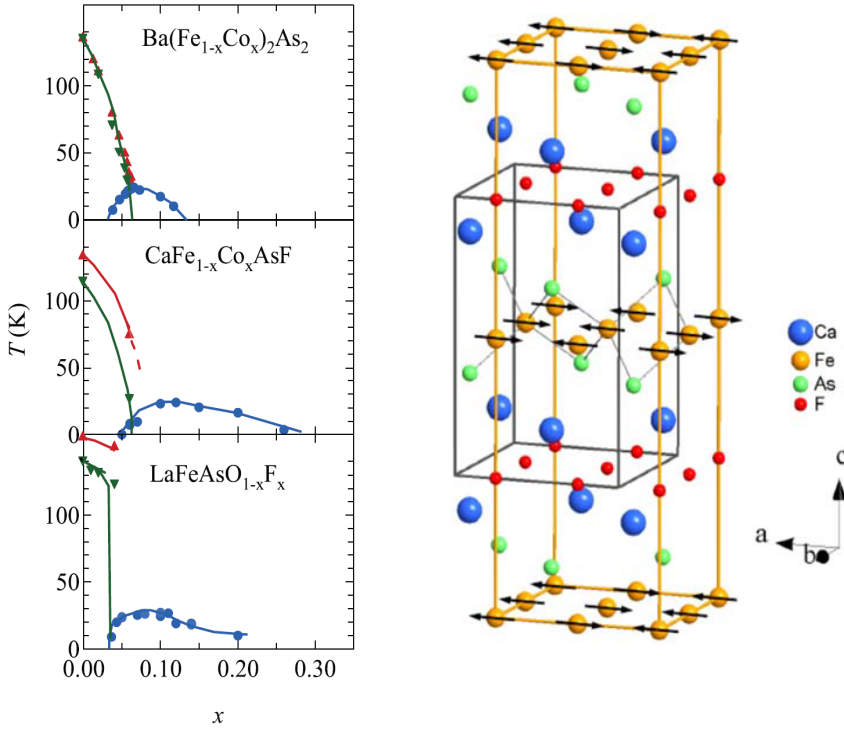


**Figure 6.1:** (left panel) Phase diagrams of  $\text{Ba}(\text{Fe}_{1-x}\text{Co}_x)_2\text{As}_2$  and  $\text{LaFeAsO}_{1-x}\text{F}_x$  compared to  $\text{CaFe}_{1-x}\text{Co}_x\text{AsF}$ . (right panel) Crystal structure plus structure of long range SDW-order of Fe-moments for  $\text{CaFeAsF}$ , obtained via neutron powder diffraction Left panel is taken from [45], whereas right panel is taken from [215].

conductivity. In this context ToF neutron scattering investigations on the spin wave excitations of the SDW order and the collective excitations of the paramagnetic phase in undoped  $\text{CaFeAsF}$  have been performed. The results from this study will be discussed in the current chapter.

### 6.1.2 Basic Properties of $\text{CaFe}_{1-x}\text{Co}_x\text{AsF}$ Materials

$\text{CaFeAsF}$  drew attention as the parent compound of superconducting materials with the highest  $T_c$  of all Fe-based superconducting materials, with  $\text{Ca}_{0.4}\text{Pr}_{0.6}\text{FeAsF}$   $T_c=52.8$  K and  $\text{Ca}_{0.4}\text{Nd}_{0.6}\text{FeAsF}$  with  $T_c=57.4$  K [216]. Aside from replacing Ca by rare earth elements Nd and Pr, doping the Fe-site by either cobalt, nickel or rhodium is another method to suppress the long range Fe-SDW wave order and induce superconductivity to

the system [45, 217–219]. Compared to the Nd- and Pr-doped compounds, the superconducting transition temperatures for the latter compounds are not very impressive, with  $T_c=16$  K (Rh-doped),  $T_c=12$  K (Ni-doped) and  $T_c=22$  K (Co-doped). However, sample availability is a factor which makes these compounds attractive again.

$\text{CaFeAsF}$ , the parent compound of the  $\text{CaFe}_{1-x}\text{Co}_x\text{AsF}$  series, crystallizes in the  $\text{ZrCuSiAs}$ -type structure with tetragonal space group  $P4/nmm$  and room-temperature lattice constants of  $a=3.879$  Å and  $c=8.593$  Å [218]. According to Xiao et al. [215] the crystal structure undergoes a structural phase transition at  $T_S=134$  K, where it lowers its symmetry from tetragonal to orthorhombic with space group  $\text{Cmme}$ . At 114 K the structural phase transition is followed by a magnetic phase transition due to the onset of the antiferromagnetic Fe-SDW order with propagation vector  $\mathbf{Q}_{AFM}=(0.5, 0.5, 0.5)$ , in tetragonal notation [215]. The in-plane components of the propagation vector  $\mathbf{Q}_{AFM}$  match the nesting vector  $\mathbf{Q}_{nesting}=(0.5, 0.5, 0)$  which connects parts of the Fermi surface, the electron and hole cylinders located at the M and  $\Gamma$  points, respectively [220]. Just as in other Fe-based superconductors, the predominant conduction bands in the proximity of the Fermi-energy are the Fe 3d bands. This suggests that also in  $\text{CaFe}_{1-x}\text{Co}_x\text{AsF}$  superconductivity is predominantly carried by the Fe-charge-carriers and thus very likely is restricted to the Fe-As layers.

In the antiferromagnetic phase below 114 K  $\text{CaFeAsF}$  exhibits an ordered Fe-moment of  $\sim 0.49 \mu_B$ , which is substantially larger than ordered moments observed for other 1111-materials like the  $\sim 0.35 \mu_B$  observed for  $\text{LaFeAsO}$  and  $\sim 0.25 \mu_B$  for  $\text{NdFeAsO}$ , but smaller than for the Sr-equivalent  $\text{SrFeAsF}$  ( $\sim 0.58 \mu_B$ ) [221].

With introduction of additional electrons to the system, in this case by doping cobalt into the Fe-layers, the antiferromagnetic Fe-SDW gets suppressed and the system becomes superconducting for a cobalt concentration of  $\sim 5\%$ . For this Co-doping concentration, the materials exhibit a coexistence of superconductivity and static antiferromagnetic order, similar to what has been observed in other 1111- and 122-materials [36–44]. The nature of this seeming coexistence in  $\text{CaFe}_{1-x}\text{Co}_x\text{AsF}$  is not entirely clear, as contrary results are reported, with proposed phase coexistence [45] as well as phase separation [44] as possible explanations. In addition to the weakened magnetic order, the structural tetragonal-orthorhombic phase-transition is pushed down to 75 K [45] with an orthorhombic distortion of  $P=(a-b)/(a+b)=0.17\%$ , which is about half the orthorhombic distortion present in the undoped compound. This might suggest a relation between ordered moment size and orthorhombic distortion, with stronger distortion leading to a larger ordered moment [215]. Aside from the reduced orthorhombicity due to doping, the crystal seems very robust against introduction of cobalt, as the lattice constants of the room temperature tetragonal phase only vary very little with increasing Co-concentration, with  $a=3.88$  Å and  $c=8.578$  Å for 5% Co-content and  $a=3.88$  Å and  $c=8.552$  Å for 10% Co-doping [218]. For  $\sim 10\%$  of introduced Co the system is optimally doped and reaches its maximum  $T_c = 22\text{K}$  [218], and the Fe-SDW as well as the orthorhombic distortion are completely suppressed.



## 6.2 Experimental Details

Two powder samples of  $\text{CaFe}_{1-x}\text{Co}_x\text{AsF}$  with doping levels of  $x = 0$  and  $x = 0.12$  have been investigated by means of the time-of-flight (ToF) inelastic neutron scattering technique. The powder samples of approximately 9 g each were synthesized by a solid state reaction method as described in [217] by collaborating scientist Dr. S. Matsuishi of the Frontier Research Center, Tokyo Institute of Technology, 4259 Nagatsuta-cho, Midori-ku, Yokohama 226-8503, Japan. The samples were very clean with impurity phases ( $\text{CaFe}_2$  and  $\text{Fe}_2\text{O}_3$ ) for both samples of less than 1%. The time-of-flight neutron scattering experiments were performed on the Fermi chopper spectrometer MERLIN at the ISIS facility [222], where data sets were obtained for two different incident neutron energies of  $E_i = 20$  meV and  $E_i = 50$  meV and sample temperatures between 6 K and 270 K. The intensity spectra were azimuthally averaged (powder average) and transformed into a  $Q$ -energy grid, as illustrated in figures 6.2. The intensity shown in these plots can be expressed in terms of the double differential cross section  $d^2\sigma/d\Omega_f dE_f$  multiplied by the factor  $(k_i/k_f)$  which relates the cross section to the dynamical structure factor  $S(\mathbf{Q}, \omega) = (k_i/k_f) d^2\sigma/d\Omega_f dE_f$ , with  $k_i$  and  $k_f$  representing the initial and final neutron wave vector  $k$ ,  $E$  the neutron energy  $\Omega$  the solid angle of the scattering process. To place the obtained data sets on an absolute intensity scale with units  $\text{mb sr}^{-1} \text{ meV}^{-1} \text{ f.u.}^{-1}$  ( $\text{sr}$ =steradian,  $\text{f.u.}$ =formula unit) the spectra were normalized to intensities obtained from a vanadium standard sample. To transform the obtained data sets into the imaginary part of the magnetic susceptibility  $\chi''(Q, \omega)$  the data were corrected for non magnetic background contributions as well as the thermal population factor. For the visualization of the 2D  $S(\mathbf{Q}, \omega)$  maps and the creation of the 1D constant energy and constant  $Q$  cuts the MSLICE program [207] was used. Throughout this chapter, the tetragonal notation will be used which leads to the antiferromagnetic wave vector of the magnetic excitations of the Fe-moments to read as  $\mathbf{Q}_{AFM}=(0.5, 0.5, 0)$ .

## 6.3 Results and Discussion

### 6.3.1 Magnetic Excitations in Superconducting $\text{CaFe}_{0.88}\text{Co}_{0.12}\text{AsF}$

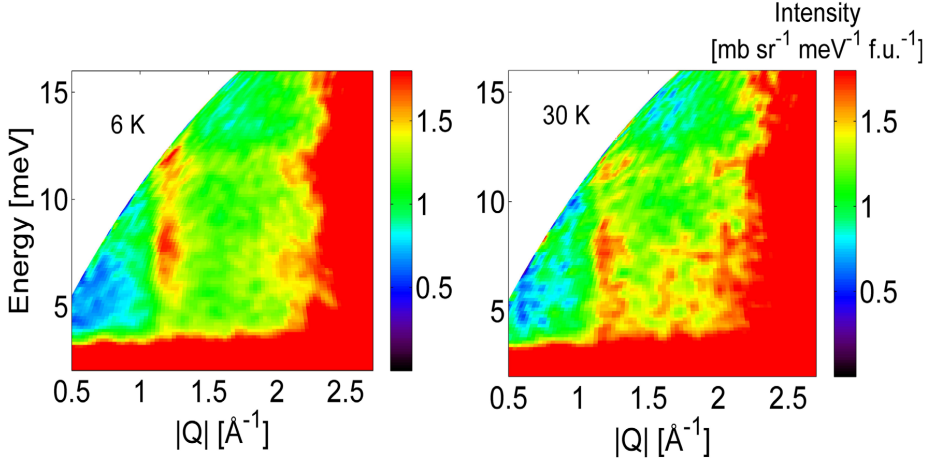


**Figure 6.2:**  $Q$ -energy spectra of the dynamical structure factor  $S(Q, \omega)$  of superconducting  $\text{CaFe}_{0.88}\text{Co}_{0.12}\text{AsF}$ , obtained via time-of-flight neutron scattering measurements with 20 meV incident neutron energy and sample temperatures of 6 K (left) and 30 K (right) on a 9 g powder sample. The rod like signal located at  $Q \sim 1.2^{-1}$  is identified as arising from short range antiferromagnetic spin fluctuations with propagation vector  $\mathbf{Q}_{AFM} = (0.5, 0.5, 0)$ .

Left and right panels in figure 6.2 are two dimensional (2D) color plots of the dynamical structure factor  $S(\mathbf{Q}, \omega)$  as a function of the absolute value of the momentum transfer  $Q = |\mathbf{Q}|^1$  and energy transfer  $\omega$  at 6 K (left panel) and 30 K (right panel), below and above  $T_c = 22$  K of optimally doped  $\text{CaFe}_{0.88}\text{Co}_{0.12}\text{AsF}$ . The feature of interest is the vertical, rod like signal rising from a momentum transfer  $Q \sim 1.2 \text{ \AA}^{-1}$ . The reciprocal lattice position of this  $Q$  value roughly corresponds to  $(0.5, 0.5, 0)_T$  in tetragonal notation, which can be associated with the nesting vector, connecting the hole and electron Fermi surfaces [220], and with the propagation vector  $\mathbf{Q}_{AFM} = (0.5, 0.5, 0)$  of the quasi two dimensional spin fluctuations present in all Fe-based superconducting materials. The fact that the signal appears at a slightly higher  $Q$  value compared to the theoretical value for the antiferromagnetic AFM wave vector  $Q_{(0.5, 0.5, 0)} = 1.10 \text{ \AA}^{-1}$ , can

<sup>1</sup>Because of the arbitrary distribution of grains in the polycrystalline sample, the obtained intensity is distributed on rings, the so called Debye Scherrer rings, where the radius of these rings is correlated to the absolute value of the scattering vector. This eliminates all directional information and leaves the absolute value of  $\mathbf{Q}$  the only spatial information of the measurement.

be attributed to powder averaging and resolution effects of the raw data, as both effects can cause the signal to appear at slightly higher  $Q$  values. For a more detailed explanation of this effect please turn to reference [223]. In regard of this deviation from the theoretical value due to averaging effects  $Q \sim 1.2 \text{ \AA}^{-1}$  is identified as the AFM wave vector  $\mathbf{Q}_{AFM}=(0.5, 0.5, 0)$ .

The observed signal noticeably decreases in intensity and broadens significantly with increasing temperature, but still persists up to 150 K (Fig. 6.3 (f)), which was the highest temperature at which data has been collected for this compound. In addition to the temperature dependence, the signal exhibits a strong momentum-dependence, as intensities for higher indexed reflections are strongly suppressed. The obtained data shows no indications of the second Brillouin zone excitation mode, which would be expected to occur at a  $Q$  position close to  $2.5 \text{ \AA}^{-1}$ , corresponding to the reciprocal lattice position  $(0.5, 1.5, 0)$ . The observed temperature- and  $Q$ -dependencies are strong indications that the observed signal indeed is of magnetic nature. Since phonon scattering intensities show an exact opposite temperature and wave vector dependence, where increasing temperature and increasing momentum transfers lead to increasing scattering intensities, the signal at  $Q \sim 1.2 \text{ \AA}^{-1}$  is identified as arising from short range quasi two dimensional AFM spin fluctuations with a propagation vector  $\mathbf{Q}_{AFM}=(0.5, 0.5, 0)$ , a prominent feature of the superconducting state of all iron based superconductors.

In the superconducting state, the excitation spectrum (Fig. 6.2 left) consists of two prominent peaks, with enhanced spectral weight between 5-10 meV plus for the region around 12 meV. For energies below 5 meV the spectrum is gapped, as magnetic intensity is strongly suppressed, almost to the non-magnetic background level. As will be shown later, the gap below 5 meV and the peak between 5-9 meV correspond to the spin gap and spin resonance, two prominent features of spin excitation spectra in the superconducting state of Fe-based materials. In contrast, the region of enhanced excitations around 12 meV very likely is not due to an enhancement of magnetic excitations but rather originates from an overlap of the very steep almost vertically dispersing magnetic excitations and a very flat almost horizontally dispersing phonon branch, which is still visible in the color maps in figure 6.2 and even stronger visible in the maps of the undoped  $\text{CaFeAsF}$  composition in figure 6.8. A similar effect has also been reported for undoped  $\text{LaFeAsF}$  where a horizontal dispersing phonon branch close to 12 meV interferes with the vertical dispersion of magnetic excitations [224]. This phonon theory is further supported by phonon density of states (DOS) measurements by Mittal et al. on  $\text{CaFeAs}_{1-x}\text{Co}_x\text{F}$ , using the very same sample which was used for the experiments presented in this study. There the authors report a very weakly dispersing phonon branch located around 12 meV [225], which is capable to explain the observed enhancement in intensity in figure 6.2.

In the normal state the spin excitation spectrum (Fig. 6.2 right) is not that obviously

---

<sup>2</sup>Unfortunately, this  $Q$ -range of the spectrum is highly dominated by strong phonon intensities, which make it impossible to detect the weak magnetic signal.

separated from the non-magnetic background, as strong non magnetic intensity occurs for momentum transfers between 1.5 and 2  $\text{\AA}^{-1}$ . Nonetheless, the rod-like excitation spectrum can still be identified. In contrast to the superconducting phase, however, the spectrum is not gapped for energies below 5 meV and the enhanced excitations around 7 meV and 12 meV are still present but not as prominent as for the superconducting state.

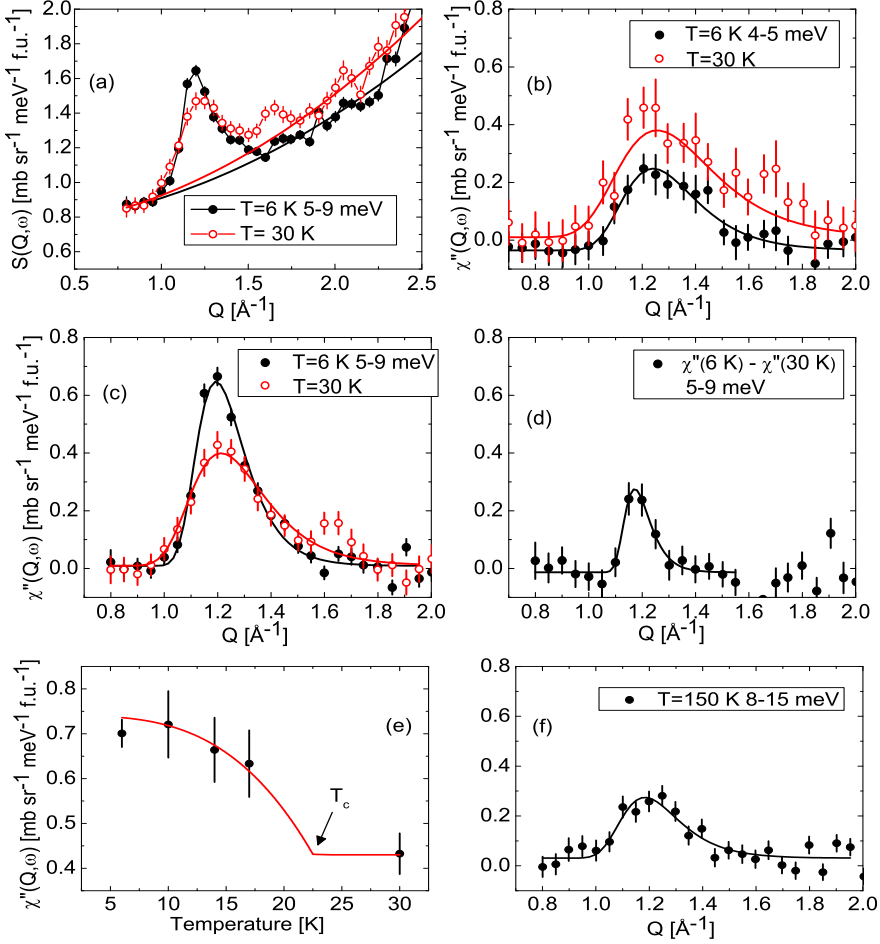
To investigate the low energy spin excitations located at  $Q \sim 1.2 \text{\AA}^{-1}$  in more detail several constant energy and constant  $Q$  cuts of the 2D  $S(Q, \omega)$  intensity maps were performed, for both temperatures 6 and 30 K. The constant energy cuts were performed with two different energy integration windows, 4-5 meV and 5-9 meV, respectively. The 4-5 meV window covers the spin gap region, whereas the 5-9 meV window covers the spin resonance region of the spectrum. To extract the purely magnetic signal from non-magnetic background contributions, a quadratic background function was subtracted from the constant energy cuts, taking into account the  $Q^2$ -dependence of phonon scattering intensities (Fig. 6.3 (a)). After background subtraction, the data were corrected for the thermal population factor and according to the fluctuation-dissipation-theorem [159, 160]  $S(Q, \omega)$  was transformed into  $\chi''(Q, \omega)$ , the imaginary part of the magnetic susceptibility,

$$\chi''(Q, \omega) = S(Q, \omega) \cdot (1 - \exp(-\frac{\hbar\omega}{k_B T})).$$

This provides the possibility to compare peak intensities obtained for different temperatures, as the correction for the thermal population factor corrects the intensities for all trivial temperature effects.

Figure 6.3 (c) illustrates the wave vector dependence of the dynamical susceptibility for temperatures of 6 (black dots) and 30 K (red dots) and the energy range 5-9 meV. For both temperatures  $\chi''(Q, \omega)$  exhibits a clean but slightly asymmetric peak centered around momentum transfer  $Q_{AFM} = 1.2 \text{\AA}^{-1}$ . The slight tail both peaks feature on the higher  $Q$  side, is an indication of the two dimensionality of the present spin fluctuations and is caused by powder averaging effects of the quasi two dimensional magnetic excitations<sup>3</sup> [223]. The peak in the superconducting state is marginally narrower compared to

<sup>3</sup>Two dimensionality means in this case, that the present magnetic Fe-Fe correlations are restricted to within the Fe-As layers and are lacking correlations between neighboring Fe-As layers along the crystallographic c-direction. As a consequence, the scattering intensities of (H, K, L)-reflections exhibit no L-dependence, aside from the gradually decrease of intensity for higher  $Q$ -values due to the magnetic form-factor decay. A Debye-Scherrer ring originating from scattering from such two-dimensional excitation exhibits one clear inner edge towards small  $Q$  and one diffuse outer edge towards larger  $Q$ . This means, the ring has a hard limit for the smallest  $Q$  that contributes to that ring, corresponding to the e.g.  $Q=(H, K, 0)$ -reflection. Smaller  $Q$  values do not correspond to the same reflection anymore and thus do not contribute to that particular ring. However, since the signal is two dimensional, lets say without correlation along  $L$ , larger  $Q$ s with  $Q=(H, K, L \neq 0)$  all still contribute to the same (H, K, 0) reflection. The intensity for these (H, K,  $L \neq 0$ ) decays gradually with increasing  $L$ , because of the form-factor decay, and so the intensity collected in the outer edge of (H, K, 0) ring fades away with increasing  $Q$  but does not show a clear edge. Thus, for



the 30 K data which could indicate a possible gain in correlation length of the interacting spins when the system becomes superconducting. However, this could also be a side effect from the enhancement of magnetic spectral weight. The most striking difference between the superconducting and normal state data, however, is the clear enhancement of the peak intensity in the superconducting state as the spectral weight for this energy region (5-9 meV) is enhanced by a factor of 1.5 relative to the normal state value. This relative enhancement is comparable to the factor observed in other pnictide systems for the intensity enhancement of the resonance signal [71, 128, 226]. Since the data is corrected for the thermal population factor this enhancement cannot be explained by temperature effects but must be ascribed to the onset of superconductivity, which clearly relates the additional spectral weight to the resonance signal. This is further supported by the typical temperature dependence of the signal, as illustrated in figure 6.3 (e). As expected for the resonance signal, the enhanced spectral weight gradually decreases with temperature and follows an order parameter like temperature dependence as it disappears close to  $T_c$ . As a result, this enhancement in spectral weight for 6 K is identified as the spin resonance appearing at the AFM wave-vector  $Q_{AFM}=(0.5, 0.5, 0)$  and excitation energies between 5 and 9 meV.

Below 5 meV the excitation spectrum in the superconducting state exhibits a prominent reduction of spectral weight as  $\chi''(Q, \omega)$  is reduced in intensity below the level of the normal state excitations at 30 K, (Fig. 6.3 (b)). Even though magnetic intensities are not completely suppressed for this energy region, a sizeable shift of spectral weight from the gap region to the resonance region of the spectrum is obvious. In contrast to this, the spectrum of the normal state excitations at 30 K does not show such a transfer of spectral weight and peak intensities for the energy windows 4-5 meV and 5-9 meV are almost identical. Consequently, the strong suppression of  $\chi''(Q, \omega)$  at 6 K and 4-5 meV is interpreted as indications of the opening of the spin gap, even if magnetic intensities are not suppressed completely. Due to strong contributions by the elastic line, it was not possible to investigate the excitation spectrum below 4 meV in order to clarify whether magnetic intensities are suppressed even further and whether the gap opens completely for energies below 4 meV. Nevertheless, the suppression of  $\chi''(Q, \omega)$  for  $T=6$  K and energy transfer between 4-5 meV is a clear indication for the existence of the spin gap.

To illustrate the energy dependence of the spin excitation spectrum in a more detailed way, constant  $Q$  cuts of the 2D  $S(Q, \omega)$  maps (Fig. 6.4 (a), (b)) were performed with an energy step size of 1 meV and two integration ranges of  $Q=1.1-1.3 \text{ \AA}^{-1}$  and  $Q=1.5-1.6 \text{ \AA}^{-1}$ , respectively. These  $Q$  values were chosen as  $Q=1.1-1.3 \text{ \AA}^{-1}$  covers  $Q_{AFM}$ , whereas  $Q=1.5-1.6 \text{ \AA}^{-1}$  is used to consider the non magnetic background since, especially

---

a  $Q$  cut through one ring, the cut exhibits an asymmetrical peak shape, with the high  $Q$ -side of the peak showing this tail like shape which decays slower than the small- $Q$  side of the peak. For further reading on this topic [223].

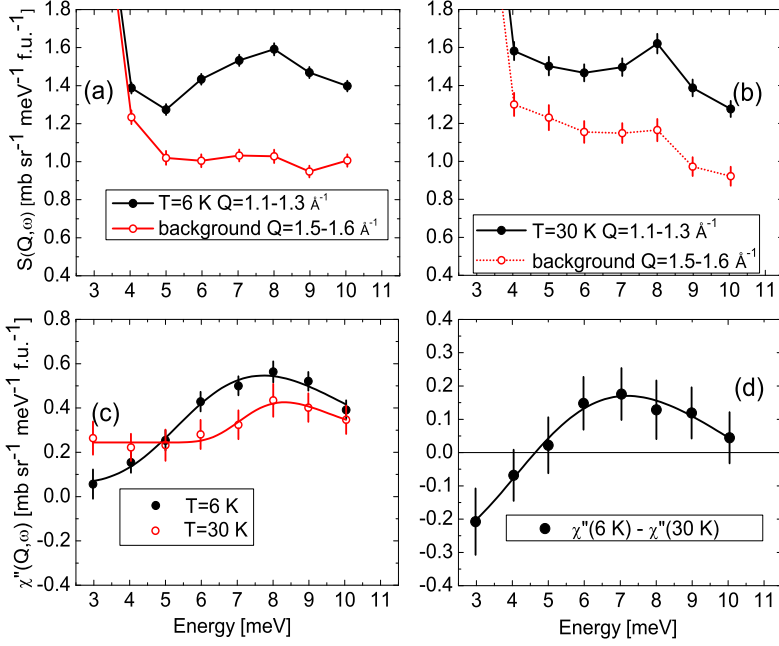


**Figure 6.4:** Constant  $Q$  cuts at temperatures 6 K (a) and 30 K (b) for  $Q$  ranges  $1.1-1.3 \text{ \AA}^{-1}$  (black dots), covering the magnetic signal, and  $1.5-1.6 \text{ \AA}^{-1}$  (red open symbols) representing the non magnetic background. The intensities of the background cuts were corrected to the level for a  $Q$  position of  $Q=1.2 \text{ \AA}^{-1}$  by using the  $Q$  quadratic background function applied for the constant energy cuts. (c) Energy dependence of the imaginary part of the magnetic susceptibility  $\chi''(Q, \omega)$  for 6 K (black dots) and 30 K (red open symbols).  $\chi''(Q, \omega)$  was obtained by subtracting background cuts from the signal cuts and correcting the data for the thermal population factor. (d) The  $\chi''(6 \text{ K}) - \chi''(30 \text{ K})$  temperature difference spectrum. Black and red solid lines in (c) and (d) are fits with asymmetric peak functions and serve as guides to the eye.

in the 30 K plots, strong phonon intensities appear for momentum transfers between  $1.4$  and  $2 \text{ \AA}^{-1}$ , and which need to be considered as eventual inadvertent contributions to the magnetic signal. The intensities of the background cuts were then corrected to a level corresponding to a  $Q$  value of  $Q=1.2 \text{ \AA}^{-1}$  by taking advantage of the quadratic background-function, which was previously used to determine the non magnetic background for the constant energy cuts.

Figures 6.4 (a) and (b) show the constant  $Q$  cuts for the  $Q$  range of the spin fluctuations  $Q=1.1-1.3 \text{ \AA}^{-1}$  (black dots) and the  $Q$  range  $Q=1.5-1.6 \text{ \AA}^{-1}$  (red dots), which is

considered as the non magnetic background. Both signal cuts show a peak for energies close to 8 meV, however, both background cuts also show similar but slightly weaker peaks around this energy. This again indicates possible contributions by a phonon branch at  $\sim 8$  meV, similar to what has been observed for the 12 meV peak. Unfortunately, if this is indeed the case the background contribution coincides with the magnetic resonance that has been identified for energies between 5-9 meV. However, the phonon density of states measurements [225] did not show any flat dispersing phonon branches at this particular energy that could explain the peak at 8 meV. As a consequence, background scattering effects caused by the instrument or sample holder are more likely the reason for this intensity. Since it was not possible to perform empty can correction measurements, instrumental background contributions cannot be excluded. However, a subtraction of the background cuts from the signal cuts, eliminates all background contributions and leaves the corrected intensities to contain solely contributions from spin excitations. Figure 6.4 (c) shows the energy dependence of  $\chi''(Q, \omega)$  which was obtained by subtracting the background cuts from the signal cuts and correcting the background corrected data for the thermal population factor. The temperature difference spectrum between 6 and 30 K in figure 6.4 (d), attained by subtracting the 30 K  $\chi''(Q, \omega)$  from the 6 K  $\chi''(Q, \omega)$ , clearly shows the presence of the spin resonance mode as an enhancement of spectral weight for energies between 5-10 meV. Fitting the difference plot with an asymmetric peak function produced a characteristic energy of the mode of  $E_R \sim (7 \pm 0.3)$  meV. For these measurements the instrument was operated with an incident neutron energy of 20 meV and a Fermi chopper frequency of 150 Hz. This resulted in an energy resolution of approximately 0.4 meV at 7 meV energy transfer. As a consequence, the energy extend of the resonance signal of almost 4 meV FWHM is not resolution limited and thus must be interpreted as an intrinsic characteristic of the resonance signal. Further, this fairly broad extend in energy of the resonance signal is not related to the characteristics of one particular sample but is more likely a universal characteristic of the resonance signal in Fe-based materials as it has been observed for a variety of different Fe-based compositions [40, 70–73, 76, 126, 128, 130, 132, 133]. Below 5 meV the spin gap opens and spectral weight is transferred from this part of the excitation spectrum into the resonance. However from the  $Q$  dependence of  $\chi''(Q, \omega)$  it cannot be said unambiguously whether the gap opens completely at lower energies or lower temperatures. The resonance energy of  $E_R \sim (7 \pm 0.3)$  meV scales to  $T_c$  with  $E_R \sim (3.7 \pm 0.2) k_B T_c$  which is slightly below the average scaling relation for the Fe-based superconductors  $E_R \sim (4.6 \pm 0.4) k_B T_c$ , [36, 72, 133, 139, 140], and the  $E_R \sim 5.1 k_B T_c$  [76, 133], determined for  $\text{LaFeAsO}_{1-x}\text{F}_x$ , the only other 1111-composition for which a resonance signal has been reported.

As discussed in the beginning of this chapter and in chapter 2 the occurrence of the resonance signal can be related to the symmetry of the superconducting gap function  $\Delta_k$ , an important characteristic of every superconducting system. To understand the occurrence of particle hole excitations in the superconducting state, the so called BCS



coherence factor needs to be considered [142–144]

$$\chi''(\mathbf{Q}, \omega) \propto \frac{1}{2} \left( 1 - \frac{\epsilon_{\mathbf{k}} \epsilon_{\mathbf{k}+\mathbf{Q}} + \Delta_{\mathbf{k}} \Delta_{\mathbf{k}+\mathbf{Q}}}{E_{\mathbf{k}} E_{\mathbf{k}+\mathbf{Q}}} \right) \quad (6.1)$$

with the quasiparticle dispersion  $\epsilon_{\mathbf{k}}$  and the quasiparticle energy  $E_{\mathbf{k}} = \sqrt{\epsilon_{\mathbf{k}}^2 + \Delta_{\mathbf{k}}^2}$ . In the superconducting state the majority of the electrons are paired in Cooper pairs. As a result, for energies below  $2\Delta$ , as these are not sufficient to break up the Cooper pairs, particle hole excitations are suppressed and the excitation spectrum is gapped for this energy region. In contrast, for energies above  $2\Delta$  Cooper pairs are broken and particle hole excitations occur, regardless of the symmetry of the gap function. However, for energies close to  $2\Delta$  this symmetry of the superconducting gap function has a great influence on the response of the system. As obvious from equation 6.1, for this particular energy region and a gap function  $\Delta_{\mathbf{k}}$  which changes sign  $\Delta_{\mathbf{k}} = -\Delta_{\mathbf{k}+\mathbf{Q}}$  for different parts of the Fermi surface connected by  $\mathbf{Q}$ , the BCS coherence factor becomes maximal. This maximal BCS coherence factor corresponds to a resonance like enhancement of particle hole excitations  $\chi''(\mathbf{Q}, \omega)$  which then results in a resonance signal in the neutron scattering spectra. In contrast to this, for a different symmetry of the gap function, without any change of the sign, the BCS coherence factor is zero around  $2\Delta$  and no resonance signal is created. With this obvious relation between the resonance signal and the symmetry of the superconducting gap function, the observation of the resonance signal provides valuable information on this crucial parameter of the superconducting state. As a result, in case of the Fe-based materials the observation of the spin resonance signal at  $\mathbf{Q}_{AFM}$  is interpreted as an indication for a superconducting gap function with sign change between the electron and hole Fermi surfaces, just as is the case for the proposed  $s_{\pm}$  symmetry. In consideration of this, the resonance signal in  $\text{CaFe}_{0.88}\text{Co}_{0.12}\text{AsF}$ , which is only present at the AFM wave vector  $\mathbf{Q}_{AFM}$ , allows for a similar interpretation and therefore also suggests a gap function with sign change between the hole and electron Fermi surfaces, which supports the  $s_{\pm}$  gap symmetry.

### 6.3.2 Spin Wave Excitations in Parent $\text{CaFeAsF}$

In addition to the just discussed superconducting sample, the spin excitation spectrum of undoped  $\text{CaFeAsF}$  has been investigated via ToF neutron scattering. Similar to the previous sample, the prominent feature again is a rod-like signal occurring at this particular  $Q$  value  $Q \sim 1.2 \text{ \AA}^{-1}$  earlier identified as the antiferromagnetic propagation vector  $\mathbf{Q}_{AFM} = (0.5, 0.5, 0)$ . Because of the significant propagation vector as well as the temperature and wave vector dependence, where high temperatures and high  $Q$ -values strongly reduce the signal, the signal obviously is of magnetic origin and thus must be arising from the spin wave excitations of the antiferromagnetic Fe-SDW order present below the Néel temperature  $T_N = 114 \text{ K}$  [215].

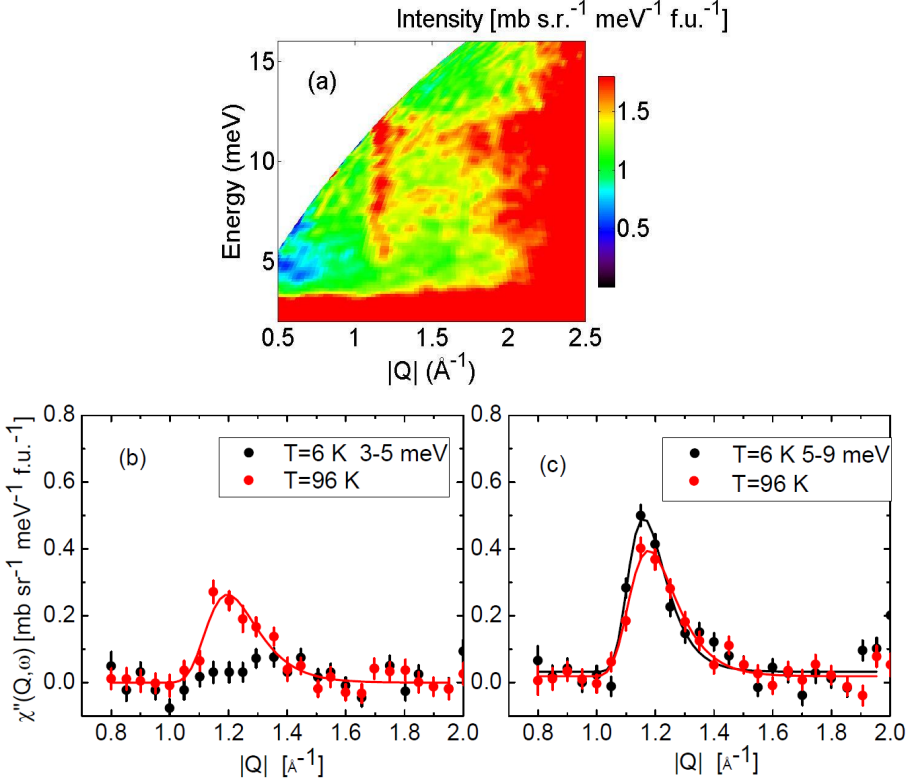


**Figure 6.5:** (a) 2D  $S(\mathbf{Q}, \omega)$  map of CaFeAsF at 6 K, obtained with incident neutron energy of 20 meV. (b) and (c)  $Q$  dependence of  $\chi''(\mathbf{Q}, \omega)$  of undoped CaFeAsF for the temperatures 6 K (black dots) and 96 K (red dots) obtained by performing constant energy cuts through the spectrum with an energy integration of (b) 3-5 meV and (c) 5-9 meV. Black and red solid lines are fits with asymmetric peak functions and are used as guides to the eye.

Identical to the superconducting compound, the observed signal rising from the AFM wave vector has a rod like shape with narrow  $Q$  extent and an almost vertical dispersion for the observed energy range. For temperatures below the Néel temperature and energies below 5 meV all magnetic scattering intensity is suppressed leaving a gap in the spin wave excitation spectrum (Fig. 6.5 (a)). The opening of a gap in the low energy region of spin wave excitation spectra can be related to single ion anisotropy effects. As illustrated in Fig. 6.5 (b) and (c) this gap is fully opened for low temperatures but gradually closes with increasing temperature until the long range order breaks down above the Néel temperature. The 5 meV gap energy is slightly smaller than what is reported,

between 7-10 meV for the 122-pnictides depending on the reference [59–63] as well as the 11 meV reported for  $\text{LaFeAsO}$  [224], the only other spin wave study on a 1111-type material, also performed on a powder sample. This much smaller gap energy indicates a smaller single ion anisotropy in  $\text{CaFeAsF}$  even compared to other 1111-materials.

In contrast to the superconducting compound the signal in  $\text{CaFeAsF}$  exhibits no indications of the peak at 7 meV, which further strengthens the point that this peak is indeed the searched for resonance mode and is unlikely to be caused by phonon contributions. However, the data show an even stronger contribution of the phonon branch at 12 meV, most prominent in figure 6.8. Figure 6.6 (a) shows the  $Q$  dependence of the magnetic susceptibility for the parent (red dots) and superconducting (black dots) compound at 6 K sample temperature. Both peaks are roughly located at the same  $Q$  position. The difference in peak position of both peaks is likely to be caused by the stronger asymmetric peak-shape of the superconducting sample. This strong peak asymmetry is caused by the two dimensionality of the spin fluctuations and on the other side the higher symmetry of the signal in the parent compound shows the more three dimensional character of the spin wave excitations, which is what is expected for spin wave excitations of the three dimensional static Fe-SDW order. In addition to the more symmetric shape the parent compound peak is also strikingly narrower than for the superconducting sample. This smaller peak width results from the steeper dispersion and the longer correlation length of the interacting spins of the magnon excitations of undoped compound, which again is expected for excitations of the long range SDW order present in the parent compound.

As figure 6.7 illustrates, below the Néel Temperature  $T_N=114$  K  $\chi''(Q, \omega)$  exhibits a clean narrow peak located at the AFM wave-vector  $Q_{AFM}$  arising from magnon like spin excitations of the long range Fe-SDW order. Between 6 K and 100 K the peak shape, peak width or integrated intensity do not exhibit any drastic variations. At 120 K which is slightly above the Néel temperature, however, the peak width increases and the integrated intensities decrease significantly, due to strong reduction in peak intensity. Further, the shape of the peak becomes more asymmetric as the tail at the higher  $Q$ -side becomes more prominent. Despite its strongly reduced intensity and the additional broadening of the signal, it can still be observed for temperatures as high as 270 K, the maximum temperature of the experiment. This broadened and weakened signal clearly illustrates the loss of correlation length of the excitations, as the long range magnetic order is broken down above  $T_N$ . The increasing asymmetry of the peak further indicates a loss of the three dimensional character of the spin wave excitations in the magnetically ordered phase. Thus, compared to the signal generated by the spin fluctuations in the normal state of the superconducting compound one recognizes tremendous similarities concerning shape, intensity and width of the observed peak (Fig. 6.6 (b)), even if the signal of the parent compound is still slightly narrower and a bit more symmetric. But still, these similarities illustrate, that the low energy spin fluctuations in the paramagnetic state of the investigated  $\text{CaFe}_{1-x}\text{Co}_x\text{AsF}$  series are

just very little affected by the Co-doping, regarding the length and dimensionality of their spin correlations. This suggests that the short range quasi 2D spin fluctuations in the low energy part of the spectrum are in fact a characteristic of the paramagnetic phase in general and are not necessarily restricted to materials with a certain doping concentration. This is very similar to what has been observed for  $\text{CaFe}_2\text{As}_2$  by Diallo et al. [61].

However, note that, as was discussed in the previous chapter, this most likely does only apply for the low energy region of the paramagnetic excitations, as it is proposed that at higher energies these broad paramagnetic excitations are replaced by narrow spin wave like excitation for higher energies [54]. Further experiments of the high energy range of the excitation spectrum are necessary to address this topic.

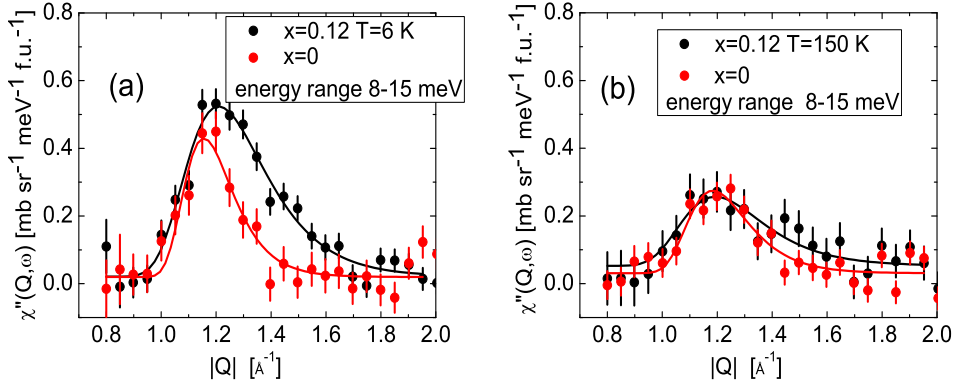


**Figure 6.6:**  $Q$  dependence of  $\chi''(Q, \omega)$  for  $\text{CaFeAsF}$  (red dots) and superconducting  $\text{CaFe}_{0.88}\text{Co}_{0.12}\text{AsF}$  (black dots) at 6 K (a) and 150 K (a) and energies between 8-15 meV. Black and red solid lines are fits with asymmetric peak functions and are used as guides to the eye.

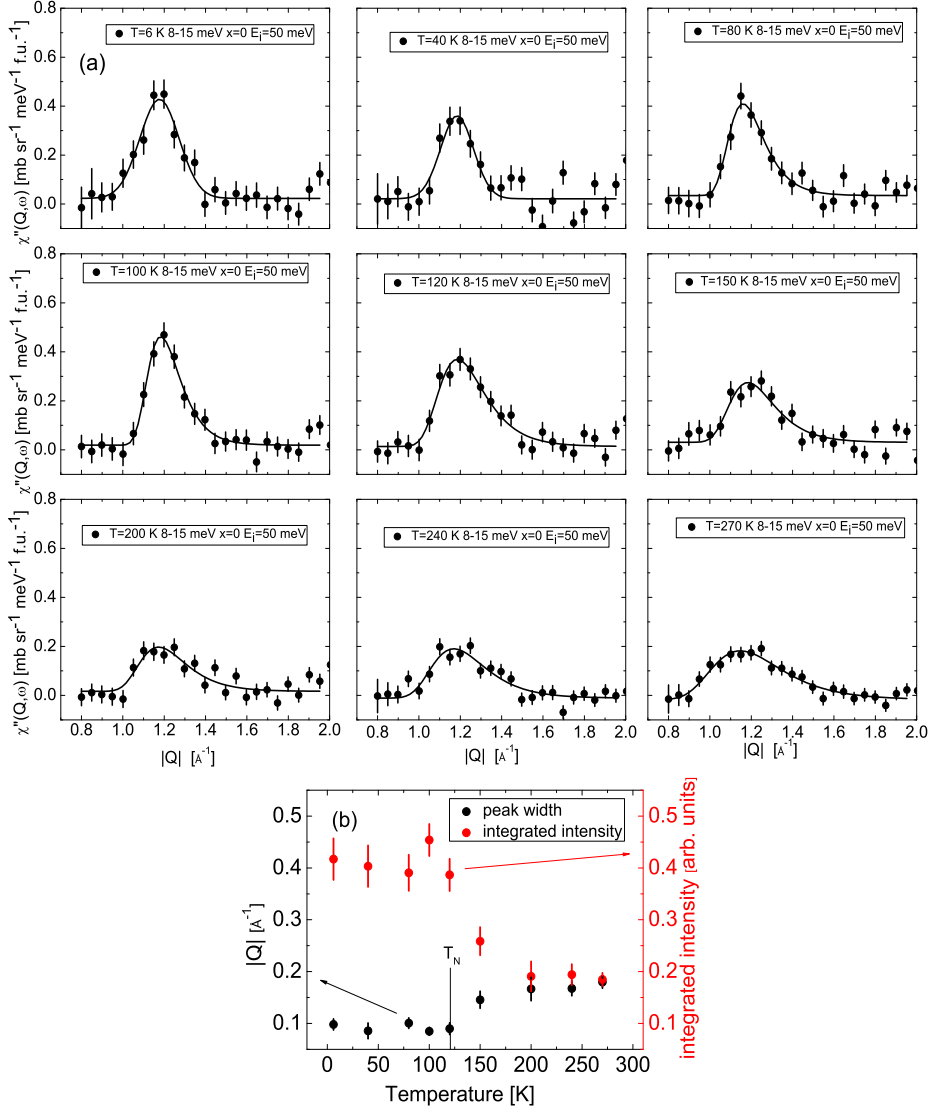


**Figure 6.7:** (a)  $Q$  dependence of  $\chi''(Q, \omega)$  for  $\text{CaFeAsF}$  at temperatures between 6 and 270 K obtained by performing constant energy cuts through the spectrum with an energy integration of 8-15 meV. The corresponding time of flight spectra were measured with an incident neutron energy of 50 meV. Black solid lines are fits with an asymmetric peak function. (b) Temperature dependence of peak width (black dots) and integrated intensity (red dots) of the signal at  $Q \sim 1.2 \text{ \AA}^{-1}$  obtained by fits of asymmetric peak functions (black lines) to  $\chi''(Q, \omega)$  from (a).

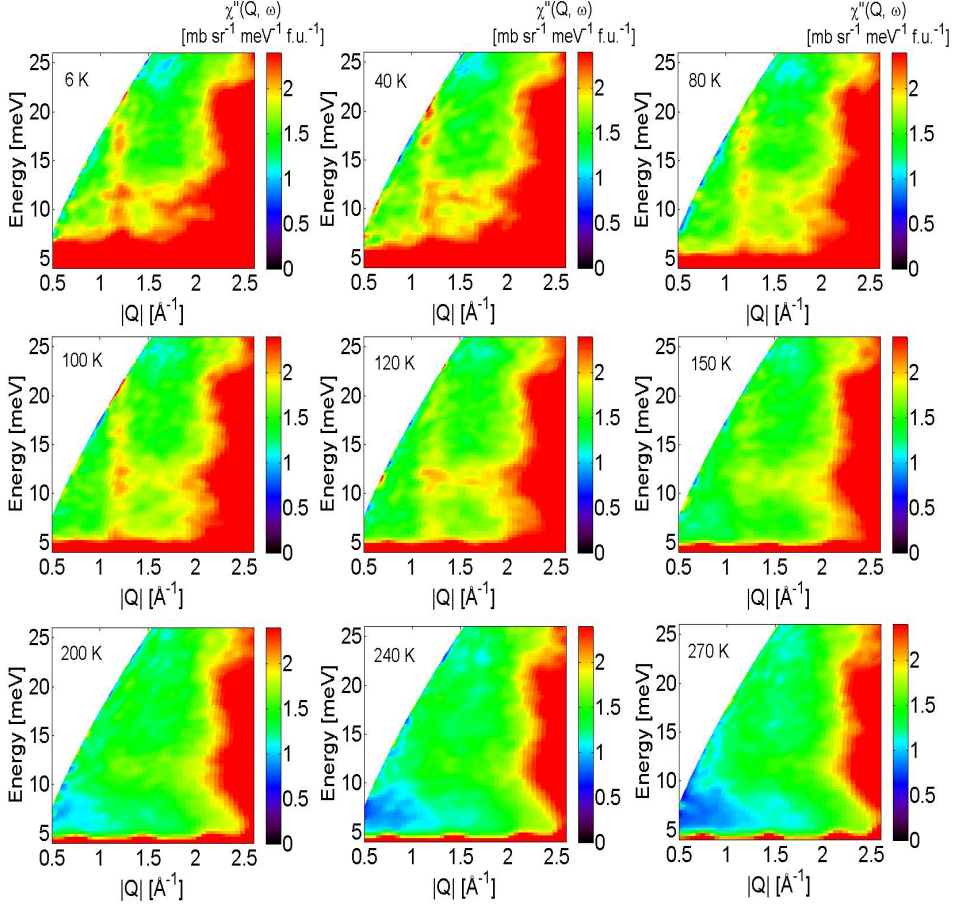


**Figure 6.8:**  $Q$ -energy spectra of  $\chi''(Q, \omega)$  for CaFeAsF at temperatures between 6 and 270 K obtained for incident neutron energies of 50 meV. The spectra correspond to the constant energy cuts at 8-15 meV energy transfer shown in figure 6.7. The intensities shown in the  $Q$ -energy spectra were corrected for the thermal population factor and therefore show  $\chi''(Q, \omega)$ . The correction was performed in order to be able to compare spectra obtained at different temperatures.

## 6.4 Conclusion

The current inelastic neutron scattering study presents the first direct observation of a spin resonance signal in the spin excitation spectrum of an oxygen-free electron-doped 1111-material, in form of optimally doped  $\text{CaFe}_{0.88}\text{Co}_{0.12}\text{AsF}$ . This adds one further class of materials to the list of pnictide and chalcogenide materials for which a resonance signal has been observed [40, 70–73, 76, 127–133]. The signal occurs at the AFM wave vector  $\mathbf{Q}_{AFM}$  for temperatures below  $T_c$  and follows an order parameter like temperature dependence as it disappears close to  $T_c$  and is absent from normal state excitations. All characteristic properties of the signal, the particular propagation vector, the relative enhancement of spectral weight caused by the signal and the energy width all are in reasonable agreement with reports of the resonance signal in other Fe-based materials. This indicates that the microscopic nature of the signal most likely is identical for all Fe-based materials. In addition, the scaling relation of the resonance energy and  $T_c$  in  $\text{CaFe}_{0.88}\text{Co}_{0.12}\text{AsF}$   $E_R \sim (3.7 \pm 0.2) k_B T_c$  is in good agreement with the average relation for the iron pnictide superconductors  $E_R \sim (4.6 \pm 0.4) k_B T_c$  [36, 72, 133, 139, 140]. This further supports a universal character of the signal and strengthens the current understanding of the resonance signal, for which the occurrence of the signal is related to the symmetry of the superconducting gap function. In this regard, the observation of the resonance signal at  $\mathbf{Q}_{AFM}$  in  $\text{CaFe}_{0.88}\text{Co}_{0.12}\text{AsF}$  supports a superconducting gap function with opposite signs on the hole and electron Fermi surfaces, most likely of  $s_{\pm}$ -symmetry. The results, therefore, promote a possible universality of this particular gap symmetry for all Fe-based materials.

In addition, it was possible to detect the low energy part of the magnon excitation spectrum in  $\text{CaFeAsF}$  up to temperatures as high as 270 K and excitation energies as high as 20 meV. Below 114 K the spectrum exhibits narrow spin wave like excitations, which are gapped for energies below 5 meV. This gap can be related to single ion anisotropy effects similar to what has been observed in several undoped Fe-based materials. The 5 meV gap energy, however, is slightly smaller than the 7-10 meV reported for the 122-materials [59–63] or the 11 meV reported for  $\text{LaFeAsO}$  [224]. This clearly indicates significantly smaller single ion anisotropy effects present in  $\text{CaFeAsF}$ , compared to other Fe-based materials.

Above the Néel temperature  $T_N=114$  K the narrow spin wave excitations are replaced by broad more 2D paramagnetic excitations. These paramagnetic excitations show a  $Q$ -dependence very similar to the quasi 2 dimensional normal state spin excitations present in superconducting  $\text{CaFe}_{0.88}\text{Co}_{0.12}\text{AsF}$ . This suggests that spin fluctuations in the paramagnetic state in  $\text{CaFe}_{1-x}\text{Co}_x\text{AsF}$  only feel very little doping dependence in regard of the length and dimensionality of the present spin correlations, at least for the low energy part of the spectrum.

# 7 Inelastic Neutron Scattering on Magnetic Excitations in Superconducting $\text{FeTe}_{0.5}\text{Se}_{0.5}$

## 7.1 Introduction

### 7.1.1 Motivation

As discussed in chapter 2, the spin resonance mode is a characteristic feature of high  $T_c$  superconductors and has been observed in the spin excitation spectrum of the superconducting phase of a large and still growing number of Fe-based and cuprate superconducting materials. Despite the effort that has been made in investigating the signal, its microscopic nature and role to the mechanism of high  $T_c$  superconductivity is still a mystery. According to the current understanding, the occurrence of the resonance signal can be related to a specific symmetry of the superconducting order parameter, as a sign change of the superconducting gap function for different parts of the Fermi surface leads to the resonance signal in the particle hole excitation spectra. In this context Maier et al. predicted for a superconducting order parameter with singlet  $s_{\pm}$  symmetry, a resonance signal in the spin excitation spectrum with an equal contribution of in-plane  $\chi''_{ab}(\mathbf{Q}, \omega)$  and out-plane  $\chi''_c(\mathbf{Q}, \omega)$  excitations, with  $\chi''_{ab}(\mathbf{Q}, \omega) \approx \chi''_c(\mathbf{Q}, \omega)$ . Whereas, a triplet symmetry of the order parameter for example leads to an anisotropic distribution to the resonance signal, which occurs exclusively for in-plane spin excitations  $\chi''_{ab}(\mathbf{Q}, \omega)$ , with  $\chi''_c(\mathbf{Q}, \omega)$  remaining featureless [118]. However, from Knight shift measurements it is known that the Cooper pairing in Fe-based materials most likely is of singlet symmetry, and so an equally strong resonance signal should be observable for both in-plane and out-of-plane spin excitations. If one thinks of the spin 1 exciton or the  $\pi$ -resonance, as explained in chapter 2, an isotropic magnetic response would correspond to an equal population of the three degenerated triplet states  $S_z = \pm 1$  and  $S_z = 0$  of the  $S=1$  resonance excitation, and thus might be what one would intuitively expect. For  $\text{BaFe}_{1.9}\text{Ni}_{0.1}\text{As}_2$  [135], however, a different observation has been made. Results from polarized neutron scattering experiments show a clearly anisotropic contribution of in-plane and out-of-plane excitations to the excitation spectrum, where the spectrum for energies below the resonance energy are dominated by  $\chi''_c(\mathbf{Q}, \omega) > \chi''_{ab}(\mathbf{Q}, \omega)$ , whereas, for the resonance region the spectrum



is dominated by  $\chi''_{ab}(\mathbf{Q}, \omega) > \chi''_c(\mathbf{Q}, \omega)$  [135]. To explain this anisotropy of the spin excitation spectrum, the authors propose a possible spin-orbital/lattice coupling, similar to what has been proposed for parent compounds [227–229]. The authors further propose that this spin anisotropy leads to a resonance signal which is rather a spin 1 doublet than spin 1 triplet. For this spin 1 doublet excitation, only the  $S_z = \pm 1$  states of the triplet are occupied whereas the  $S_z = 0$  state remains unoccupied. Such a scenario requires that the occupation of the  $S_z = \pm 1$  states is accomplished by the in-plane spin flip excitations  $\chi''_{ab}(\mathbf{Q}, \omega)$ , whereas the out-of-plane excitations  $\chi''_c(\mathbf{Q}, \omega)$  are responsible for the occupation of the  $S_z = 0$  state. The absence of  $\chi''_c(\mathbf{Q}, \omega)$  then leads to the conclusion of the unoccupied  $S_z = 0$  state and the resulting doublet excitation as explanation for the resonance mode.

As the results on the spin anisotropy in  $\text{BaFe}_{1.9}\text{Ni}_{0.1}\text{As}_2$  are not directly compatible with the current theoretical picture of the spin resonance signal, the main focus of this study is to investigate the spin anisotropy of the resonance signal in another Fe-based superconducting material. For this, polarized inelastic neutron scattering experiments on the low energy spin excitations with propagation vector  $\mathbf{Q}_{AFM}=(0.5, 0.5, 0)$  in superconducting  $\text{FeTe}_{0.5}\text{Se}_{0.5}$  have been performed. The results from this study are discussed in the current chapter.

### 7.1.2 Magnetic Excitations in Doped $\text{Fe}_{1-y}\text{Te}_{1-x}\text{Se}_x$ Materials

In 11-materials partial substitution of Telluride by Selenium is a way to suppress the static magnetic order and induce superconductivity in the system. In the superconducting phase where the static magnetic order with  $\mathbf{Q}=(0.5, 0, 0.5)$  is completely suppressed, strong two dimensional spin fluctuations with a propagation vector close to  $\mathbf{Q}_{AFM}=(0.5, 0.5, 0)$  are present. The propagation vector of the 2D spin fluctuations is comparable to the nesting vector  $\mathbf{Q}_{nesting}=(0.5, 0.5, 0)$ , which connects the hole and electron pockets of the Fermi surface. The Fermi surfaces of 11- 122- and 1111-materials are very similar with electron and hole pockets located at the M- and  $\Gamma$ -points, respectively. This results in similar nesting conditions described by  $\mathbf{Q}_{nesting}=(0.5, 0.5, 0)$ . In all superconducting Fe-based materials, regardless if of 11-, 1111- or 122-type, the superconducting phases exhibit enhanced spin fluctuations with a propagation vector matching this nesting vector. Aside from these similarities, the spin fluctuations close to  $\mathbf{Q}_{AFM}=(0.5, 0.5, 0)$  in the 11-materials, however, possess properties slightly deviating from the spin fluctuations in the 122- and 1111-materials. As excitations in the 1111- and 122-materials are completely commensurate, in superconducting 11-materials they consist of two counter-propagating modes located at transverse incommensurate positions to  $\mathbf{Q}_{AFM}=(0.5, 0.5, 0)$  [34, 129, 141, 230–232]. This incommensurate position varies with the amount of incorporated Selenium, as for Se-content close to 50% the two incommensurate modes tend to move towards the commensurate  $(0.5, 0.5, 0)$  position, whereas for higher or lower Se-content the modes turn away from the commensurate position again. With

increasing energy the two counter-propagating modes located traverse to  $\mathbf{Q}_{AFM}=(0.5, 0.5, 0)$  move further away from the commensurate position as they disperse towards the  $(1, 0, 0)$  and  $(0, 1, 0)$  positions in reciprocal space, respectively [129, 230]. The fact that the two counterpropagating modes are not part of a spin wave cone but consist of two separate wave vectors, indicates that itinerant mechanisms are most likely responsible for the formation of the fluctuations in 11-materials [129].

Just as in most Fe-based superconductors, for temperatures below  $T_c$  the spectrum of spin excitations around  $(0.5, 0.5, 0)$  exhibits the occurrence of the spin resonance signal at the resonance energy  $E_R$  accompanied by the opening of the spin gap for energies below  $E_R$  [34, 129–132, 233]. In contrast to the 1111- and 122-materials, however, the resonance in  $\text{Fe}_{1-y}\text{Te}_{1-x}\text{Se}_x$  arises from two excitation modes slightly separated from each other located in transverse direction to the nesting vector  $\mathbf{Q}_{AFM}=(0.5, 0.5, 0)$ . Another deviation from the 122-materials, and especially from optimal doped  $\text{Ba}(\text{Fe}_{1-x}\text{Co}_x)_2\text{As}_2$  is the temperature dependence of the resonance energy. As in optimal doped  $\text{Ba}(\text{Fe}_{1-x}\text{Co}_x)_2\text{As}_2$  the resonance energy  $E_R$  seemingly exhibits a relation to the superconducting gap, and disperses to zero for increasing temperature [72], the energy of the resonance signal in  $\text{Fe}_{1-y}\text{Te}_{1-x}\text{Se}_x$  remains constant with temperature [141].

## 7.2 Experimental Details

Polarized neutron scattering experiments on a large high quality single crystal of the nominal composition  $\text{FeTe}_{0.5}\text{Se}_{0.5}$  have been performed. The single crystal sample, with an approximate mass of 15 g, was grown via the Bridgeman method by collaborating scientist Dr. B. C. Sales of the Oak Ridge National Laboratory, Oak Ridge, Tennessee, USA. Characterization measurements (conductivity, specific heat, magnetization, etc.) revealed bulk superconductivity with a transition temperature of just slightly below 15 K, which places the sample in the optimal doped region of the phase diagram. Single crystal x-ray diffraction measurements determined the common tetragonal crystal structure with lattice constants  $a=3.815 \text{ \AA}$  and  $c=6.069 \text{ \AA}$ . Further details on the characterization of the sample can be found in ref. [234], where this sample is referred to as crystal B.

The inelastic neutron scattering experiments were performed on the thermal three-axis spectrometer IN22 at the Institute Laue-Langevin, Grenoble [235]. The crystal was aligned with its crystallographic c-axis perpendicular to the scattering plane. This provides access to the  $\mathbf{Q}_{AFM}=(0.5, 0.5, 0)$  reflection corresponding to the propagation vector of the short range spin fluctuations which also coincides with the nesting vector. The sample was placed in a standard ILL-orange cryostat and data were taken for selected sample temperatures between 6 K and 200 K. The spectrometer was operated in the fixed  $\mathbf{k}_f$ -mode with a final wave vector of  $\mathbf{k}_f=2.662 \text{ \AA}^{-1}$  for the low energy scans and  $\mathbf{k}_f=3.84 \text{ \AA}^{-1}$  for the scans with 30 meV energy transfer. No collimation has been used, but a graphite filter was placed in the scattered beam in order to suppress contaminations

by higher order neutron wavelengths. The experiment was performed with the Heusler-monochromator and Heusler-analyzer in vertically focusing mode, in order to increase intensity. The energy resolution with this experimental set up is approximately 0.8 meV at the elastic position. The Heusler-monochromator works as a monochromator by selecting the wavelength of the incident neutron beam, and additionally polarizes the neutron beam. To perform the Longitudinal Polarization Analysis the CRYOPAD device has been installed. This device provides a magnetic field free environment for the sample and further enables the user to control the polarization of the incoming and scattered neutron beam, without any interference of the guide fields at the sample position [236]. Throughout this chapter tetragonal notation will be used to index reflections. This results in  $\mathbf{Q}_{AFM}=(0.5, 0.5, 0)$  as the antiferromagnetic wave vector of the magnetic excitations of the Fe-moments.

### 7.2.1 Longitudinal Polarization Analysis

In order to perform a Longitudinal Polarization Analysis, scattering data were taken for six different neutron cross sections, three non-spin-flip  $\sigma_{\alpha}^{NSF}$  and three spin-flip  $\sigma_{\alpha}^{SF}$ , with  $\alpha=x, y, z$ . As discussed in chapter 3, x, y, z defines a cartesian linked to the experimental set up, where x is parallel to the scattering vector  $\mathbf{Q}$ , y is perpendicular to  $\mathbf{Q}$  but within the scattering plane and z points vertical perpendicular to the scattering plane. Also previously discussed, a spin-flip (SF) process flips the spin of the scattered neutron ( $\uparrow\downarrow$  or  $\downarrow\uparrow$ ) whereas a non-spin-flip (NSF) process conserves the neutron spin direction ( $\uparrow\uparrow$  or  $\downarrow\downarrow$ ). The six different cross sections were measured for selected momentum and energy transfers. An exemplary spin flip cross section for a neutron polarization direction  $\mathbf{P}$  parallel to  $\mathbf{Q}$  reads as [159, 162, 164]

$$\sigma_{xx}^{SF} = \left( \frac{d^2\sigma}{d\omega dE} \right)_{\mathbf{P}||\mathbf{x}}^{SF} = \frac{k_f}{k_i} \frac{(\gamma r_e)^2}{g^2 \mu_B^2} \frac{1}{\pi} F^2(\mathbf{Q}) \times \frac{\chi''_{yy}(\mathbf{Q}, \omega) + \chi''_{zz}(\mathbf{Q}, \omega)}{1 - \exp(-\hbar\omega/k_B T)} \quad (7.1)$$

where  $F^2(\mathbf{Q})$  is the magnetic form factor and  $\chi''_{\alpha\alpha}(\mathbf{Q}, \omega)$  is the generalized susceptibility corresponding to magnetic fluctuations along the  $\alpha=x, y, z$  direction.

The crystal structure of the investigated sample  $\text{FeTe}_{0.5}\text{Se}_{0.5}$  is tetragonal and consequently the generalized susceptibility can vary between excitations with moment directions within the ab-plane  $\chi''_{ab}(\mathbf{Q}, \omega)$  and excitations with moment directions along the crystallographic c-direction  $\chi''_c(\mathbf{Q}, \omega)$ . Because of the orientation of the sample, with its crystallographic c-direction perpendicular to the scattering plane, for this experiment  $\chi''_{yy}(\mathbf{Q}, \omega)$  corresponds to  $\chi''_{ab}(\mathbf{Q}, \omega)$  and  $\chi''_{zz}(\mathbf{Q}, \omega)$  describes  $\chi''_c(\mathbf{Q}, \omega)$ . Because of, (1) the fact that neutrons only scatter from magnetic fluctuations perpendicular to the scattering vector  $\mathbf{Q}$  and (2) the fact that fluctuations perpendicular to the neutron polarization  $\mathbf{P}$  scatter in the spin-flip (SF) channel, whereas fluctuations parallel to the incident neutron polarization scatter in the non-spin-flip (NSF) channel, in-plane and out-of-plane components  $\chi''_{ab}(\mathbf{Q}, \omega)$  and  $\chi''_c(\mathbf{Q}, \omega)$  can be separated completely. The six different spin

dependent neutron cross sections [159, 162, 164], obtained during the experiments read as,

$$\begin{aligned}
 \sigma_{xx}^{NSF} &\propto N(\mathbf{Q}, \omega) + BG^{NSF} \\
 \sigma_{yy}^{NSF} &\propto \chi''_{ab}(\mathbf{Q}, \omega) + N(\mathbf{Q}, \omega) + BG^{NSF} \\
 \sigma_{zz}^{NSF} &\propto \chi''_c(\mathbf{Q}, \omega) + N(\mathbf{Q}, \omega) + BG^{NSF} \\
 \sigma_{xx}^{SF} &\propto \chi''_{ab}(\mathbf{Q}, \omega) + \chi''_c(\mathbf{Q}, \omega) + BG^{SF} \\
 \sigma_{yy}^{SF} &\propto \chi''_c(\mathbf{Q}, \omega) + BG^{SF} \\
 \sigma_{zz}^{SF} &\propto \chi''_{ab}(\mathbf{Q}, \omega) + BG^{SF}
 \end{aligned} \tag{7.2}$$

Here the nuclear spin incoherent cross section has been neglected.  $BG^{NSF}$  and  $BG^{SF}$  stand for non magnetic background contributions, whereas  $N(\mathbf{Q}, \omega)$  is the coherent nuclear cross section, which in this case considers phonon scattering.

Obviously, x-polarization provides the possibility to separate magnetic and nuclear intensities, as for this polarization nuclear scattering processes are always non-spin-flip, whereas magnetic processes are always spin-flip. Consequently the corresponding (SF) and (NSF) cross sections are only affected by either scattering process, magnetic or nuclear.

The relations in (7.2) show that the conducted experiments were suited to probe  $\chi''_{ab}(\mathbf{Q}, \omega)$  and  $\chi''_c(\mathbf{Q}, \omega)$ , and so determine the amount of spin fluctuations with fluctuating moment within the ab-plane and along the crystallographic c-direction. Obviously,  $\chi''_{ab}(\mathbf{Q}, \omega)$  and  $\chi''_c(\mathbf{Q}, \omega)$  can be extracted from the obtained cross sections by,

$$\begin{aligned}
 \sigma_{xx}^{SF} - \sigma_{yy}^{SF} = \sigma_{yy}^{NSF} - \sigma_{xx}^{NSF} &\propto \chi''_{ab}(\mathbf{Q}, \omega) \\
 \sigma_{xx}^{SF} - \sigma_{zz}^{SF} = \sigma_{zz}^{NSF} - \sigma_{xx}^{NSF} &\propto \chi''_c(\mathbf{Q}, \omega)
 \end{aligned} \tag{7.3}$$

## 7.3 Results and Discussion

The first part of the investigation on the spin resonance was to determine the nature of the mode by performing constant energy and constant  $\mathbf{Q}$ -scans through the particle hole excitation spectrum located at  $\mathbf{Q}_{AFM}=(0.5, 0.5, 0)$ , using a neutron polarization parallel to the scattering vector, x-polarization. Note that this polarization direction leads to a complete separation of magnetic and nuclear scattering intensities.

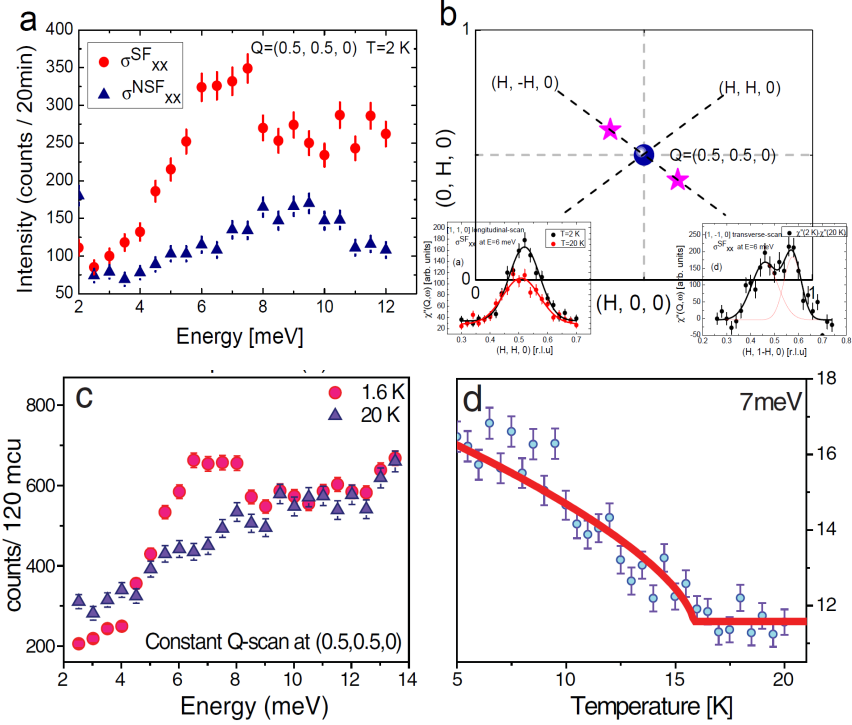


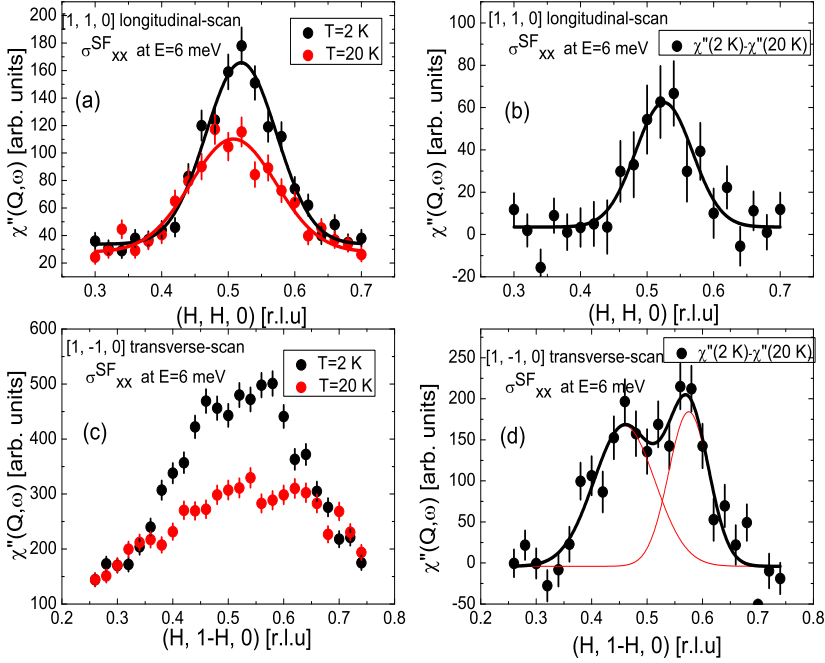
**Figure 7.1:** (a) Constant  $\mathbf{Q}$ -scans performed at 2 K sample temperature. The depicted intensities were obtained via polarized neutron scattering experiments using an incident neutron polarization parallel to the scattering vector  $\mathbf{Q}=(0.5, 0.5, 0)$ . Shown are intensities obtained in the non-spin-flip (blue triangles) and spin-flip (red dots) channel. (b) Diagram of the  $(H, H, 0)$ -reciprocal plane. Illustrated are the positions of the incommensurate excitations (stars) located in transverse direction to  $\mathbf{Q}=(0.5, 0.5, 0)$ . The dotted lines mark the directions of constant energy scans in longitudinal and transverse direction through  $\mathbf{Q}=(0.5, 0.5, 0)$ . The two insets illustrate intensities resulting from performing longitudinal and transverse scans through  $\mathbf{Q}=(0.5, 0.5, 0)$ . The scans are shown in detail in figure 7.2. (c) Constant  $\mathbf{Q}$ -scans with wave vector  $\mathbf{Q}=(0.5, 0.5, 0)$ , performed at sample temperatures 1.6 K (red dots) and 20 K (violet triangles). (d) Temperature dependence of the scattering intensity obtained for the resonance energy 7 meV. The red solid line is a power law fit to the data. Figures (c) and (d) resulted from non-polarized neutron experiments performed on the same sample and are taken from ref. [132].

Prior to this polarized neutron scattering study, Mook et al. [132] performed non-polarized inelastic neutron scattering experiments on this particular sample used for the present investigations. Figure 7.1 (c) illustrates constant  $\mathbf{Q}$ -scans at  $\mathbf{Q}=(0.5, 0.5, 0)$

for two sample temperatures 1.6 K and 20 K, on this sample, which is referred to as sample B in reference [132]. The energy scans clearly show the spin resonance mode for energies between 5 and 8 meV, as the enhancement in scattering intensity of the 1.6 K scan compared to the 20 K data. For energies below 5 meV a gap in the excitation spectrum of the superconducting phase opens as the intensity drops below the level of the 20 K scan for this region of the spectrum. The enhanced intensity between 5-9 meV follows an order parameter like temperature dependence which leads to a complete disappearance around 16 K, close to the superconducting transition temperature (fig. 7.1 (d)). These results by Mook et al. clearly prove the existence of the resonance signal in this particular sample, used for the present study.

Figure 7.1 (a) shows the energy dependence of (SF) (red dots) and (NSF) (blue triangles) scattering intensities obtained with an incident neutron polarization  $\mathbf{P}_x$  parallel to the scattering vector  $\mathbf{Q}=(0.5, 0.5, 0)$ , at 2 K sample temperature. The intensity obtained in the (SF) channel, which according to equations (7.2) is exclusively due to magnetic scattering processes, shows a clear peak between 5-9 meV, which matches very well the peak in figure 7.1 (c). Due to the good agreement between the (SF) intensity in 7.1 (a) and the low temperature data in 7.1 (c) the observed peak in 7.1 (a) is identified as the spin resonance signal. In contrast to the (SF) intensity, the (NSF) intensity is featureless for the energy region of the resonance 5-9 meV, which shows that nuclear contributions to the resonance signal are negligible. The fact that the resonance signal exclusively appears in the (SF) channel clearly proves the magnetic nature of the spin resonance excitation. With this, the presented results are consistent with earlier reports on the magnetic nature of the signal for optimal doped  $\text{BaFe}_{1.9}\text{Ni}_{0.1}\text{As}_2$  [135] as well as for  $\text{FeTe}_{0.5}\text{Se}_{0.5}$  [137] and other cuprate materials [120, 122, 134, 136] and so confirm that spin flip particle hole excitations lead to the signal.

In addition to the energy dependence, the wave vector dependence of the resonance signal was investigated by performing constant energy-scans with 6 meV energy transfer, through the resonance wave vector  $\mathbf{Q}=(0.5, 0.5, 0)$  in both longitudinal and transverse direction, as illustrated in fig. 7.1 (b). The intensities of the longitudinal and transverse constant energy scans, shown in figure 7.2, have been corrected for the thermal population factor  $n(T, \omega)=(1-\exp(-\hbar\omega/k_B T))$ , which accounts for the temperature dependent Boson population of excited states according to Bose statistics. This correction eliminates all trivial temperature effects and consequently makes a comparison possible of scattering intensities taken at different sample temperatures. In addition, according to the fluctuation-dissipation theorem, the correction transforms the obtained intensity into the dynamical part of the magnetic susceptibility  $\chi''(\mathbf{Q}, \omega) \propto \chi''_{ab}(\mathbf{Q}, \omega) + \chi''_c(\mathbf{Q}, \omega)$ .



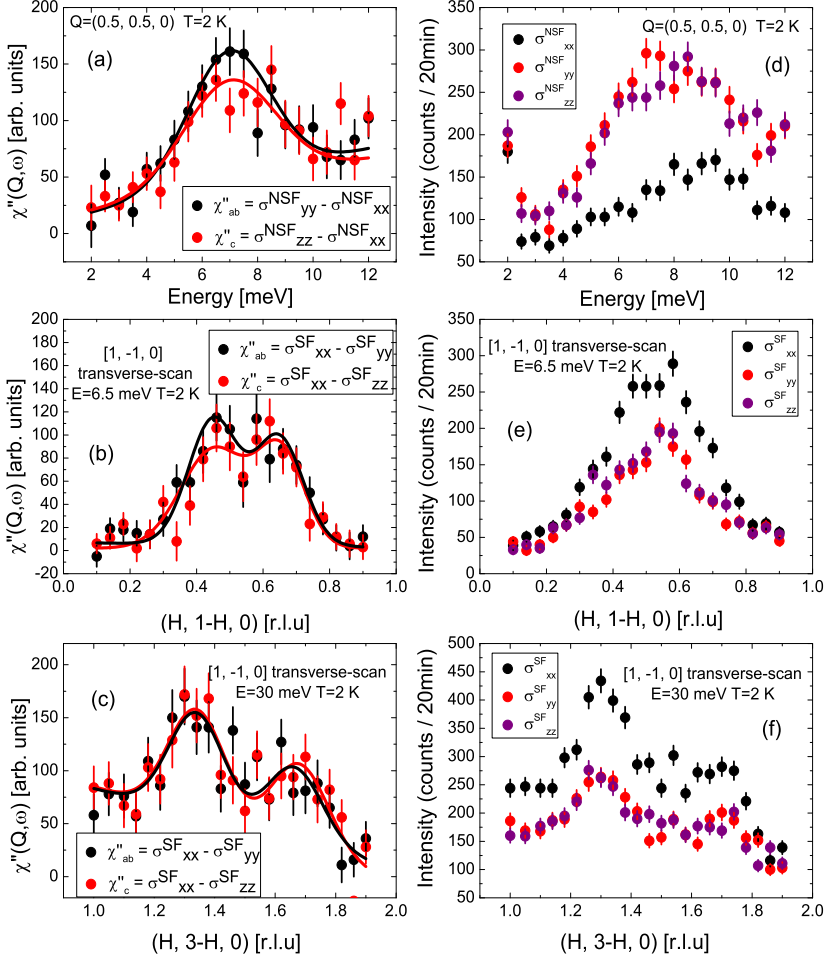
**Figure 7.2:** (a) and (c) Longitudinal and transverse constant energy-scans through  $\mathbf{Q}=(0.5, 0.5, 0)$  at the resonance energy 6 meV and temperatures of 2 K (black dots) and 20 K (red dots). (b) and (d)  $Q$ -dependence of the spin resonance signal in longitudinal and transverse direction, obtained by performing  $\chi''(2\text{ K}) - \chi''(20\text{ K})$  from (a) and (c), respectively. Illustrated intensities in (a) and (c) were obtained in the spin-flip channel with x-polarization and thus show purely magnetic excitations. They were further corrected for the thermal population factor. Red and black solid lines are least square fits of Gaussian peak functions to the data and serve as guides to the eye.

Figure 7.2 shows the longitudinal ((a) and (b)) and transverse ((c) and (d))  $Q$ -dependence of the magnetic susceptibility  $\chi''(\mathbf{Q}, \omega)$ . The illustrated intensities were obtained in the (SF)-channel with x-polarization of the incident neutron beam and, therefore, represent purely magnetic intensity. The prominent result from figure 7.2, is a splitting of the resonance signal in  $(H, -H, 0)$ -direction, obvious from the difference plots in (fig. 7.2 (b) (d)), which clearly show a splitting of the signal in transverse direction whereas in longitudinal direction it features a single peak. The result is an incommensurate resonance signal consisting of two separated modes located at slightly asymmetric positions  $\mathbf{Q}_l=(0.46, 0.54, 0)$  and  $\mathbf{Q}_r=(0.57, 0.43, 0)$ . This incommensurability of the resonance signal seems to be an exclusive characteristic of the 11-materials as it has been observed for several 11-compositions but for neither

the 122-, 1111- nor the  $\text{KFe}_2\text{Se}_2$  materials. One explanation for the splitting might be a special nesting condition [231]. This nesting condition is supported by the fact that the resonance signal obviously is a feature of the spectrum of spin fluctuations with propagation vector  $\mathbf{Q}_{AFM}=(0.5, 0.5, 0)$ , and which for 11-materials consists of two counterpropagating modes located in transverse direction to  $\mathbf{Q}_{AFM}=(0.5, 0.5, 0)$  and dispersing towards  $\mathbf{Q}=(1, 0, 0)$  and  $\mathbf{Q}=(0, 1, 0)$ , respectively [230]. A consequence of this dispersion is that in most reports the resonance signal is seen as arising from two modes. This either shows in a broadened flat top peak or in two overlapping peaks [34, 129, 231, 233, 237], similar to what is shown in figure 7.2 (d). Since the two spin fluctuation modes are not part of spin wave cones but emerge from two separate propagation vectors, an itinerant approach seems much better suited to describe the nature of the magnetic interactions with this particular wave vector [129, 230]. As shown here, the splitting of the resonance signal is entirely due to a split signal of spin flip particle hole excitations without any inadvertent non-magnetic contributions. Assuming that two incommensurate nesting conditions are driving the spin fluctuations [231], the splitting of the resonance signal seems natural and consistent with the spin 1 exciton model, as the formation of the exciton obviously would follow the nesting condition and result in a split resonance signal integrated into the spin excitation spectrum.

After clarifying the purely magnetic nature of the spin resonance signal, one question remains regarding the contributions of in-plane and out-of-plane spin excitations to the signal. According to equations (7.3) it is possible to separate the in-plane  $\chi''_{ab}(\mathbf{Q}, \omega)$  and out-of-plane  $\chi''_c(\mathbf{Q}, \omega)$  components of the imaginary part of the spin susceptibility, by subtracting intensities obtained for different incident neutron polarizations. This can be done for intensities obtained either in the (SF)- or (NSF)-channel. Note that in the following both possibilities are practised as for the energy dependence  $\chi''_{ab}(\mathbf{Q}, \omega)$  and  $\chi''_c(\mathbf{Q}, \omega)$  were obtained through (NSF)intensities, whereas for the  $\mathbf{Q}$  dependencies (SF) intensities were used.





**Figure 7.3:** (a) Energy dependence of the in-plane  $\chi''_{ab}(\mathbf{Q}, \omega)$  (black dots) and out-of-plane  $\chi''_c(\mathbf{Q}, \omega)$  (red dots) spin excitations with wave-vector  $\mathbf{Q}=(0.5, 0.5, 0)$  and 2 K sample temperature. The two components were obtained by subtracting (NSF)-intensities obtained with x-polarization from (NSF)-intensities obtained with y- and z-polarizations, respectively, as illustrated in (d). (b) Transverse  $\mathbf{Q}$ -dependence along the (H, -H, 0)-direction through  $\mathbf{Q}=(0.5, 0.5, 0)$  of  $\chi''_{ab}(\mathbf{Q}, \omega)$  (black dots) and  $\chi''_c(\mathbf{Q}, \omega)$  (red dots) at 2 K and resonance energy 6.5 meV. (c) Transverse  $\mathbf{Q}$ -dependence along the (H, -H, 0)-direction through  $\mathbf{Q}=(1.5, 1.5, 0)$  of  $\chi''_{ab}(\mathbf{Q}, \omega)$  (black dots) and  $\chi''_c(\mathbf{Q}, \omega)$  (red dots) at 2 K and 30 meV. The two components of  $\chi''(\mathbf{Q}, \omega)$  from (b) and (c) were obtained by subtracting (SF)-intensities obtained with y- and z-polarization from (SF)-intensities obtained with x-polarization, respectively, as illustrated in (e) and (f). The intensities in (a)-(c) were corrected for the thermal population factor. Red and black solid lines are least square fits of Gaussian peak functions to the data and serve as guides to the eye.

Figure 7.3 illustrates the energy- and  $\mathbf{Q}$ -dependence of the in-plane  $\chi''_{ab}(\mathbf{Q}, \omega)$  and out-of-plane  $\chi''_c(\mathbf{Q}, \omega)$  magnetic susceptibility in the superconducting state. The main result from the current polarization analysis is that spin fluctuations with propagation vectors close to  $\mathbf{Q}_{AFM} = (0.5, 0.5, 0)$  consist of an almost completely isotropic distribution of in-plane and out-of-plane polarization of the spin fluctuations for energies up to 30 meV. Only for fluctuations directly at the resonance energy a slight deviation from this isotropic polarization is present, as for this energy region in-plane fluctuations  $\chi''_{ab}(\mathbf{Q}, \omega)$  are slightly enhanced in respect to  $\chi''_c(\mathbf{Q}, \omega)$ , only visible from the energy dependence in figure 7.3 (a). This small enhancement of  $\chi''_{ab}(\mathbf{Q}, \omega)$  of approximately 10 % relative to  $\chi''_c(\mathbf{Q}, \omega)$  is only observable right at the peak maximum at 7 meV but is absent in the  $\mathbf{Q}$ -scans. Both, the in-plane and out-of-plane components of  $\chi''(\mathbf{Q}, \omega)$  do not show any substantial difference in the  $\mathbf{Q}$  scan at 6.5 meV. As a consequence, aside from the small region at 7 meV, the majority of the spectrum up to 30 meV is clearly isotropic. This isotropy obviously illustrates the paramagnetic nature of these collective excitations, where spins are free to turn in each direction.

Similar results have been reported for  $\text{FeTe}_{0.5}\text{Se}_{0.5}$  by Babkevich et al. [137]. However, there the authors report a larger anisotropy, with an enhancement of  $\chi''_{ab}(\mathbf{Q}, \omega)$  of about 20%. Further, this anisotropy is present for a slightly larger energy region above and below the resonance energy  $E_R$ . This different anisotropy for these nominal identical compositions suggests that the degree of anisotropy might in fact be related to sample properties of the  $\text{FeTe}_{1-x}\text{Se}_x$  compositions. Note that the sample used in this study has a slightly higher  $T_c$  of 15 K compared to the 14 K of their sample even though both samples were supposed to have identical doping concentrations. If sample properties indeed play a role, the spin fluctuations in the superconducting state of optimal doped  $\text{FeTe}_{0.5}\text{Se}_{0.5}$  have to be considered isotropic, even for the resonance energy. As discussed in the beginning of the chapter, an isotropic spin resonance supports the singlet-triplet excitation, as a possible microscopic explanation for the resonance signal. Therefore, the presented results are interpreted as supportive to the singlet triplet excitation as possible microscopic description of the signal in 11-materials.

For overdoped  $\text{Ba}(\text{Fe}_{0.925}\text{Ni}_{0.075})_2\text{As}_2$  comparable results have been reported by Liu et al. [238]. There the authors report completely isotropic spin excitations  $\chi''_{ab}(\mathbf{Q}, \omega) \approx \chi''_c(\mathbf{Q}, \omega)$  for energies up to 15 meV, including an isotropic spin resonance signal around 7 meV. The authors also interpret this isotropic spin resonance signal as due to the proposed singlet triplet excitation.

In contrast to these reports, in optimal doped  $\text{Ba}(\text{Fe}_{0.95}\text{Ni}_{0.05})_2\text{As}_2$  the magnetic excitations are clearly anisotropic, with  $\chi''_c(\mathbf{Q}, \omega) > \chi''_{ab}(\mathbf{Q}, \omega)$  for energies below the resonance energy and  $\chi''_{ab}(\mathbf{Q}, \omega) > \chi''_c(\mathbf{Q}, \omega)$  for energies close to the resonance energy [135]. A similar situation has also been reported by Steffens et al. [226] for optimal doped  $\text{Ba}(\text{Fe}_{0.94}\text{Co}_{0.06})_2\text{As}_2$ . Here again excitations below the resonance energy of 8 meV are dominated by  $\chi''_c(\mathbf{Q}, \omega)$ , but this time the resonance at 8 meV is completely isotropic. For the anisotropic low energy part the authors further propose a second resonance signal around 4 meV exclusively polarized in out-of-plane direction. The anisotropy

of the excitation spectrum in these two doped compositions shows great similarities to the low energy excitations of undoped  $\text{BaFe}_2\text{As}_2$  [65], where again the low energy region of the excitation spectrum is predominantly polarized in out of plane direction. The authors suggest spin-orbit coupling effects and orbital degrees of freedom, as proposed for undoped Fe-based materials [35, 239], as possibly responsible for the spin anisotropy. In consideration of these similarities of the magnetic response between the undoped and lower doped 122-materials, one interpretation can be that these spin-orbit coupling effects are still present in the lower doped materials and cause the anisotropic magnetic excitations in the superconducting phase of these materials. As in overdoped  $\text{Ba}(\text{Fe}_{0.925}\text{Ni}_{0.075})_2\text{As}_2$  the spin anisotropy is absent, these orbital effects seemingly become less prominent for higher doping, with the result that spins are free to turn in all directions again. With the assumption that these orbital effects indeed are the reason for the anisotropic excitations, the situation is still compatible with the singlet-triplet excitation as explanation for the resonance signal in these materials. However, whether these orbital effects play a comparable role in doped  $\text{FeTe}_{1-x}\text{Se}_x$  materials is not conclusive from the current results. Similar to  $\text{Ba}(\text{Fe}_{0.925}\text{Ni}_{0.075})_2\text{As}_2$ , the mostly isotropic fluctuations in  $\text{FeTe}_{0.5}\text{Se}_{0.5}$  can be interpreted in terms of a reduced impact of orbital effects, possibly caused by the large separation in the phase diagram between the superconducting phase and the magnetically ordered phase. However, note that the small anisotropy present at  $E_R$  shows the opposite polarization direction to the anisotropy in the 122-materials, which might indicate a different origin than in the 122-materials. So, in order to clarify if these orbital effects are effective in the 11-materials, polarized data of lower doped  $\text{FeTe}_{1-x}\text{Se}_x$  materials are mandatory. It should be mentioned, however, that after all the magnetic characteristics of the 11-materials show some distinct differences to the 122-materials, such as a propagation vector of the static magnetic order which does not match the nesting vector, the additional spin ice phase separating the magnetic ordered and superconducting phases and the spectrum of the spin fluctuations at  $\mathbf{Q}_{AFM}=(0.5, 0.5, 0)$  consisting of two separate excitation modes. And so comparing the mechanisms active in the 11-materials to the mechanisms in the 1111- and 122-materials might just have a limited applicability.

Regarding the second resonance signal observed in optimal doped  $\text{Ba}(\text{Fe}_{0.94}\text{Co}_{0.06})_2\text{As}_2$  [226] slightly below the original resonance and consisting exclusively of out-of-plane excitations, conclusive statements cannot be made from the current data. The results of this study do not show any indications for a second resonance signal located at lower energies in  $\text{FeTe}_{0.5}\text{Se}_{0.5}$ . However, this could also be because of the strong antiferromagnetic L-dependence of the mode, which in  $\text{Ba}(\text{Fe}_{0.94}\text{Co}_{0.06})_2\text{As}_2$  occurs most intense for the (0.5, 0.5, 1) reflection and much weaker at (0.5, 0.5, 0). With the set up the experiments of this study were conducted with the (H, H, 0) scattering plane, any zone center reflections in (0, 0, L) direction, such as (0.5, 0.5, 1) were not accessible. The absence of any resonance signal at (0.5, 0.5, 0) in  $\text{FeTe}_{0.5}\text{Se}_{0.5}$  can be interpreted as either the complete nonexistence of a second resonance or an even stronger antiferromagnetic L-dependence of a possible second resonance with all

intensity concentrated for  $(0.5, 0.5, L=\text{odd})$  reflections. However, this strong  $(0, 0, L)$  dependence of a second resonance seems rather unlikely.

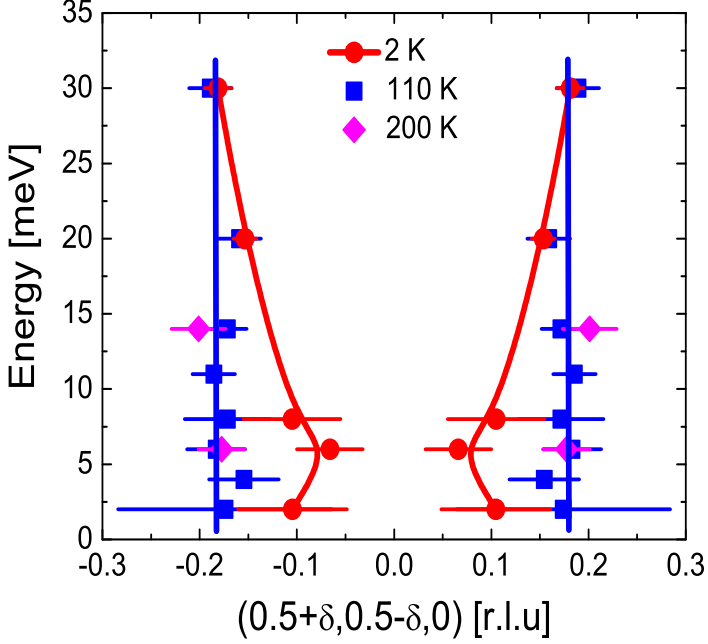


**Figure 7.4:**  $\mathbf{Q}$ -energy dispersion of the spin excitations obtained via polarized neutron scattering. Illustrated are intensities obtained for the (SF)-channel with x-polarized incident neutrons. According to equations (7.2) the here illustrated cross section  $\sigma_{xx}^{SF}$  is proportional to  $\chi''_{ab}(\mathbf{Q}, \omega) + \chi''_c(\mathbf{Q}, \omega)$  and thus describes purely magnetic intensity. The intensities were obtained through transverse constant energy-scans in  $(H, -H, 0)$ -direction through  $\mathbf{Q}=(0.5, 0.5, 0)$ , for sample temperatures 2 K (red dots), 110 K (blue squares) and 200 K (pink diamonds). Red and blue solid lines serve as guides to the eye. The constant energy scans and Gaussian fits that lead to this dispersion can be found in figure A.10 in the appendix.

In addition to the superconducting state, an investigation of the spin excitations in the normal state for temperatures above  $T_c$  has been performed. Here the focus was on the transverse dispersion of the two counter-propagating modes for energies up to 30 meV. Figure 7.4 illustrates the  $\mathbf{Q}$ -energy dispersion of the spin fluctuations in transverse  $(H, -H, 0)$ -direction. The dispersion was obtained by performing constant energy transverse

scans through the commensurate positions  $\mathbf{Q}=(0.5, 0.5, 0)$  and  $\mathbf{Q}=(1.5, 1.5, 0)$  at various temperatures and energies, as illustrated in figure A.10 in the appendix. Collecting (SF)-intensity with x-polarization of the incident neutrons, provided purely magnetic intensities proportional to  $\chi''_{ab}(\mathbf{Q}, \omega) + \chi''_c(\mathbf{Q}, \omega)$ . The peak positions of the two split peaks corresponding to the two modes were determined by least square fits of Gaussian peak functions to the transverse scans.

As figure 7.4 shows, the spin fluctuation spectrum of the superconducting state (2 K), represented by the red dots, exhibits an obvious hourglass type dispersion, with a narrow part close to the resonance energy at 7 meV, as the two counter-propagating modes move towards the commensurate  $\mathbf{Q}=(0.5, 0.5, 0)$  position, and two wider parts for energies above and below 7 meV, where the modes tend to move further away from the commensurate position. A very similar hourglass dispersion has been reported for two superconducting and non-superconducting  $\text{FeTe}_{1-x}\text{Se}_x$  compositions [231]. This observation of a similar hourglass dispersion also in a non-superconducting compound suggests that the feature is independent from the superconducting state. This is supported by results for cuprate materials where the hourglass dispersion is observed for superconducting as well as non superconducting materials [240–245]. A widely accepted explanation for this prominent shape of the dispersion is not available so far. A pattern of alternating spin and charge stripes has been proposed as one possible explanation for cuprate materials [246], but this of course cannot explain the hourglass shape present for all those materials without any stripe order.

Motivated by the metallic nature of the Fe-based superconductors Li et al. [231] proposed a special nesting condition in a multi-band itinerant picture as a possible origin for the hourglass shape of the dispersion in the  $\text{FeTe}_{1-x}\text{Se}_x$  system, a scenario closer to what is observed in metallic chromium [247, 248].

For increasing temperatures the hourglass shape disappears, as low energy excitations move further away from the commensurate position and appear at incommensurate positions similar to positions of the mode at higher energies. This leaves the transverse  $\mathbf{Q}$ -energy dispersion almost straight vertical. A similar effect of a less prominent hourglass shape with increasing temperature has also been observed for the superconducting and non superconducting  $\text{FeTe}_{1-x}\text{Se}_x$  compositions [231]. This shows that the feature obviously is a low temperature effect, its relation to the superconducting phase, however, cannot be unambiguously established.

## 7.4 Conclusion

Polarized inelastic neutron scattering experiments on a large superconducting single crystal sample of optimal doped  $\text{FeTe}_{0.5}\text{Se}_{0.5}$  have been performed and a Longitudinal Polarization Analysis of data, obtained for energies between 2 meV and 30 meV and sample temperatures between 2 K and 200 K has been conducted.

A spin resonance signal with resonance energy  $E_R = (7 \pm 1)$  meV and propagation vector close to  $\mathbf{Q}=(0.5, 0.5, 0)$  has been detected. And by taking advantage of the technique of polarized inelastic neutron scattering it was possible to identify the signal to be exclusively magnetic in nature. It was found that in transverse direction the signal splits into two modes. This splitting is interpreted as a result of a specific nesting condition, which is further supported by the fact that the spin excitations at  $\mathbf{Q}=(0.5, 0.5, 0)$  for energies above and below the resonance energy also consist of two counterpropagating modes located in transverse direction to  $\mathbf{Q}=(0.5, 0.5, 0)$ .

Regarding the spin anisotropy of the spin excitations it was found that low energy spin excitations with propagation vector close to  $\mathbf{Q}=(0.5, 0.5, 0)$  and energies up to 30 meV are mostly isotropic with equal contributions by in-plane  $\chi''_{ab}(\mathbf{Q}, \omega)$  and out-of-plane excitations  $\chi''_c(\mathbf{q}, \omega)$ . The resonance mode at 7 meV exhibits a marginal anisotropy as in-plane fluctuations are slightly enhanced for the energy region 6-8 meV. A spin resonance signal with similar spin isotropy has also been observed for another  $\text{FeTe}_{0.5}\text{Se}_{0.5}$  sample [137] and in overdoped  $\text{BaFe}_{1.85}\text{Ni}_{0.15}\text{As}_2$  [238]. This suggests that a spin isotropic resonance signal might be a universal feature for higher doped Fe-based materials, which in the phase diagram are separated from the magnetically ordered phase. An isotropic resonance signal is consistent with the proposed  $s_{\pm}$  symmetry for the superconducting gap function [116] for which a resonance mode with  $\chi''_{ab}(\mathbf{Q}, \omega) \approx \chi''_c(\mathbf{Q}, \omega)$  has been predicted. In this context, the isotropic spin resonance is interpreted as to be supportive for the proposed singlet-triplet excitation.

The  $\mathbf{Q}$ -energy dispersion of the spin excitations located around  $\mathbf{Q}=(0.5, 0.5, 0)$  in the superconducting state (2 K sample temperature) exhibits a prominent hourglass shape. The excitations consist of two counter-propagating modes located in transverse direction to  $\mathbf{Q}=(0.5, 0.5, 0)$ . For energies close to the resonance energy  $E_R=7$  meV the two modes move closer to the commensurate position and move away from this position again for energies below and above  $E_R$ , creating this prominent hourglass type shape of the excitation spectrum. A similar shaped dispersions has been reported for a superconducting and a non-superconducting  $\text{FeTe}_{1-x}\text{Se}_x$  sample [231], and according to the authors a special nesting condition in a multi-band itinerant picture might be a possible origin for the hourglass shape of the dispersion in the  $\text{FeTe}_{1-x}\text{Se}_x$  system. With increasing temperature across  $T_c$  the hourglass shape disappears, as low energy excitations move to more incommensurate positions. This leaves the hourglass dispersion to be a low temperature effect, however, not necessarily related to the presence of the superconducting phase.



## 8 Summary and Outlook

In this study several different aspects of magnetic properties on a series of different Fe-based superconducting materials have been studied using the techniques of polarized and non polarized neutron diffraction and neutron spectroscopy. The eight samples, that were investigated in the course of this thesis, represent the three main classes of Fe-based materials, the so called 11-, 1111- and 122-materials. The main part of the studies focused on investigations of the excitation spectra of spin wave excitations of the static Fe SDW order as well as of the spin fluctuations present in the superconducting phase. Whereas, a small part focused on a unique phenomenon of coexistence of static magnetic order and superconductivity. The main results obtained via the neutron scattering experiments will be outlined in the following.

**$\text{EuFe}_2(\text{As}_{1-x}\text{P}_x)_2$  and  $\text{Eu}(\text{Fe}_{1-x}\text{Co}_x)_2\text{As}_2$**  On the two doped  $\text{EuFe}_2\text{As}_2$  systems valuable information on the effect of impurity doping on the static order of the magnetic sublattice of the  $\text{Eu}^{2+}$ -moments was obtained by performing single crystal neutron diffraction and polarized neutron diffraction experiments.

The diffraction experiments on the  $\text{EuFe}_2(\text{As}_{1-x}\text{P}_x)_2$  showed that partial substitution of As by P leads to a modification of the A-type magnetic structure of the Eu-sublattice present in undoped  $\text{EuFe}_2\text{As}_2$ . For 15% P-doping the magnetic structure is transformed into a ferromagnetic type structure with magnetic moments tilted out of the Eu-layers along the c-axis. This leads to a sizeable ferromagnetic component of the Eu-sublattice with a ferromagnetically ordered moment along the c-axis approximately close to the  $6.8 \mu_B$  saturation magnetic moment of the undoped composition. The astonishing of this result is the coexistence of this large ferromagnetically ordered moment and bulk superconductivity. After several predictions of the coexistence of superconductivity and ferromagnetic order in these materials, based on characterization measurements as well as Mössbauer spectroscopy, which all report a microscopic coexistence rather than a phase separation of both phenomena, the presented neutron scattering results display the first clear and direct observation of the long range ferromagnetic order of the Eu-sublattice coexisting with superconductivity.

The partial substitution of Fe by Co in  $\text{Eu}(\text{Fe}_{1-x}\text{Co}_x)_2\text{As}_2$  has a different effect on the static magnetic order of the  $\text{Eu}^{2+}$ -moments. Here it was found that Co-doping leads to a helical type structure, with magnetic moments rotated around the crystallographic c-axis but oriented within the basal planes.



**Ba(Fe<sub>1-x</sub>Co<sub>x</sub>)<sub>2</sub>As<sub>2</sub>** In underdoped Ba(Fe<sub>0.95</sub>Co<sub>0.05</sub>)<sub>2</sub>As<sub>2</sub> a thorough study of the low energy spin excitation spectrum has been conducted using the technique of time-of-flight neutron spectroscopy. It was possible to perform a quantitative analysis of the spin wave excitations of the static SDW-order using a linear spin wave model based on a local moment Heisenberg Hamiltonian. The model provides a reasonable description of the obtained data. The resulting exchange parameters are reduced to about 75% of the values reported for undoped BaFe<sub>2</sub>As<sub>2</sub>. The best fit results were achieved for a strong anisotropy of the in-plane exchange parameters, similar to what is reported for undoped 122-materials. Spin wave excitations obtained for the phase of coexistence of superconductivity and SDW-order do not show a dramatic difference to the spin wave excitations above  $T_c$ . Above the Néel temperature the excitations appear broadened and reduced in intensity but can still be described by the spin wave model, with similar anisotropic exchange parameters. In addition to the linear spin wave model, the low energy paramagnetic excitations can further be described using a model based on spin diffusion theory. The in-plane correlation lengths of the paramagnetic excitations, resulting from the spin diffusion model analysis, match really well correlation lengths of paramagnetic excitations reported for 122-materials with different doping levels. This supports the idea of paramagnetic excitations with properties universal for all Fe-based materials, independent of the doping concentrations. Since both models describe excitations in all three phases equally well, magnetic excitations in underdoped Ba(Fe<sub>0.95</sub>Co<sub>0.05</sub>)<sub>2</sub>As<sub>2</sub> need to be considered intermediate to the spin wave like excitations of the undoped materials and the short range spin fluctuations of the optimally doped materials.

**CaFe<sub>1-x</sub>Co<sub>x</sub>AsF** Time-of-flight neutron spectroscopy investigations on the low energy excitation spectrum of spin fluctuations with propagation vector  $\mathbf{Q}=(0.5, 0.5, 0)$  in superconducting CaFe<sub>0.88</sub>Co<sub>0.12</sub>AsF were performed. Below  $T_c$  the excitation spectrum exhibits a neutron spin resonance signal with characteristic energy of  $E_R=7$  meV and an excitation gap for energies below 5 meV. The presented results are the first observation of the spin resonance signal in the class of oxygen free electron doped 1111-materials. The resonance energy of  $(7\pm0.3)$  meV provides a scaling relation to the critical temperature of  $E_R \sim (3.7 \pm 0.2) k_B T_c$ , which is in good agreement to the average scaling relation for the iron pnictide superconductors  $E_R \sim (4.6 \pm 0.4) k_B T_c$ . According to the current understanding, the observation of the resonance signal promotes a superconducting gap function with  $s_{\pm}$ -symmetry for the CaFe<sub>1-x</sub>Co<sub>x</sub>AsF materials. It further supports the idea of a universal  $s_{\pm}$ -symmetry of the gap function in all Fe-based materials.

The low energy spin excitation spectrum at  $\mathbf{Q}_{AFM}=(0.5, 0.5, 0.5)$  of undoped CaFeAsF shows narrow spin wave excitations below  $T_N$  and broad rather 2D paramagnetic excitations above  $T_N$ . In the ordered phase the spin wave spectrum is gapped for energies below 5 meV. The gap energy of 5 meV is slightly below the 10 meV reported for 122-materials, which indicates smaller single ion anisotropy effects in this material. The paramagnetic excitations persist up to 270 K and exhibit strong similarities concerning

---

correlation lengths and dimensionality with paramagnetic excitations in the superconducting sample  $\text{CaFe}_{0.88}\text{Co}_{0.12}\text{AsF}$ .

**FeTe<sub>0.5</sub>Se<sub>0.5</sub>** Inelastic polarized neutron scattering study on the low energy excitation spectrum of spin fluctuations with propagation vector  $\mathbf{Q}_{AFM}=(0.5, 0.5, 0)$  in optimally doped  $\text{FeTe}_{0.5}\text{Se}_{0.5}$  have been performed. Below  $T_c$  a spin resonance signal occurs at energies between 5-9 meV, accompanied by the spin gap below 5 meV. The resonance signal is of purely magnetic origin. Along the transverse (H, -H, 0) direction the resonance signal splits into two overlapping peaks, whereas in (H, H, 0) direction the signal is peaked at  $\mathbf{Q}_{AFM}=(0.5, 0.5, 0)$ . The resonance signal as well as the rest of the excitation spectrum up to 30 meV is isotropic with equal contributions of in plane and out of plane spin excitations  $\chi''_{ab}(\mathbf{Q}, \omega) \approx \chi''_c(\mathbf{Q}, \omega)$ . This spin isotropy of the resonance signal is compatible with the theoretic understanding and promotes the  $s_{\pm}$  gap symmetry. It is further compatible with the singlet-triplet excitations as a possible microscopic origin of the signal. At low temperatures the low energy spin excitation spectrum exhibits a hourglass shaped energy dispersion.

**Outlook** Since its discovery in 2008 the field of Fe-based superconductors has been very active and fast evolving due to the constant strong effort by numerous research groups. As a result of this strong push by the community a level of understanding has been achieved which is far beyond the field's relatively short time of existence.

However, the initial high hopes set into the Fe-based materials that these materials would contribute to a better understanding of the mechanism of superconductivity in the cuprate materials so far have not been fulfilled. Instead it quickly showed that aside from some obvious and characteristic similarities between cuprates and Fe-based superconductors both systems exhibit many fundamental differences and must be considered as two distinct systems. However, the fact that these systems are so fundamentally different in many areas makes the similarities that both have even more important. It seems unlikely that just by coincidence the two classes of superconducting materials with the highest  $T_c$  observed so far share such a characteristic phase diagram with a close proximity of magnetism and superconductivity and with strong magnetic fluctuations present in the entire superconducting phase. More likely this is an indication that magnetic properties indeed play an important role in the formations of high  $T_c$  superconductivity. Another characteristic both systems share and which is believed to be important for the formation of high  $T_c$  superconductivity is a moderate strength of correlations present in the electronic system. For both material classes the conduction electrons show moderately strong correlations, with correlation strengths located between the weak coupling limit of itinerant metals and the strong coupling present in the localized Mott regime. Again it seems rather unlikely that just by chance these two distinct systems show such comparable correlation strengths. And instead it is argued that the right strength of

electronic correlations, not too strong and not too weak, might in fact be an important condition to produce high coupling strengths. In addition to the moderate electronic correlations it is further argued that the system's ability to avoid Coulomb repulsion of the Cooper pair electrons is also of importance in order to produce these high coupling strengths responsible for high transition temperatures. In the cuprates and the Fe-based superconductors this minimization of Coulomb repulsion between the two electrons of one Cooper pair is accomplished by the particular symmetry of the respective superconducting gap functions.

As a result, it is argued that each of these three properties or more likely the right combination of all three might in fact be essential conditions for high  $T_c$  superconductivity. If this indeed is the case or if high  $T_c$  superconductivity is related to some other characteristics can only be answered by a much better understanding and a much more complete picture of the Fe-based and cuprate materials. For the future, this will demand a continuation of the current efforts on both cuprates and Fe-based materials. However, aside from these two classes of materials an intensified search for other superconducting materials with maybe even higher transition temperatures, seems also quite reasonable. The discovery of the Fe-based materials showed that high  $T_c$  obviously is not restricted to cuprate materials and so it would be rather surprising if the effect could not be observed in other materials as well.

If all this is considered, the impact and importance of the Fe-based superconductors to the field of high  $T_c$  superconductivity cannot be overestimated. As the cuprate materials introduced the phenomenon of high  $T_c$  superconductivity the Fe-based materials show that this phenomenon is not restricted to copper oxides and further indicate that other high  $T_c$  systems might exist. And maybe in a few years from now, scientists will look back at the Fe-based materials as the class of materials which lead them to the discovery of high  $T_c$  materials for which it finally was possible to completely understand the phenomenon of high  $T_c$  superconductivity or which lead to a variety of commercial applications.

# A Appendix

## A.1 Spin Fluctuations in Metallic Materials

### A.1.1 The Magnetic Susceptibility in the Itinerant Approach

Magnetism and magnetic properties of condensed matter materials, can be described by applying two contrary models that approach the magnetic nature of the system from two contrary points of view. One model approaches the problem from the highly correlated point of view and considers the magnetic moments to be strongly localized in real space typically at the crystallographic positions of the magnetic ions and interacting via exchange interactions. This model usually works very well for materials whose unpaired electrons are strongly bound to the atomic nuclei, and which usually show only little to no metallic behavior. Magnetic correlations for those types of materials can be very well modeled via the use of a local moment Heisenberg Hamiltonian, just as it has been introduced in a very basic way in chapter 3.

The second model approaches the problem from the very weakly correlated side and thus usually works very well for metallic materials with very loose valence electrons and for which the local moment picture usually does not provide satisfying results. This second model considers the itinerant nature of the valence electrons and their contributions to magnetism, and in contrast to the local moment picture, where magnetic properties are discussed with respect to real space, the picture of itinerant magnetism discusses the magnetic properties carried by the itinerant electrons in momentum-space.

These two approaches obviously are conceptually very different and describe two opposite ends of the spectrum, where on the one end the valence electrons are very tightly bound to the positions of the magnetic ions with very little overlap of orbitals from neighboring sites. Whereas, on the other end the electrons are very loosely bound, more or less detached from the atomic cores with great overlap of orbitals from neighboring sites. Which model is the correct one to describe the nature of magnetism of the Fe-based superconductors is still a subject of debate. Many magnetic features strongly suggest a not negligible contribution by the itinerant conduction electrons, whereas other features can be described in a reasonable way by a local moment approach. This locates the Fe-based materials into the intermediate region between strongly correlated and completely itinerant materials, however still more on the itinerant side than on the localized side. Thus it seems essential to spend some time on introducing the fundamentals of the model of itinerant magnetism.

Here the most basic features of the itinerant model will be outlined without going into much detail. Especially the derivation of any of the necessary equations will completely be neglected. However all formulas can be found in many very good fundamental text books and review articles [249–251].

In a metallic material, the itinerant conduction electrons are responsible for the magnetic properties, and as a result magnetic properties are directly related to the band structure and the Fermiology of the material. As Pauli stated, only the electrons close to the Fermi surface are able to contribute, whereas the majority of the valence electrons remain in-active. As a result, the response of such a system is characterized by the density of states at the Fermi level  $N(E_F)$ , which strikingly shows in the so-called Pauli susceptibility as it is directly proportional to  $N(E_F)$ :

$$\chi_P = \mu_0 \mu_B^2 N(E_F) \quad (\text{A.1})$$

$\chi_P$  is usually a very small and almost temperature independent quantity. The fact that only electrons close to the Fermi level contribute explains the small value for  $\chi_P$  and the usually high Fermi temperature for normal metallic materials causes the small temperature dependence.

The Pauli susceptibility in (A.1) completely neglects any contribution by interactions between the conduction electrons. However, interactions between electrons of the Fermi gas lead to very important effects, which can change the magnetic response dramatically. And one way to incorporate interactions into the discussion is by applying a so-called mean-field approach. In this approach, interactions between a given electron and the surrounding electron gas are interpreted as interactions of this particular electron with an applied magnetic field. This field results of a superposition of a possible external magnetic field and a field produced by the polarization of the electron gas consisting of all other conduction electrons. This so-called molecular field or mean field causes a polarization of the electron gas but at the same time the mean field itself is induced by a polarization of the electron gas in the first place. As a result, this approach gives rise to a positive feedback mechanism which enhances the susceptibility over the value  $\chi_P$ . The actual effective field felt by the conduction electrons consequently consists of a superposition of the two magnetic fields, the external magnetic field and the mean field  $\mathbf{H}_{eff} = \mathbf{H}_{ext} + \frac{U}{\mu_0 \mu_B^2} \mathbf{M}$ . Here  $U$  represents the power of the molecular field, which is exactly the Coulomb energy, and  $\chi$  is the real, normalized magnetic response and  $\mathbf{M} = \chi \mathbf{H}$  is the magnetization causing and being influenced by the mean field at the same time. Consequently  $\mathbf{M}$  is also  $\mathbf{M} = \chi_P \mathbf{H}_{eff}$ . If this is taken into account, the magnetic susceptibility of the system turns into,

$$\begin{aligned} \chi &= \frac{\partial \mathbf{M}}{\partial \mathbf{H}} = \chi_P \left( 1 + \frac{U}{\mu_0 \mu_B^2} \chi \right) \\ &= \frac{\chi_P}{1 - \frac{U}{\mu_0 \mu_B^2} \chi_P}. \end{aligned} \quad (\text{A.2})$$

This shows that the Pauli paramagnetism is enhanced by the factor  $(1 - \frac{U}{\mu_0 \mu_B} \chi_P)^{-1} = (1 - UN(E_F))^{-1}$  induced by the molecular field. For the case that  $UN(E_F) \geq 1$  spontaneous ferromagnetic order will occur and the inequality is the well-known Stoner criterion for the occurrence of ferromagnetism. Note, the driving forces that induce the mean field are exchange interactions of the electrons. As a result, the field is driven by Coulomb interactions within the electron gas and not by magnetic dipolar interactions even though the resulting field has the characteristics of a magnetic field.

### The Generalized Susceptibility

The generalized susceptibility expresses the most general form of magnetic response of the system to an applied magnetic field varying both in space and time. Such a magnetic field is characterized by its wave-vector  $\mathbf{q}$  and frequency  $\omega$  and presents a perturbation to the electron gas which results in quantum transitions of the electrons from quantum states  $(\mathbf{k}, E_{\mathbf{k}})$  into  $(\mathbf{k} + \mathbf{q}, E_{\mathbf{k}+\mathbf{q}})$ . Each excitation from quantum state  $\mathbf{k}$  to quantum state  $\mathbf{k} + \mathbf{q}$  requires a certain amount of energy  $\hbar\omega = E_{\mathbf{k}+\mathbf{q}} - E_{\mathbf{k}}$ , where the energies  $E_{\mathbf{k}}$  and  $E_{\mathbf{k}+\mathbf{q}}$  of the particular quantum states are given by the band dispersion of the material. Taking into account a possible exchange splitting  $\Delta$ <sup>1</sup> of the electron bands into two ( $\uparrow \downarrow$ ) spin subbands will turn the spin of the band electrons into another degree of freedom, and the energies  $E_{\mathbf{k}}$  of the various quantum states now also depend on the spin directions ( $\uparrow$  or  $\downarrow$ ). This leads to the quantum state energies  $E_{\mathbf{k}}^{\sigma} = E_{\mathbf{k}} + \frac{1}{2}\sigma\Delta$ , where  $\sigma = +, -$  labels the spin polarization. A perturbation by such a magnetic field, varying in space and time, on the band electrons of the system leads to a magnetic response in first order (linear response), which reads in its general form as,

$$\chi_0^{\sigma_1 \sigma_2}(\mathbf{q}, \omega) = \mu_0 (g\mu_B)^2 \frac{1}{N} \lim_{\epsilon \rightarrow 0+} \sum_{\mathbf{k}} \frac{f(E_{\mathbf{k}+\mathbf{q}} + \frac{1}{2}\sigma_2\Delta) - f(E_{\mathbf{k}} + \frac{1}{2}\sigma_1\Delta)}{E_{\mathbf{k}+\mathbf{q}} - E_{\mathbf{k}} - \hbar\omega + \frac{1}{2}(\sigma_2 - \sigma_1)\Delta + \epsilon i}. \quad (\text{A.3})$$

This is the so-called Lindhard function, which provides a model for the magnetic response of metallic systems. The function  $f(E)$  is the Fermi distribution, and accounts for the occupation of the initial  $(\mathbf{k}, E_{\mathbf{k}}, \sigma_1)$  and final  $(\mathbf{k} + \mathbf{q}, E_{\mathbf{k}+\mathbf{q}}, \sigma_2)$  states and thus regards the probability of a transition from one quantum state to another. Note that, due to the Pauli principle excitations are only possible from occupied states into empty states. The denominator of the Lindhard function considers the energies of the initial and final quantum states plus the excitation energy  $\hbar\omega$  and thus secures the energy conservation for any possible excitations. In this chapter only the main properties of the function will be outlined very briefly. A detailed descrip-

---

<sup>1</sup>In the course of this thesis  $\Delta$  was reserved for the superconducting gap function. In this chapter, however, it will represent the subband splitting. The context should prevent from any confusion caused by this double use of the symbol.

tion of the complete function and its derivation, however, can be found in refs. [158, 250].

The Lindhard function usually is a complex function consisting of a real and an imaginary part. For this thesis, however, the imaginary part is of special interest as it considers the fluctuations of the system and thus considers the particle hole excitations that are accessible via the inelastic neutron scattering cross section. With the following expression,

$$\text{Im} \lim_{\epsilon \rightarrow 0+} \frac{1}{x + \epsilon i} = -\pi \delta(x) \quad (\text{A.4})$$

the imaginary part of the magnetic susceptibility can be expressed in terms of,

$$\text{Im} \chi_0^{\sigma_1 \sigma_2}(\mathbf{q}, \omega) = \pi \mu_0 (g \mu_B)^2 \frac{1}{N} \sum_{\mathbf{k}} \left( f(E_{\mathbf{k}}^{\sigma_1}) - f(E_{\mathbf{k}+\mathbf{q}}^{\sigma_2}) \right) \cdot \delta(E_{\mathbf{k}+\mathbf{q}}^{\sigma_2} - E_{\mathbf{k}}^{\sigma_1} - \hbar \omega) \quad (\text{A.5})$$

The sum over the Brillouin zone considers all possible excitations of electrons from the quantum state  $(\mathbf{k}, \sigma_1, E_{\mathbf{k}}^{\sigma_1})$  into the quantum state  $(\mathbf{k} + \mathbf{q}, \sigma_2, E_{\mathbf{k}+\mathbf{q}}^{\sigma_2})$ . The  $\delta$ -functions regard the energy conservation for all possible excitations. This means, such an excitation creates an electron-hole pair, where an electron is excited from its initial ground state  $(\mathbf{k}, \sigma_1, E_{\mathbf{k}}^{\sigma_1})$  into the excited state and leaves a hole  $(-\mathbf{k}, \sigma_1, E_{\mathbf{k}}^{\sigma_1})$ . Such particle-hole excitations can occur from any occupied state into any empty state, and for a given  $\mathbf{q}$  usually excitations with different energies  $\omega$  are possible. In  $\mathbf{q} - \omega$ -space all these possible excitations form a continuum whose boundaries are determined by the band dispersion. This is the so-called Stoner-continuum of single-particle excitations and which is directly represented by  $\chi''(\mathbf{q}, \omega)$ , the imaginary part of the magnetic susceptibility.  $\chi''(\mathbf{q}, \omega)$  as it is defined by eq. (A.5) possesses the following symmetry with  $\text{Im} \chi_0^{\sigma_1 \sigma_2}(\mathbf{q}, \omega) = -\text{Im} \chi_0^{\sigma_2 \sigma_1}(-\mathbf{q}, -\omega)$  and is zero for  $\omega = 0$ , as it only considers the dynamic part of the magnetic response.

Regarding the spin of the initial and excited quantum states, there are four possible excitation, two non-spin-flip excitations where the spin orientation remains the same ( $+\rightarrow +$ ) and ( $-\rightarrow -$ ), as well as two spin-flip excitations, where the spin orientation of the excited state is opposite to the orientation of the initial state ( $+\rightarrow -$ ) and ( $-\rightarrow +$ ).

In a paramagnet with ( $\Delta = 0$ ), zero exchange splitting of bands, and without any external field and consequently no anisotropy in spin space, all these four possible excitations are of course equivalent and the situation simplifies a lot. Otherwise, the spin-flip excitations correspond to the transverse, and the non-spin-flip excitations to the longitudinal part of the susceptibility. In the case of a non-zero exchange splitting of the bands with  $\Delta \neq 0$ , the continuum of spin-flip excitations looks very different from the one of non-spin-flip excitations.

## The Consideration of Exchange Interactions

As it was shown for the Pauli susceptibility, the actual magnetic response is enhanced by the Stoner-factor, caused by exchange interactions. In a similar way this enhancement can be applied to the generalized susceptibility  $\chi_0$ , which then leads to

$$\chi(\mathbf{q}, \omega) = \frac{\chi_0(\mathbf{q}, \omega)}{1 - \frac{U}{\mu_0(g\mu_B)^2} \chi_0(\mathbf{q}, \omega)} \quad (\text{A.6})$$

Note that  $U$  used here in principle can have a  $\mathbf{q}$  dependence, which however, often is neglected. Equation (A.6) obviously shows that due to the enhancement caused by the Stoner-factor,  $\chi$  will diverge anytime the denominator becomes zero. Thus the system has potential magnetic instabilities which can lead to long range magnetic ordered ground states (Spin Density Wave order). The formation of these long range magnetic order, so-called static Spin Density Waves, are heavily dependent on the exchange interactions as well as band dispersions and the Fermiology of the system. A brief introduction of the SDW state will be given in the following section.

### A.1.2 The Response Function of the One Dimensional Electron Gas

For highly anisotropic metallic materials, a group of materials the iron based superconductors arguably can be included to, some new effects can occur, which shall be outlined in this section. In order to cover the high degree of anisotropy in these materials the idealized situation of one-dimensional metals will be discussed here, as many expressions will become much easier that way.

Derivations of all formulas and a more detailed discussion of the topic presented in the following section can be found in [251].

In the following the response to a  $q$ -dependent but time independent external field of the one dimensional free electron gas will be discussed. The Fermi surface for such a 1D electronic system basically consists of two points in momentum-space  $-k_F$  and  $k_F$ . As already discussed in previous sections only states close to the Fermi surface can contribute to the response of the systems, and as result for the 1D electron gas only states with wave-vectors near  $2k_F$ , twice the Fermi vector, are available. So for the case of the one dimensional free electron gas and wave-vectors near  $2k_F$ , twice the Fermi vector, the Lindhard response function as it was introduced in its generalized form in equation (A.3) can be expressed in the form,

$$\chi(q) = -e^2 N(E_F) \ln \left| \frac{q + 2k_F}{q - 2k_F} \right|, \quad (\text{A.7})$$



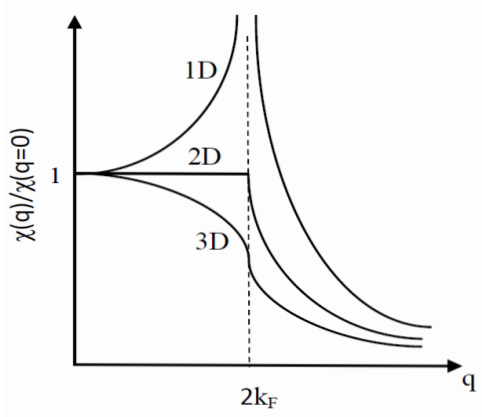


**Figure A.1:** Sketch of the normalized response function  $\chi(\mathbf{q})$  for the case of a 1D, 2D and 3D free electron gas, in the small wave-vector limit. Illustrated is the divergence of  $\chi(\mathbf{q})$  at  $q = 2k_F$  for the 1 dimensional free electron gas.

where  $N(E_F)$  represents the density of states at the Fermi energy per spin direction. As already mentioned in the previous part, the Pauli-principle is the reason why only states close to the Fermi-surface are available as possible initial states for any quantum state transition. Thus the density of states has a major influence on the electronic response to any external perturbation, and thus determines the properties of  $\chi(\mathbf{q})$ .

For small wave vectors  $q$ , the system's response can be reproduced by the so-called Thomas-Fermi approximation  $\chi(q) = -e^2 N(E_F)$ , which is independent of the system's dimensionality. However, for wave vectors equal  $2k_F$ , the response of the system  $\chi(q)$  becomes strongly dependent on the dimensionality of the electronic system. As illustrated in figure A.1 close to  $2k_F$   $\chi(\mathbf{q})$  exhibits a reversal point of the slope in the 3D case which develops into a full singularity for the 1D case. This divergence of  $\chi(q)$  for  $q = 2k_F$  has several important consequences, as an external periodic perturbation with periodic modulation equal to  $2k_F$  can lead to a divergent charge redistribution. This suggests, that for  $T = 0$  the electron gas itself would be unstable with respect to the formation of a periodically varying electron charge or spin density, with a period

$$\lambda_0 = \frac{\pi}{k_F}. \quad (\text{A.8})$$

The reason for this divergence of the response of the 1D electron gas is related to the unique topology of the Fermi surface of the 1D electron gas. The relation becomes most apparent if one considers the response function for  $d$  dimensions, as defined in equation (A.3), in this slightly simplified form

$$\chi(\mathbf{q}) = \int \frac{d\mathbf{k}}{(2\pi)^d} \frac{f_{\mathbf{k}} - f_{\mathbf{k}+\mathbf{q}}}{E_{\mathbf{k}} - E_{\mathbf{k}+\mathbf{q}}} \quad (\text{A.9})$$

The equation shows that the strongest contribution to the system's response comes from pairs of states, one occupied  $f_k = 1$ , one empty  $f_{k+2k_F} = 0$  and separated in reciprocal space by twice the Fermi vector  $q = 2k_F$ <sup>2</sup>. These pairs of states give a divergent contribution to the integral of the Lindhard function, regardless of the dimensionality of the electronic system. However, for higher dimensional systems the number of states available to create these pairs is very small, as pointed out earlier only states located on the Fermi-surface can contribute here. But, if the system's dimensionality is reduced the number of available states drastically increases. The reason for this is the already mentioned particular topology of the Fermi surface of such low dimensional electronic systems. A common feature of low dimensional electronic systems is the effect of Fermi surface nesting. This term describes the situation where parts of the Fermi surface are parallel to other parts of that Fermi surface. The effect of these parallel parts is that for wave vectors connecting these parallel parts, so-called nesting vectors, the number of paired states contributing to (A.9) is dramatically enhanced. Figure A.2 illustrates three possible idealized Fermi surfaces for a 1D, 2D and 3D free electron gas, where the red regions illustrate the available states for creation of such pairs. The 1D Fermi surface from figure A.2 is of course an idealized situation, and occurs, if at all, only for extremely anisotropic systems. However situations where the Fermi surface is quasi 1D with large areas of the Fermi surface which are nested (parallel) can indeed be observed experimentally for real materials. For wave-vectors close to the nesting vector, which connects the parallel parts, the system is 1D and consequently the Lindhard function will diverge and the electronic system will be unstable.

---

<sup>2</sup>At  $T=0$  K the Fermi distribution of occupied states is a step function which is equal one for energies below and equal the Fermi energy  $f(E \leq E_F) = 1$  as all states are completely occupied up to the Fermi energy. For energies above the Fermi energy  $f(E > E_F) = 0$  the Fermi distribution is zero as all states above  $E_F$  are empty.

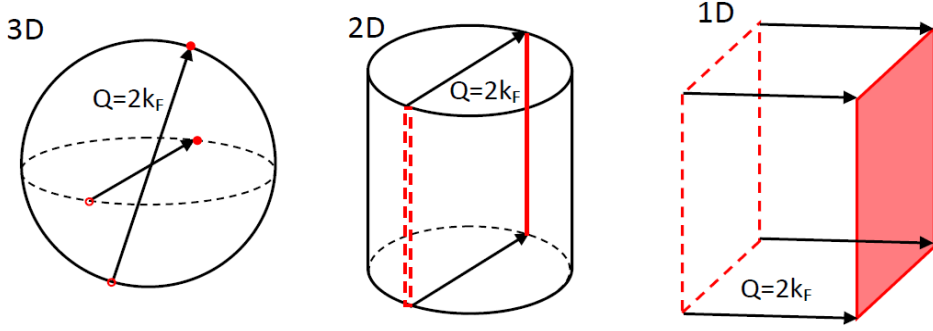


**Figure A.2:** Sketch of simplified Fermi surfaces for the case of a 1D, 2D and 3D free electron gas. The red shaded areas illustrate the regions on the Fermi surface that can be located on top of each other by a translation of the Fermi surface by the translation vector  $Q_{\text{nesting}} = 2k_F$ . Thus these regions represent the states available for forming the pairs with  $f_k = 1$  and  $f_{k+Q_{\text{nesting}}} = 0$  plus  $E_k = E_{k+Q_{\text{nesting}}}$  from equation (A.9).

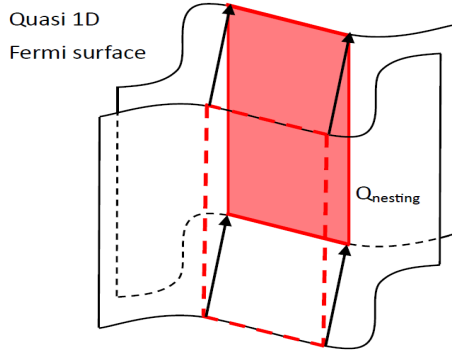


**Figure A.3:** Sketch of a simplified Fermi surface for the case of a quasi 1D free electron gas. The red shaded areas illustrate the regions on the Fermi surface which are parallel and for which the electron gas is quasi 1D. As for the 1D electron gas states in these regions represent the states available for forming the pairs with  $f_k = 1$  and  $f_{k+Q_{\text{nesting}}} = 0$  plus  $E_k = E_{k+Q_{\text{nesting}}}$  from equation (A.9).

### A.1.3 Instabilities in a One Dimensional Electron Gas

As already mentioned in the previous sections interactions between electrons of the electron gas are very important and lead to several important effects. These effects

related to the various types of interactions in the 1D electron gas will be introduced here. Without specifying the particular interactions present in the material it will be assumed that an external potential  $\phi^{ext}(q)$  induces a density fluctuation  $\rho^{ind}(q)$ , which will lead to a potential  $\phi^{ind}(q)$  induced by the density fluctuation,

$$\phi^{ind}(q) = -g\rho^{ind}(q), \quad (\text{A.10})$$

where  $g$  is a  $q$ -independent coupling constant, which accounts for the various interactions available to affect the electron gas. The positive feedback mechanism leads to,

$$\rho^{ind}(q) = \chi(q)\phi(q) = \chi(q)\left[\phi^{ext}(q) + \phi^{ind}(q)\right] \quad (\text{A.11})$$

which combined with equation (A.10) gives the following expression for the induced density fluctuation,

$$\rho^{ind}(q, T) = \frac{\chi(q, T)\phi^{ext}(q)}{1 + g\chi(q, T)}. \quad (\text{A.12})$$

According to equation (A.12) the density fluctuations become enhanced by the interactions within the electron gas, represented by the  $g$ -factor, and for  $g < 0$  the system becomes unstable when the following is valid,

$$1 + g\chi(q, T) = 0 \quad (\text{A.13})$$

the system becomes unstable to the spontaneous formation of divergent density fluctuations. For the case of electron-electron interactions and small wave vectors  $q = 0$ , expression (A.13) is the well known Stoner-criterion for the onset of spontaneous ferromagnetic order of the conduction electrons, which was introduced in one of the previous sections. However, since the general case is discussed here and the nature of the interactions, considered by the  $g$ -factor, are not specified, this expression shows the system is unstable in regard of the formation of several different ordered ground states. In the following some of these possible ground states will be outlined briefly.

The density fluctuation  $\rho^{ind}(q)$  reflects the formation of the electron-electron or electron-hole pairs of quantum states located at different parts of the Fermi surface and the ground state of the system at  $T = 0$  would be a coherent superposition of these various pair states, where the nature of the ground state, which is dependent on the nature of the predominant pair states, depends on the nature of the electron-electron or electron-phonon interactions present in the system. To briefly introduce these various ground-states, it is helpful to assume a 1D Fermi surface which consists of just two points at  $\pm k_F$ . Further it shall be defined that electrons and holes located at the right or left side are denoted as  $e_+$  and  $e_-$  as well as  $h_+$  and  $h_-$ . When further the spin of each particle  $\sigma$  is considered, these four possibilities for pair formations may occur,

$e_+, \sigma; e_-, -\sigma$	pairs with total momentum	$q = 0$	singlet superconductor
	pairs with total spin	$S = 0$	
$e_+, \sigma; e_-, \sigma$	pairs with	$q = 0$	triplet superconductor
		$S = 1$	
$e_+, \sigma; h_-, \sigma$	pairs with	$q = 2k_F$	charge density wave
		$S = 0$	
$e_+, \sigma; h_-, -\sigma$	pairs with	$q = 2k_F$	spin density wave
		$S = 1$	

The first two states listed here, develop as electron-electron pairs with zero total momentum, and the interaction channel is called the particle-particle or Cooper channel. The resulting ground states for these interactions are the well known singlet or triplet superconducting states in metals. The second two states consist of particle-hole pairs with a net total momentum of  $q = 2k_F$  and they result from the divergence of the charge and spin density fluctuations around  $q = 2k_F$ . This interaction channel is referred to as the particle-hole or Peierls channel. The ground-states resulting from these pair formations are the Charge Density Wave (CDW), for zero total spin, and the Spin Density Wave (SDW) with a total spin of  $S = 1$  for each electron hole pair. These two states exhibit a periodic variation of the charge or spin density with a period associated with the spatial variation of the charge or spin density of  $\lambda_0 = \pi/k_F$ . Which of these four states occurs depends on the properties of the predominant electron-electron and electron-phonon interactions present in the system.

#### A.1.4 The Spin Density Wave Groundstate

As the static magnetic order of the Fe-magnetic moments in the Fe-based materials is referred to as a possible SDW-instability the case of the SDW formation will be outlined in the following.

The driving force behind the formation of the spin density wave groundstate are the electron-electron interactions of the conduction electrons in metallic materials. Below the transition temperature these interactions are sufficiently strong to overcome temperature related fluctuation effects and as a result the static spatial varying spin density wave forms. The spin density can be written as,

$$S(x) = \frac{1}{2} \sum_{k, k'} \left( a_{k, \uparrow}^\dagger a_{k', \uparrow} - a_{k, \downarrow}^\dagger a_{k', \downarrow} \right) e^{-i(k-k')x}, \quad (\text{A.14})$$

where  $a$ ,  $a^\dagger$  are the creation annihilation operators for particles with wave vector  $k$  and spin  $\uparrow, \downarrow$ . Since the magnetic response is diverging at  $q = 2k_F$  the contributions

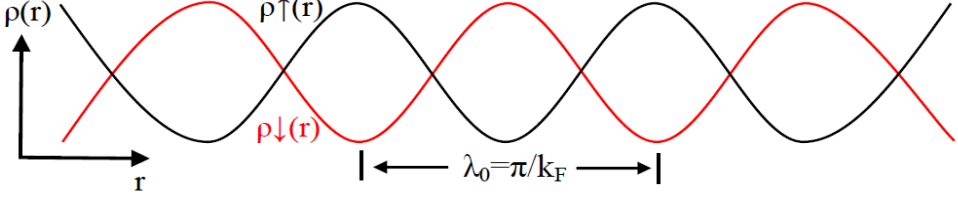


**Figure A.4:** The Spin Density Wave modulation illustrated as two charge density modulations present in the two spin subbands with the black solid line representing the charge density for the  $\uparrow$ -subband and the red line representing the  $\downarrow$ -subband.

with  $k' = k \pm 2k_F$  will be dominant and others can be neglected. This then leaves the expectation value of  $S(x)$  to be,

$$\langle S(x) \rangle = \frac{1}{2} \sum_k \left( \langle a_{k,\uparrow}^\dagger a_{k+2k_F,\uparrow} \rangle - \langle a_{k,\downarrow}^\dagger a_{k+2k_F,\downarrow} \rangle \right) e^{i2k_F x} + c.c. \quad (\text{A.15})$$

which can be transformed into,

$$\begin{aligned} S &= |S| e^{i\phi} = \langle n_{2k_F,\uparrow} \rangle = \sum_k \langle a_{k,\uparrow}^\dagger a_{k+2k_F,\uparrow} \rangle \\ &= - \sum_k \langle a_{k,\downarrow}^\dagger a_{k+2k_F,\downarrow} \rangle = - \langle n_{2k_F,\downarrow} \rangle. \end{aligned} \quad (\text{A.16})$$

Here the SDW is expressed in terms of density modulations present in each of the two spin subbands. It was further assumed that these density modulations have the same wavelengths but exhibit opposite signs in the two  $\uparrow$  and  $\downarrow$  subbands. All this considered, the spin density then can be described by

$$\langle S(x) \rangle = 2|S| \cos(2k_F x + \phi), \quad (\text{A.17})$$

which leads to a spatial dependent magnetic moment,

$$\langle \mu(x) \rangle = \mu_0 \cos(2k_F x + \phi), \quad (\text{A.18})$$

where  $\mu_0 = 4\mu_B|S|$ . So in an over simplified picture the spin density wave can be interpreted as two charge density waves present in the two spin subbands, respectively. The two charge density modulations have identical wavelengths and amplitudes but are phase shifted by  $\pi$ .

$$\rho_\uparrow(x) = \rho_0 \left( 1 + \frac{\Delta}{v_F k_F \lambda_e} \cos(2k_F x + \phi) \right) \quad (\text{A.19})$$

$$\rho_\downarrow(x) = \rho_0 \left( 1 + \frac{\Delta}{v_F k_F \lambda_e} \cos(2k_F x + \phi + \pi) \right) \quad (\text{A.20})$$

Here  $\lambda_e = UN(E_F)$  is the dimensionless electron-electron coupling strength constant. Due to the  $\pi$  phase shift between the two charge density modulations of the two  $\uparrow$  and  $\downarrow$  subbands, the overall charge density remains constant  $\rho_{\uparrow}(x) - \rho_{\downarrow}(x) = \rho_0$ . As a result only a modulation of the spin distribution in  $k$ -space occurs but no charge density wave. The situation for the idealized one dimensional electron gas can easily be transferred to the situation of a quasi one dimensional case, where only parts of the Fermi surface exhibit perfect nesting. In this case the expression for the spin density from (A.17) turns into,

$$\langle \mathbf{S}(x) \rangle = 2\mathbf{S} \cos(\mathbf{Q}_{\text{nesting}} \cdot \mathbf{r} + \phi) \quad (\text{A.21})$$

where  $2k_F$  has been substituted with the nesting vector  $\mathbf{Q}_{\text{nesting}}$  which spans the parallel regions of the Fermi surface. The nesting vector can be a three dimensional vector, depending on the topology of the Fermi surface. The resulting Spin Density Wave can either be commensurate or incommensurate, which means that the period of its modulation either is an integer multiple of the underlying crystal structure or where the period of its modulation does not fit the modulation of crystal structure.

### Collective Excitations of the Spin Density Wave Groundstate

Because of the magnetic nature of the Spin Density Wave and the fact that it can be interpreted as a superposition of two Charge Density Waves in the  $\uparrow$  and  $\downarrow$  subbands, respectively, the SDW ground-state possesses both charge and spin degrees of freedom, which results in a variety of collective excitations.

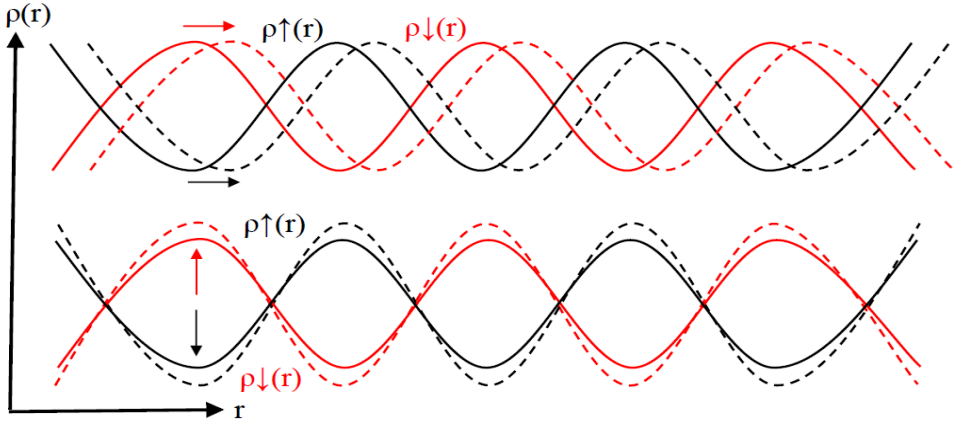


**Figure A.5:** The phase and amplitude excitations of the Spin Density Wave ground-state in the  $q = 0$  limit for the  $\uparrow$ - (black solid line) and  $\downarrow$ -subbands (red solid line). Upper panel: phase excited SDW (dashed lines). Lower panel: amplitude excited SDW (dashed lines). Modifications of phase and amplitude are illustrated by black and red arrows.

The upper panel of figure A.5 illustrates a so-called phase excitation of the SDW ground-state. Here the two CDW modulations in the two spin subbands experience a displacement synonymous to a phase shift. In this case both modulations experience the phase shift in the same direction. And because both CDW modulations are displaced in the same direction, no net CDW modulation results from this phase excitation as  $\rho_{\uparrow}(x) - \rho_{\downarrow}(x) = \text{const}$  is still valid. As a result, the excitation is restricted to the SDW groundstate. The bottom panel of A.5 illustrates an amplitude excitation of the CDW modulations. Here again no net charge modulation results from the excitations, as the amplitudes of the two CDW modulations become modified in identical fashion assuring that  $\rho_{\uparrow}(x) - \rho_{\downarrow}(x) = \text{const}$  is still valid. Obviously it is important that no net CDW modulation occurs because the picture used here to describe the SDW as a superposition of two CDW in the two subbands is only a simplified model to illustrate the spin density modulation. In reality no charge density modulation exists in the system.

Aside from the charge degree of freedom, the spin degree of freedom and its excitations are the more relevant ones for the iron based superconductors. The collective excitations in the spin channel form narrow excitation branches in  $q$ - $\omega$  space for the low energy and long wave-length region. For this low energy part of the excitation spectrum the collective excitations behave very similar to the magnon excitations of local moment Heisenberg antiferromagnets and thus can be modeled very well using a local moment approach. The one magnon cross section of a Heisenberg antiferromagnet can be used to describe the magnon excitations of the Spin Density Wave ground state. The Hamiltonian which describes the excitations of the SDW modulation is the well known Heisenberg Hamiltonian,

$$\mathcal{H} = \left( \frac{\mu}{\mu_B} \right) J_{eff} \sum_{i,j} \mathbf{S}_i \cdot \mathbf{S}_j - g\mu \mathbf{H} \sum_i \mathbf{S}_i. \quad (\text{A.22})$$

Here  $\mu/\mu_B = 4|S|$  is the reduced effective magnetic moment of the SDW modulation. It usually deviates from the magnetic moment of the local moment model which corresponds to the number of unpaired electrons located at the magnetic ions in the system. In itinerant systems the effective magnetic moment can have any value and usually is not of integer value.

For a more detailed discussion on the topic of spin and charge density waves please turn to [251].



## A.2 Details of Time-of-Flight Neutron Data Treatment

### A.2.1 The Resolution of a ToF Instrument

One very important property of any scattering instrument is its resolution, as the obtained intensity of every scattering experiment always is a convolution of the scattering function  $S(Q, \omega)$  and the instrumental resolution  $R(Q, \omega)$ . The instrumental resolution will impact the accuracy of determining the exact value for both the momentum and energy transfer, as it will introduce additional uncertainties to the measurement. In this part, where resolution effects only will be introduced in a brief manner, the focus will be on the energy resolution only. In a later passage a more detailed investigation on resolution effects will also touch the wave-vector part of the resolution function.

The energy resolution is a function of time-of-flight of the scattered neutrons and consists of several contributions by components of the instrument, introducing uncertainties to the actual time-of-flight of the detected neutrons. Some of these instrument components which contribute to the resolution, affect the time-of-flight of the detected neutron by either adding uncertainties concerning the neutron velocity, or by adding uncertainties concerning the neutrons' flight paths. The most important contributions affecting the energy resolution in a ToF experiment are introduced here.

- Finite pulse widths of the incident neutron pulse. The width of the neutron pulse here is considered in terms of time-of-flight, which leaves a large pulse width to correspond to a large uncertainty in times-of-flight. Consequently each chopper used in the spectrometer will produce an uncertainty caused by the finite opening time, which will result in a finite width of the pulse and a finite time velocity distribution of the incident neutrons. The most important to name here, are the pulse shape chopper located right behind the moderator. It modifies the shape of the pulse emitted by the moderator. Or if no pulse shape chopper is used, the pulse shape resulting from the incomplete moderation of the incident neutrons. The second to name is the sample chopper, which is located close to the sample and extracts a certain velocity out of the incoming neutron pulse. The finite pulse widths finally result in an uncertainty in time-of-flight of the detected neutrons.
- Inaccuracies in the determination of the exact flight path of the neutrons, which results in an uncertainty in time-of-flight of neutrons traveling that flight path. One component to name here, are the sample properties, such as dimensions or mosaicity, which result in a flight path difference of neutrons scattered at different parts of the sample. The second component is the finite volume of the detector tube, which also leads to an uncertainty in flight path and finally to an inaccuracy in time-of-flight of the detected neutrons.

- The instrument dimensions will have an influence on the accuracy in determination of the times-of-flight. First, long flight paths will reduce the impact of the relative flight path inaccuracies caused by the finite volumes of the sample and detector, as well as the relative time-of-flight uncertainties due to the finite pulse widths, as it will increase the overall time-of-flight. Second, long flight paths, especially  $L_1$ , pulse shape chopper to sample chopper distance, will help to separate fast from slow neutrons and thus helps to reduce the velocity distribution after the sample chopper.
- Like the instrument dimensions, the neutron velocity also affects the impact of the uncertainties caused by the pulse widths and flight path differences, as high velocities and consequently short times-of-flight increase the relative ToF uncertainties leading to a poor resolution, whereas low velocities and consequently long ToF's reduce the impact of the relative uncertainties and result in higher resolution.

If the time-of-flight uncertainties, which are caused by the finite opening times of the pulse shape chopper and the sample chopper are taken into account and labeled as  $\Delta t_p$  and  $\Delta t_c$ , respectively, and if further the various contributions to the flight path uncertainties are merged into  $\Delta L$ , the energy resolution of a classical ToF instrument reads as follows,

$$\Delta\omega = \sqrt{\left(\frac{\partial\omega}{\partial t_p}\Delta t_p\right)^2 + \left(\frac{\partial\omega}{\partial t_c}\Delta t_c\right)^2 + \left(\frac{\partial\omega}{\partial L}\Delta L\right)^2}. \quad (\text{A.23})$$

### A.2.2 Resolution Correction for the Spin Wave Analysis

All formulas regarding the energy- or  $Q$ -dependence of the instrumental resolution used in this section are taken from reference [252].

As previously mentioned, the intensity obtained via a neutron scattering experiment always results from a convolution of the scattering function  $S(Q, \omega)$ , which carries all the information about the intrinsic properties of the sample, and a resolution function  $R(Q, \omega)$ , which considers the inaccuracies in determination of the momentum- and energy-transfers, caused by components of the instrument. For some experiments the distortion of the obtained signal by resolution effects can become that serious that a subsequent correction of the data for these resolution contributions is essential. The instrumental resolution also is an important factor when choosing the right experimental set up for a particular experiment. For triple-axis experiments for example choosing between the focusing and de-focusing geometry will affect the detected signal in a dramatic way, as a clean narrow peak on the focusing side turns a broad hump undistinguishable from background for a de-focusing geometry. This is of course an extreme case, but it shows that the instrumental resolution can be a critical factor

and often needs to be taken into account during the data treatment. In this part the issue of resolution correction and how it has been performed in the course of the data treatment of the time-of-flight data which was obtained at the cold chopper spectrometer AMATERAS shall be outlined.

As discussed in chapter 5, the spin wave analysis of the time-of-flight data was performed using the tobyfit program [210]. This software was developed at the ISIS neutron scattering facility, for modeling magnetic excitation spectra obtained via ToF experiments. It uses Monte-Carlo methods to convolute user defined scattering functions with resolution functions, considering the instrumental resolution, and perform least square fits to several data sets simultaneously. tobyfit is a well accepted tool for the treatment of magnetic excitation spectra obtained by time-of-flight neutron experiments, plus it is well documented and available even for external users. This and the fact, that no comparable software is available from J-PARC still to this time, lead to the decision to apply this software for the data treatment. However, tobyfit was not necessarily the perfect solution for the data treatment, mainly because the software has been developed at ISIS exclusively for data treatment of data obtained using ISIS instruments, and more importantly it was not possible to implement a customized resolution function for the experimental set up that was used at AMATERAS. Instead tobyfit considers the instrumental resolution in a way where the instrument and set up can be chosen from a set of several ISIS instruments and various possible experimental set ups and the resulting resolution is then automatically implemented into the fitting process. Thus a more indirect path was needed in order to consider the instrumental resolution in the data treatment of the AMATERAS data. So instead of implementing the correct resolution function for the experiments right away, the resolution for AMATERAS with the particular experimental set up was calculated, and then compared to the resolution for a specific ISIS instrument and a specific experimental set up. This instrument and the set of experimental parameters, which produced a resolution matching the AMATERAS resolution was then used in tobyfit to represent the instrumental resolution, during the spin wave fitting process. Details of this resolution correction will be outlined here.

For the spin wave data analysis, only the energy part was considered, whereas the  $Q$ -part of the resolution function was neglected. This was done because it was not possible to determine the  $Q$ -part of the resolution for the ISIS instruments, and therefore, it did not make sense to calculate the  $Q$ -resolution for AMATERAS. Thus the function used to evaluate resolution effects in the experiment reads as,

$$\Delta\omega = \frac{m_n}{\hbar} \cdot \left\{ \left( \frac{v_i^3}{L_1} + \frac{v_f^3 L_2}{L_1 L_3} \right)^2 \delta t_p^2 + \left( \frac{v_i^3}{L_1} + \frac{v_f^3 (L_1 + L_2)}{L_1 L_3} \right)^2 \delta t_c^2 + \left( \frac{v_f^3}{L_3} \right)^2 \delta t_d^2 \right\}^{1/2} \quad (\text{A.24})$$

where,

- $\hbar\omega = m_n/2 \cdot (v_i^2 - v_f^2)$  is the neutron energy transfer
- $m_n$  is the neutron mass
- $v_i$  and  $v_f$  are the initial and final neutron velocities
- $L_1$  is the distance from the pulse shaping chopper to the sample chopper
- $L_2$  is the distance from sample chopper to the sample
- $L_3$  is the sample-detector distance
- $\delta t_p$  is the pulse width at the pulse shaping chopper
- $\delta t_c$  is the pulse width at the sample chopper
- $\delta t_d$  is the uncertainty of the time-of-flight in the secondary spectrometer resulting from physical extension of the sample and the neutron detection volume

Equation (A.24), expresses the energy part of the resolution function for a disc chopper time-of-flight spectrometer [252] and thus should be suitable for AMATERAS, which in fact is a disc chopper instrument. Similar to what has been introduced as the energy-resolution for a ToF instrument in (A.23), the main contributions in (A.24) result from the pulse widths at the two choppers, the pulse shape chopper and the sample chopper, with the third contribution coming from the time-of-flight uncertainties caused by the finite dimensions of the sample and the detection volume. In the calculation for AMATERAS none of the other choppers operated at AMATERAS have been considered. Even though these in principle also contribute to the time-of-flight uncertainties.

After calculating the energy resolution for several different incident neutron energies via equation (A.24) the CHOP program [253] was used to find an ISIS instrument with an experimental set up, that matched the calculated energy resolution of the experiment. CHOP is a software tool used at ISIS in order to simulate the energy resolution and neutron flux for a given ISIS instrument and specific experimental set up. Using CHOP produced a set of hypothetical experimental parameters, which later would be used in the spin wave analysis. The parameters considered by CHOP to simulate the energy resolution are: the dimensions of the instrument, the Fermi chopper properties and the moderator properties. The sample properties are neglected in CHOP as it only considers contributions by the instrument. Sample contributions were introduced into the resolution function via tobyfit at a later stage. Consequently in the calculation for AMATERAS using (A.24) sample contributions were also neglected, as they would have the least impact of the three terms anyway.

ISIS instruments all use Fermi choppers instead of disc choppers to select the wavelength or neutron velocity of the incident neutrons. Fermi choppers have a different contribution to the instrumental resolution than disc choppers which cannot necessarily

be compared to each other. Thus the Fermi chopper properties play the part of the sample chopper, and replace the second term in (A.24). In addition to this, the moderator contributions would replace the contributions of the pulse shape chopper expressed in the first term of (A.24). The moderator contributions to the instrumental resolution were determined via the Ikeda-Carpenter model. The moderator, which is placed behind the source thermalizes the incoming neutrons, which means a reduction of the neutron velocities via inelastic scattering processes between the incoming neutrons and the moderator material. However not all neutrons are slowed down in the same way, and as result neutrons with varying velocities are emitted by the moderator, which corresponds to a neutron pulse with certain pulse width. Ikeda and Carpenter [254] have developed a model to describe this influence on the pulse shape of the incoming neutron pulse by the moderator and their model gives a description for the transmission probability for incoming neutrons, regarding time and neutron velocity,

$$\begin{aligned}
P(v, t) &= (at)^2 e^{-at} \otimes [(1 - R)\delta(t) + R e^{-bt}] \\
&= \frac{2}{a} \left\{ (1 - R)(at)^2 e^{-at} + R \frac{a^2 b}{(a - b)^3} \right. \\
&\quad \times \left. [2e^{-bt} - [2 + 2(a - b)t + (a - b)^2 t^2] e^{-at}] \right\}, \tag{A.25}
\end{aligned}$$

where  $\otimes$  denotes a convolution and  $\delta(t)$  is the Dirac  $\delta$ -distribution. The first term of the moderator speed-time distribution is considered the slowing-down term and describes the neutrons, which leak out of the moderator without complete thermalization. Whereas the second term (the storage term) represents the time distribution of the thermalized neutrons. According to equation (A.25), three parameters contribute to the speed-time distribution,  $a = \Sigma v t$  with  $\Sigma$  which is the macroscopic neutron cross section of the moderator material,  $b$  the inverse time constant for the storage term and  $R$ , which illustrates a switch function between these two terms and which is expressed in terms of a Boltzmann-function  $R = \exp(-\hbar\omega/\hbar\omega_0)$ , where  $\hbar\omega$  is the neutron energy and  $\hbar\omega_0 = f k_B T_{mod}$  is a characteristic energy for the moderator with  $T_{mod}$  being the moderator temperature and  $f$  a scaling factor. The different parameters in (A.25) can be determined by fitting the Ikeda-Carpenter model to the incoherent elastic line of the excitation spectrum from a vanadium standard sample. Since vanadium is an almost perfect incoherent scatterer, the scattered intensity has no wave-vector dependence which means, that almost no Bragg peaks occur. Thus the shape of the elastic line<sup>3</sup> then corresponds to the speed-time distribution of the incoming neutrons, in other words it depicts the pulse shape of the incoming neutrons transmitted by the moderator. Unfortunately, due to the sudden ending to the experiments caused by the severe earthquake in Japan on 11th March 2011, it was not possible to perform a measurement on a vanadium sample during the experiments at AMATERAS. So in

---

<sup>3</sup>The term elastic line means the region of the spectrum with zero energy transfer. By performing an energy cut through this region the shape (in energy) of the elastic line can be determined.

order to determine moderator parameters the Ikeda-Carpenter model was fitted to the incoherent elastic line of the sample scans. A  $Q_h - Q_k$ -integration range was chosen, for which magnetic or nuclear Bragg peaks are absent and thus all scattered intensity in the elastic line would be completely of incoherent nature,  $Q_h = 1.3 - 2.7$  [r.l.u.],  $Q_k = -0.5 - 0.5$  [r.l.u.]. Figure A.6 shows the energy cut, which was performed at this particular  $Q_h - Q_k$  integration window and the solid line depicts the best fit of the Ikeda-Carpenter model to the data. The resulting values for the moderator contribution

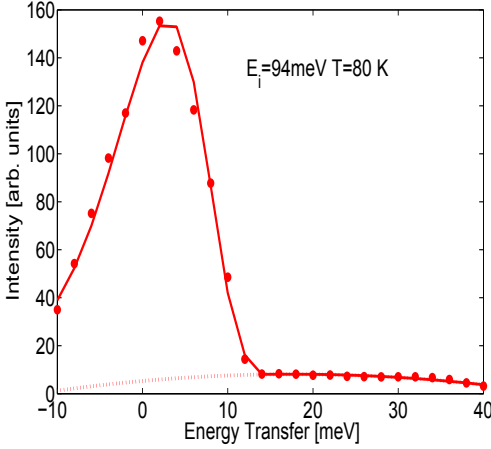
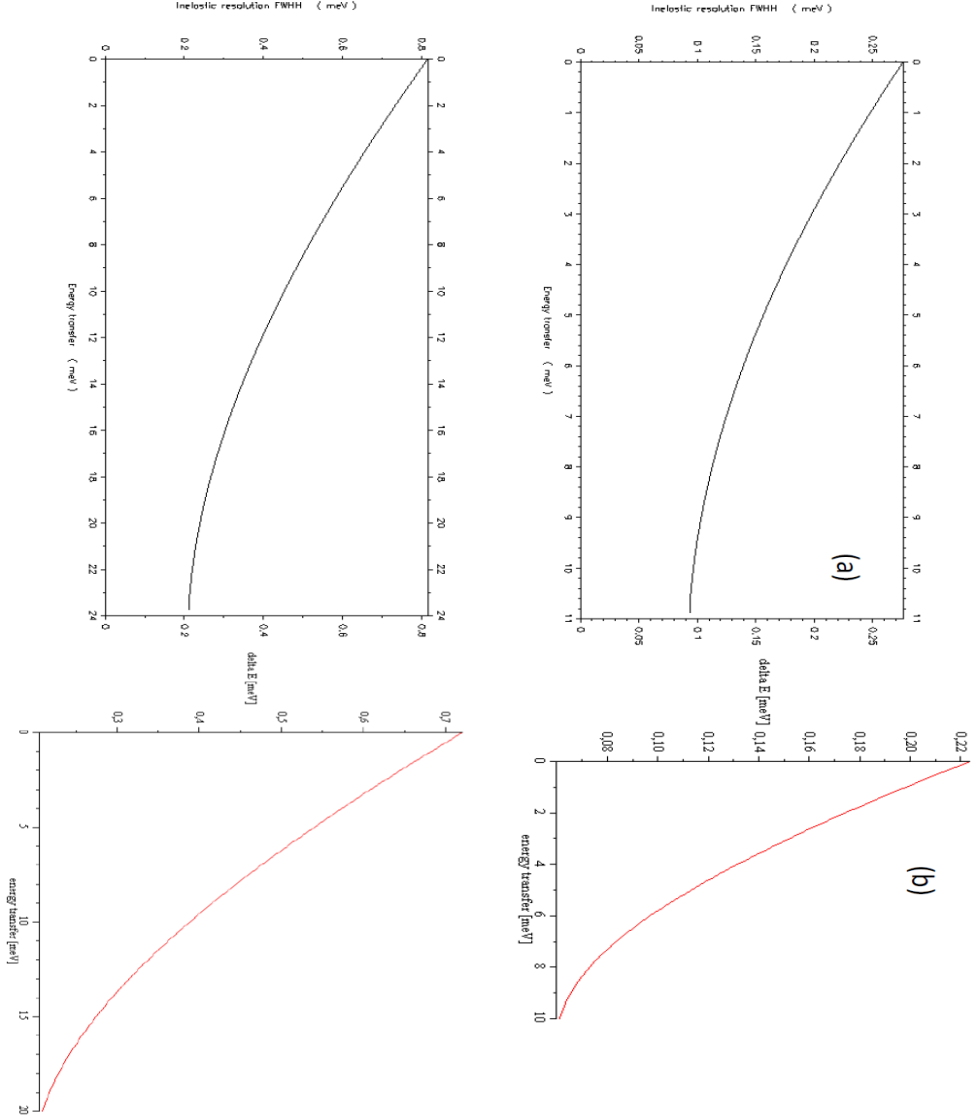


**Figure A.6:** Constant  $\mathbf{Q}$ -cut at the  $\mathbf{Q}_h - \mathbf{Q}_k$  integration range  $\mathbf{Q}_h = 1.3 - 2.7$  [r.l.u.] ;  $\mathbf{Q}_k = -0.5 - 0.5$  [r.l.u.]. The displayed data was obtained for a sample temperature of 80 K and an incident neutron energy of 94 meV. The shown data is not corrected for the thermal-population factor and thus features the scattering function  $S(\mathbf{Q}, \omega)$ . The red solid line is the best fit to the data of the Ikeda-Carpenter model, which was used to determine the moderator contributions to the pulse shape. The red dashed line represents the background which was fitted simultaneously to the model.

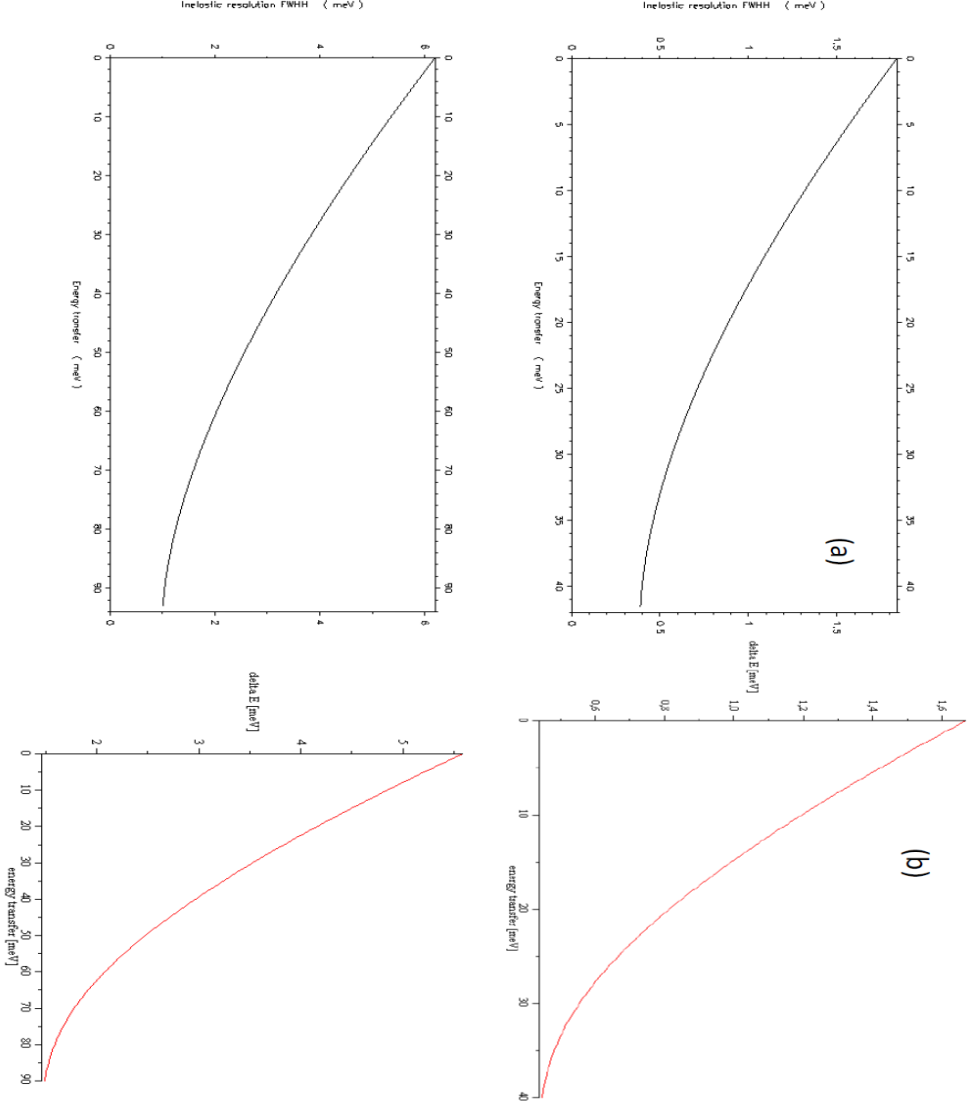
were then used in CHOP to determine the Fermi chopper parameters for MARI. All the parameters, Fermi chopper, moderator, instrument dimensions and sample properties were then combined in tobyfit to produce the resolution function for the fitting process.

Figure A.8 shows a collection of plots of the energy resolution for different energy transfers a) calculated with CHOP for MARI calculated via equation (A.24) for AMATERAS and b) calculated via equation (A.24) for AMATERAS.

Summarizing, a set of experimental parameters for the instrument MARI was produced, which result in an energy resolution matching the one calculated for AMATERAS using equation (A.24). Using the CHOP program produced a set of Fermi chopper properties whereas the moderator properties were received by fitting the Ikeda-Carpenter model to an energy cut through the elastic line of the ToF data. These moderator parameters were then introduced to CHOP and were used to determine the chopper parameters. As the next step, all the parameters were combined with the sample properties, dimensions and mosaicity, and spectrometer dimensions, to represent the instrumental



**Figure A.7:** Column a) energy resolution, determined using the CHOP program with a set of experimental set up parameters and for 11 meV incident neutron energy (upper panel) and 24 meV incident neutron energy (lower panel). Column b) displays the energy resolution of the instrument AMATERAS, calculated using equation (A.24) for 11 meV incident neutron energy (upper panel) and 24 meV incident neutron energy (lower panel). The x-axes of the diagrams represent the energy transfer in meV and the y-axes the energy resolution in meV. The scope of this figure is to illustrate the reasonable match between the energy resolution calculated for AMATERAS and the energy resolution which was used for the spin wave fitting using tobyfit.



**Figure A.8:** Column a) energy resolution, determined using the CHOP program with a set of experimental set up parameters and for 42 meV incident neutron energy (upper panel) and 94 meV incident neutron energy (lower panel). Column b) displays the energy resolution of the instrument AMATERAS, calculated using equation (A.24) for 42 meV incident neutron energy (upper panel) and 94 meV incident neutron energy (lower panel).. The x-axes of the diagrams represent the energy transfer in meV and the y-axes the energy resolution in meV. The scope of this figure is to illustrate the reasonable match between the energy resolution calculated for AMATERAS and the energy resolution which was used for the spin wave fitting using tobyfit.



resolution in the fitting process using tobyfit. This indirect approach to the resolution correction obviously has its flaws, as one has no real grip of the actual properties of the used resolution function and in principle uses more of an approximation, than the real instrumental resolution. Especially the  $Q$ -part of the used resolution function is not known, since it was not possible to model the  $Q$ -resolution using the CHOP program. Nevertheless the applied resolution function still seems a reasonable approximation of the actual instrumental resolution and the impact, of using the not hundred percent correct resolution function, should not be crucial on the spin wave analysis.

### A.2.3 Resolution Correction for the Spin Diffusion Model Analysis

All formulas regarding the energy- or  $Q$ -dependence of the instrumental resolution used in this section are taken from reference [252].

For the part of the data analysis of the AMATERAS time-of-flight data, using the spin diffusion models, a different approach for the resolution correction was chosen. Instead of using tobyfit for this part the fitting of the model as well as the resolution correction was performed for each 1D constant energy cut individually and afterwards the corrected results were averaged over all performed fits. In this section some details of the resolution correction performed during the analysis with the spin diffusion models will be discussed. In the case of the spin diffusion models, and in contrast to the spin wave analysis, the energy resolution was completely neglected and the lone focus was on the wave-vector part of the resolution function. The energy resolution did not play any role in this part of the data treatment, because each cut was treated separately and the only interest was in the impact of resolution effects on the  $Q$ -broadening. Second, all constant energy cuts, used for the data analysis, had to be performed over a certain energy integration range. For low incident neutron energies, up to 24 meV, this energy integration range was 1-2 meV. For the higher incident energies 42 and 94 meV, this energy integration increased to 10 and 20 meV respectively. This was necessary, in order to compensate for low scattering intensities, resulting in poor experimental statistics. So in all cases the energy integration was much larger, than the energy resolution, which leaves the energy resolution in principle irrelevant for this part of the data treatment.

The  $Q$ -resolution for a disc-chopper spectrometer can be expressed, very similar to what has been done for the energy-contribution in equation (A.24). Since most of the contributing terms are angle dependent it simplifies the expression, when splitting the scattering vector  $\mathbf{Q}$  into two parts, one parallel  $Q_{\parallel} = \mathbf{k}_i \cdot \hat{\mathbf{e}}_{\parallel}$  and one perpendicular  $Q_{\perp} = \mathbf{k}_i \cdot \hat{\mathbf{e}}_{\perp}$  to the incident beam direction. These components then read as,

$$Q_{\parallel} = \frac{m_n}{\hbar} \cdot [v_i - v_f \cdot \cos(2\theta)] \quad (\text{A.26})$$

$$Q_{\perp} = \frac{m_n}{\hbar} \cdot [-v_f \cdot \sin(2\theta)] \quad (\text{A.27})$$

which leaves the  $Q$ -resolution to be,

$$\delta Q = \frac{1}{Q} \cdot [Q_{\parallel}^2 (\delta Q_{\parallel})^2 + Q_{\perp}^2 (\delta Q_{\perp})^2]^{1/2} \quad (\text{A.28})$$

where  $Q$  is the absolute value of the scattering vector  $\mathbf{Q}$  and  $\delta Q_{\parallel}$  and  $\delta Q_{\perp}$  the following two expressions,

$$\begin{aligned} \delta Q_{\parallel} = & \frac{m_n}{\hbar} \cdot \left\{ \frac{1}{L_1^2} \cdot \left( v_i^2 + v_f^2 \cdot \frac{L_2}{L_3} \cdot \cos(2\theta) \right)^2 \cdot \delta t_p^2 \right. \\ & + \frac{1}{L_1^2} \cdot \left( v_i^2 + v_f^2 \cdot \frac{L_1 + L_2}{L_3} \cdot \cos(2\theta) \right)^2 \cdot \delta t_c^2 \\ & \left. + \left( \frac{v_f^2}{L_3} \cdot \cos(2\theta) \right) \cdot \delta t_d^2 + (v_f \cdot \sin(2\theta))^2 \cdot (\delta 2\theta)^2 \right\}^{1/2} \end{aligned} \quad (\text{A.29})$$

$$\begin{aligned} \delta Q_{\perp} = & \frac{m_n}{\hbar} \cdot \left\{ \left( \frac{v_f L_2}{L_1 L_3} \cdot \sin(2\theta) \right)^2 \cdot \delta t_p^2 \right. \\ & + \left( \frac{v_f^2}{L_1} \cdot \frac{L_1 + L_2}{L_3} \cdot \sin(2\theta) \right)^2 \cdot \delta t_c^2 \\ & \left. + \left( \frac{v_f^2}{L_3} \cdot \sin(2\theta) \right) \cdot \delta t_d^2 + (v_f \cdot \cos(2\theta))^2 \cdot (\delta 2\theta)^2 \right\}^{1/2} \end{aligned} \quad (\text{A.30})$$

with  $\delta 2\theta$  representing the  $Q$ -uncertainty resulting from sample mosaic, beam divergence and other factors. All other parameters have the same meaning, as explained before for the case of the energy resolution.

The spin diffusion model, which was used in the data analysis, is mathematically very similar to a Lorentzian peak function and both functions have almost identical peak shapes, which is illustrated in figures A.9 b) and e) for low and high energy transfers. Further, can be seen in figures A.9 a) and d), that the peak shape of the diffusion model is also very similar to the peak shape of a Voigt profile. The procedure of the resolution correction was based on these similarities, and instead of convoluting the diffusion model with the  $Q$ -resolution from (A.28) and fitting the resulting function to the data, which is not a trivial task for two rather complex functions, an approximation of the resolution effects was made by fitting the Lorentz and Voigt profiles to the data and comparing the relative changes in peak widths of the Lorentzian and the Lorentzian part of the Voigt profile. Just as a quick reminder, a Voigt profile is a convolution of a Gaussian and a Lorentzian peak function. So in this case the Gaussian part of the Voigt profile was interpreted as the  $Q$ -dependence of the resolution function and the complete Voigt profile as a resolution convoluted Lorentzian peak function, where further the Lorentzian part was interpreted as an approximation of the diffusion model. Further it was assumed

that the  $Q$ -dependence of the resolution function would have a shape similar to the one of a Gaussian peak function. So, the  $Q$ -resolution was calculated for several incident neutron energies and energy transfers using equation (A.28), the resulting value was interpreted as the peak width of the Gaussian part of the Voigt profile, the Gaussian width was held fixed at this value and only the Lorentzian part of the Voigt was fitted to the data. As the next step the Lorentzian peak function was fitted to the data and the two Lorentzian widths, the one of the Lorentz part of the Voigt profile and the width of the real Lorentz peak function, were compared afterwards. The broadening of the real Lorentzian relative to the Lorentzian part of the Voigt profile was then identified as the resolution effect, and was later used to correct the results from the spin diffusion model fits for the resolution effects. As already mentioned in chapter 5, each correlation length, obtained from each single cut, was corrected for its relative resolution effect individually and the corrected values were then averaged, to give the final result for the resolution corrected correlation lengths. The resolution broadening which was obtained for the longitudinal cuts was also applied for the transverse direction.

This whole procedure to correct the resolution effect on the  $Q$ -broadening, of course again has its weaknesses, especially that the diffusion models were not directly convoluted with the resolution function but rather an approximation of the possible resolution effects was performed. However, both Lorentzian and Voigt peak profiles match the peak profile of the diffusion model very well, for the low energy range below 35 meV energy transfer, and still reasonably well for energy transfers above 35 meV. In addition, by comparing the Lorentzian peak widths, obtained by the Lorentzian and the Voigt fits, a broadening of the Lorentzian peaks of less than 5%, for energy transfers lower than 25 meV, and around 9% for energy transfers above 25 meV was observed. Consequently, even the uncorrected values, obtained via the analysis with the diffusion models, still are absolutely reasonable. This also provides some confidence that the results, obtained via the spin wave fitting, are not heavily distorted by resolution effects. The incompleteness of the obtained data, very likely, has a much greater impact on the outcome of the spin wave analysis anyway.

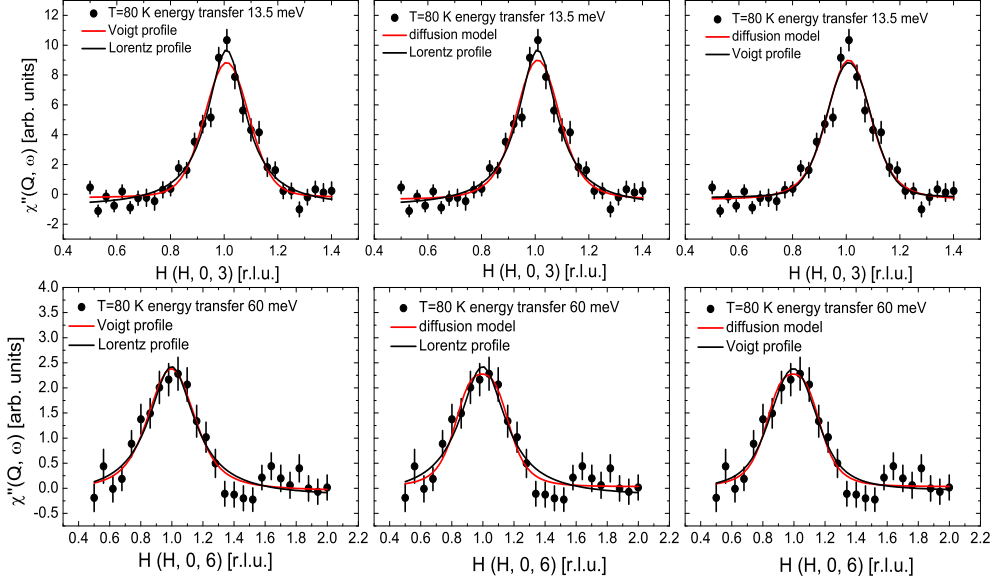


**Figure A.9:** Collection of constant energy cuts in  $\mathbf{Q}_h$ -direction. The upper row features cuts performed at energy transfer 13.5 meV, whereas the lower row features cuts performed at 60 meV energy transfer. Solid red and black lines are best fits of Voigt profile and Lorentzian peak functions as well as the diffusion model. The scope of this figure is to show the decent agreement of the  $\mathbf{Q}$  dependencies of the three peak functions, for the energy range between 13.5 meV and 60 meV. All depicted data have been corrected for the thermal-population factor and therefore represent the dynamical magnetic susceptibility of the system  $\chi''(\mathbf{Q}, \omega)$ .

## A.3 Additional Data

### A.3.1 $\text{FeTe}_{0.5}\text{Se}_{0.5}$ Transverse Constant Energy Scans

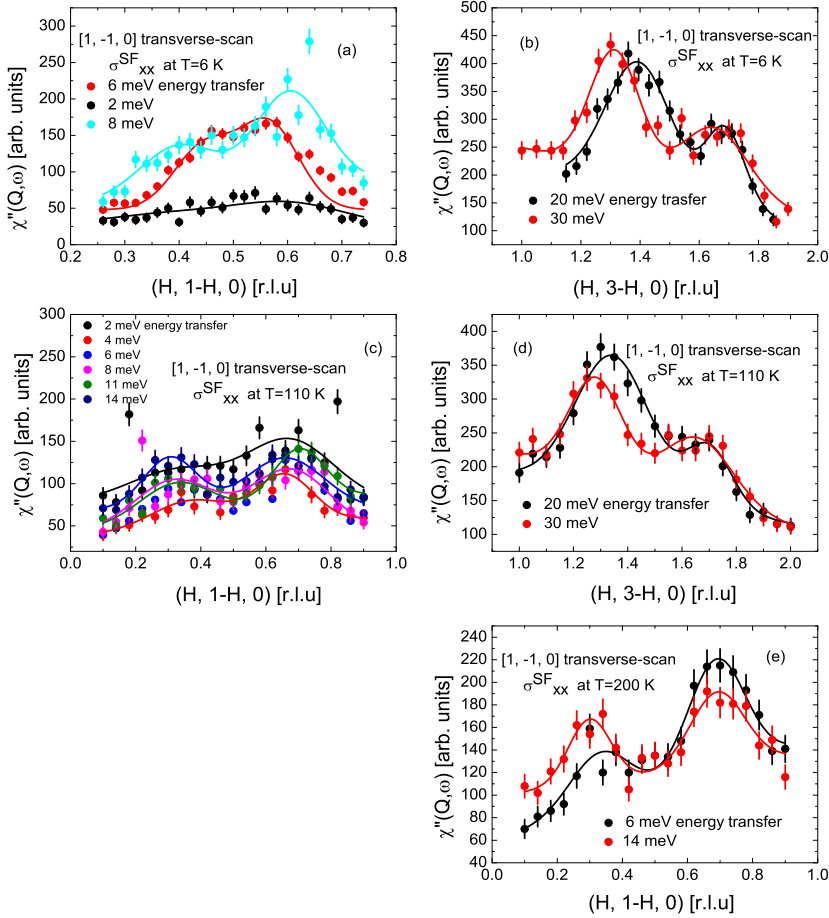


**Figure A.10:** (a)-(e) Transverse constant energy scans performed at 6 K (a) and (b), 110 K (c) and (d) and 200 K (e). The presented intensities were obtained for x-polarization and for spin flip scattering and therefore illustrate purely magnetic scattering intensity. The scans were performed at  $\mathbf{Q}_{\text{AFM}}=(0.5, 0.5, 0)$  in the first Brillouin zone (a), (c) and  $\mathbf{Q}_{\text{AFM}}=(1.5, 1.5, 0)$  in the second Brillouin zone (b), (d) and (e). Solid lines are fits with Gaussian peak functions. The peak positions obtained through these fits were used to create the dispersion relation illustrated in figure 7.4.

# Bibliography

- [1] J. G. BEDNORZ and K. A. MÜLLER, *Zeitschrift für Physik B* **64**, 189 (1986).
- [2] J. BARDEEN, L. N. COOPER, and J. R. SCHRIEFFER, *Physical Review* **108**, 1175 (1957).
- [3] H. KAMERLINGH ONNES, *Leiden Comm.* , 120b, 122b, 124c (1911).
- [4] W. MEISSNER and R. OCHSENFELD, *Naturwissenschaften* **21**, 787 (1933).
- [5] J. BARDEEN, L. N. COOPER, and J. R. SCHRIEFFER, *Physical Review* **106**, 162 (1957).
- [6] L. N. COOPER, *Physical Review* **104**, 1189 (1956).
- [7] F. LONDON and H. LONDON, *Superfluids, Vol.1, Macroscopic Theory of Superconductivity*, John Wiley & Sons, New York, United States of America, 1950.
- [8] D. SCHOENBERG, *Superconductivity*, Cambridge University Press, Cambridge, England, 1952.
- [9] G. RICKAYZEN, *Theory of Superconductivity*, Interscience Publishers John Wiley & Sons, New York, United States of America, 1965.
- [10] M. TINKHAM, *The Theory of Superconductivity*, Interscience Publishers John Wiley & Sons, New York, United States of America, 1962.
- [11] P. F. DAHL, *Superconductivity. Its Historical Roots and Development from Mercury to the Ceramic Oxides.*, American Institute of Physics, New York, United States of America, 1992.
- [12] W. BUCKEL and R. KLEINER, *Superconductivity: Fundamentals and Applications*, WILEY-VCH Verlag GmbH & Co. KGaA, Weinheim, Germany, 2004.
- [13] M. K. WU, J. R. ASHBURN, C. J. TORNG, P. H. HOR, R. L. MENG, L. GAO, Z. J. HUANG, Y. Q. WANG, and C. W. CHU, *Physical Review Letters* **58**, 908 (1987).
- [14] H. MAEDA, Y. TANAKA, M. FUKUTOMI, and T. ASANO, *Japanese Journal of Applied Physics* **27**, 209 (1988).

- [15] Z. Z. SHENG and A. M. HERMANN, *Nature* **332**, 138 (1988).
- [16] A. SCHILLING, M. CANTONI, J. D. GUO, and H. R. OTT, *Nature* **363**, 56 (1993).
- [17] D. A. BONN, *Nature Physics* **2**, 159 (2006).
- [18] N. P. ARMITAGE, P. FOURNIER, and R. L. GREENE, *Review of Modern Physics* **82**, 2421 (2010).
- [19] Y. KAMIHARA, T. WATANABE, M. HIRANO, and H. HOSONO, *Journal of the American Chemical Society* **130**, 3296 (2008).
- [20] Z.-A. REN, J. YANG, W. LU, W. YI, X.-L. SHEN, Z.-C. LI, G.-C. CHE, X.-L. DONG, L.-L. SUN, F. ZHOU, and Z.-X. ZHAO, *Europhysics Letters* **82**, 57002 (2008).
- [21] H. KITO, H. EISAKI, and A. IYO, *Journal of the Physical Society of Japan* **77**, 063707 (2008).
- [22] Z.-A. REN, W. LU, J. YANG, W. YI, X.-L. SHEN, C. ZHENG, G.-C. CHE, X.-L. DONG, L.-L. SUN, F. ZHOU, and Z.-X. ZHAO, *Chinese Physics Letters* **25**, 2215 (2008).
- [23] C. WANG, L. LI, S. CHI, Z. ZHU, Z. REN, Y. LI, Y. WANG, X. LIN, Y. LUO, S. JIANG, X. XU, G. CAO, and Z. XU, *Europhysics Letters* **83**, 67006 (2008).
- [24] M. ROTTER, M. TEGEL, and D. JOHRENDT, *Physical Review Letters* **101**, 107006 (2008).
- [25] J. H. TAPP, Z. TANG, B. LV, K. SASMAL, B. LORENZ, P. C. W. CHU, and A. M. GULOY, *Physical Review B* **78**, 060505 (2008).
- [26] X. C. WANG, Q. Q. LIU, Y. X. LV, W. B. GAO, L. X. YANG, R. C. YU, F. Y. LI, and C. Q. JIN, *Solid State Communications* **148**, 538 (2008).
- [27] M. J. PITCHER, D. R. PARKER, P. ADAMSON, S. J. C. HERKELRATH, A. T. BOOTHROYD, R. M. IBBERSON, M. BRUNELLI, and S. J. CLARKE, *Chemical Communications* **2008**, 5918 (2008).
- [28] F. C. HSU, J.-Y. LUO, K.-W. YEH, T.-K. CHEN, T.-W. HUANG, P. M. WU, Y.-C. LEE, Y.-L. HUANG, Y.-Y. CHU, D.-C. YAN, and M.-K. WU, *Proceedings of the National Academy of Sciences* **105**, 14262 (2008).
- [29] C. W. CHU, *Nature Physics* **5**, 787 (2009).

- 
- [30] C.-H. LEE, A. IYO, H. EISAKI, H. KITO, M. T. FERNANDEZ-DIAZ, T. ITO, K. KIHOU, M. MATSUHATA, M. BRADEN, and K. YAMADA, *Journal of the Physical Society of Japan* **77**, 083704 (2008).
- [31] J. ZHAO, Q. HUANG, C. DE LA CRUZ, S. LI, J. W. LYNN, Y. CHEN, M. A. GREEN, G. F. CHEN, G. LI, J. L. LUO, N. L. WANG, and P. DAI, *Nature Materials* **7**, 953 (2008).
- [32] S. A. J. KIMBER, A. KREYSSIG, Y.-Z. ZHANG, H. O. JESCHKE, R. VALENTÍ, F. YOKAICHIYA, E. COLOMBIER, J. YAN, T. C. HANSEN, T. CHATTERJI, R. J. MCQUEENEY, P. C. CANFIELD, A. I. GOLDMAN, and D. N. ARGYRIOU, *Nature Materials* **8**, 471 (2009).
- [33] S. NANDI, M. G. KIM, A. KREYSSIG, R. M. FERNANDES, D. K. PRATT, A. THALER, N. NI, S. L. BUD'KO, P. C. CANFIELD, J. SCHMALIAN, R. J. MCQUEENEY, and A. I. GOLDMAN, *Physical Review Letters* **104**, 057006 (2010).
- [34] T. J. LIU, J. HU, B. QIAN, D. FOBES, Z. Q. MAO, W. BAO, M. REEHUIS, S. A. J. KIMBER, K. PROKES, S. MATAS, D. N. ARGYRIOU, A. HIESS, A. ROTARU, H. PHAM, L. SPINU, Y. QIU, V. THAMPY, A. T. SAVICI, J. A. RODRIGUEZ, and C. BROHOLM, *Nature Materials* **9**, 718 (2010).
- [35] C.-C. LEE, W.-G. YIN, and W. KU, *Physical Review Letters* **103**, 267001 (2009).
- [36] M. WANG, H. LUO, J. ZHAO, C. ZHANG, M. WANG, K. MARTY, S. CHI, J. W. LYNN, A. SCHNEIDEWIND, S. LI, and P. DAI, *Physical Review B* **81**, 174524 (2010).
- [37] N. NI, M. E. TILLMAN, J.-Q. YAN, A. KRACHER, S. T. HANNAHS, S. L. BUD'KO, and P. C. CANFIELD, *Physical Review B* **78**, 214515 (2008).
- [38] C. LESTER, J.-H. CHU, J. G. ANALYTIS, S. C. CAPELLI, A. S. ERICKSON, C. L. CONDRON, M. F. TONEY, I. R. FISHER, and S. M. HAYDEN, *Physical Review B* **79**, 144523 (2009).
- [39] D. K. PRATT, W. TIAN, A. KREYSSIG, J. L. ZARESTKY, S. NANDI, N. NI, S. L. BUD'KO, P. C. CANFIELD, A. I. GOLDMAN, and R. J. MCQUEENEY, *Physical Review Letters* **103**, 087001 (2009).
- [40] A. D. CHRISTIANSON, M. D. LUMSDEN, S. E. NAGLER, G. J. MACDOUGALL, M. A. MCGUIRE, A. S. SEFAT, R. JIN, B. C. SALES, and D. MANDRUS, *Physical Review Letters* **103**, 087002 (2009).
- [41] M. ROTTER, M. TEGEL, I. SCHELLENBERG, F. M. SCHAPPACHER, R. PÖTTGEN, J. DEISENHOFER, A. GÜNTHER, F. SCHRETTLE, A. LOIDL, and D. JOHRENDT, *New Journal of Physics* **11**, 025014 (2009).



- [42] J. T. PARK, D. S. INOSOV, C. NIEDERMAYER, G. L. SUN, D. HAUG, N. B. CHRISTENSEN, R. DINNEBIER, A. V. BORIS, A. J. DREW, L. SCHULZ, T. SHAPOVAL, U. WOLFF, V. NEU, X. YANG, C. T. LIN, B. KEIMER, and V. HINKOV, *Physical Review Letters* **102**, 117006 (2009).
- [43] R. H. LIU, G. WU, T. WU, D. F. FANG, H. CHEN, S. Y. LI, K. LIU, Y. L. XIE, X. F. WANG, R. L. YANG, L. DING, C. HE, D. L. FENG, and X. H. CHEN, *Physical Review Letters* **101**, 087001 (2008).
- [44] S. TAKESHITA and R. KADONO, *New Journal of Physics* **11**, 035006 (2009).
- [45] T. NAKANO, S. TSUTSUMI, N. FUJIWARA, S. MATSUISHI, and H. HOSONO, *Physical Review B* **83**, 180508 (2011).
- [46] J. WEN, G. XU, Z. XU, Z. W. LIN, Q. LI, W. RATCLIFF, G. GU, and J. M. TRANQUADA, *Physical Review B* **80**, 104506 (2009).
- [47] J. ZHAO, Q. HUANG, C. DE LA CRUZ, J. W. LYNN, M. D. LUMSDEN, Z. A. REN, J. YANG, X. SHEN, X. DONG, Z. ZHAO, and P. DAI, *Physical Review B* **78**, 132504 (2008).
- [48] D. C. JOHNSTON, *Advances in Physics* **59**, 803 (2010).
- [49] T. YILDIRIM, *Physical Review Letters* **101**, 057010 (2008).
- [50] Q. SI and E. ABRAHAMS, *Physical Review Letters* **101**, 076401 (2008).
- [51] W. BAO, Y. QIU, Q. HUANG, M. A. GREEN, P. ZAJDEL, M. R. FITZSIMMONS, M. ZHERNENKOV, S. CHANG, M. FANG, B. QIAN, E. K. VEHTEDT, J. YANG, H. M. PHAM, L. SPINU, and Z. Q. MAO, *Physical Review Letters* **102**, 247001 (2009).
- [52] F. MA, W. JI, J. HU, Z.-Y. LU, and T. XIANG, *Physical Review Letters* **102**, 177003 (2009).
- [53] I. A. ZALIZNYAK, Z. XU, J. M. TRANQUADA, G. GU, A. M. TSVELIK, and M. B. STONE, *Physical Review Letters* **107**, 216403 (2011).
- [54] L. HARRIGER, H. LUO, M. LIU, C. FROST, J. HU, M. NORMAN, and P. DAI, *Physical Review B* **84**, 054544 (2011).
- [55] J. ZHAO, D. T. ADROJA, D.-X. YAO, R. BEWLEY, S. LI, X. F. WANG, G. WU, X. H. CHEN, J. HU, and P. DAI, *Nature Physics* **5**, 555 (2009).
- [56] R. A. EWINGS, T. G. PERRING, J. GILLET, S. D. DAS, S. E. SEBASTIAN, A. E. TAYLOR, T. GUIDI, and A. T. BOOTHROYD, *Physical Review B* **83**, 214519 (2011).

- 
- [57] O. J. LIPSCOMBE, G. F. CHEN, C. FANG, T. G. PERRING, D. L. ABERNATHY, A. D. CHRISTIANSON, T. EGAMI, N. WANG, J. HU, and P. DAI, *Physical Review Letters* **106**, 057004 (2011).
- [58] M. LIU, L. W. HARRIGER, H. LUO, M. WANG, R. A. EWINGS, T. GUIDI, H. PARK, K. HAULE, G. KOTLIAR, S. M. HAYDEN, and P. DAI, *Nature Physics* **8**, 376 (2012).
- [59] J. ZHAO, D.-X. YAO, S. LI, T. HONG, Y. CHEN, S. CHANG, W. RATCLIFF, J. W. LYNN, H. A. MOOK, G. F. CHEN, J. L. LUO, N. L. WANG, E. W. CARLSON, J. HU, and P. DAI, *Physical Review Letters* **101**, 167203 (2008).
- [60] R. J. MCQUEENEY, S. O. DIALLO, V. P. ANTROPOV, G. D. SAMOLYUK, C. BROHOLM, N. NI, S. NANDI, M. YETHIRAJ, J. L. ZARESTKY, J. J. PULIKKOTIL, A. KREYSSIG, M. D. LUMSDEN, B. N. HARMON, P. C. CANFIELD, and A. I. GOLDMAN, *Physical Review Letters* **101**, 227205 (2008).
- [61] S. O. DIALLO, D. K. PRATT, R. M. FERNANDES, W. TIAN, J. L. ZARESTKY, M. LUMSDEN, T. G. PERRING, C. L. BROHOLM, N. NI, S. L. BUD'KO, P. C. CANFIELD, H.-F. LI, D. VAKNIN, A. KREYSSIG, A. I. GOLDMAN, and R. J. MCQUEENEY, *Physical Review B* **81**, 214407 (2010).
- [62] R. A. EWINGS, T. G. PERRING, R. I. BEWLEY, T. GUIDI, M. J. PITCHER, D. R. PARKER, S. J. CLARKE, and A. T. BOOTHROYD, *Physical Review B* **78**, 220501 (2008).
- [63] K. MATAN, R. MORINAGA, K. IIDA, and T. J. SATO, *Physical Review B* **79**, 054526 (2009).
- [64] J. T. PARK, G. FRIEMEL, T. LOEW, V. HINKOV, Y. LI, B. H. MIN, D. L. SUN, A. IVANOV, A. PIOVANO, C. T. LIN, B. KEIMER, Y. S. KWON, and D. S. INOSOV, *Physical Review B* **86**, 024437 (2012).
- [65] N. QURESHI, P. STEFFENS, S. WURMEHL, S. ASWARTHAM, B. BÜCHNER, and M. BRADEN, *Physical Review B* **86**, 060410 (2012).
- [66] C. FANG, H. YAO, W.-F. TSAI, J. HU, and S. A. KIVELSON, *Physical Review B* **77**, 224509 (2008).
- [67] T.-M. CHUANG, M. P. ALLAN, J. LEE, Y. XIE, N. NI, S. L. BUD'KO, G. S. BOEBINGER, P. C. CANFIELD, and J. C. DAVIS, *Science* **327**, 181 (2010).
- [68] J.-H. CHU, J. G. ANALYTIS, K. DE GREVE, P. L. MCMAHON, Z. ISLAM, Y. YAMAMOTO, and I. R. FISHER, *Science* **329**, 824 (2010).

- [69] A. DUSZA, A. LUCARELLI, F. PFUNER, J.-H. CHU, I. R. FISHER, and L. DE-GIORGI, *Europhysics Letters* **93**, 37002 (2011).
- [70] D. K. PRATT, A. KREYSSIG, S. NANDI, N. NI, A. THALER, M. D. LUMSDEN, W. TIAN, J. L. ZARESTKY, S. L. BUD'KO, P. C. CANFIELD, A. I. GOLDMAN, and R. J. MCQUEENEY, *Physical Review B* **81**, 140510 (2010).
- [71] M. LUMSDEN, A. D. CHRISTIANSON, D. PARSHALL, M. STONE, S. NAGLER, G. MACDOUGALL, H. MOOK, K. LOKSHIN, T. EGAMI, D. ABERNATHY, E. GOREMYCHKIN, R. OSBORN, M. MCGUIRE, A. SEFAT, R. JIN, B. SALES, and D. MANDRUS, *Physical Review Letters* **102**, 107005 (2009).
- [72] D. S. INOSOV, J. T. PARK, P. BOURGES, D. L. SUN, Y. SIDIS, A. SCHNEIDEWIND, K. HRADIL, D. HAUG, C. T. LIN, B. KEIMER, and V. HINKOV, *Nature Physics* **6**, 178 (2009).
- [73] S. CHI, A. SCHNEIDEWIND, J. ZHAO, L. W. HARRIGER, L. LI, Y. LUO, G. CAO, Z. XU, M. LOEWENHAUPT, J. HU, and P. DAI, *Physical Review Letters* **102**, 107006 (2009).
- [74] H.-F. LI, C. BROHOLM, D. VAKNIN, R. FERNANDES, D. ABERNATHY, M. STONE, D. PRATT, W. TIAN, Y. QIU, N. NI, S. DIALLO, J. ZARESTKY, S. BUD'KO, P. CANFIELD, and R. MCQUEENEY, *Physical Review B* **82**, 140503(R) (2010).
- [75] K. MATAN, S. IBUKA, R. MORINAGA, S. CHI, J. W. LYNN, A. D. CHRISTIANSON, M. D. LUMSDEN, and T. J. SATO, *Physical Review B* **82**, 054515 (2010).
- [76] S. WAKIMOTO, K. KODAMA, M. ISHIKADO, M. MATSUDA, R. KAJIMOTO, M. ARAI, K. KAKURAI, F. ESAKA, A. IYO, H. KITO, H. EISAKI, and S.-I. SHAMOTO, *Journal of the Physical Society of Japan* **79**, 074715 (2010).
- [77] D. J. SINGH and M.-H. DU, *Physical Review Letters* **100**, 237003 (2008).
- [78] I. I. MAZIN, D. J. SINGH, M. D. JOHANNES, and M. H. DU, *Physical Review Letters* **101**, 057003 (2008).
- [79] I. I. MAZIN and J. SCHMALIAN, *Physica C: Superconductivity* **469**, 614 (2009).
- [80] P. LARSON and S. SATPATHY, *Physical Review B* **79**, 054502 (2009).
- [81] D. J. SINGH, *Physical Review B* **78**, 094511 (2008).
- [82] A. SUBEDI, L. ZHANG, D. J. SINGH, and M. H. DU, *Physical Review B* **78**, 134514 (2008).

- 
- [83] L. ZHANG, D. J. SINGH, and M. H. DU, *Physical Review B* **79**, 012506 (2009).
- [84] K. HAULE, J. H. SHIM, and G. KOTLIAR, *Physical Review Letters* **100**, 226402 (2008).
- [85] I. A. NEKRASOV, Z. V. PCHELKINA, and M. V. SADOVSKII, *JETP Letters* **88**, 155 (2008).
- [86] P. HIRSCHFELD, M. M. KORSHUNOV, and I. I. MAZIN, *Reports on Progress in Physics* **74**, 124508 (2011).
- [87] L. BOERI, O. V. DOLGOV, and A. A. GOLUBOV, *Physical Review Letters* **101**, 026403 (2008).
- [88] R. MITTAL, Y. SU, S. ROLS, T. CHATTERJI, S. L. CHAPLOT, H. SCHOBBER, M. ROTTER, D. JOHRENDT, and T. BRUECKEL, *Physical Review B* **78**, 104514 (2008).
- [89] M. ZBIRI, H. SCHOBBER, M. R. JOHNSON, S. ROLS, R. MITTAL, Y. SU, M. ROTTER, and D. JOHRENDT, *Physical Review B* **79**, 064511 (2009).
- [90] R. MITTAL, L. PINTSCHOVIOUS, D. LAMAGO, R. HEID, K.-P. BOHNEN, D. REZNIK, S. CHAPLOT, Y. SU, N. KUMAR, S. DHAR, A. THAMIZHAVEL, and T. BRUECKEL, *Physical Review Letters* **102**, 217001 (2009).
- [91] R. H. LIU, T. WU, G. WU, H. CHEN, X. F. WANG, Y. L. XIE, J. J. YING, Y. J. YAN, Q. J. LI, B. C. SHI, W. S. CHU, Z. Y. WU, and X. H. CHEN, *Nature* **459**, 64 (2009).
- [92] R. KHASANOV, M. BENDELE, A. BUSSMANN-HOLDER, and H. KELLER, *Physical Review B* **82**, 212505 (2010).
- [93] P. M. SHIRAGE, K. KIHOU, K. MIYAZAWA, C.-H. LEE, H. KITO, H. EISAKI, T. YANAGISAWA, Y. TANAKA, and A. IYO, *Physical Review Letters* **103**, 257003 (2009).
- [94] P. M. SHIRAGE, K. MIYAZAWA, K. KIHOU, H. KITO, Y. YOSHIDA, Y. TANAKA, H. EISAKI, and A. IYO, *Physical Review Letters* **105**, 037004 (2010).
- [95] N. F. BERK and J. R. SCHRIEFFER, *Physical Review Letters* **17**, 433 (1966).
- [96] D. J. SCALAPINO, E. LOH, and J. E. HIRSCH, *Physical Review B* **34**, 8190 (1986).
- [97] K. MIYAKE, S. SCHMITT-RINK, and C. M. VARMA, *Physical Review B* **34**, 6554 (1986).
- [98] D. J. SCALAPINO, *Physics Reports* **250**, 329 (1995).

- [99] H.-J. GRAFE, D. PAAR, G. LANG, N. J. CURRO, G. BEHR, J. WERNER, J. HAMANN-BORRERO, C. HESS, N. LEPS, R. KLINGELER, and B. BÜCHNER, *Physical Review Letters* **101**, 047003 (2008).
- [100] K. MATANO, Z. A. REN, X. L. DONG, L. L. SUN, Z. X. ZHAO, and G.-Q. ZHENG, *Europhysics Letters* **83**, 57001 (2008).
- [101] K. MATANO, Z. LI, G. L. SUN, C. T. LIN, M. ICHIOKA, and G.-Q. ZHENG, *Europhysics Letters* **87**, 27012 (2009).
- [102] M. YASHIMA, H. NISHIMURA, H. MUKUDA, Y. KITAOKA, K. MIYAZAWA, P. M. SHIRAGE, K. KIHOU, H. KITO, and A. EISAKI, IYO, *Journal of the Physical Society of Japan* **78**, 103702 (2009).
- [103] F. NING, K. AHILAN, T. IMAI, A. S. SEFAT, R. JIN, M. A. MCGUIRE, B. C. SALES, and D. MANDRUS, *Journal of the Physical Society of Japan* **77**, 103705 (2008).
- [104] K. NAKAYAMA, T. SATO, P. RICHARD, Y. M. XU, Y. SEKIBA, S. SOUMA, G. F. CHEN, J. L. LUO, N. L. WANG, H. DING, and T. TAKAHASHI, *Europhysics Letters* **85**, 67002 (2009).
- [105] H. DING, P. RICHARD, K. NAKAYAMA, K. SUGAWARA, T. ARAKANE, Y. SEKIBA, A. TAKAYAMA, S. SOUMA, T. SATO, T. TAKAHASHI, Z. WANG, X. DAI, Z. FANG, G. F. CHEN, J. L. LUO, and N. L. WANG, *Europhysics Letters* **83**, 47001 (2008).
- [106] X.-P. WANG, T. QIAN, P. RICHARD, P. ZHANG, J. DONG, H. D. WANG, C. H. DONG, M. H. FANG, and H. DING, *Europhysics Letters* **93**, 57001 (2011).
- [107] D. V. EVTUSHINSKY, D. S. INOSOV, V. B. ZABOLOTNYY, A. KOITZSCH, M. KNUPFER, B. BÜCHNER, M. S. VIAZOVSKA, G. L. SUN, V. HINKOV, A. V. BORIS, C. T. LIN, B. KEIMER, A. VARYKHALOV, A. A. KORDYUK, and S. V. BORISENKO, *Physical Review B* **79**, 054517 (2009).
- [108] T. KONDO, A. F. SANTANDER-SYRO, O. COPIE, C. LIU, M. E. TILLMAN, E. D. MUN, J. SCHMALIAN, S. L. BUD'KO, M. A. TANATAR, P. C. CANFIELD, and A. KAMINSKI, *Physical Review Letters* **101**, 147003 (2008).
- [109] L. WRAY, D. QIAN, D. HSIEH, Y. XIA, L. LI, J. G. CHECKELSKY, A. PASUPATHY, K. K. GOMES, C. V. PARKER, A. V. FEDOROV, G. F. CHEN, J. L. LUO, A. YAZDANI, N. P. ONG, N. L. WANG, and M. Z. HASAN, *Physical Review B* **78**, 184508 (2008).

- 
- [110] J.-P. REID, M. A. TANATAR, X. G. LUO, H. SHAKERIPOUR, N. DOIRON-LEYRAUD, N. NI, S. L. BUD'KO, P. C. CANFIELD, R. PROZOROV, and L. TAILLEFER, *Physical Review B* **82**, 064501 (2010).
- [111] M. YAMASHITA, Y. SENSU, T. SHIBAUCHI, S. KASAHARA, K. HASHIMOTO, D. WATANABE, H. IKEDA, T. TERASHIMA, I. VEKHTER, A. B. VORONTSOV, and Y. MATSUDA, *Physical Review B* **84**, 060507 (2011).
- [112] Y. ZHANG, Z. R. YE, Q. Q. GE, F. CHEN, J. JIANG, M. XU, B. P. XIE, and D. L. FENG, *Nature Physics* **8**, 371 (2012).
- [113] F. WANG, H. ZHAI, and D.-H. LEE, *Physical Review B* **81**, 184512 (2010).
- [114] R. THOMALE, C. PLATT, W. HANKE, and B. A. BERNEVIG, *Physical Review Letters* **106**, 187003 (2011).
- [115] K. KUROKI, H. USUI, S. ONARI, R. ARITA, and H. AOKI, *Physical Review B* **79**, 224511 (2009).
- [116] T. MAIER and D. SCALAPINO, *Physical Review B* **78**, 020514(R) (2008).
- [117] M. KORSHUNOV and I. EREMIN, *Physical Review B* **78**, 140509(R) (2008).
- [118] T. MAIER, S. GRASER, D. SCALAPINO, and P. HIRSCHFELD, *Physical Review B* **79**, 134520 (2009).
- [119] J. ROSSAT-MIGNOD, L. P. REGNAULT, C. VETTIER, P. BOURGES, P. BURLET, J. BOSSY, J. Y. HENRY, and G. LAPERTOT, *Physica C: Superconductivity* **185**, 86 (1991).
- [120] H. A. MOOK, M. YETHIRAJ, G. AEPPLI, T. E. MASON, and T. ARMSTRONG, *Physical Review Letters* **70**, 3490 (1993).
- [121] H. F. FONG, B. KEIMER, P. W. ANDERSON, D. REZNIK, F. DOĞAN, and I. A. AKSAY, *Physical Review Letters* **75**, 316 (1995).
- [122] H. F. FONG, B. KEIMER, D. REZNIK, D. L. MILIUS, and I. A. AKSAY, *Physical Review B* **54**, 6708 (1996).
- [123] P. BOURGES, L. P. REGNAULT, Y. SIDIS, and C. VETTIER, *Physical Review B* **53**, 876 (1996).
- [124] N. METOKI, Y. HAGA, Y. KOIKE, and Y. O<sup>-</sup>NUKI, *Physical Review Letters* **80**, 5417 (1998).
- [125] C. STOCK, C. BROHOLM, J. HUDIS, H. J. KANG, and C. PETROVIC, *Physical Review Letters* **100**, 087001 (2008).

- [126] A. D. CHRISTIANSON, E. A. GOREMYCHKIN, R. OSBORN, S. ROSENKRANZ, M. D. LUMSDEN, C. D. MALLIAKAS, I. S. TODOROV, H. CLAUS, D. Y. CHUNG, M. G. KANATZIDIS, R. I. BEWLEY, and T. GUIDI, *Nature* **456**, 930 (2008).
- [127] S. LI, Y. CHEN, S. CHANG, J. LYNN, L. LI, Y. LUO, G. CAO, Z. XU, and P. DAI, *Physical Review B* **79**, 174527 (2009).
- [128] M. ISHIKADO, Y. NAGAI, K. KODAMA, R. KAJIMOTO, M. NAKAMURA, Y. INAMURA, S. WAKIMOTO, H. NAKAMURA, M. MACHIDA, K. SUZUKI, H. USUI, K. KUROKI, A. IYO, H. EISAKI, M. ARAI, and S.-I. SHAMOTO, *Physical Review B* **84**, 144517 (2011).
- [129] D. N. ARGYRIOU, A. HIESS, A. AKBARI, I. EREMIN, M. M. KORSHUNOV, J. HU, B. QIAN, Z. MAO, Y. QIU, C. BROHOLM, and W. BAO, *Physical Review B* **81**, 220503 (2010).
- [130] Y. QIU, W. BAO, Y. ZHAO, C. BROHOLM, V. STANEV, Z. TESANOVIC, Y. C. GASPAROVIC, S. CHANG, J. HU, B. QIAN, M. FANG, and Z. MAO, *Physical Review Letters* **103**, 067008 (2009).
- [131] P. BABKEVICH, M. BENDELE, A. T. BOOTHROYD, K. CONDER, S. N. GVASALIYA, R. KHASANOV, E. POMJAKUSHINA, and B. ROESSLI, *Journal of Physics: Condensed Matter* **22**, 142202 (2010).
- [132] H. A. MOOK, M. D. LUMSDEN, A. D. CHRISTIANSON, S. E. NAGLER, B. C. SALES, R. JIN, M. A. MCGUIRE, A. S. SEFAT, D. MANDRUS, T. EGAMI, and C. DE LA CRUZ, *Physical Review Letters* **104**, 187002 (2010).
- [133] S.-I. SHAMOTO, M. ISHIKADO, A. D. CHRISTIANSON, M. D. LUMSDEN, S. WAKIMOTO, K. KODAMA, A. IYO, and M. ARAI, *Physical Review B* **82**, 172508 (2010).
- [134] C. BOULLIER, L. P. REGNAULT, J. LORENZO, H. RØNNOW, U. AMMERLAHL, G. DHALENNE, and A. REVCOLEVSCHI, *Physica B: Condensed Matter* **350**, 40 (2004).
- [135] O. LIPSCOMBE, L. HARRIGER, P. FREEMAN, M. ENDERLE, C. ZHANG, M. WANG, T. EGAMI, J. HU, T. XIANG, M. NORMAN, and P. DAI, *Physical Review B* **82**, 064515 (2010).
- [136] N. S. HEADINGS, S. M. HAYDEN, J. KULDA, N. H. BABU, and D. A. CARDWELL, *Physical Review B* **84**, 104513 (2011).
- [137] P. BABKEVICH, B. ROESSLI, S. GVASALIYA, L. P. REGNAULT, P. FREEMAN, E. POMJAKUSHINA, K. CONDER, and A. BOOTHROYD, *Physical Review B* **83**, 180506(R) (2011).

- [138] G. YU, Y. LI, E. M. MOTOYAMA, and M. GREVEN, *Nature Physics* **5**, 873 (2009).
- [139] J. T. PARK, D. S. INOSOV, A. YARESKO, S. GRASER, D. L. SUN, P. BOURGES, Y. SIDIS, Y. LI, J. H. KIM, D. HAUG, A. IVANOV, K. HRADIL, A. SCHNEIDWIND, P. LINK, E. FAULHABER, I. GLAVATSKYY, C. T. LIN, B. KEIMER, and V. HINKOV, *Physical Review B* **82**, 134503 (2010).
- [140] D. S. INOSOV, J. T. PARK, A. CHARNUKHA, Y. LI, A. V. BORIS, B. KEIMER, and V. HINKOV, *Physical Review B* **83**, 214520 (2011).
- [141] L. W. HARRIGER, O. J. LIPSCOMBE, C. ZHANG, H. LUO, M. WANG, K. MARTY, M. D. LUMSDEN, and P. DAI, *Physical Review B* **85**, 054511 (2012).
- [142] J. R. SCHRIEFFER, *Theory of superconductivity*, W. A. Benjamin Inc., New York, United States of America, 1970.
- [143] N. BULUT and D. J. SCALAPINO, *Physical Review B* **47**, 3419 (1993).
- [144] N. BULUT and D. J. SCALAPINO, *Physical Review B* **53**, 5149 (1996).
- [145] M. LAVAGNA and G. STEMMANN, *Physical Review B* **49**, 4235 (1994).
- [146] A. A. ABRIKOSOV, *Physical Review B* **57**, 8656 (1998).
- [147] M. VOJTA, C. BURAGOHAIN, and S. SACHDEV, *Physical Review B* **61**, 15152 (2000).
- [148] E. DEMLER and S.-C. ZHANG, *Physical Review Letters* **75**, 4126 (1995).
- [149] E. DEMLER, H. KOHNO, and S.-C. ZHANG, *Physical Review B* **58**, 5719 (1998).
- [150] E. DEMLER, W. HANKE, and S.-C. ZHANG, *Review of Modern Physics* **76**, 909 (2004).
- [151] M. ESCHRIG, *Advances in Physics* **55**, 47 (2006).
- [152] A. V. CHUBUKOV, D. V. EFREMOV, and I. EREMIN, *Physical Review B* **78**, 134512 (2008).
- [153] A. BARDASIS and J. R. SCHRIEFFER, *Physical Review* **121**, 1050 (1961).
- [154] S. ZHANG, *Physical Review Letters* **65**, 120 (1990).
- [155] M. D. LUMSDEN and A. D. CHRISTIANSON, *Journal of Physics: Condensed Matter* **22**, 203203 (2010).
- [156] F. BLOCH, *Physical Review* **50**, 259 (1936).



- [157] C. G. SHULL, E. O. WOLLAN, and W. A. STRAUER, *Physical Review* **81**, 483 (1951).
- [158] W. MARSHALL and S. W. LOVESEY, *Theory of Thermal Neutron Scattering*, Claredon Press, Oxford, England, 1971.
- [159] G. L. SQUIRES, *Introduction to the Theory of Thermal Neutron Scattering*, Cambridge University Press, Cambridge, England, 1978.
- [160] G. SHIRANE, M. SHAPIRO, and J. M. TRANQUADA, *Neutron Scattering with a Triple-Axis Spectrometer*, University Press, Oxford, England, 2002.
- [161] T. CHATTERJI, *Neutron Scattering from Magnetic Materials*, Elsevier, Amsterdam, Netherlands, 2006.
- [162] M. BLUME, *Physical Review* **130**, 1670 (1963).
- [163] S. V. MALEYEV, V. G. BARYAKHTAR, and R. A. SURIS, *Soviets Physics - Solid State* **4**, 2533 (1963).
- [164] R. M. MOON, T. RISTE, and W. C. KOEHLER, *Physical Review* **181**, 920 (1969).
- [165] M. RUSSINA and F. MEZEI, *Nuclear Instruments and Methods in Physics Research Section A: Accelerators, Spectrometers, Detectors and Associated Equipment* **604**, 624 (2009).
- [166] Y. XIAO, Y. SU, M. MEVEN, R. MITTAL, C. M. N. KUMAR, T. CHATTERJI, S. PRICE, J. PERSSON, N. KUMAR, S. K. DHAR, A. THAMIZHAVEL, and T. BRUECKEL, *Physical Review B* **80**, 174424 (2009).
- [167] H. RAFFIUS, E. MÖRSEN, B. D. MOSEL, W. MÜLLER-WARMUTH, W. JEITSCHKO, L. TERBÜCHTE, and T. VOMHOF, *Journal of Physics and Chemistry of Solids* **54**, 135 (1993).
- [168] R. MARCHAND and W. JEITSCHKO, *Journal of Solid State Chemistry* **24**, 351 (1978).
- [169] H. JEEVAN, Z. HOSSAIN, D. KASINATHAN, H. ROSNER, C. GEIBEL, and P. GEGENWART, *Physical Review B* **78**, 052502 (2008).
- [170] Z. REN, Z. ZHU, S. JIANG, X. XU, Q. TAO, C. WANG, C. FENG, G. CAO, and Z. XU, *Physical Review B* **78**, 052501 (2008).
- [171] J. HERRERO-MARTIN, V. SCAGNOLI, C. MAZZOLI, Y. SU, R. MITTAL, Y. XIAO, T. BRUECKEL, N. KUMAR, S. K. DHAR, A. THAMIZHAVEL, and L. PAOLASINI, *Physical Review B* **80**, 134411 (2009).

- 
- [172] M. A. RUDERMAN and C. KITTEL, *Physical Review* **96**, 99 (1954).
- [173] T. KASUYA, *Progress of Theoretical Physics* **16**, 45 (1956).
- [174] K. YOSIDA, *Physical Review* **106**, 893 (1957).
- [175] S. JIANG, Y. LUO, Z. REN, Z. ZHU, C. WANG, X. XU, Q. TAO, G. CAO, and Z. XU, *New Journal of Physics* **11**, 025007 (2009).
- [176] Y. XIAO, Y. SU, W. SCHMIDT, K. SCHMALZL, C. M. N. KUMAR, S. PRICE, T. CHATTERJI, R. MITTAL, L. J. CHANG, S. NANDI, N. KUMAR, S. K. DHAR, A. THAMIZHAVEL, and T. BRUECKEL, *Physical Review B* **81**, 220406 (2010).
- [177] C. F. MICLEA, M. NICKLAS, H. S. JEEVAN, D. KASINATHAN, Z. HOSSAIN, H. ROSNER, P. GEGENWART, C. GEIBEL, and F. STEGLICH, *Physical Review B* **79**, 212509 (2009).
- [178] T. TERASHIMA, M. TOMITA, M. KIMATA, H. SATSUKAWA, A. HARADA, K. HAZAMA, S. UJI, H. S. SUZUKI, T. MATSUMOTO, and K. MURATA, *Journal of the Physical Society of Japan* **78**, 118001 (2009).
- [179] A. MITSUDA, T. MATOBA, H. WADA, F. ISHIKAWA, and Y. YAMADA, *Journal of the Physical Society of Japan* **79**, 073704 (2010).
- [180] K. MATSUBAYASHI, K. MUNAKATA, M. ISOBE, N. KATAYAMA, K. OHGUSHI, Y. UEDA, N. KAWAMURA, M. MIZUMAKI, N. ISHIMATSU, M. HEDO, I. UMEHARA, and Y. UWATOKO, *Physical Review B* **84**, 024502 (2011).
- [181] Y. QI, Z. GAO, L. WANG, D. WANG, X. ZHANG, and Y. MA, *New Journal of Physics* **10**, 123003 (2008).
- [182] ANUPAM, P. L. PAULOSE, H. S. JEEVAN, C. GEIBEL, and Z. HOSSAIN, *Journal of Physics: Condensed Matter* **21**, 265701 (2009).
- [183] H. S. JEEVAN, Z. HOSSAIN, D. KASINATHAN, H. ROSNER, C. GEIBEL, and P. GEGENWART, *Physical Review B* **78**, 092406 (2008).
- [184] ANUPAM, P. L. PAULOSE, S. RAMAKRISHNAN, and Z. HOSSAIN, *Journal of Physics: Condensed Matter* **23**, 455702 (2011).
- [185] Z. REN, X. LIN, Q. TAO, S. JIANG, Z. ZHU, C. WANG, G. CAO, and Z. XU, *Physical Review B* **79**, 094426 (2009).
- [186] S. JIANG, H. XING, G. XUAN, Z. REN, C. WANG, Z.-A. XU, and G. CAO, *Physical Review B* **80**, 184514 (2009).

- [187] M. NICKLAS, M. KUMAR, E. LENGYEL, W. SCHNELLE, and A. LEITHE-JASPER, *Journal of Physics: Conference Series* **273**, 012101 (2011).
- [188] Z. REN, Q. TAO, S. JIANG, C. FENG, C. WANG, J. DAI, G. CAO, and Z. XU, *Physical Review Letters* **102**, 137002 (2009).
- [189] H. S. JEEVAN, D. KASINATHAN, H. ROSNER, and P. GEGENWART, *Physical Review B* **83**, 054511 (2011).
- [190] G. CAO, S. XU, Z. REN, S. JIANG, C. FENG, and Z. XU, *Journal of Physics: Condensed Matter* **23**, 464204 (2011).
- [191] I. NOWIK, I. FELNER, Z. REN, G. H. CAO, and Z. A. XU, *Journal of Physics: Condensed Matter* **23**, 065701 (2011).
- [192] S. ZAPF, D. WU, L. BOGANI, H. S. JEEVAN, P. GEGENWART, and M. DRESSEL, *Physical Review B* **84**, 140503 (2011).
- [193] D. H. RYAN, J. M. CADOGAN, S. XU, Z. XU, and G. CAO, *Physical Review B* **83**, 132403 (2011).
- [194] [HTTP://WWW.ILL.EU/INSTRUMENTS-SUPPORT/INSTRUMENTS GROUPS/INSTRUMENTS/D23](http://www.ill.eu/instruments-support/instruments-groups/instruments/d23).
- [195] [HTTP://WWW.FRM2.TUM.DE/WISSENSCHAFTLICHE NUTZUNG/SPEKTROMETRIE/DNS](http://www.frm2.tum.de/wissenschaftliche-nutzung/spektrometrie/dns).
- [196] J. J. YING, T. WU, Q. J. ZHENG, Y. HE, G. WU, Q. J. LI, Y. J. YAN, Y. L. XIE, R. H. LIU, X. F. WANG, and X. H. CHEN, *Physical Review B* **81**, 052503 (2010).
- [197] C. FENG, Z. REN, S. XU, S. JIANG, Z. XU, G. CAO, I. NOWIK, I. FELNER, K. MATSUBAYASHI, and Y. UWATOKO, *Physical Review B* **82**, 094426 (2010).
- [198] P. CANFIELD, P. GAMMEL, and D. BISHOP, *Physics Today* **51**, 40 (1998).
- [199] J. W. LYNN, B. KEIMER, C. ULRICH, C. BERNHARD, and J. L. TALLON, *Physical Review B* **61**, 14964(R) (2000).
- [200] G. AEPPLI, E. BUCHER, C. BROHOLM, J. K. KJEMS, J. BAUMANN, and J. HUFNAGL, *Physical Review Letters* **60**, 615 (1988).
- [201] E. D. ISAACS, P. ZSCHACK, C. L. BROHOLM, C. BURNS, G. AEPPLI, A. P. RAMIREZ, T. T. M. PALSTRA, R. W. ERWIN, N. STÜCHELI, and E. BUCHER, *Physical Review Letters* **75**, 1178 (1995).

- 
- [202] J. G. LUSSIER, M. MAO, A. SCHRÖDER, J. D. GARRETT, B. D. GAULIN, S. M. SHAPIRO, and W. J. L. BUYERS, *Physical Review B* **56**, 11749 (1997).
- [203] P. MARSIK, K. KIM, A. DUBROKA, M. RÖSSLE, V. MALIK, L. SCHULZ, C. WANG, C. NIEDERMAYER, A. DREW, M. WILLIS, T. WOLF, and C. BERNHARD, *Physical Review Letters* **105**, 057001 (2010).
- [204] R. M. FERNANDES, D. K. PRATT, W. TIAN, J. ZARESTKY, A. KREYSSIG, S. NANDI, M. G. KIM, A. THALER, N. NI, P. C. CANFIELD, R. J. MCQUEENEY, J. SCHMALIAN, and A. I. GOLDMAN, *Physical Review B* **81**, 140501(R) (2010).
- [205] R. FERNANDES and J. SCHMALIAN, *Physical Review B* **82**, 014521 (2010).
- [206] [HTTP://J.PARC.JP/MATLIFE/EN/INSTRUMENTATION/NS\\_SPEC.HTML](http://J.PARC.JP/MATLIFE/EN/INSTRUMENTATION/NS_SPEC.HTML).
- [207] [HTTP://MSLICE.ISIS.RL.AC.UK](http://MSLICE.ISIS.RL.AC.UK).
- [208] S. DIALLO, V. ANTROPOV, T. PERRING, C. BROHOLM, J. PULIKKOTIL, N. NI, S. BUD'KO, P. CANFIELD, A. KREYSSIG, A. I. GOLDMAN, and R. J. MCQUEENEY, *Physical Review Letters* **102**, 187206 (2009).
- [209] C. LESTER, J.-H. CHU, J. G. ANALYTIS, T. G. PERRING, I. R. FISHER, and S. M. HAYDEN, *Physical Review B* **81**, 064505 (2010).
- [210] [HTTP://TOBYFIT.ISIS.RL.AC.UK/MAIN\\_PAGE](http://TOBYFIT.ISIS.RL.AC.UK/MAIN_PAGE).
- [211] P. J. BROWN, *Magnetic Form Factors / International Tables for Crystallography Vol. C*, Kluwer Academic, Dordrecht-Boston-London, United States of America, 2004.
- [212] L. W. HARRIGER, A. SCHNEIDEWIND, S. LI, J. ZHAO, Z. LI, W. LU, X. DONG, F. ZHOU, Z. ZHAO, J. HU, and P. DAI, *Physical Review Letters* **103**, 087005 (2009).
- [213] K. NAKAYAMA and T. MORIYA, *Journal of the Physical Society of Japan* **56**, 2918 (1987).
- [214] A. ISHIGAKI and T. MORIYA, *Journal of the Physical Society of Japan* **65**, 3402 (1996).
- [215] Y. XIAO, Y. SU, R. MITTAL, T. CHATTERJI, T. HANSEN, C. M. N. KUMAR, S. MATSUISHI, H. HOSONO, and T. BRUECKEL, *Physical Review B* **79**, 060504 (2009).
- [216] P. CHENG, B. SHEN, G. MU, X. ZHU, F. HAN, B. ZENG, and H.-H. WEN, *Europhysics Letters* **85**, 67003 (2009).

- [217] S. MATSUISHI, Y. INOUE, T. NOMURA, H. YANAGI, M. HIRANO, and H. HOSONO, *Journal of the American Chemical Society* **130**, 14428 (2008).
- [218] S. MATSUISHI, Y. INOUE, T. NOMURA, Y. KAMIHARA, M. HIRANO, and H. HOSONO, *New Journal of Physics* **11**, 025012 (2009).
- [219] T.-L. XIA and T.-S. ZHAO, *Superconductor Science and Technology* **24**, 095006 (2011).
- [220] I. R. SHEIN and A. L. IVANOVSKII, *JETP Letters* **88**, 683 (2009).
- [221] Y. XIAO, Y. SU, R. MITTAL, T. CHATTERJI, T. HANSEN, S. PRICE, C. M. N. KUMAR, J. PERSSON, S. MATSUISHI, Y. INOUE, H. HOSONO, and T. BRUECKEL, *Physical Review B* **81**, 094523 (2010).
- [222] R. I. BEWLEY, R. S. ECCLESTON, K. A. MCEWEN, S. M. HAYDEN, M. T. DOVE, S. M. BENNINGTON, J. R. TREADGOLD, and R. L. S. COLEMAN, *Physica B: Condensed Matter* **385-386**, 1029 (2006).
- [223] B. E. WARREN, *Physical Review* **59**, 693 (1941).
- [224] M. ISHIKADO, R. KAJIMOTO, S.-I. SHAMOTO, M. ARAI, A. IYO, K. MIYAZAWA, P. M. SHIRAGE, H. KITO, H. EISAKI, S. KIM, H. HOSONO, T. GUIDI, R. BEWLEY, and S. M. BENNINGTON, *Journal of the Physical Society of Japan* **78**, 043705 (2009).
- [225] R. MITTAL, M. ZBIRI, S. ROLS, Y. SU, Y. XIAO, H. SCHÖBER, S. L. CHAPLOT, M. JOHNSON, T. CHATTERJI, S. MATSUISHI, H. HOSONO, and T. BRUECKEL, *Physical Review B* **79**, 214514 (2009).
- [226] P. STEFFENS, C. H. LEE, N. QURESHI, K. KIHOU, A. IYO, H. EISAKI, and M. BRADEN, *Physical Review Letters* **110**, 137001 (2013).
- [227] Q. HUANG, Y. QIU, W. BAO, M. A. GREEN, J. W. LYNN, Y. C. GASPAROVIC, T. WU, G. WU, and X. H. CHEN, *Physical Review Letters* **101**, 257003 (2008).
- [228] J. ZHAO, W. RATCLIFF, J. W. LYNN, G. F. CHEN, J. L. LUO, N. L. WANG, J. HU, and P. DAI, *Physical Review B* **78**, 140504 (2008).
- [229] A. I. GOLDMAN, D. N. ARGYRIOU, B. OULADDIAF, T. CHATTERJI, A. KREYSSIG, S. NANDI, N. NI, S. L. BUD'KO, P. C. CANFIELD, and R. J. MCQUEENEY, *Physical Review B* **78**, 100506 (2008).
- [230] M. D. LUMSDEN, A. D. CHRISTIANSON, E. A. GOREMYCHKIN, S. E. NAGLER, H. A. MOOK, M. B. STONE, D. L. ABERNATHY, T. GUIDI, G. J. MACDOUGALL, C. DE LA CRUZ, A. S. SEFAT, M. A. MCGUIRE, B. C. SALES, and D. MANDRUS, *Nature Physics* **6**, 182 (2010).

- 
- [231] S. LI, C. ZHANG, M. WANG, H.-Q. LUO, X. LU, E. FAULHABER, A. SCHNEID-DEWIND, P. LINK, J. HU, T. XIANG, and P. DAI, *Physical Review Letters* **105**, 157002 (2010).
- [232] Z. XU, J. WEN, G. XU, S. CHI, W. KU, G. GU, and J. M. TRANQUADA, *Physical Review B* **84**, 052506 (2011).
- [233] S.-H. LEE, G. XU, W. KU, J. S. WEN, C. C. LEE, N. KATAYAMA, Z. J. XU, S. JI, Z. W. LIN, G. D. GU, H.-B. YANG, P. D. JOHNSON, Z.-H. PAN, T. VALLA, M. FUJITA, T. J. SATO, S. CHANG, K. YAMADA, and J. M. TRANQUADA, *Physical Review B* **81**, 220502 (2010).
- [234] B. C. SALES, A. S. SEFAT, M. A. MCGUIRE, R. Y. JIN, D. MANDRUS, and Y. MOZHARIVSKYJ, *Physical Review B* **79**, 094521 (2009).
- [235] [HTTP://WWW.ILL.EU/INSTRUMENTS-SUPPORT/INSTRUMENTS GROUPS/INSTRUMENTS/IN22](http://www.ill.eu/instruments-support/instruments-groups/instruments/in22).
- [236] L. P. REGNAULT, B. GEFFRAY, P. FOUILLOUX, B. LONGUET, F. MANTEGEZZA, F. TASSET, E. LELIÈVRE-BERNA, E. BOURGEAT-LAMI, M. THOMAS, and Y. GIBERT, *Physica B: Condensed Matter* **335**, 255 (2003).
- [237] Z. XU, J. WEN, G. XU, Q. JIE, Z. LIN, Q. LI, S. CHI, D. K. SINGH, G. GU, and J. M. TRANQUADA, *Physical Review B* **82**, 104525 (2010).
- [238] M. LIU, C. LESTER, J. KULDA, X. LU, H. LUO, M. WANG, S. M. HAYDEN, and P. DAI, *Physical Review B* **85**, 214516 (2012).
- [239] F. KRÜGER, S. KUMAR, J. ZAAANEN, and J. VAN DEN BRINK, *Physical Review B* **79**, 054504 (2009).
- [240] M. ARAI, T. NISHIJIMA, Y. ENDOH, T. EGAMI, S. TAJIMA, K. TOMIMOTO, Y. SHIOHARA, M. TAKAHASHI, A. GARRETT, and S. M. BENNINGTON, *Physical Review Letters* **83**, 608 (1999).
- [241] D. REZNIK, P. BOURGES, L. PINTSCHOVIOUS, Y. ENDOH, Y. SIDIS, T. MASUI, and S. TAJIMA, *Physical Review Letters* **93**, 207003 (2004).
- [242] C. STOCK, W. J. L. BUYERS, R. A. COWLEY, P. S. CLEGG, R. COLDEA, C. D. FROST, R. LIANG, D. PEETS, D. BONN, W. N. HARDY, and R. J. BIRGENEAU, *Physical Review B* **71**, 024522 (2005).
- [243] B. FAUQUÉ, Y. SIDIS, L. CAPOGNA, A. IVANOV, K. HRADIL, C. ULRICH, A. I. RYKOV, B. KEIMER, and P. BOURGES, *Physical Review B* **76**, 214512 (2007).

- [244] N. B. CHRISTENSEN, D. F. MCMORROW, H. M. RØNNOW, B. LAKE, S. M. HAYDEN, G. AEPPLI, T. G. PERRING, M. MANGKORNTONG, M. NOHARA, and H. TAKAGI, *Physical Review Letters* **93**, 147002 (2004).
- [245] M. MATSUDA, M. FUJITA, S. WAKIMOTO, J. A. FERNANDEZ-BACA, J. M. TRANQUADA, and K. YAMADA, *Physical Review Letters* **101**, 197001 (2008).
- [246] J. M. TRANQUADA, H. WOO, T. G. PERRING, H. GOKA, G. D. GU, G. XU, M. FUJITA, and K. YAMADA, *Nature* **429**, 534 (2004).
- [247] R. S. FISHMAN and S. H. LIU, *Physical Review B* **54**, 7252 (1996).
- [248] Y. ENDOH, T. FUKUDA, K. YAMADA, and M. TAKEDA, *Journal of the Physical Society of Japan* **63**, 3572 (1994).
- [249] R. D. LOWDE and C. G. WINDSOR, *Advances in Physics* **19**, 813 (1951).
- [250] T. MORIYA, *Spin Fluctuations in Itinerant Electron Magnetism*, Springer-Verlag, Berlin Heidelberg, Germany, 1985.
- [251] G. GRÜNER, *Density Waves in Solids*, Westview Press, Boulder, United States of America, 2000.
- [252] G. EHLERS, A. A. PODLESNYAK, J. L. NIEDZIELA, E. B. IVERSON, and P. E. SOKOL, *The Review of Scientific Instruments* **82**, 085108 (2011).
- [253] [HTTP://WWW.ISIS.STFC.AC.UK/GROUPS/EXCITATIONS/SOFTWARE/CHOPMANUAL6826.PDF](http://www.isis.stfc.ac.uk/groups/excitations/software/chop/CHOPMANUAL6826.PDF).
- [254] S. IKEDA and J. M. CARPENTER, *Nuclear Instruments and Methods in Physics Research Section A: Accelerators, Spectrometers, Detectors and Associated Equipment* **239**, 536 (1985).

# Acknowledgements

This work would not have been possible without the help and support by a number of people. Here I want to thank them for their contribution to this thesis.

Above all I thank **Prof. Dr. Thomas Brückel** for giving me the opportunity for this thesis. With the excellent scientific environment provided by his institute I had the chance to work on a challenging field, visit many interesting places, meet new people and experience top-level science at first hand. Without his contribution this project would never have materialized. I thank **Prof. Dr. Carsten Honerkamp** for agreeing to read my thesis and taking second reviewing duties of this work. Especially, I thank **Yixi Su** for his supervision of my thesis and all the support he provided in every aspect of my work. With your support, new ideas and our scientific exchange on a daily basis you had a major influence on the outcome of this project. I also want to thank you for all the beamtime we spent together at the ILL, ISIS and J-PARC. I really enjoyed working with you and appreciate all your support. I further thank **Yinguo Xiao** and **Shibabrata Nandi** who both supported me with my work. Thanks guys for all the beamtime we spent together in Grenoble, for helping me out with software issues, performing measurements for me in Jülich, our countless discussions and everything I forgot to mention. I really enjoyed working with both of you.

I also thank all the instrument scientists I worked with over the years. With their enthusiasm, constant effort and willingness to help in all aspects of the experiments they provided a comfortable working atmosphere and contributed in a major way to the success of my experiments. I thank **Louis-Pierre Regnault**, **Karin Schmalzl** and **Wolfgang Schmidt** for their great support to my experiments at D23 and IN22, **Devashibhai Adroja** and **Tatiana Guidi** for their support and their contributions to the experiments at ISIS, **K. Nakajima** and **S. Kawamura** for their support of my experiments at AMATERAS and of course **Yixi Su** for his help at DNS. The same appreciation goes to collaborating scientists **T. Wolf**, **H. S. Jeevan**, **A. Thamizhavel**, **S. Matsuishi** and **B. C. Sales** who provided me with high quality samples and by this had a strong impact on the success of my experimental work.

I thank all my fellow students and all the people at JCNS and the FRM-2 who provided this relaxed working atmosphere and helped to make my stay at JCNS Garching as comfortable as it was.

Finally, I thank Petra, my family and all my friends for the support and encouragement through the years that helped me finish this project. Thank you!





# Published Work

- **Evidence of spin resonance signal in oxygen free superconducting  $\text{CaFe}_{0.88}\text{Co}_{0.12}\text{AsF}$ : An inelastic neutron scattering study**

S. Price, Y. Su, Y. Xiao, D. Adroja, T. Guidi, R. Mittal, S. Nandi, S. Matsuishi, H. Hosono and T. Brückel, *Journal of the Physical Society of Japan* **82**, 104716 (2013)

All work considering this article: the neutron scattering measurements, data analysis, writing of abstract and main body of text, creation of all figures and the scientific content have been performed by myself in correspondence with the listed co-authors. The samples were allocated by co-authors S. Matsuishi and H. Hosono.



# Selbstständigkeitsversicherung

Ich versichere, dass die vorliegende Dissertation von mir selbstständig angefertigt wurde und dass benutzte Hilfsmittel vollständig angegeben und aus anderen Quellen stammende Daten sowie Abbildungen unter Angabe der jeweiligen Quelle gekennzeichnet sind. Ich versichere weiterhin, dass die vorliegende Arbeit weder im In- noch im Ausland in gleicher oder ähnlicher Form einer anderen Prüfungsbehörde vorgelegt, oder vorveröffentlicht wurde, abgesehen von gekennzeichneteter und angegebener Teilveröffentlichungen, die sich im Publikationsverfahren befinden. Weiterhin versichere ich, dass die vorliegende Arbeit keine bestehenden Betriebsgeheimnisse oder Urheberrechte verletzt. Die Bestimmungen der Promotionsverordnung sind mir bekannt. Die vorliegende Dissertation wurde von Prof. Dr. Thomas Brückel betreut.

München den 13.03.2013

Stephen Price



# Lebenslauf

**Stephen Price** 01.07.1977 (Solingen)  
2009-2013 Promotion Physik  
FZ-Jülich/RWTH Aachen  
*Interplay between Magnetism and Superconductivity  
in Iron Based High Temperature Superconductors*  
Betreuer: Prof. Dr. Brückel  
2003-2008 Diplomstudium Physik  
Universität zu Köln  
1999-2003 Diplomstudium Meteorologie  
Universität zu Köln (ohne Abschluss)  
1997-1998 Grundwehrdienst  
1997 Abitur



Band / Volume 65

**Solutions of Exercises in “An Introduction to Dynamics of Colloids”**

J. K. G. Dhont, K. Kang (2013), 143 pp

ISBN: 978-3-89336-882-2

Band / Volume 66

**Strukturelle und chemische Charakterisierung von selbst-assemblierten Monolagen organischer Moleküle auf Oberflächen**

M. Müller (2013), 168 pp

ISBN: 978-3-89336-883-9

Band / Volume 67

**Adsorption of (hetero-)organic Phthalocyanine and PTCDA thin films on Ag(111)**

C. Kleimann (2013), iv, 149 pp

ISBN: 978-3-89336-888-4

Band / Volume 68

**High-energy high-momentum surface spin waves of ultrathin epitaxial 3d transition metal films**

R. Jayaraman (2013), ix, 135 pp

ISBN: 978-3-89336-890-7

Band / Volume 69

**Magnetic Oxide Heterostructures: EuO on Cubic Oxides and on Silicon**

C. Caspers (2013), xiii, 153 pp

ISBN: 978-3-89336-891-4

Band / Volume 70

**Femtosecond Spin Dynamics in Magnetic Multilayers Employing High Harmonics of Laser Radiation**

D. Rudolf (2013), vi, 121 pp

ISBN: 978-3-89336-894-5

Band / Volume 71

**Development and application of a massively parallel KKR Green function method for large scale systems**

A. R. Thieß (2013), ii, 173 pp

ISBN: 978-3-89336-906-5

Band / Volume 72

**Conformational Dynamics of Calmodulin and Ribosome-Nascent Chain Complexes Studied by Time-Resolved Fluorescence Anisotropy**

P. Lamprou (2013), 182 pp

ISBN: 978-3-89336-907-2



Band / Volume 73

**Stereoselective synthesis of vicinal diols with enzymatic cascade reactions**

J. Kulig (2013), XV, 177 pp

ISBN: 978-3-89336-911-9

Band / Volume 74

**Computing Solids**

**Models, ab-initio methods and supercomputing**

Lecture Notes of the 45<sup>th</sup> IFF Spring School 2014

March 10 – 21, 2014 Jülich, Germany

ed. by S. Blügel, N. Helbig, V. Meden, D. Wortmann (2014), ca. 1000 pp

ISBN: 978-3-89336-912-6

Band / Volume 75

**Aberrationskorrigierte Photoemissionsmikroskopie an magnetischen Systemen: Von statischer Charakterisierung zu zeitaufgelöster Abbildung**

F. Nickel (2013), x, 99 pp

ISBN: 978-3-89336-913-3

Band / Volume 76

**Temperature-Induced Metamagnetic Transition and Domain Structures of Single-Crystalline FeRh Thin Films on MgO(100)**

X. Zhou (2013), xi, 104 pp

ISBN: 978-3-89336-919-5

Band / Volume 77

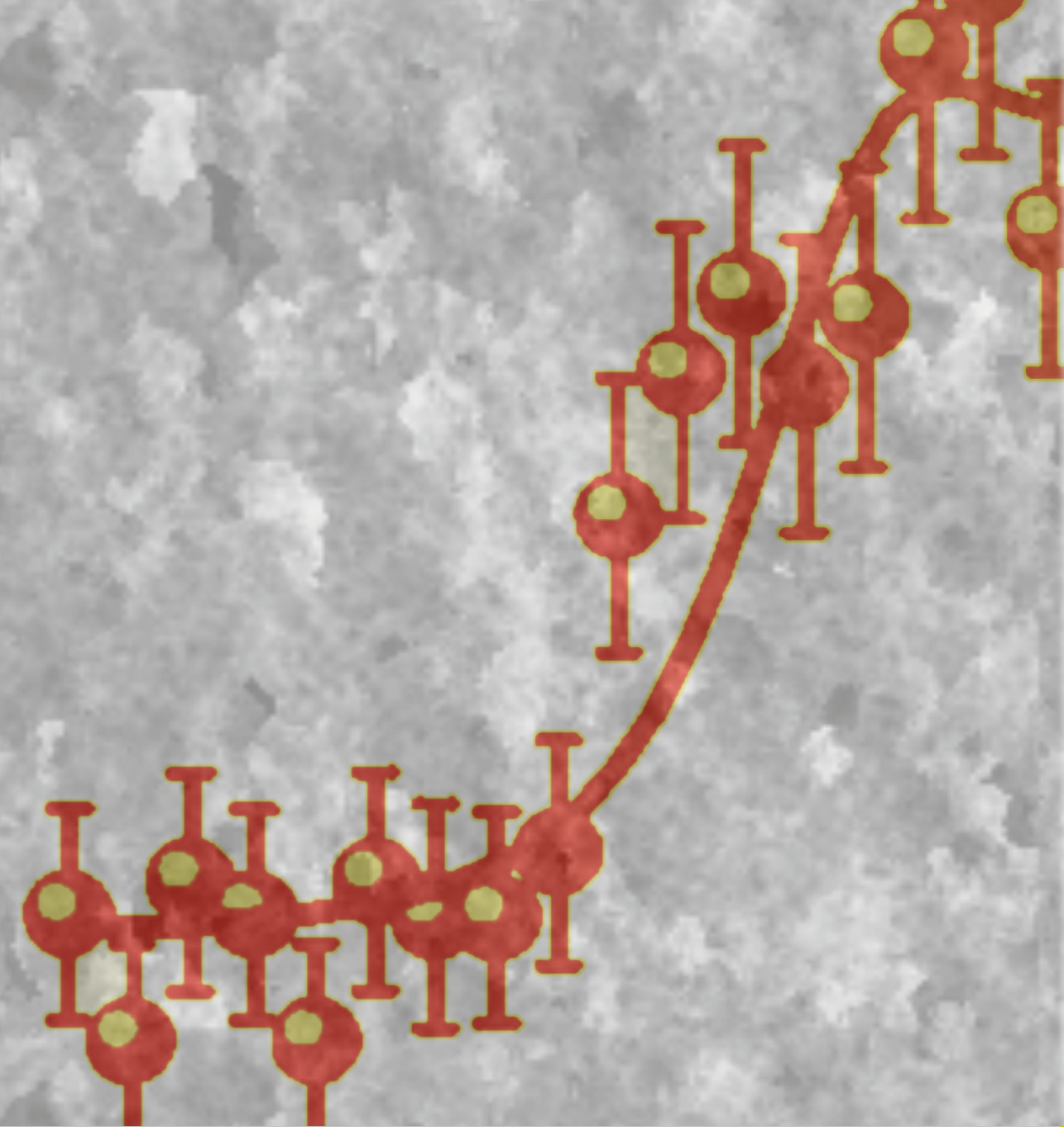
**Interplay between Magnetism and Superconductivity in Iron Based High Temperature Superconductors**

S. Price (2013), 196 pp

ISBN: 978-3-89336-921-8

Weitere **Schriften des Verlags im Forschungszentrum Jülich** unter  
<http://www.zb1.fz-juelich.de/verlagextern1/index.asp>





**Schlüsseltechnologien / Key Technologies**  
**Band / Volume 77**  
**ISBN 978-3-89336-921-8**